Pyrene based Metal Organic Frameworks.

Thesis submitted in accordance with the requirements of the University of Liverpool for the degree of Doctor in Philosophy by Thomas Ian Mangnall.

November 2015.

Contents

Abstract

Metal Organic Frameworks (MOFs) are a type of multifunctional porous material. Comprised of metal centres or metal clusters known as Secondary Building Units (SBUs) linked together into an extended 1, 2 or 3 dimensional structure by bridging organic ligands coordinated to the metal SBUs. MOFs offer the opportunity to customise the pore size and chemical functionality of the framework. The degree of customisation possible from the wide array of different metal clusters and organic ligands MOFs have been proposed for many applications such as gas storage, separation, catalysis, photocatalysis, sensing and drug delivery. In this thesis the synthesis and characterisation of pyrene based MOFs is presented and the hydrogen evolution photocatalytic applications are tested. This thesis contains details on three different MOFs. Firstly a new aluminium pyrene MOF which was characterised and tested for photocatalysis and CO_2 and CH_4 storage applications; which also had platinum nanoparticles successfully incorporated within the pores. Secondly a very recently reported zirconium pyrene MOF was made, had its photocatalytic applications explored for the first time and had platinum deposited within the pores. Thirdly a new Europium Pyrene MOF was developed using high throughput techniques and its new structure was calculated from single crystal XRD.

Extended Abstract

Chapter 1 contains an overview of the history of MOF chemistry, the applications of MOFs and notable examples of MOFs utilised for those applications.

Chapter 2 contains a description of the various synthesis techniques used for MOF chemistry and an explanation as to the various characterisation methods used.

Chapter 3 describes the synthesis of the 1,3,6,8-tetrakis(p-benzoic acid)pyrene ($TBAPyH_4$) linker used throughout this thesis and the synthesis of AlTBAPy and how these synthesis conditions were arrived at. There is also contained the characterisation methods and results for the AlTBAPy MOF. The initial characterisation was carried out using Powder XRD techniques and this chapter describes how those results were used to establish the structure of the AlTBAPy MOF; using a least squares unit cell refinement technique to compare it to a known isostructural MOF. Also SEM images were measured to show that the material was phase pure. CHN combustion analysis combined with results from the thermogravimetric analysis confirmed the composition of the AlTBAPy MOF. The nitrogen adsorption isotherm was also measured for AlTBAPy in order to determine the porosity and surface area of the MOF. Optical spectroscopy, namely UV/Vis and fluorescence spectra were measured showing that there is a strong absorption of visible light, corresponding to the $\pi \rightarrow \pi^*$ transition in the pyrene and a strong fluorescence corresponding to the pyrene $\pi^* \rightarrow \pi$ decay. There was minimal difference from the free $TBAPyH_4$ optical properties. Water splitting hydrogen evolution reactions were carried out using a suspension of AlTBAPy in a solution of Na_2EDTA as a sacrificial electron donor, colloidal platinum nanoparticles as a cocatalyst and sodium citrate to buffer the mixture to pH 6, this reaction was done with and without methyl viologen as an electron transfer reagent. No hydrogen was produced in either reaction though the AlTBAPy was able to photocatalytically reduce the methyl viologen. The reduced methyl viologen should have been able to proceed with the reaction however when the suspension settled it was clear that the reduced methyl viologen remained trapped within the pores of the AlTBAPy while TEM images showed the platinum on the surface. Platinum nanoparticles were

photo deposited within the AlTBAPy and the Pt@AlTBAPy was characterised by PXRD, CHN and ICP-OES elemental analysis and nitrogen adsorption isotherms to demonstrate the successful insertion. The hydrogen evolution reaction was repeated to the same result. Also the AlTBAPy was tested for CO_2 adsorption for carbon capture and storage applications. The CO_2 adsorption isotherm was measured at three different temperatures and the heat of adsorption calculated. The AlTBAPy showed results typical for similar MOFs but was less effective than state of the art materials which have been reported. The AlTBAPy was also tested for methane storage applications, again three isotherms were measured at different temperatures and the heat of adsorption calculated. The heat of adsorption for Methane for AlTBAPy was close to the ideal value for the reversible storage of methane.

Chapter 4 describes our synthesis of the recently reported NU-1000 and the characterisation methods and results for the NU-1000 synthesised here. This material was characterised in a similar way to the AlTBAPy in chapter 3. The photocatalytic applications of NU-1000 were tested for the first time; water splitting hydrogen evolution reactions were carried out following a similar procedure to the tests done using the AlTBAPy contained in chapter 3. No hydrogen was produced in either reaction though the NU-1000 was able to photocatalytically reduce the methyl viologen. Again it became clear once the MOF had settled out of suspension that the reduced methyl viologen remained trapped within the pores of the NU-1000 while TEM images showed the platinum on the surface. Platinum nanoparticles were photo deposited within the NU-1000 for the first time and the Pt@NU-1000 characterised by PXRD, CHN and ICP-OES elemental analysis and nitrogen adsorption isotherms. The hydrogen evolution reaction was repeated to the same result.

Chapter 5 describes the high throughput methods utilised to develop the synthesis of a new Europium Pyrene MOF. The optimum synthesis conditions for producing a sample of crystals of EuTBAPy large enough to be used for SCXRD and the conditions required to produce phase pure EuTBAPy sample are also reported. The structure as calculated from the SCXRD pattern is reported and a least squares refinement carried out on the PXRD pattern measured for the bulk phase to demonstrate that it is the same structure. SEM images are presented demonstrating that the synthesis produces a phase pure material without amorphous impurities while CHN combustion analysis and thermogravimetric analysis demonstrate the composition of EuTBAPy.

Acknowledgements.

This thesis is the conclusion of four years' work not just by myself but with the help and assistance of many others. Firstly, I would like to thank my supervisor Prof Matt Rosseinsky for all of his helpful advice and suggestions, it has been a privilege to learn from him and his extensive scientific knowledge. I am grateful for the opportunities provided working in such a large well-funded research group. I would also like to thank my secondary supervisor Dr John Claridge who was always available for discussion and willing to impart his experience and knowledge of the world of science. I would also like to thank Prof Jim Darwent for his help with the photocatalysis aspects of this work, his friendly and informative discussions were highly useful. A great deal of thanks must go to Jane Remmer who was able to deal with any admin problem which may arise and offer advice what preparations were required for meetings with Matt.

I would also like to thank Dr Carlos Marti Gastaldo the help, assistance and information on MOF chemistry, synthesis and characterisation willingly and patiently provided in the early days of my PhD were invaluable. I'd also like to thank Dr Alex Katsoulidis for his highly informative discussions on MOFs and his help especially with adsorption measurements. Dr John Warren, Dr Garry Miller and Dr George Whitehead the group crystallographers who measured and analysed SCXRD patterns for me and helped me with analysis of PXRD patterns along with Dr Phil Chater who also helped me with PXRD. I was helped with the development and execution of my organic synthesis by Dr Michael Briggs and Dr Mark Prestly both of who gave up their time to ensure I was performing the synthesis correctly and to help me scale up and optimise the synthesis. Also I wish to thank Dr Chris Ireland and Dr Bo Liu for their help and advice with the photocatalysis experiments. Thanks

also go to Dr Marco Zanella for measuring my electron micrographs while demonstrating how the instrument works, also for his help with all the equipment. I would also like to thank Dr Hongjun Niu and Mike Chatterton for maintain the equipment and helping me to understand how it works and how to fix common problems with many pieces of equipment.

Thanks must go to the whole group though, every member of the group has been a help in some way and has made the four years very enjoyable. Especially of note was Oliver Wilcocx who started on the same day as myself so as we went through the process of a PhD together, Jibreel Hadad for being nice/gullible enough to do any favour I asked of him, Tim Johnson as any conversation is improved by terrible tortured puns, Rachel Coulter and her many rabbits and also Zoe Taylor, Harry Sandson, Darren Hodgeman, Anita Peacock, Dr Noemie Perret, Dr Hripsime Gasparyan and no doubt several others. Also to my friend Christopher Grey on our ongoing research project continuing from undergrad to rate as many ales as possible.

I also most importantly wish to thank my mum Christine for her support and encouragement, without which none of this would have been possible. I'd also like to thank my whole family especially, my Uncle Sid, Aunty Sylvia, Grandma, Aunty Viv, Sister Emily and my Nan who sadly passed away the day before my Viva.

Abbreviations.

bdc	Benzene Dicarboxylate
BET	Brunner-Emmett-Teller Model
bpdc	Biphenyl Dicarboxylate
COF	Covalent Organic Framework
DEF	Diethylformamide
DMF	Dimethylformamide
EtOH	Ethanol
5-FU	Fluorouracil
GC	Gas Chromatography
HOMO	Highest Occupied Molecular Orbital
IRMOF	Isoreticular Metal Organic Framework
LMCT	Ligand To Metal Charge Transfer
LUMO	Lowest Unoccupied Molecular Orbital
MeOH	Methanol
MLCT	Metal To Ligand Charge Transfer
MOF	Metal Organic Framework.
MV	Methyl Viologen dichloride
NMR	Nuclear Magnetic Resonance Spectroscopy
PBS	Phosphate-buffered saline
PXRD	Powder X-Ray Diffraction
Py	Pyrene
SBU	Secondary Building Unit
SCXRD	Single Crystal X-Ray Diffraction
SEM	Scanning Electron Microscope

$TBAPyH_4$	1,3,6,8-tetrakis(p-benzoic acid)Pyrene
TEM	Transmission Electron Microscope
TGA	Thermogravimetric Analysis
THF	Tetrahydrofuran
UV/Vis	Ultra Violet/Visible Light Spectroscopy
XRD	X-Ray Diffraction

1. Introduction

1.1. General Introduction

Metal Organic Frameworks (MOFs) are an interesting and exciting class of porous materials. Their varied composition enables them to exhibit many different properties opening up a wide range of potential applications including separations, gas storage, catalysis, photocatalysis, sensing and drug delivery.[1-8] Composed of metal cations or metal cation oxide or hydroxide clusters which are connected into a framework by forming coordination complexes with bridging organic linkers, usually di, tri or tetra carboxylates, though several imidazolate and peptide based MOFs have been reported.[9, 10] The variety of different metals with different coordination geometries and chemical characteristics combined with the wide range of potential bridging linkers means that there are a wide range of topologies of MOF available with varying pore sizes and surface areas which can be tailored to the application required.[12-19] MOFs can also be synthesized with free metal sites, reactive functional groups on the organic linkers or postsynthetically modified to include reactive moieties into the framework. This also allows a very diverse range of reactivity from MOFs, coupled with the large internal surface area which can prove highly useful for heterogeneous catalysis and adsorption applications.[7, 26, 28, 29]

1.2. Porous Materials

Porous materials have been studied for over a century as their porosity endows them with many useful properties. The porosity allows for applications as molecular sieves, for gas separation and storage while the large internal surface area provides an advantage for heterogeneous catalysis. Porous materials are divided into three categories depending on the diameter of their pores. Microporous materials

have a pore size diameter below 20 Å, mesoporous materials have a pore size diameter between 20 and 500 Å while materials with a pore size above 500 Å are defined as being macroporous.[30] It is also possible to define porous materials by their composition of which there are three main types, inorganic porous materials such as zeolites and aluminosilicates, organic porous materials such as organic cages and covalent organic frameworks (COFs) and hybrid porous materials such as metal organic frameworks (MOFs).

1.2.1. Inorganic Porous Materials

The first type of porous material to be discovered was the zeolites. Naturally occurring in volcanic rock they were first discovered in 1756 when A.F. Cronstedt heated a sample of stilbite and noted the steam emitted as the water within the pores was boiled off. Zeolites are a type of aluminosilicate with the general formula of $M_{x/y}^{n+}[(AlO_2)_x(SiO_2)_y]^{x-}$. The zeolite structure arises from varying ratios of corner sharing AlO_4 and SiO_4 tetrahedra with M^{n+} as a counter ion, usually an alkali or alkaline earth metal (see Figure 1). It was with the development of synthetic zeolites by Union Carbide in the 1940's and early 1950's and the exploration of their potential properties that zeolite chemistry began to emerge.[31, 32] However it is still difficult to tailor the pore size to the application required simply by varying the ratio of Si to Al within the framework; this problem was solved through the addition of organic templates to the reaction mixture. These organic templates, usually quaternary ammonium salts where the size of the organic groups could be changed to produce different templating effects, as the cation acts as the counter ion M in the zeolite; direct the formation of the AlO_4 and SiO_4 tetrahedra to adopt different topologies which would not be possible without the organic template.[33] The organic template can then be removed by acid washing or calcination leaving an empty pore

space.[34] Further structural variation can be achieved by replacing two Si^{+4} ions by one Al^{+3} or Ga^{+3} and one P^{+5} ion. This opens up the possibility of the group 13 ions adopting trigonal bipyramidal or octahedral geometries altering the structure of the material. These alumina-phosphates and gallo-phosphates are able to adopt structures with much larger pores than zeolites, in some cases with diameters across the pores up to 29-30 Å.[35, 36]

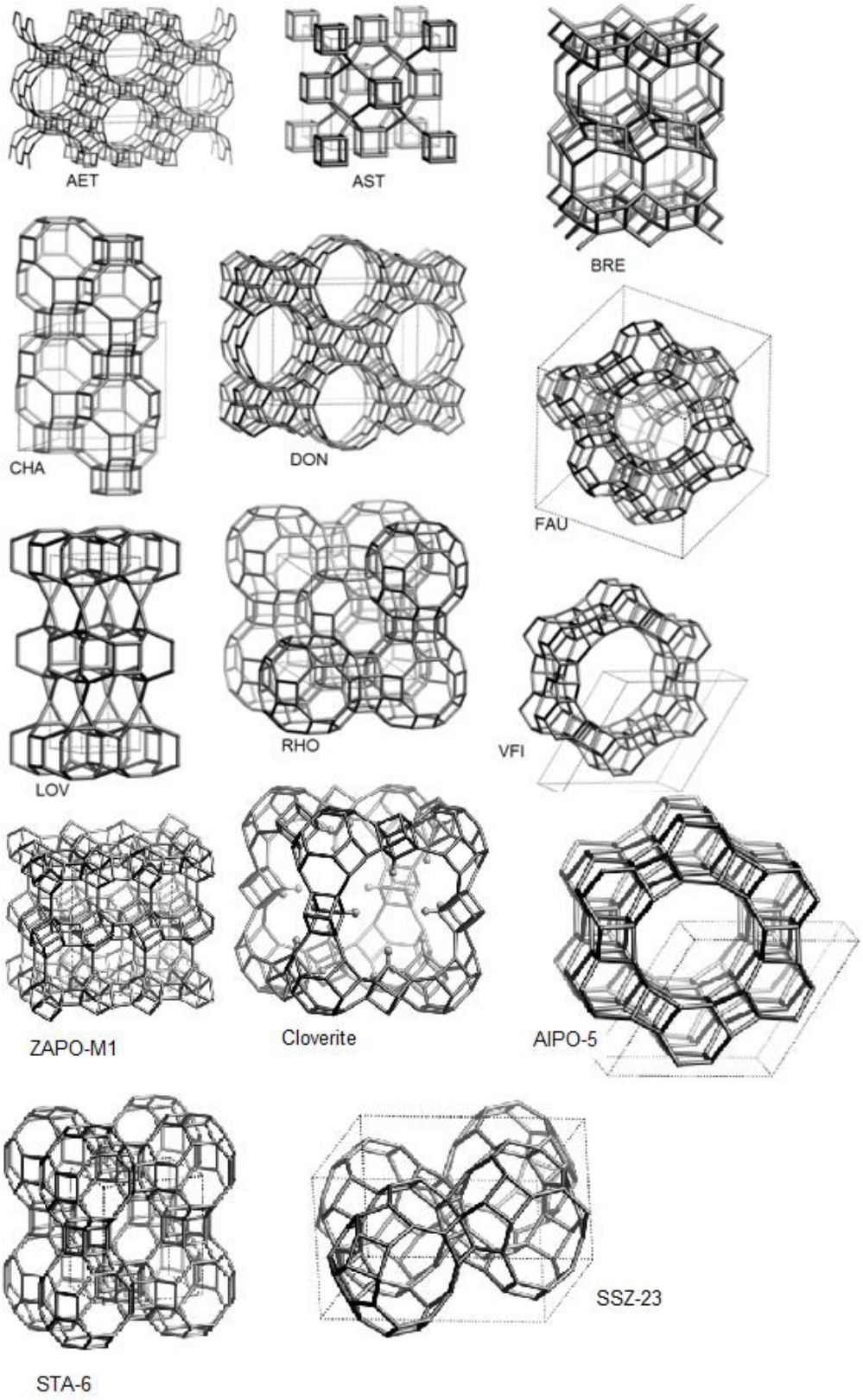

Figure 1: A selection of some of the different Zeolite topologies reported showing the variation in structure and pore size and shape possible. Figure adapted from reference [37].

Hundreds of different of zeolite frameworks have been reported with many different pore shapes and sizes (see Figure 1). Zeolites have been reported containing small slit like channels such as ZAPO-M1, with channels with diameters of 2.5 Å X 5.1 Å ringed by 8 tetrahedra. Yet some Zeolites can be synthesised with very large pores up to the 20 tetrahedra ringed pores with diameters of 4.0 Å X 13.2 Å of cloverite. Also as well as a wide range of pore sizes there are different shapes of pore, many zeolites have symmetrical circular pores which can be a range of different sizes in different zeolites such as the 7.3 Å diameter 12 tetrahedra pores of AlPO-5 or the 4.2 Å diameter 8 tetrahedra pores of STA-6. There are zeolites which have narrow slit like pores such as the 9 tetrahedra pores of SSZ-23 which have pore diameter of 3.7 Å in height and 5.3 Å in the width. There are also zeolites which have channels running in 1, 2 or 3 dimensions through the structure.[37] This range of possible pore sizes and shapes means zeolites are highly useful porous materials for size or shape selective applications such as molecular sieving or selective catalysis.

Zeolites can be used for catalysis where Brønsted acid sites within the framework protruding into the pores can catalyse reactions. Including the cracking of long chain hydrocarbons into shorter ones and isomerisation reactions can also be catalysed. [33] The advantage of using a zeolite is that the pore size offers size selectivity for these reactions. It is also possible to use zeolites as molecular sieves for separations; the pores are capable of separating gas molecules of different sizes as only molecules smaller than the pores of the zeolite can enter, larger molecules will pass quickly around the zeolite. Zeolites are also used for ion exchange where the loosely bound non framework cations can be exchanged for different ions, this is useful in the purification of polluted water or the softening of heavy drinking water.[33]

1.2.2. Organic Porous Materials

One of the problems with inorganic porous frameworks is a lack of functionality severely limiting their use as catalysts and restricting their use for adsorption. This can potentially be overcome by using organic compounds which are much more easily functionalised. Polymerisation of monomers with a rigid geometry allows the production of either a porous organic cage or an extended covalent organic framework (COF).[20, 38] There are a variety of different synthesis methods for producing porous organic materials, condensation using Suzuki or Sonogashira coupling, imine condensation, boron condensation and triazine trimerization have all been reported as popular synthesis routs to organic porous materials.[20, 38-40] The first COF was reported by Côté et al and synthesised by condensing phenyl diboronic acid to produce COF-1 and hexahydroxy triphenylene to produce COF-5. Through π-π interactions the 2D sheets formed from these condensation reactions produced porous 3D frameworks (see Figure 3) which exhibited large surface areas of 711 m^2g^{-1} for COF-1 and 1590 m^2g^{-1} for COF-5,demonstrating the high degree of porosity displayed by these materials.[20] Fully covalent 3D COFs are more difficult to synthesise but have been reported. By substituting the planer monomer with a tetrahedral monomer a 3D structure can be synthesised. COF-108 was an early 3D fully covalent framework reported by El-Kaderi in 2007 and at the time was the least dense crystalline material reported. Synthesised from tetrahedral tetra(4-

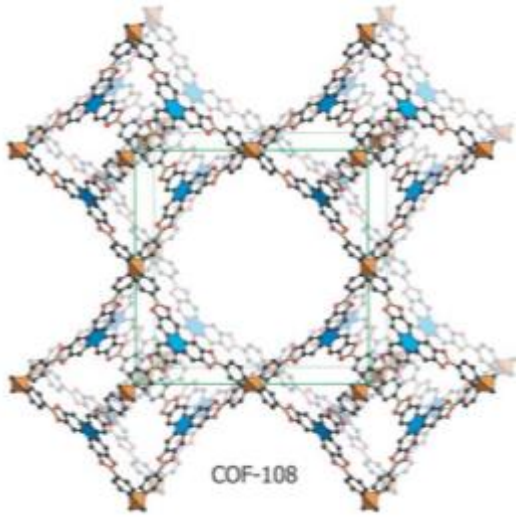

Figure 2: Structure of COF-108. C is coloured grey, B orange and O red Figure adapted from reference [22].

dihydroxyborylphenyl)silane and triangular hexahydroxytriphenylene using boron condensation produced the highly porous COF-108 (see Figure 2).[22]

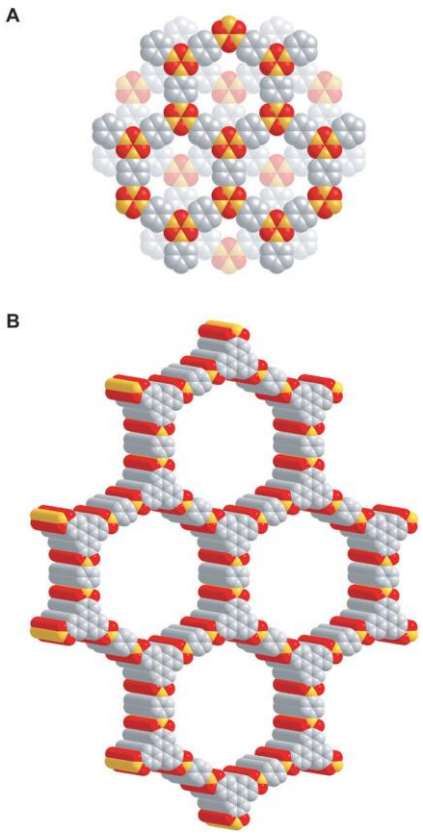

Figure 3: Structure of COF-1 (A) & COF-5 (B). C is coloured grey, B yellow and O red. Figure adapted from reference [20].

COFs have been reported to be very good at gas storage in particular to hydrogen, methane and carbon dioxide. It has been reported that COFs which contain medium sized 3D pores are more effective at gas adsorption than 2D COFs, however 3D COFs are much more difficult to synthesise. COF-102 a 3D COF composed of tetra(4-(dihydroxy)borylphenyl)methanecondensed using dehydration of the boron acid produces a B_3O_3 ring acting as a node joining each tetrahedral monomer to another. COF-102 was reported as being superior to any other COF for gas adsorption, it exhibited uptakes of 72.4 mg g^{-1}, 187 mg g^{-1} and 1200 mg g^{-12} of hydrogen, methane and carbon dioxide respectively. The large adsorption of gas within this COF is related to its large BET surface area of 3620 m^2g^{-1} with larger surface areas corresponding to greater adsorption of gasses.[41] However despite these advantages organic porous materials prove difficult to synthesise and many are unstable rapidly decomposing with exposure to moisture or heat.

1.2.3. Hybrid Porous Materials/Metal Organic Frameworks (MOFs)

It is possible to have further control of the topology of the porous framework produced and access to a greater degree of functionality if metal cations are used as

the nodes of the framework. It is possible to utilise the set coordination geometries of the transition metals, arising from the directionality of the d orbitals, coupled with a rigid organic linker with bridging coordination modes can be combined to produce a Metal Organic Framework (MOF). The range of different metal and linker geometries available results in a highly diverse range of possible structures. MOFs are a kind of porous coordination polymer composed of metal cation or metal cation clusters bridged by rigid organic linkers. There have been a great many different linkers and different kinds of linker used for MOF synthesis; carboxylate linkers are the most commonly used, the bidentate carboxylate potentially providing greater stability and a wider range of possible coordination geometries; however, nitrogen based linkers have also been used (see Figure 4). Figure 4 shows some of the organic linkers which have been used in MOF synthesis, the wide range of different sizes and shapes of molecules is clear. Larger organic linkers will produce MOFs with larger pores as has been shown by the UiO series of MOFs whereby addition of further phenyl rings to the linear molecule, replacing benzene dicarboxylic acid with biphenyl dicarboxylic acid and triphenyl dicarboxylic acid, extends the linker and thus expands the pores.[19] It's also possible by adding more carboxylic acids to the linker to extend the connectivity, many MOFs use a dicarboxylic acid linker in order to link two SBU nodes but it is possible to enhance the stability and produce MOFs with different topologies and pore size and shapes by using tri or tetra carboxylates or linkers which can link 4 SBUs. Non linear linkers are also an effective way to tailor the pore size and shape, naphthalene or alkene based linkers can be used to produce unusual pore shapes while triangular or square linkers can also be used. An additional advantage of MOFs is that functionality can be introduced to the organic linker, a reactive site, hydrophobic chain or metal accepting site such as a bipyridyl

or porphyrin can be incorporated into the organic linker expanding the possible chemistry the resultant MOF can perform.

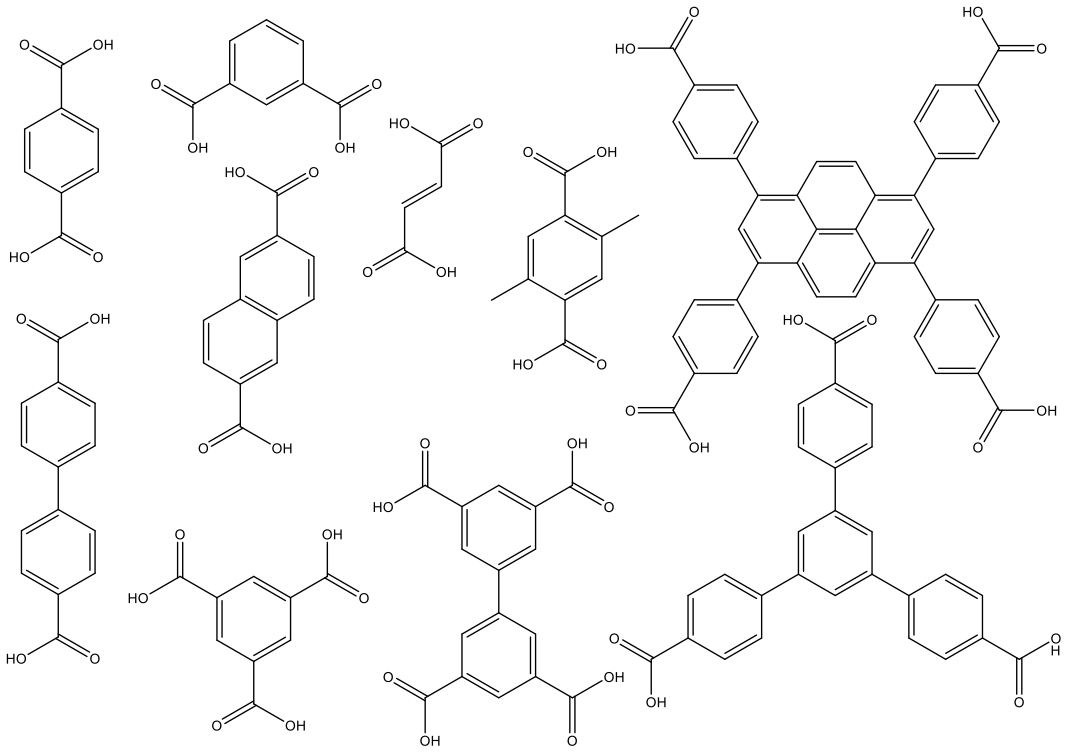

Figure 4: Common Organic Linkers used for MOF synthesis.

Many metals not only produce complexes with individual metals but also form clusters with the carboxylates of the organic linkers and any hydroxide ligands in the solution synthesis. These clusters are often used for the synthesis of MOFs as the greater coordination number they usually offer results in a more stable framework while opening up a wider range of possible geometries. There have been over 131 carboxylate transition metal clusters have been reported which can act as SBUs and can exhibit coordination numbers from two up to sixty six.[42] The different SBU complexes not only allow for a wide range of potential MOF structures but also many contain open metal sites which can be used for catalysis or to enhance gas storage applications.[28] A variety of different common SBUs are shown in Figure 5. The $Zr_6O_4(OH)_4(RCO_2)_{12}$ cluster of the UiO series of MOFs is noted for its high

stability, the large coordination number and the oxophilicity of zircronium makes the UiO MOFs highly stable.[19] The $Zn_4O(RCO_2)_6$ SBU utilised for the IRMOF series was first reported for MOF-5; the ease at which MOFs with a wide variety of different carboxylate linkers can be synthesised containing this SBU soon lead to zinc becoming one of the most popular metals to use in MOF synthesis despite its limited stability.[25] The copper paddlewheel SBU first used in the MOF HKUST-1 is also a widely used SBU; although only offering connectivity in 2 dimensions in a square shape the copper Paddlewheel does contain removable water bonded axially protruding into the pores of the MOF, through heating it is possible to remove these water molecules and expose open metal sites which can be used for catalysis or post synthetic modification.[17] Many MOFs have also utilised Chromium as the metal source as it is frequently stable and can adopt several different SBU clusters which unlike zirconium and zinc MOFs are susceptible to hydrolysis from water; commonly the cluster for MIL-101 containing three chromium octahedra linked by an oxygen is produced and produces a geometry of tetrahedral cages with large pore sizes of up to 29 Å.[43] When a 3+ metal cation is used such as aluminium or iron the metal does not adopt a distinct cluster but rather forms an infinite chain running in one direction through the MOF parallel to the other chains; these chains are composed of M^{3+} octahedra with the carboxylates of the linker linking adjacent octahedra in the equatorial position while the octahedra are also joined by a shared hydroxide group in the axial position. This was first seen in the Aluminium MOF MIL-53 and the flexibility of this chain allows the MOF to breathe and reversibly change shape as different solvents are added to the pores.[13] Titanium can also be used as a metal source for MOF synthesis and results in an unusual eight membered

ring consisting of TiO_5OH octahedra. In the case of MIL-125 these rings are linked by benzene dicarboxylate linkers to twelve others.[44]

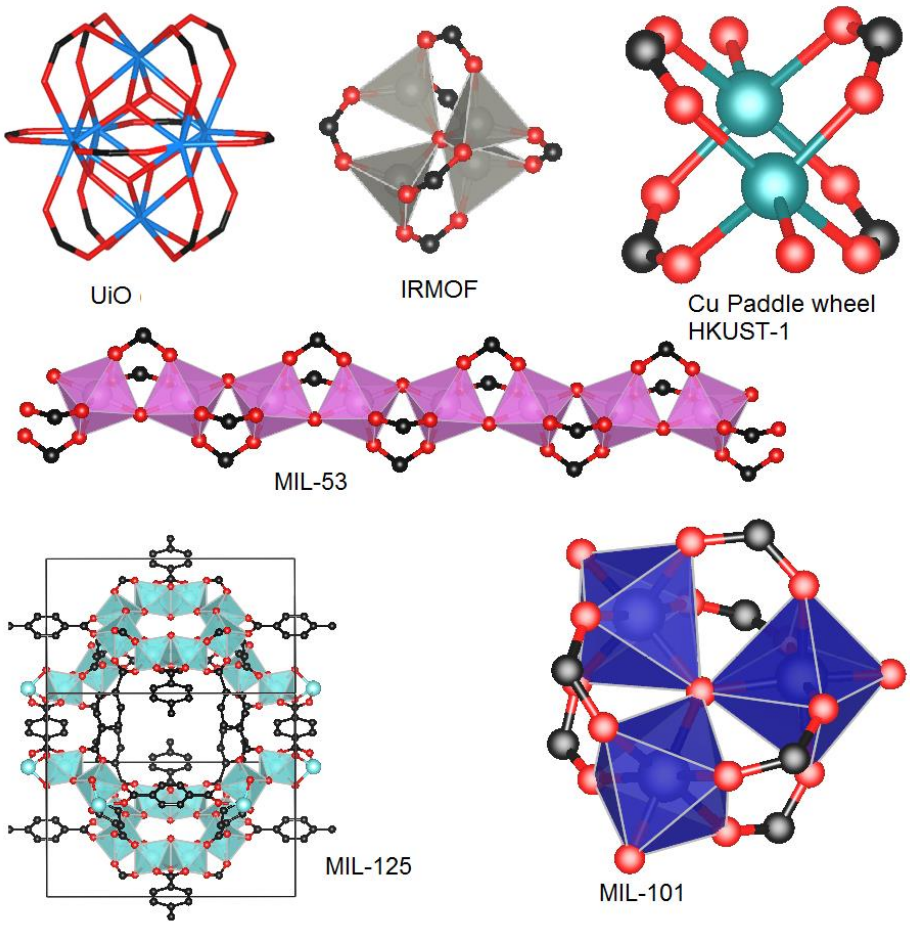

Figure 5: Selected SBU of some MOFs. In all examples O is red and the organic linker is black. UiO blue is Zr, IRMOF Zn is grey, HKUST-1 Cu is turquoise, MIL-53 Al is pink though most M^{+3} cations adopt similar structures, MIL-125 Ti is light blue and MIL-101 Co is dark blue.[13, 17, 25, 43-45]

The wide range of possible SBU coordination environments and linker shapes and sizes allows a wide range of framework topologies with tuneable pore sizes and shapes which can be tailored to the required application. While functionality can be introduced easily either onto the open metal sites of the SBU or incorporated into the linker post synthetic modification where some of the linkers or the cations in the

framework may be exchanged or nanoparticles introduced into the pores can also been readily performed with many MOFs further enhancing the potential functionality and applications of MOFs.[15, 46-48] However there are difficulties with MOFs, most critically their chemical and moisture stability. Many MOFs are unstable to water, some even decomposing when in contact with the moisture in the air, the water replaces the linkers on the SBU causing the framework to collapse. Many other MOFs show stability to moisture but then when activated the surface tension of the solvent within the pores being removed causes the framework to collapse necessitating a complex activation procedure.[49, 50]

1.2. History of Metal Organic Frameworks and Common Examples

Coordination polymers have been known and studied since the late 1950's though it was not until 1989 when Hoskins and Robson synthesised a highly porous framework consisting of Cu^{+} coordinated to four tetrahedral 4,4',4",4"'-tetracyanotetraphenylmethane molecules that the first MOF was synthesised (see Figure 6).[16, 51]

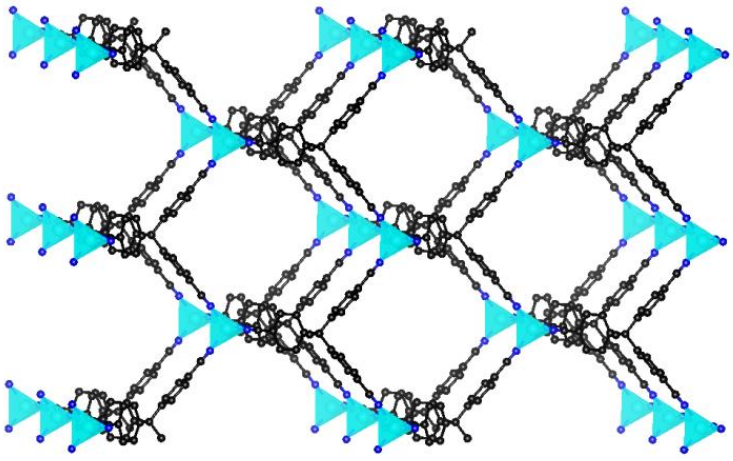

Figure 6: $Cu[C(C_6H_4CN)_4]$. Cu is coloured light blue tetrahedra, N dark blue and C black.[16]

The potential variety of different topologies synthesised by using interchangeable metals and organic linkers in the synthesis was instantly identified however it was not until nine or ten years later when MOF-2, $Ni_2(4,4'\text{-bipy})_3(NO_3)_4$, HKUST-1 and MOF-5, the first MOFs to retain their structure and crystallinity upon activation that MOF Chemistry began to move forwards at an increased rate.[12, 17, 52, 53]

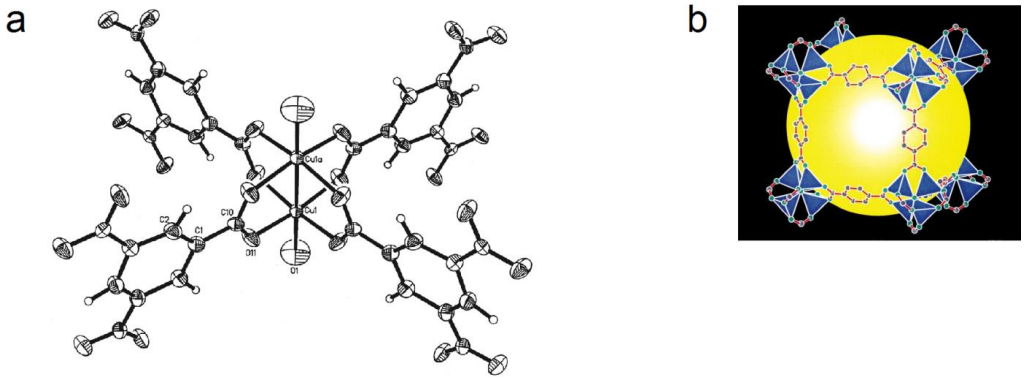

Figure 7: a: Structure of HKUST-1. Figure adapted from reference [17]. b: Structure of MOF-5, Zn is coloured blue, O green and C grey. Figure adapted from reference[12].

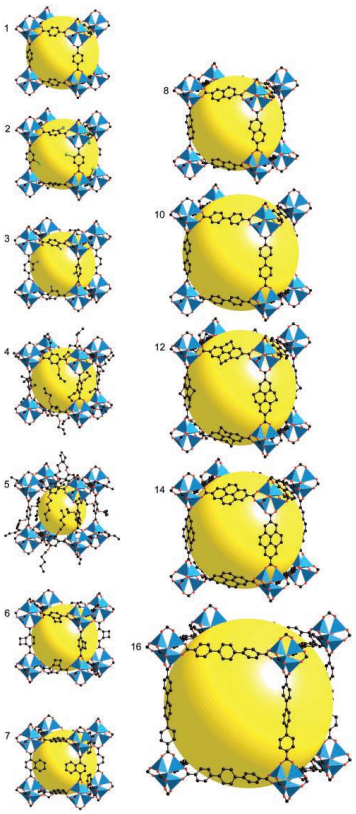

Figure 8: The IRMOF series of MOF, $Zn_4O(CO_2R)_6$ clusters linked by a variety of linkers. Figure adapted from reference [25].

HKUST-1 was a copper based MOF comprised of two copper ions bridged by four carboxylates from benzene tri-carboxylate linkers with axial hydroxide groups on each copper (see Figure 7a). HKUST-1 showed the potential for postsynthetic modification of MOFs, although impossible to synthesise directly once the HKUST-1 MOF had been synthesised it was possible to exchange the hydroxides for pyridine, greatly enhancing the functionality of the MOF.[17]

MOF-5 (or IRMOF-1) was synthesised as part of a series of MOFs composed of $Zn_4O(CO_2R)_6$ clusters linked by benzene dicarboxylate linkers (see Figure 7b). It was found that it was possible to replace the benzene dicarboxylate linker in the synthesis with a range of different organic dicarboxylate linkers of different sizes and with different functionalities; thus demonstrating the versatility of MOF synthesis and how once the synthesis conditions have been identified how easily a wide range of MOFs with different pore sizes and different functionalities could be produced simply by using a different linker (see Figure 8).[25] However, although the IRMOF series of MOFs demonstrated stability when activated and at high temperatures up to 300 °C there were limitations with the chemical stability; unstable to water IRMOFs would collapse after a few hours exposure to the moisture in the air as the water

displaced the linkers. This instability severely limits the potential applications for many Zinc MOFs.

MIL-53 utilised an unusual aluminium SBU, composed of an infinite chain of $Al(OH)_2(O_2CR)_2$ octahedra with the hydroxides and carboxylates bridging adjacent octahedra, the chains being linked by benzene dicarboxylate linkers to produce a porous framework (see Figure 9).[13] MIL-53 also highlighted an unusual property of some MOFs, though stable when activated and soaked in water the structure would reversibly change, the pores narrowing when water was present. This breathing effect arises as hydrogen bonding between the water and the oxygens on the Aluminium chain causes the chain to twist and the structure to distort narrowing the pores (see Figure 9).[13]

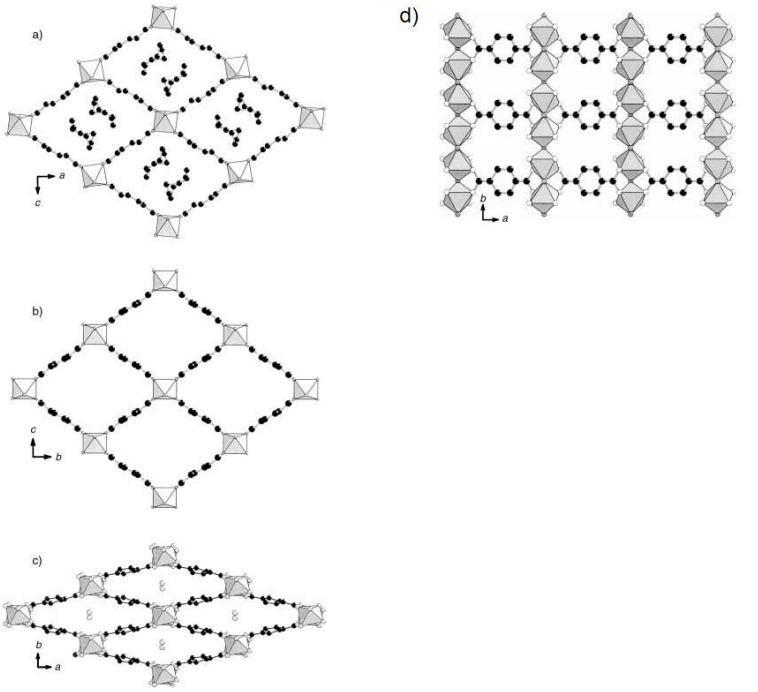

Figure 9: Structure of MIL-53. a) Showing the structure of the as made material with solvent within the pores. b) Showing the structure of the activated MIL-53. c) Showing how the structure changes when water enters the pores of MIL-53. d) Showing the chains of $AlO_4(OH)_2$ octahedra. Figure adapted from reference [13].

With a high charge density and high oxophilicity coupled with its propensity to form clusters zirconium has been used to produce highly stable MOFs. The UiO series of MOFs are composed of a Zr_6 octahedron capped across the faces by alternating oxides and hydroxides with the Zirconium ions linked across the edges of the octahedron by the carboxylate groups of the linker (see Figure 10b), benzene

dicarboxylate in the case of UiO-66, biphenyl dicarboxylate in the case of UiO-67 and triphenyl dicarboxylate in the case of UiO-68, this results in twelve linkers bound to each SBU cluster which provides great stability (see Figure 10).[19] This arrangement forms a series of octahedral and tetrahedral cages which confer a large pore volume and internal surface area to the UiO-66, this is further enhanced through the extension of the organic linkers to produce UiO-67 and UiO-68.[45] However although the UiO series of MOFs are water stable the large porosity of UiO-67 and UiO-68 mean that removal of a solvent with a high surface tension, such as water, from within the pores does result in the structure collapsing.[54]

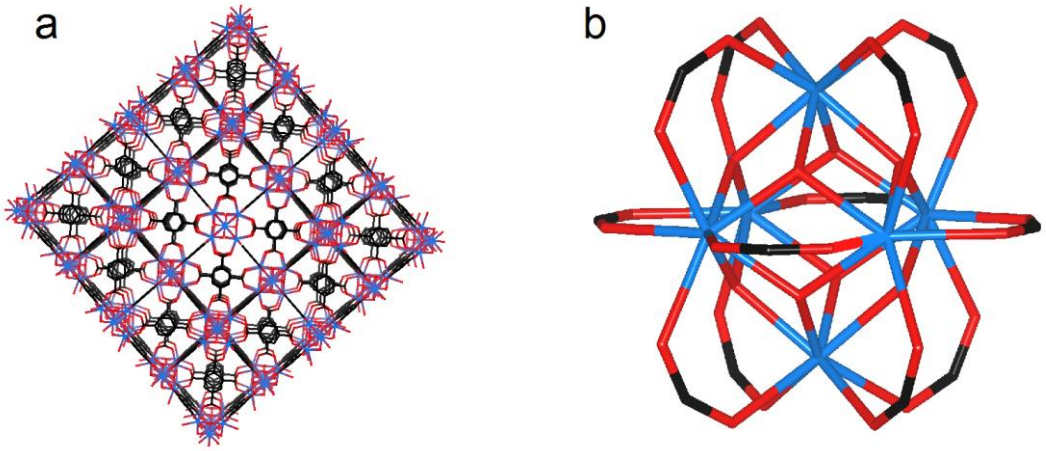

Figure 10: a: Structure of UiO-66. b: Structure of the SBU of the UIO family of MOFs.[45]

There have been other noteworthy MOFs reported including MOFs with porphyrin based linkers which have shown applications for gas separation and photocatalysis, bio-MOFs have been synthesised using peptide linkers to make then biologically compatible and MOFs have been synthesised from lanthanides to produce unusual fluorescent structures.[10, 18, 55, 56]

1.3. Applications of Metal Organic Frameworks

1.3.1. Separation

Separation and purification of mixtures of gases and liquids is an essential process in chemistry in order to purify a product after synthesis or to separate isomers such as the isomers of xylene, or removing pollutants such as carbon dioxide from waste streams.[5, 57] Methods for separation include distillation, crystallisation, extraction, adsorption, absorption and membrane separation. Distillation is the most common method used in the chemical industry however it is not always a feasible method for thermally unstable compounds or compounds with similar boiling points and can be energy expensive to heat large amounts of material.[58] One of the easiest ways to perform separation is by passing the mixture through a column packed with a porous material which will have a different affinity to some of the molecules in the mixture over others and thus be able to separate them through adsorptive separation. Adsorptive separation depends on steric, kinetic and equilibrium effects and the different interactions between the components of the mixture and the adsorbent. Most separations have been performed using silica, zeolites or activated carbons however the ability to precisely control the pore size and the ease of functionalization inherent to MOFs has lead them to becoming effective new candidates for use in separations. There are several different mechanisms by which separation may take place:

1. Molecular sieving effect. The size or shape of the pores prevent one of the substances in the mixture from entering which is thus able to flow through the column unimpeded while the other substance is able to enter the pores and is either slowed or trapped by interactions with the pore walls of the adsorbent.

The molecular sieving effect has been utilised to a great extent in zeolites which find their main use as molecular sieves; however of primary importance in separations especially of small similarly sized gas molecules is a narrow pore size distribution and precise control of the pore size which MOFs can offer. A MOF has been reported composed of manganese ions linked by very short formate linkers in an octahedral geometry, this produces very small pores, only 5.5 Å in diameter and joined by windows only 4.5 Å in diameter. These small windows mean that large gas molecules such as Ar, N_2 and CH_4 can not enter the pores while smaller molecules like H_2 and CO_2 can enter and adsorb within the MOF pores and thus be separated from mixtures of gasses.[59]

2. Thermodynamic equilibrium effect. This arises where the adsorbent material has different interactions to different adsorbates and so one is preferentially adsorbed onto the surface of the material. An amine functionalised MIL-53 synthesised using 2-aminoterephthalic acid as the linker has been reported for separation of CO_2 and CH_4. The basic amine sites have a strong affinity for the CO_2 while the lack of apolar adsorption sites for the CH_4 results in the MOF having very low uptake of CH_4.[60] The strength of this interaction is able to completely separate the CO_2 and isolate pure CH_4 at room temperature and atmospheric pressure, adsorbing 0.83 mmol g^{-1} CO_2 while no CH_4 was adsorbed by the MOF at all.[60]
3. The Kinetic effect arises due to different diffusion rates through the pores of a MOF. Hexane has various isomers which must be separated to enhance their use in fuels, this is currently done using cryogenic distillation which is a difficult and costly procedure. A zinc based MOF has been synthesised using

two different linkers, 1,4-benzenedicarboxylate (BDC) and 1,4-diazabicyclo [2,2,2]octane (dabco), these two linkers result in a structure which has two different sized pores running through it (see Figure 11). nHexane with its small linear chain structure is capable of passing through both sets of pores and as such experiences a much greater affinity to the MOF than the branched 3-methylpentane, and 2,2-dimethylbutane which can only enter the larger channels. This means that this MOF is capable of separating these three isomers.[61]

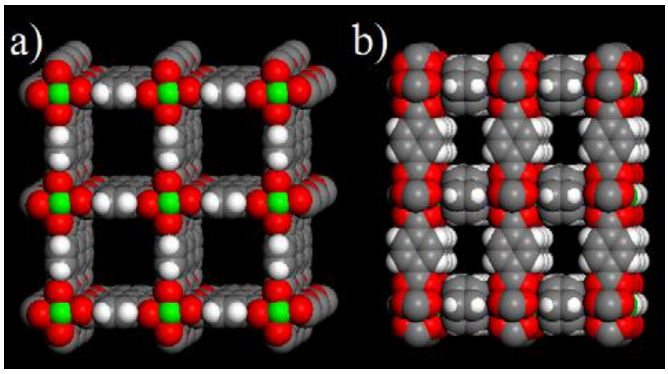

Figure 11: Structure of Zn(BDC)(Dabco)0.5 showing the two different sized channels. Zn is coloured green, C grey, O red, N blue & H white. Figure adapted from reference [61].

4. The Quantum Sieving Effect. This effect arises in materials with sub-nanometre sized pores where the difference between the pore size and the hard core of the molecule is not significantly larger than the de Broglie wavelength.[62] The main use is for the separation of tritium and deuterium from hydrogen, the heavier isotopes having a greater affinity to the porous material.[63] Calculations have been performed on several MOFs to look for quantum sieving effects, the $Cu(Fpymo)_2$ MOF with pores of 2.9 Å diameter and the CPL-1 MOF with pores 3.0 Å diameter were capable of separating tritium, deuterium and hydrogen through quantum sieving effects.[64]

1.3.2. Gas Storage

Storage of gases is a problematic issue, to date gasses have to be stored under high pressures, this causes issues with safety due to the risk of explosion in the case of flammable gasses or a sudden release of any high pressure gas if the canister was to be damaged; coupled with this there is the heightened cost required for the compressors needed to fill the high pressure canisters. By adsorbing the gas into the pores of a porous material the same volume of gas may be transported a much lower pressure and therefore more safely. There are two ways in which a gas can adsorb onto a material, through van der Waals interactions in a process known as physisorption; this requires a large surface area as larger surface areas result in larger Van der Waals attractions; the alternative is chemisorption where a chemical bond is formed between the adsorbent and the adsorbate. The advantage of MOFs is that they possess a large internal surface area and their pore size and shape can be tailored to suit the application which can enhance physisorption. While the ease of functionalising MOFs to enhance chemisorption means that they prove highly useful for gas storage applications.[65, 66]

Hydrogen gas has been identified as a potential fuel to be used, it is carbon free and therefore more environmentally friendly than currently used fuel derived from oil, as such hydrogen would be a highly desirable energy source. However hydrogen gas has a very low density and therefore needs to be highly compressed or liquefied to be transported in sufficient quantities to be of use, this requires compressors and/or cryogenics both of which are expensive both financially and energetically. In order to overcome this a lightweight porous material is required which is capable of reversibly adsorbing hydrogen onto the surface and storing it at a density similar to that of liquid hydrogen. The current target for density of Hydrogen

stored is set out by the U.S. Department of Energy to be 1.8 kg(H_2) kg(System)$^{-1}$ by 2020 with an ultimate aim of 2.5 kg(H_2) kg(System)$^{-1}$.[67] Although it would be expected that a higher surface area would result in greater adsorption it has been found that this is not necessarily the case for hydrogen adsorption into the pores of MOFs. The NOTT family of MOFs are composed of $Cu_2(H_2O)_2(O_2CR)_4$ paddle wheel units linked by biphenyl, terphenyl and quatraphenyl tetracarboxylic acids.[68] By extending the linker length the surface area was increased, from 1670 m^2g^{-1}, 2247 m^2g^{-1} and 2932 m^2g^{-1} respectively; however the amount of hydrogen gas uptake at 1 bar remains similar 2.59%, 2.52% and 2.24%.[68] This suggest that the Van der Waals interaction between the hydrogen and the internal surface of the MOF is weak and the uptake is optimised when the pores are small enough that there is an interaction between the hydrogen and both sides of the pore wall; as the pore becomes larger the attractive potential field of the opposite wall falls away. [68] However many MOFs have coordinatively unsaturated free metal sites and interactions between the hydrogen and the metal can be exploited to enhance the uptake of hydrogen by the MOF. The copper based MOF-505 is composed of four 3,3',5,5'-biphenyltetracarboxylic acid linkers coordinated to two copper ions each copper ion with a water molecule bound to it in the paddle wheel motif (see Figure 12). It was found that the hydrogen uptake capacity was greatly enhanced by removing the water molecules from the copper SBU to expose the metal.[69] MOF-505 undergoes two different mass loses under activation, during this the surface area increases from 967 m^2g^{-1} through 1343 m^2g^{-1} to 1830 m^2g^{-1} however the hydrogen adsorption capacity increases from 14.1 mg g^{-1} to 19.7 mg g^1 during the first mass loss then as the water is removed from the copper ions in the MOF the hydrogen adsorption capacity

increases drastically to 24.7 mg g^{-1} showing there is strong chemisorption of Hydrogen to the open Copper sites.[69]

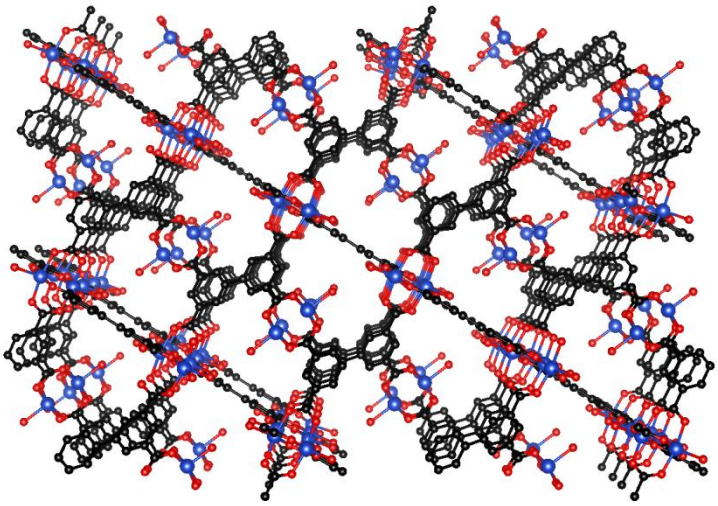

Figure 12: Structure of MOF-505 showing the removable Water Oxygens protruding into the pores of the MOF. Cu is coloured blue, O red and C Black.[69]

Another potential gas which can be used as a fuel which is cleaner, cheaper and more readily available than petroleum derived fuels is methane from natural gas. However methane storage poses similar problems to that of hydrogen with its low energy density meaning the storage and transport of natural gas in sufficient quantities to be useful proves difficult.[11] A potential solution to this problem again would be the liquefaction of the gas, however this process involves several compressions to produce high enough pressures and so the infrastructure required is too expensive to become widely available. Also once liquefied the gas must be kept cold to prevent boil off, meaning large amounts of heavy insulation is required to keep the storage tanks cold.[1, 11] It has been found that the ideal pore size and shape for the adsorption of methane into a MOF are long slit like pores with a diameter of 7.6 Å, wide enough to form a monolayer of methane on each side of the pore.[11] With methane adsorption the heat or enthalpy of adsorption is critical, too low and insufficient methane will be adsorbed, too high and the methane will not be released

to be used, calculations show that the optimum heat of adsorption for a storage material for methane is 18.8 kJ mol^{-1}. Mg_2(dobdc) and Co_2(dobdc) both exhibit initial heats of adsorption around this value however the heat of adsorption diminishes rapidly once the free metal sites on the MOF have become occupied (see Figure 13).[11] Similarly to hydrogen adsorption the interaction between both pore walls and open metal sites are important in methane adsorption. PCN-14 is a MOF composed of the copper paddlewheel SBU linked by 5,50-(9,10-anthracenediyl)di-isophthalate (adip), PCN-14 contains both open metal copper sites and a large anthracene based linker which can act as a second pore wall while allowing the MOF to maintain a large pore volume (see Figure 14). PCN-14 exhibits an absolute methane adsorption of 230 v/v which is larger than the Department of Energy target of 180 v/v and one of the largest methane capacity of a MOF reported to date. However the heat of adsorption is also one of the highest reported at 30 kJ mol^{-1} which will limit the applications of this MOF.[70]

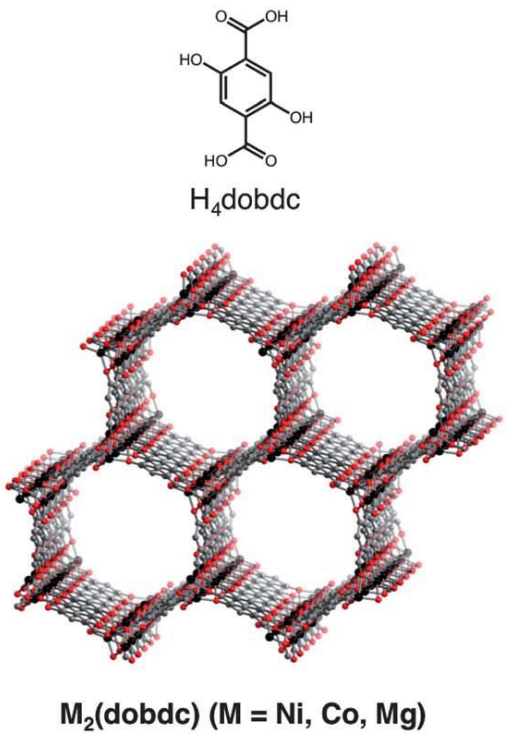

Figure 13: Structure of Mg_2(dobdc) and Co_2(dobdc) . Mg and Co are coloured black, C is grey and O red. Figure adapted from Reference [11].

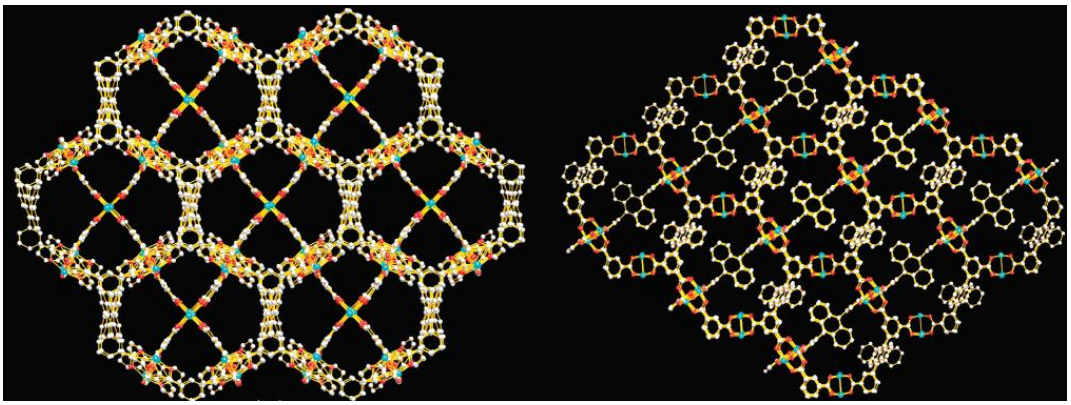

Figure 14: Structure of PCN-14. Figure adapted from reference [70].

Acetylene is also a widely used gas for welding and in the chemical industry. However acetylene is a highly explosive gas and when stored at pressures over 2 atm can undergo exothermic reaction to produce benzene and vinylacetylene causing the acetylene to explode.[65] The MOF MAF-2 which is composed of a copper diethyl triazolate framework with ethyl groups protruding into the pores which stabilises the interaction between the acetylene and the MOF (see Figure 15), has been reported to adsorb 102 v/v at 1.5 bar of acetylene, 40 times more than can be stored in a gas cylinder.[71] The X-Ray diffraction results show the acetylene to be located around the ethyl groups indicating a strong interaction between the two (see Figure 15). [71]

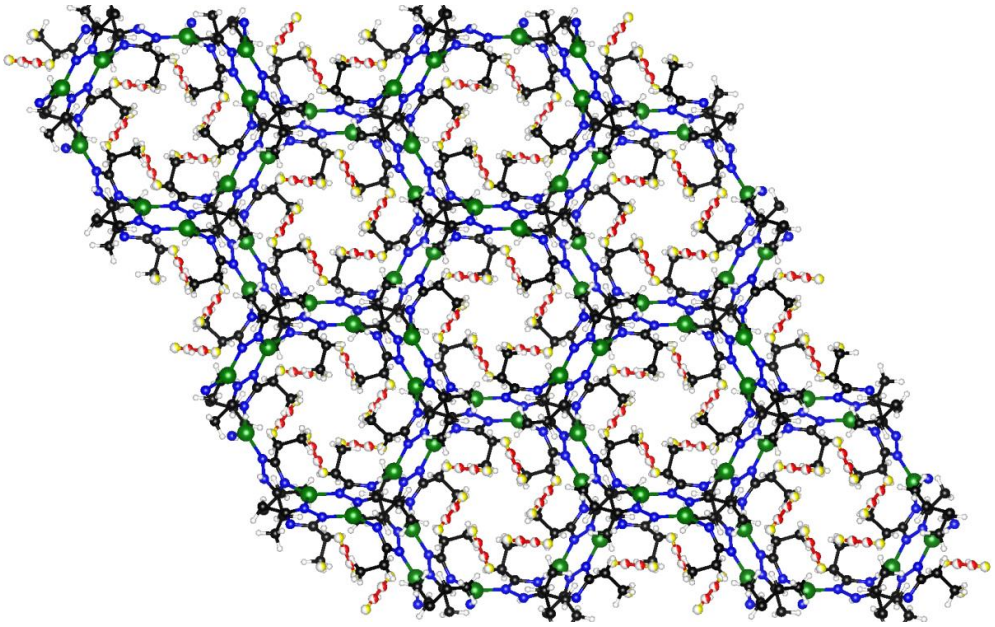

Figure 15: MAF-2. Structure showing the ethyl groups protruding into the pores of the MOF and the interaction of the Acetylene with the MOF. Framework Cu is coloured green, C black, N blue, H white. Acetylene C is coloured red & Acetylene H yellow, fractional occupancy is identified by the proportion of each atom coloured. [71]

MOF-74 is composed of 2,5-dihydroxyterephthalate linking either Co, Mn, Mg or Zn based SBUs with open metal sites in four isostructural MOFs. These MOFs have been tested for acetylene adsorption and it has been shown that the adsorption amount and the energy of adsorption increases with the ability of the metal to polarise the acetylene with the largest adsorption being for Co then Mn then Mg then Zn, the CoMOF-74 is capable of adsorbing 230 v/v.[72]

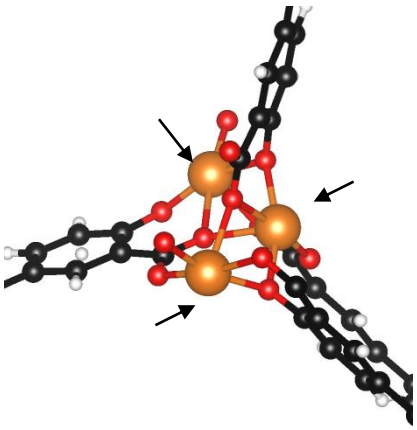

Figure 16:Structure of Mg2(dobpdc) Mg cluster showing open metal sites indicated with arrows. Mg is orange, C is black O is red.[26]

It is not just fuel gasses which MOFs show applications for storage, the environmental impact from CO_2 emissions causing global warming is a cause for concern; ways of capturing and storing CO_2 are being looked at as a way of reducing

emissions. The current technology uses amine scrubbers which although have a high uptake are difficult to reactivate.[57, 73] As has been the case for other gasses adsorbed by MOFs free metal sites enhance the adsorption of CO_2. The Mg_2dopdc MOF is composed of magnesium clusters joined by 4,4-dioxido-3,3'-biphenyldicarboxylateexhibits (see Figure 16), this MOF exhibits a large adsorption capacity for CO_2 of 4.85 mmol g^{-1} due to its open magnesium metal sites.[26] Alternatively by incorporating a basic group into the MOF framework the attraction between CO_2 and the base will enhance adsorption. The PEI-MIL-101-100 MOF contains polyethyleneimine chains bound to the chromium cluster SBUs, the basicity of which provides an adsorption capacity for CO_2 of 4.02 mmol g^{-1} (see Figure 17).[24]

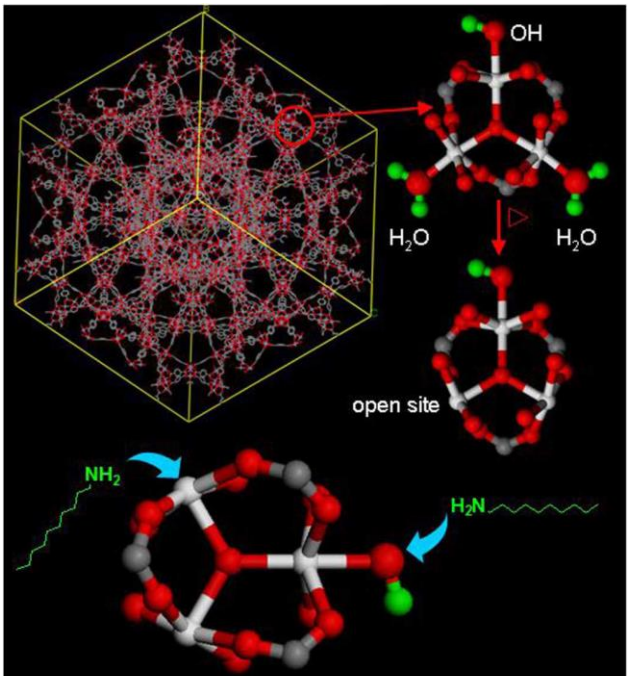

Figure 17: Structure of MIL-101 and how polyethyleneimine is incorporated into the MOF from PEI-MIL-101-100. Figure adapted from reference [24].

1.3.3. Drug Delivery

Many drugs which are highly effective in small doses over long time periods can have damaging effects if administered in one large amount, a way of administering the drug where it can then be released slowly is desirable. One way of doing this is to encapsulate the drug into a MOF. With large surface areas and pore sizes which can be varied to suite the adsorbate required, coupled with the ease of functionalization and post-synthetic modification to bind to the drug MOFs display

great potential as drug delivery systems. Also while much MOF research is attempting to enhance the stability of MOFs some instability allowing the framework to decompose slowly is a desirable characteristic for drug delivery, the decomposition products can be metabolised and expelled from the body thus preventing the accumulation of MOF within the body; also the slow decomposition of the MOF may be used as the method for releasing the drug. There are some problems however with MOFs used for drug delivery; many of the metals used in MOF construction are toxic, however there have been many MOFs reported using metals the toxicity of which is acceptable for their use in medicine, metals such as Ca, Cu, Mn, Mg, Zn, Fe, Ti and Zr can all be used. The toxicity of the linker must also be considered, many linkers are suitable for biological applications especially polycarboxylates, imidazolates and amines. Ideally however a linker would be used which can be metabolised by the body, however few MOFs containing these endogenous linkers have been reported, most commonly they contain amino acids such as glutamic acid, nucleobases such as adenine or saccharides such as γ-cyclodextrin.[74] Another difficulty particular to MOFs for biological applications arises due to the crystallite size. To have biological applications the crystallites must be small enough to be suspended in solutions within the body's cells.[74] Various synthesis methods have been reported which produce nanocrystalites of MOF including ultrasonic and microwave synthesis, where reaction times can produce a pronounced effect on the crystallite size.[75, 76]

Like many materials MOFs exhibit different stabilities in different pH mediums, as cancerous tumour cells are a lower pH than healthy cells, pH 5 as opposed to pH 7.4, this variable stability can be utilised for targeted delivery of anti-cancer drugs directly to the tumour minimising the often severe side effects of these

drugs. ZIF-8 is a zinc based MOF composed of Zn(2-methylimidazolate)$_2$. ZIF-8 contains large 11.6 Å pores with a large surface area of 1630 m^2g^{-1}, this means it exhibits a high uptake of the anti-cancer drug Fuorouracil (5-FU) adsorbing up to 45.4 wt%. The 5-FU loaded ZIF-8 was then placed in phosphate-buffered saline (PBS) buffer at pH 7.4 where the MOF was stable for up to a week; 50% of the 5-FU diffuses out of the pores of the MOF quickly upon immersion in PBS buffer while the rest of the 5-FU diffuses out slowly over the course of the week. The 5-FU loaded ZIF-8 was also tested in pH 5.0 acetate buffer where upon it decomposed completely releasing all the 5-FU (see Figure 18). This shows that MOFs can be used for targeted drug delivery, releasing most of the drug quickly only when inside the cells where the drug is required, drastically reducing side effects and the dose required.[77]

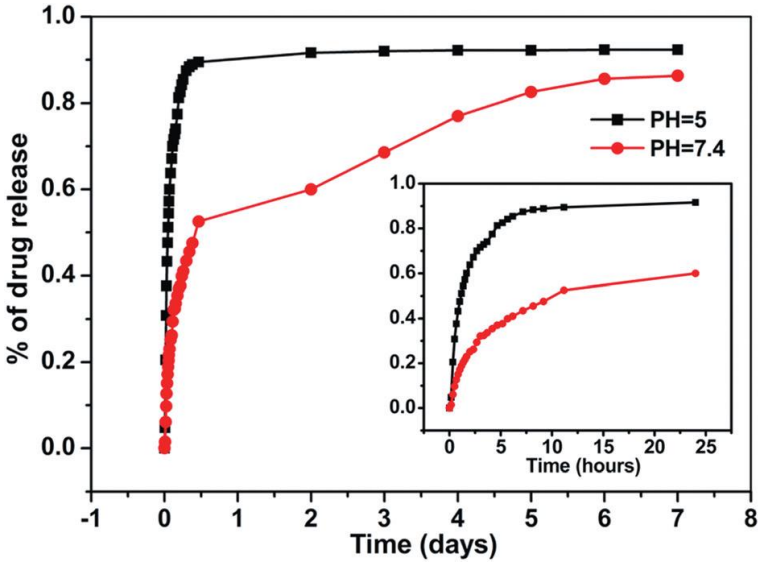

Figure 18: 5-Fu delivery from ZIF-8 Inset shows the release process from 0 to 24 h. Figure adapted from reference [77].

1.3.4. Sensing

There have been many MOFs reported which exhibit fluorescent properties, these can arise in several different ways. Intraligand fluorescence arises where a

fluorescent ligand is incorporated into the framework, such as the pyrene based 1,3,6,8-tetrakis(p-benzoic acid)pyrene in the indium based InTBAPy MOF.[14]

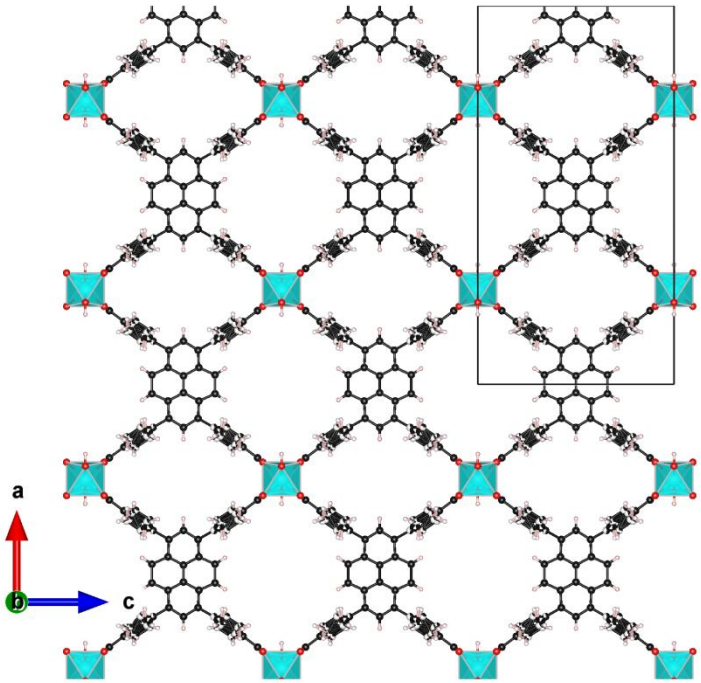

Figure 19: Structure of the InTBAPy MOF. In is coloured blue, C black and O red.[14]

The advantage of using a MOF is that for many of these organic fluorescent compounds the excited state is quenched due to interactions between the molecules, which is inhibited in the MOF framework as all the linkers are held apart across the pore space; or through non radiative decay arising from vibration and rotation of the molecule which again is inhibited due to the rigid framework of the MOF. The InTBAPy MOF is capable of sensing a variety of different types of molecules as various host-guest interactions alter the structure of the MOF and thus affects the emission. Polar aprotic guests such as DMF increase the porosity and order in the MOF which blue shifts the fluorescence from the activated MOF, while hydrogen bonding with water results in a decrease in excited state lifetime and a red shifting of the fluorescence. Non polar solvents also affect the structure and fluorescence of

InTBAPy resulting in a lowering of the fluorescence intensity when dioxane or toluene is present.[14]

It is also possible to produce MOFs with fluorescent metals, usually lanthanides where the f-f transitions produce fluorescence especially when attached to an antenna which can be incorporated into the linker.[78] A MOF composed of europium linked by 2'-fluoro-biphenyl-3,4',5-tricarboxylate linkers has been synthesised which exhibits strong florescence from the f-f transitions of the europium when activated (see Figure 20). However, the introduction of small organic molecules into the pores of the MOF quenches the europium fluorescence to different degrees, DMF for example shows no quenching of the fluorescence, methanol, ethanol and propanol show increasing quenching while acetone quenches the fluorescence completely. Also studied was the effect of various metal ions in a solution of DMF when introduced to the MOF; the closed shell ions showed minimal effect on the fluorescent quenching while other metal ions showed varying degrees of quenching, especially copper cations which almost completely quenched the Europium florescence.[79] This is due to the different interactions between the quencher and the exposed Europium sites which can be seen in the crystal structure, occupied by the oxygen of a water molecule, exposed to the open pore space (see Figure 20).

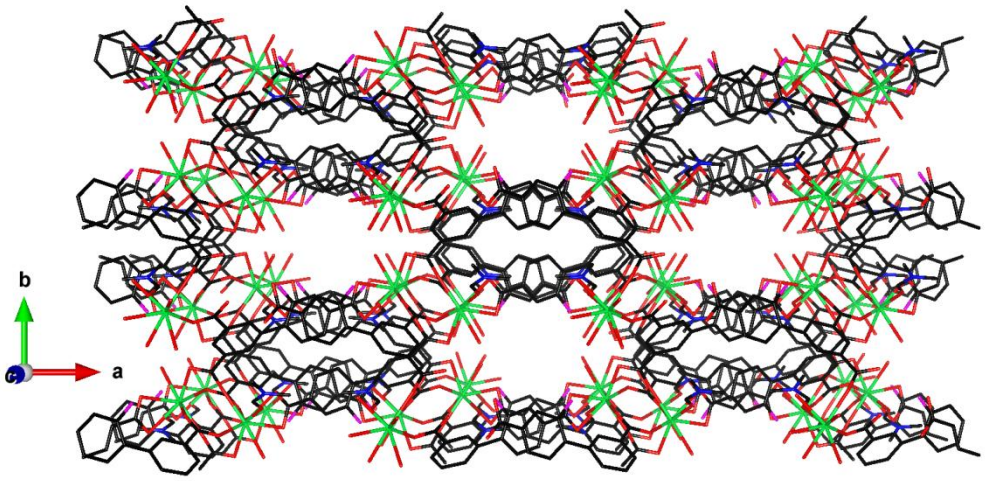

Figure 20:Europium 20-fluoro-biphenyl-3,40,5-tricarboxylate MOF. [79]

MOFs can also be used for sensing due to the absorption of light due to the d-d transitions from their transition metals present in the SBU. The copper based MOF HKUST-1 contains water coordinated to the copper sites, this water can be removed by heating the MOF to over 100 °C leaving free metal sites which is accompanied by a colour change from turquoise to dark blue, this colour change is reversible when the MOF is re-exposed to water vapour.[17]

1.3.5. Catalysis

MOFs also have displayed applications in heterogeneous catalysis. A large internal surface area is beneficial for any catalyst but the ease the pore size can be tailored for size selective catalysis also provides another potential advantage for using MOFs. There are different ways MOFs can act as catalysts, MOFs with open metal sites can act as Lewis acids or linkers with catalytic activity can be incorporated into the structure. A MOF has been reported which uses 1,3,5-benzenetristetrazol-5-yl (BTT) as a linker with Mn^{+2} to produce a $Mn_3[(Mn_4Cl)_3(BTT)_8(CH_3OH)_{10}]_2$ MOF which contains open Mn^{+2} sites (see Figure 21). These Mn^{+2} sites are Lewis acidic and so capable of catalyzing cyanosilylation reactions of aromatic aldehydes and ketones. Not only were high yields for the reaction reported but also that size selectivity was seen due to the pore size of the MOF, the larger biphenyl and 4-phenoxyphenyl substituted reagents produced much lower yields.[27]

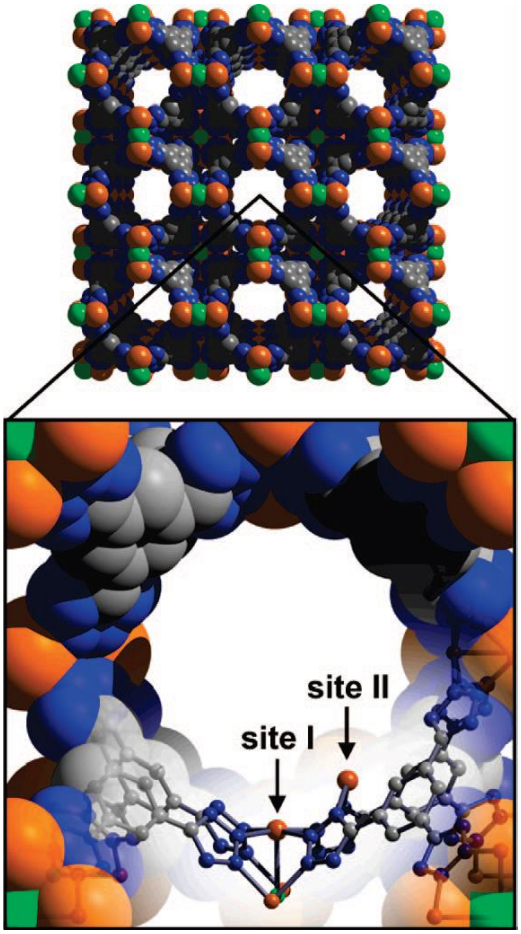

Figure 21: Structure of $Mn_3[(Mn_4Cl)_3(BTT)_8(CH_3OH)_{10}]_2$ MOF which displays the two catalytically active open Mn sites. Mn is coloured orage, C grey, N blue & Cl green. Figure adapted from reference [27].

Another alternative is to utilise a catalytically active site in the organic linker of the MOF. MOFs have been reported containing porphyrin based linkers which can then have metal ions incorporated in them and can perform catalysis common for

these compounds, with the advantage of being incorporated into a high surface area solid MOF framework. A MOF has been reported consisting of SBUs consisting of 2 zinc ions linked into a net by 1,2,4,5-tetrakis(4-carboxyphenyl)benzene which are then linked by (5,15-dipyridyl-10,20-bis(pentafluorophenyl))porphyrin pillars which are metallated with zinc (see Figure 22). This ZnPO-MOF is capable of catalysing acyl transfer reactions from *N*-acetylimidazole to 3-pyridylcarbinol by coordinating the imidazole and the pyridine to the Lewis acidic zinc porprhyns. There is also the advantage of using a MOF for catalysis that the framework will orientate the reagents into a more efficient orientation and distance from each other for the reaction to proceed.[23]

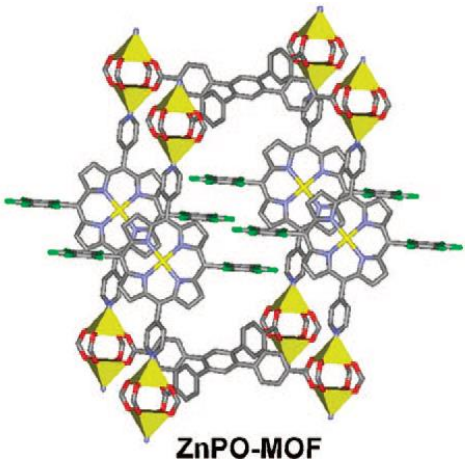

Figure 22: Structure of ZnPO-MOF. Zn is coloured yellow, blue, O red and C grey. Figure adapted from reference [23].

Metal nanoparticles are often used for catalysis and there have been many MOFs with nanoparticles inserted within the pores reported. An advantage is that the pore of the MOF restricts the growth of the metal nanoparticle and produces a much narrower particle size distribution and can keep particles from agglomerating and becoming too large and therefore maintaining a high metal surface area.[46] There have been many reported depositions of metal nanoparticles within MOFs, Pd has been deposited within MOF-5 and used for Suzuki & Sonogashira coupling, Au in MIL-101 has been reported for 1-phenylethanol oxidation, while Pt, Ag & Ni have all been deposited in MOFs and used for catalysis.[46]

1.4. Photocatalysis

1.4.1. Semi-conductor Photocatalysis.

Extended structure materials due to the similar energy levels of the atomic orbitals of the repeating atoms end up with large indistinct bands, a valence band filled with electrons and a conduction band empty of electrons; as opposed to the discrete molecular bonding and antibonding orbitals as would normally be found with individual small molecules. These materials can be divided into three categories. Conductors have no band gap between the upper energy of the valence band and the lower energy of the conduction band. This means that due to thermal equilibrium electrons are able to transfer freely between the valence and conduction bands and so an electrical current can flow. Insulators have a large band gap between the valence and conduction bands and it requires a large amount of energy to excite an electron from the valence band into the conduction band and so no current can flow. The third type of material is a semi-conductor, this is a material where there is a band gap between the valence and conduction bands however the energy difference is small enough that it is possible to excite an electron from the valence band to the conduction band. After this excitation the result is a high energy electron (e^-) free to move through the material in the conduction band and a highly oxidising positively charged hole (h^+) free to move throughout the structure in the valence band, these are known as the charge carriers. These charge

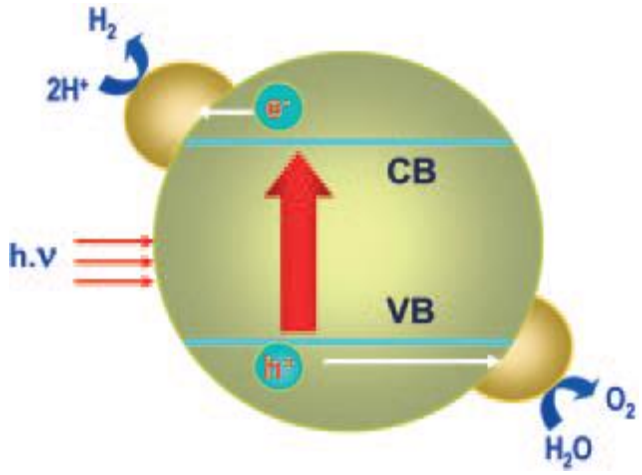

Figure 23: Schematic diagram showing the principles of water splitting reactions using a semiconductor photocatalyst. Figure adapted from reference [21].

carriers are then capable of performing chemical reactions such as the mineralisation of organic pollutants in aquatic environments, the production of H_2O_2, the destruction of bacteria, viruses and cancer cells, nitrogen fixation, self cleaning glass and perhaps most interestingly the splitting of water into O_2 & H_2.[21, 80-85] The band gap for semi-conductors is frequently such that excitation is possible through absorption of a photon of light which makes them appealing photocatalysts. However there are several significant disadvantages regarding semiconductor photocatalysts. Primarily the rapid charge recombination of electron and hole; the total amount of energy applied to the photocatalyst must be greater than the amount required purely for the excitation, sufficient energy for charge migration must be provided so the electron and hole separate. However defects in the crystal or the structure can result in traps for the charge carriers and encourage charge recombination preventing reactions. The charge recombination can be reduced through the addition of sacrificial electron donors such as EDTA, alcohols or sulphides to quench the holes for when a reduction catalyst is required, or an oxidising agent such as Ag^+ or Fe^{3+} to accept the electrons when an oxidation reaction requires catalysis. It is also possible to attach a co-catalyst to the surface of the semi-conductor, or add a co-catalyst to the reaction which is capable of accepting the electron, such as platinum, and thus preventing charge recombination. This is also advantageous as a cocatalyst can be used which has an affinity for the reagent further enhancing the rate of reaction. Another disadvantage is that the majority of

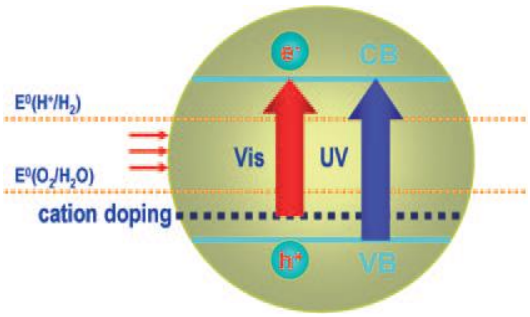

Figure 24: Schematic diagram showing how cation doping affects the energy required for excitation of a semiconductor. Figure adapted from reference [21].

semiconductors absorb light in the UV range of the spectrum, the Earth's atmosphere filters out the majority of UV light meaning the intensity at ground level is too weak to be of practical use, it is therefore necessary to devise a catalyst which is capable of absorbing visible light. The band gap can be altered through doping the semiconductor with different materials, doping with cations which have electrons of an energy within the band gap of the semiconductor can be used to create impurity levels which are at a higher energy than the electrons in the valence band, these dopant electrons may be excited to the conduction band requiring less energy to do so than excitation from the valence band potentially shifting the absorption from UV into Visible light (see Figure 24). Also it is possible to dope semiconductors using anions with higher energy electrons than the anions in the semiconductor, the orbitals of the semiconductor anions and the dopant anions will merge and shift the valence band upwards in energy thus narrowing the band gap. Metal oxide semiconductors for example can be doped with nitrogen or sulphur to replace some of the oxygen in the material, these dopant anions with their higher energy valence electrons will merge into the valence band and shift the band edge up in energy.[21] However doping may result in a more difficult synthesis and a less crystalline product, any defects within the crystal structure will enhance charge recombination. It is also possible to utilise a visible light absorbing dye as a sensitiser; the dye would become excited through the absorption of visible light then transfer the excited electron through ligand to metal charge transfer (LMCT) into the conduction band of the semiconductor (see Figure 25). However this only has an effect for the dye molecules in the first layer directly in contact with the semiconductor which limits the amount of light which can be absorbed.[21, 86]

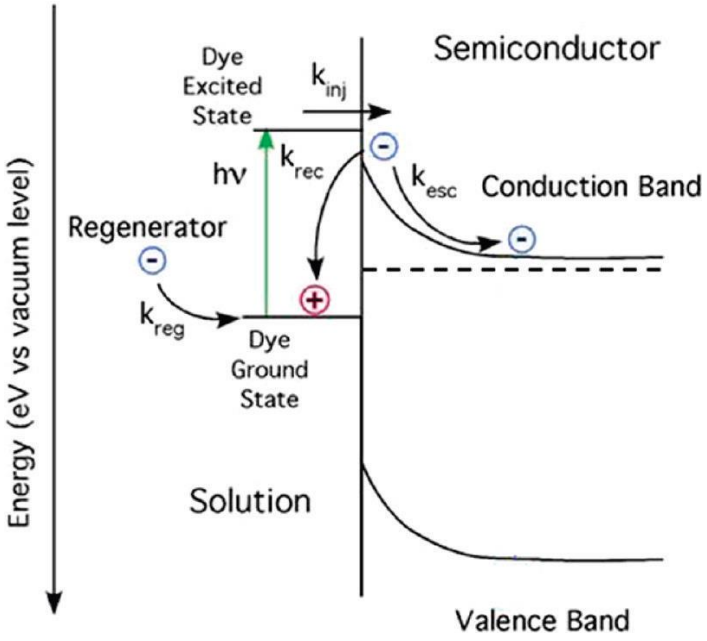

Figure 25: Diagram showing electron transfer in a dye sensitised semiconductor photocatalyst. Figure adapted from reference [86].

1.4.1.1. MOFs as Semi-Conductor Photocatalysts.

Most semiconductors are composed of metal oxides where the metal has fully vacant valence orbitals, usually d orbitals, which comprise the conduction band while the full oxygen p orbitals form the valence band. Many MOFs contain SBUs which are comprised of metals which have vacant d orbitals and oxygen with full p orbitals from the carboxylate of the linker and thus it has been reported that many MOFs contains SBUs which act as semiconductors and are capable of photocatalysis. The IRMOF series which includes MOF-5 with the $Zn_4O(CO_2)_6$ SBU, the $Zr_6O_4(OH)_4(CO_2)_{12}$ cluster of the UiO series of MOFs, the $Ti_{16}O_{72}C_{96}H_{56}$ MIL-125 MOF and the 1,4-benzenedicarboxylic linked Cr_3O units of MIL-101(Cr) have all been described as either quantum dots linked by organic linkers or extended semiconductor frameworks supported by laser flash photolysis and DFT calculations.[87-91] However there is debate as to if these MOFs are truly semiconductors, some argue that the defining feature of a semiconductor is its ability

to conduct electrical current when excited, MOFs when measured show very poor or no photoconductivity suggesting that rather than being semiconductors they are isolated molecular photocatalysts joined in a framework.[92] Regardless of this MOFs have been reported to be photocatalytically active in reactions which are carried out by their traditional semiconductor counterparts. Zirconium based UiO-66 and titanium based MIL-125 have both been reported to be active in hydrogen evolution photocatalytic water splitting reactions when exposed to UV light, much like TiO_2 and ZrO_2.[21, 88, 89]

An advantage to using MOFs as semiconductor photocatalysts arises when sensitisers are used to allow the adsorption of visible light as oppose to UV light. Normally the dye to be used as a sensitiser would have to be coated onto the surface of the semiconductor, this is disadvantageous as only dye molecules directly in contact with the surface act as sensitisers and only for the small area of the semiconductor they're in contact with. A popular choice for sensitising dyes are highly conjugated organic molecules much like the linkers used in MOFs and it has been show that MOF linkers can act as a sensitiser of the metal oxide SBU. This is highly advantageous as every metal oxide cluster is bound to several sensitising linkers meaning the whole bulk of the material can be sensitised not just the surface. This phenomenon was noted when studying the photoluminescence spectra of MOF-5, it was reported that MOF-5 absorbed light at 350 nm similar to the disodium salt of the terephthalic acid linker which absorbed light at 355nm, however the fluorescence spectrum revealed that MOF-5 was fluorescent at 518 nm similar to the fluorescence of ZnO at 560 nm (see Figure 26). This strongly suggests that the linker is acting as a sensitiser becoming excited through the absorption of visible

light then transferring its excited electron into the conduction band of the zinc oxide SBU.[87]

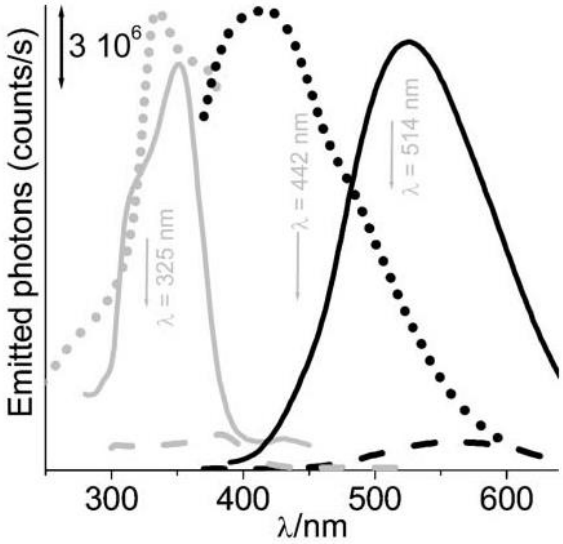

Figure 26: Photoluminescence spectra of MOF-5 (solid line), terephthalic acid disodium salt (dots) and ZnO (dashes). Excitation spectra in grey & emission spectra in black. Figure adapted from reference [87].

From this more of the IRMOF series was studied and the band gap measured for different organic linkers and it was found that the band gap could be reduced by utilising larger organic linkers with greater degrees of conjugation or more electron rich linkers.[2] This principle has been utilised to produce visible light hydrogen evolution photocatalytic water splitting MOFs, by adding an amine group to the aromatic ring of the benzene dicarboxylate linker used in the synthesis of the UV active UiO-66 and MIL-125 MOFs. The absorption of the linker can be shifted to the visible religion of the spectrum, and thus it has been reported that MIL-125(NH_2) is active in hydrogen evolution water splitting reactions when exposed to visible light.[89, 93] It is not simply organic dyes which can act as sensitisers for MOFs, a Titanium MOF has been synthesised which uses a visible light absorbing Ruthenium complex linker, bis(4'-(4-carboxyphenyl)-terpyridine)Ru(II). The excited ruthenium

complex is then able to transfer an electron to the catalytically active titanium oxo cluster which forms the SBU of the MOF.[94]

1.4.2. Molecular photocatalysts.

An alternative to semiconductor photocatalysts are molecular photocatalysts. Unlike semiconductors where the extended structure merges the molecular orbitals into bands a molecular photocatalyst acts as an individual molecule or complex with discrete molecular orbitals, but with an energy gap between the frontier orbitals, the HOMO and LUMO, being of suitable energy that an electron can be excited through absorption of light. Many of these molecular photocatalysts are conjugated organic dyes or metal complexes, it is possible to synthesise some of these molecular photocatalysts as MOF linkers by incorporating carboxylic acid groups onto the ends of the molecules. Incorporating the molecular photocatalyst into a MOF provides the advantage of being able to utilise homogeneous catalysts as a heterogeneous catalyst making it easier to extract from the reaction mixture and recycle the catalyst or by increasing the surface area of poorly soluble catalysts which may clump together.

Porphyrins have long been known for their photocatalytic properties and are utilised in nature for photosynthesis. It is possible to produce hydrogen from a solution of zinc porphyrin using EDTA as a sacrificial electron donor and colloidal platinum as a cocatalyst.[95] It is also possible to incorporate four benzene carboxylic acids onto the porphyrin to make a linker (TCPP) which can be incorporated into a MOF while still retaining its photocatalytic properties. A MOF has been reported composed of chains of Aluminium octahedra linked by a TCPP and it has been reported that this MOF is capable of producing hydrogen photocatalytically in a similar manner to the free porphyrin in solution.[18] Also a Zirconium MOF with TCPP as a linker (PCN-222) has been reported containing large hexagonal channels;

PCN-222 is capable of producing excited singlet oxygen when exposed to light. Singlet oxygen is useful as a mild oxidising agent and so PCN-222 can be used for the partial oxidation of the sulphide in a mustard gas derivative to the less harmful sulphoxide without oxidising it further to the toxic sulphone. This shows that this porphyrin based MOF can be used to photocatalytically decontaminate mustard gas.[96]

The photocatalytic oxidation of water is also an important reaction and has been demonstrated by several ruthenium and iridium complexes, usually based around bipyridine comblexes.[97, 98] A common linker used for MOF synthesis is the biphenyldicarboxylic acid linker, it is possible to replace the phenyl rings with pyridyl rings to produce a 2,2′-Bipyridine-5,5′-dicarboxylic acid linker, this can be used to synthesise a MOF through the carboxylic acids but also as a ligand for ruthenium or iridium complexes through the pyridine nitrogens. Using this linker an UiO-67 derivative MOF has been synthesised which incorporates various Ruthenium and Iridium water oxidation metal catalyst into its 2,2′-Bipyridine-5,5′-dicarboxylic acid linker.[7]

1.4.3. Pyrene photocatalysis.

Pyrene has long been known for its optical properties, strong absorption of light, long excited state lifetime which can vary due to crystallite morphology and impurities but can be as long as 113 ns; also Pyrene has a high fluorescence quantum yield of 0.68.[99, 100] These features are favourable for a photocatalyst. The strong adsorption means that maximum use of the light can be made, the high quantum yield indicates that pyrene could be an efficient photocatalyst as a relatively large number of the photons absorbed will result in an excitation. While the long excited state lifetime will provide a greater probability of a reaction taking place before the

excited state decays, further enhancing the efficiency. The likely route for quenching of the excited state is through intermolecular interactions, the rigid MOF framework holds the Pyrene moiety of the TBAPy linkers separate preventing quenching by this route. The porous characteristics of the MOF are also favourable, with a large surface area for catalysis to occur on which is beneficial for any heterogeneous catalyst.

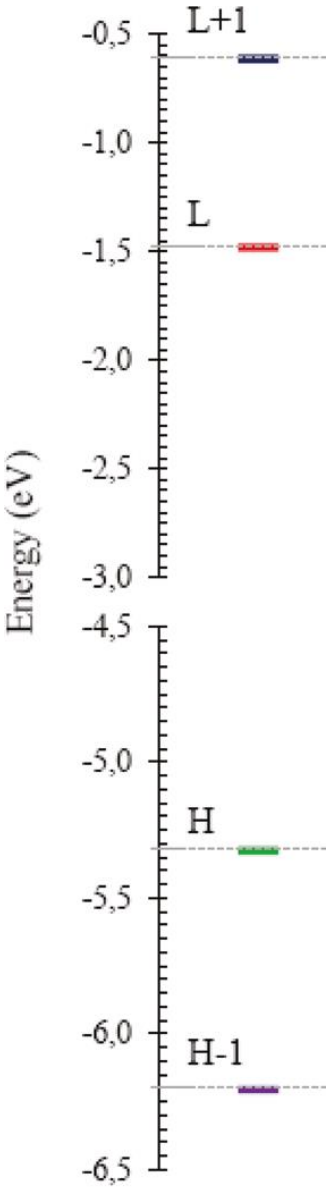

Figure 27: Frontier orbitals of pyrene. Figure adapted from reference [103].

The electron configuration and energy levels of the molecular orbitals of Pyrene also appear promising for photocatalysis. The energy level transition for Pyrene excitation has been reported to have been calculated to be 4.15 eV which is larger than the 1.23 eV required to perform a photocatalytic water splitting reaction for hydrogen evolution; it is essential that this value is larger than the minimum value to provide the energy for charge migration and overcome inefficiency in the catalyst.[21, 101] Density functional calculations have been reported showing that the LUMO of Pyrene has an energy of -1.55 eV. This can be converted to an electrode potential relative to the standard hydrogen electrode (SHE) by subtracting this absolute value from -4.44 eV, the absolute electrode potential of the SHE. This shows the LUMO energy of pyrene relative to the SHE is -2.89 eV.[102] -2.89 eV is more negative than the 0 V standard potential for the reduction of hydrogen. This means that the energy level of the excited electron in pyrene is sufficiently

reducing to reduce H^+ to H_2.[103] However the energy of the HOMO is reported to be -5.70 eV, this corresponds to 1.26 eV relative to the SHE; in order to perform complete water splitting the HOMO must have a potential above the 1.23 V oxidation potential of water. Pyrene is only slightly above this value suggesting that though it may be possible for pyrene based photocatalysts to oxidise water it is unlikely to be very efficient. This means that pyrene based photocatalysts will only be able to complete the hydrogen evolution half reaction for water splitting. However this isn't uncommon and by the addition of a sacrificial electron donor the reaction may proceed and hydrogen may be generated (see Figure 27).[21, 103]

An aluminium porphyrin MOF has been reported by Fateeva et al which is capable of photocatalytic water splitting hydrogen evolution reactions. This MOF adopts a similar structure to the AlTBAPy MOF with infinite aluminium octahedra chains linked by tetra carboxylate square planer linkers.[18] DFT calculations on the energy levels of porphyrin have been reported and show that free base tetraphenyl porphyrin, similar to the linker used in this MOF, has a LUMO of energy -2.478 eV which corresponds to E_{SHE}= -1.962 eV and a HOMO of energy -5.089 eV corresponding to E_{SHE}= 0.649 eV.[104] These energy levels are similar to those reported for pyrene. Pyrene has a HOMO at 1.26 eV just above the level required for water oxidation, however the HOMO of the free base porphyrin is below the 1.23 V required for water oxidation. This indicates that both HOMOs of pyrene and porphyrin are likely to be too reducing to perform oxidisation of water for oxygen evolution. However pyrene and porphyrin also have similar LUMO energies, -1.92 eV for porphyrin compared to -2.89 eV for pyrene, both of these are more negative than the reduction potential of H_2 of 0 eV and so both should be able to photocatalytically reduce water to evolve hydrogen which we know the porphyrin

MOF is able to do.[18] The pyrene HOMO energy level is more negative than that of the porphyrin and so should be more effective at hydrogen evolution. However the gap between the frontier orbitals is larger for pyrene, 3.84 eV compared to 2.611 eV for porphyrin, this means that the porphyrin will be more efficient at absorbing light, capable of absorbing more light at lower wavelengths likely giving pyrene based photocatalysts a higher efficiency than porphyrin photocatalysts.[18, 103, 104] The photocatalytic production of hydrogen from water under visible light is a much desired process to produce a carbon free renewable fuel and it is possible that a pyrene based MOF could perform this reaction, therefore it was attempted using AlTBAPy.[105, 106]

The energy levels of the zirconium MOF UiO-66 have been reported, it is known that UiO-66 is capable of performing hydrogen evolution water splitting reactions when exposed to UV light, this is due to the large band gap reported to be 4.56 eV.[45, 89] The energy of the valence band of UiO-66 is -2.24 eV relative to the SHE, this is more negative than the LUMO of pyrene which has an energy of -2.98 eV. This means that the LUMO of pyrene is more reducing than the conduction band of UiO-66 which is composed mostly of the empty d orbitals of the zirconium cluster common both to UiO-66 and NU-1000; this indicates that it may be possible to transfer an electron from the excited pyrene into the conduction band of the zirconium cluster in the NU-1000 MOF sensitising it for photocatalysis.[45, 103] However it is also reported that the band gap for UiO-66 is highly sensitive to the linker used, meaning the energy levels for NU-1000 may be very different to those for UiO-66 and thus the ability of pyrene to act as a sensitiser may not hold true for NU-1000.

1.5. Conclusions

The discovery and development of MOFs over the last 25 years has opened up a new area of research into porous materials. The traditional uses of porous materials such as separation and storage can have their effectiveness augmented through the ease at which the pore size can be tailored and the wide range of functionality which can be incorporated into a MOF framework. Additionally this ease of functionalization drastically widens the catalysis applications for porous materials and introduces porous frameworks which themselves can have photocatalytic properties. There is still a great deal of work to be done on MOFs to optimise synthesis, develop new framework topologies and explore the range of metals and linkers that can be used. Though MOFs show such a wide range of applications their effectiveness is still usually not as good as the state of the art materials currently used.

1. V. C. Menon, S. Komarneni and V. C. Menon, *Journal of Porous Materials*, 1998, **5**, 43-58.
2. J. Gascon, M. D. Hernández-Alonso, A. R. Almeida, G. P. van Klink, F. Kapteijn and G. Mul, *ChemSusChem*, 2008, **1**, 981-983.
3. J. Li, R. J. Kuppler and H. Zhou, *Chemical Society Reviews*, 2009, **38**, 1477-1504.
4. Q. Yang, H. Jobic, F. Salles, D. Kolokolov, V. Guillerm, C. Serre and G. Maurin, *Chemistry - A European Journal*, 2011, **17**, 8882-8889.
5. F. Vermoortele, M. Maes, P. Z. Moghadam, M. J. Lennox, F. Ragon, M. Boulhout, S. Biswas, K. G. Laurier, I. Beurroies, R. Denoyel, M. Roeffaers, N. Stock, T. Düren, C. Serre and D. E. Vos, *Journal of the American Chemical Society*, 2011, **133**, 18526-18529.
6. S. Proch, J. Herrmannsdörfer, R. Kempe, C. Kern, A. Jess, L. Seyfatrh and J. Senker, *Chemistry - A European Journal*, 2008, **14**, 8204-8212.
7. C. Wang, Z. Xie, K. E. deKrafft and W. Lin, *Journal of the American Chemical Society*, 2011, **133**, 13445-13454.
8. J. An, S. J. Geib and N. L. Rosi, *Journal of the Ameircan Chemical Society*, 2009, **131**, 8376-8377.
9. K. S. Park, Z. Ni, A. P. Coté, J. Y. Choi, R. Huang, F. J. Uribe-Romo, H. K. Chae, M. O'Keeffe and O. M. Yaghi, *Proceedings of the National Academy of Sciences of the United States of America*, 2006, **103**, 10186-10191.
10. A. Mantion, L. Massuger, P. Rabu, P. Cornelia, L. B. McCusker and A. Taubert, *Journal of the American Chemical Society*, 2008, **130**, 2517-2526.
11. J. A. Mason, M. Veenstra and J. R. Long, *Chemical Science*, 2014, **5**, 32-51.
12. H. Li, M. Eddaoudi, M. O'Keeffe and O. M. Yaghi, *Nature*, 1999, **402**, 276-279.

13. T. Loiseau, C. Serre, C. Huguenard, G. Fink, F. Taulelle, M. Henry, T. Bataille and G. Féré, *Chemistry - A European Journal*, 2004, **10**, 1373-1382.
14. K. C. Stylianou, R. Heck, S. Y. Chong, J. Bacsa, J. T. Jones, Y. Z. Khimyak, D. Bradshaw and M. J. Rosseinsky, *Journal of the American Chemical Society*, 2010, **132**, 1-12.
15. J. E. Mondloch, W. Bury, D. Fairen-Jimenez, S. Kwon, E. J. DeMarco, M. H. Weston, A. A. Sarjeant, S. T. Nguyen, P. C. Stair, R. Q. Snurr, O. K. Farha and J. T. Hupp, *Journal of the American Chemical Society*, 2013, **135**, 10294-10297.
16. B. F. Hoskins and R. Robson, *Journal of the American Chemical Society*, 1989, **111**, 5962-5942.
17. S. S. Chui, S. M. Lo, J. P. Charmant, A. G. Orpen and I. D. Williams, *Science*, 1999, **283**, 1148-1150.
18. A. Fateeva, P. Chater, C. P. Ireland, A. Tahir, Y. Khimyak, P. Wiper, J. Darwent and M. J. Rosseinsky, *Angewandte Chemie International Edition*, 2012, **51**, 7440-7444.
19. J. H. Cavka, S. Jakobsen, U. Olsbye, N. Guillou, C. Lamberti, S. Bordiga and K. P. Lillerud, *Journal of the American Chemical Society*, 2008, **130**, 13850-13851.
20. A. P. Coté, A. I. Benin, N. W. Ockwig, M. O'Keeffe, A. J. Matzger and O. M. Yaghi, *Science*, 2005, **310**, 1166-1170.
21. R. M. Yerga, M. C. Galvan, F. Valle, V. Mano and J. L. Fierro, *ChemSusChem*, 2009, **2**, 471-485.
22. H. M. El-Kaderi, J. R. Hunt, J. L. Mendoza-Cortés, A. P. Coté, R. E. Taylor, M. O'Keeffe and O. M. Yaghi, *Science*, 2007, **316**, 268-272.
23. Abraham, M. Shultz, O. K. Farha, J. T. Hupp and S. Nguyen, *Journal of the American Chemical Society*, 2009, **131**, 4204-4205.
24. Y. Lin, Q. Yan, C. Kong and L. Chen, *Scientific Reports*, 2013, **3**, 1859.
25. M. Eddaoudi, J. Kim, N. Rosi, D. Vodak, J. Wachter, M. O'Keeffe and O. M. Yaghi, *Science*, 2002, **295**, 469-472.
26. T. M. McDonald, W. R. Lee, J. A. Mason, B. M. Wiers, C. S. Hong and J. Long, *Journal of the American Chemical Society*, 2012, **134**, 7056-7065.
27. S. Horike, M. Dinca, K. Tamaki and J. R. Long, *Journal of the American Chemical Society*, 2008, **130**, 5854-5855.
28. A. Demessence, D. M. D'Alessandro, M. L. Foo and J. R. Long, *Journal of the American Chemical Society*, 2009, **131**, 8784-8786.
29. C. Wang, K. E. deKrafft and W. Lin, *Journal of the American Chemical Society*, 2012, **134**, 7211-7214.
30. K. S. Sing, D. H. Everett, R. A. Haul, L. Moscou, R. A. Pierotti, J. Rouqiérol and T. Siemieniewska, *Pure and Applied Chemistry*, 1985, **57**, 1365-3075.
31. D. W. Breck, W. G. Eversole, R. M. Milton, T. B. Reed and T. L. Thomas, *Journal of the American Chemical Society*, 1956, **78**, 5963-5972.
32. T. B. Reed and D. W. Breck, *Journal of the American Chemical Society*, 1958, **78**, 5972-5977.
33. V. Speybroeck, K. Hemelsoet, L. Joos, M. Waroquier, R. G. Bell and C. R. Catlow, *Chemical Society Reviews*, 2015, **44**, 7044-7111.
34. J. S. Beck, J. C. Vartuli, G. J. Kennedy, C. T. Kresge, W. J. Roth and S. E. Schramm, *Chemistry of Materials*, 1994, **6**, 1816-1821.
35. S. T. Wilson, B. M. Lok, C. A. Messina, T. R. Cannan and E. M. Flanigen, *Journal of the American Chemical Society*, 1982, **104**, 1146-1147.
36. M. Estermann, L. B. McCusker, C. Baerlocher, A. Merrouche and H. Kessler, *Nature*, 1991, **352**, 320-323.
37. C. Baerlocher, W. M. Meier and D. H. Olson, *Atlas of Zeolite Framework Types*, Elsevier, 2001.

38. T. Tozawa, J. T. Jones, S. I. Swamy, S. Jiang, D. J. Adams, S. Shakespeare, R. Clowes, D. Bradshaw, T. Hasell, S. Y. Chong, C. Tang, S. Thompson, J. Parker, A. Trewin, J. Bacsa, A. M. Slawin, A. Steiner and A. I. Cooper, *Nature Materials*, 2009, **8**, 973-978.
39. Q. Chen, M. Luo, T. Wang, J. Wang, D. Zhou, Y. Han, C. Zhang, C. Yan and B. Han, *Macromolecules*, 2011, **44**, 5573-5577.
40. P. Kuhn, M. Antonietti and A. Thomas, *Angewandte Chemie International Edition*, 2008, **47**, 3450-3453.
41. H. Furukawa and O. M. Yaghi, *Journal of the American Chemical Society*, 2009, **131**, 8875-8883.
42. D. J. Tranchemontagne, J. L. Mendoza-Cortés, M. O'Keeffe and O. M. Yaghi, *Chemical Society Reviews*, 2009, **38**, 1257-1283.
43. G. Férey, C. Mellot-Draznieks, C. Serre, F. Fillange, J. Dutour, S. Surblé and I. Margiolaki, *Science*, 2005, **309**, 2040-2042.
44. M. Dan-Hardi, C. Serre, T. Frot, L. Rozes, G. Maurin, C. Sanchez and G. Férey, *Journal of the American Chemical Society*, 2009, **131**, 10857-10859.
45. L. Valenzano, B. Civalleri, S. Chavan, S. Bordiga, M. H. Nilsen, S. Jakobsen, K. P. Lillerud and C. Lamberti, *Chemistry of Materials*, 2011, **23**, 1700-1718.
46. A. Dhakshinamoorthy and H. Garcia, *Chemical Society Reviews*, 2012, 1-23.
47. M. Kim, J. F. Cahill, H. Fei, K. A. Prather and S. M. Cohen, *Journal of the American Chemical Societry*, 2012, 1-7.
48. M. Kim, J. F. Cahill, Y. Su, K. A. Prather and S. M. Cohen, *Chemical Science*, 2010, **3**, 126-130.
49. D. Ma, Y. Li and Z. Li, *Chemical Communications*, 2011, **47**, 7377-7379.
50. A. P. Nelson, O. K. Farha, K. L. Mulfort and J. T. Hupp, *Journal of the American Chemical Society*, 2009, **131**, 458-460.
51. F. W. Knoboch and W. H. Rauscher, *Journal of Polymer Science*, 1959, **38**, 261-262.
52. H. Li, M. Eddaoudi, T. Groy and O. M. Yaghi, *Journal of the American Chmeical Society*, 1998, **120**, 8571-8572.
53. C. J. Kepert and M. J. Rosseinsky, *Chemical Communications*, 1999, 375-376.
54. J. E. Mondloch, M. J. Katz, N. Planas, D. Semrouni, L. Gagliardi, J. T. Hupp and O. K. Farha, *Chemical Communications*, 2014, **50**, 8944-8946.
55. B. F. Abrahms, B. F. Hoslins, D. M. Michail and R. Robson, *Nature*, 1994, **369**, 727-729.
56. Y. Chen and S. Ma, *Reviews in Inorganic Chemistry*, 2012, **32**, 81-100.
57. Z. Zhang, Z. Yao, S. Xiang and B. Chen, *Energy & Enviromental Science*, 2014, **7**, 2868-2899.
58. J. Li, J. Sculley and H. Zhou, *Chemical Reviews*, 2012, **112**, 869-932.
59. D. Dybtsev, H. Chun, S. H. Yoon, D. Kin and K. Kim, *Journal of the American Chemical Society*, 2004, **126**, 32-33.
60. S. Couck, J. F. Denayer, G. Baron, T. Rémy, J. Gascon and F. Kapteijn, *Journal of the American Chemical Society*, 2009, **131**, 6326-6327.
61. P. S. Barcia, F. Zapata, J. A. Silva, A. E. Rodrigues and B. Chen, *The Journal of Physical Chemistry B*, 2007, **111**, 6101-6103.
62. J. J. Beenakker, D. V. Borman and S. Y. Krylov, *Chemical Physics Letters*, 1995, **232**, 379-382.
63. J. Cai, Y. Xing and X. Zhao, *RSC Advances*, 2012, **2**, 8579-8586.
64. D. Liu, W. Wang, J. Mi, C. Zhong, Q. Yang and D. Wu, *Industrial & Engineering Chemistry Research*, 2012, **51**, 434-442.
65. R. B. Getman, Y. Bae, C. E. Wilmer and R. Q. Snurr, *Chemical Reviews*, 2012, **112**, 703-723.
66. S. K. Bhatia and A. L. Myers, *Langmuir*, 2006, **22**, 1688-1700.

67. U. S. D. o. E. Office of Energy Efficiency & Renewable Energy, *Materials-Based Hydrogen Storage*, http://energy.gov/eere/fuelcells/materials-based-hydrogen-storage, Accessed 23rd September, 2015.
68. X. Lin, J. Jia, X. Zhao, M. Thomas, A. J. Blake, G. S. Walker, N. R. Champness, P. Hubberstey and M. Schroder, *Angewandte Chemie International Edition*, 2006, **45**, 7358-7364.
69. B. Chen, N. W. Ockwig, A. R. Millward, D. S. Contreras and O. M. Yaghi, *Angewandte Chemie International Edition*, 2005, **44**, 4745-4749.
70. S. Ma, D. Sun, J. M. Simmons, C. D. Collier, D. Yuan and H. Zhou, *Journal of the American Chemical Society*, 2008, **130**, 1012-1016.
71. J. Zhang and X. Chen, *Journal of the American Chemical Society*, 2009, **131**, 5516-5521.
72. S. Xiang, W. Zhou, Z. Zhang, M. Green, Y. Liu and B. Chen, *Angewandte Chemie International Edition*, 2010, **49**, 4615-4618.
73. R. S. Haszeldine, *Science*, **325**, 1647-1652.
74. C. Sun, C. Qin, X. Wang and Z. Su, *Expert Opinion on Drug Delivery*, 2013, **10**, 89-101.
75. L. Qiu, Z. Li, Y. Wu, W. Wang, T. Xu and X. Jiang, *Chemical Communications*, 2008, 3642-3644.
76. S. H. Jhung, J. H. Lee, J. W. Yoon, C. Serre, G. Férey and J. S. Chang, *Advanced Materials*, 2007, **19**, 121-124.
77. C. Sun, C. Qin, X. Wang, G. Yang, K. Shao, Y. Lan, Z. Su, P. Huang, C. Wang and E. Wang, *Dalton Transactions*, 2012, **41**, 6906-6909.
78. E. G. Moore, A. P. Samuel and K. N. Raymond, *Accounts of Chemical Research*, 2009, **42**, 542-552.
79. Z. Hao, X. Song, M. Zhu, X. Meng, S. Zhao, S. Su, W. Yang, S. Song and H. Zhang, *Journal of Materials Chemistry A*, 2013, **1**, 11043-11050.
80. M. R. Hoffmann, S. T. Martin, W. Choi and D. W. Bahnemann, *Chemical Reviews*, 1995, **95**, 69-96.
81. J. C. Ireland, P. Klostermann, E. W. Rice and R. M. Clark, *Appled and Enviromental Microbiology*, 1993, **59**, 1668-1670.
82. J. C. Sjogren and R. A. Sierka, *Applied and Enviromental Microbiology*, 1994, **60**, 344-347.
83. R. Cai, Y. Kubota, T. Shuin, H. Sakai, K. Hashimoto and A. Fukishima, *Cancer Research*, 1992, **52**, 2346-2348.
84. M. M. Kahn, D. Chatterjee and M. Bala, *Journal of Photochemistry and Photobiology A: Chemistry*, 1992, **67**, 349-352.
85. R. Wang, K. Hashimoto, A. Fujishima, M. Chikuni, E. Kojima, A. Kitamura, M. Shimohigoshi and T. Watanabe, *Nature*, 1997, **388**, 431-432.
86. M. T. Spitler and B. A. Parkinson, *Accounts of Chemical Research*, 2009, **42**, 2017-2029.
87. S. Bordiga, C. Lamberti, G. Ricchiardi, L. Regli, F. Bonino, A. Damin, K. Lillerud, M. Bjorgen and A. Zecchina, *Chemical Communications*, 2004, **40**, 2300-2301.
88. A. Walsh and C. R. Catlow, *ChemPhysChem*, 2010, **11**, 2341-2344.
89. C. Gomes Silva, I. Luz, F. X. Llabrés i Xamena, A. Corma and H. García, *Chemistry - A European Journal*, **16**, 11133-11138.
90. M. Wen, K. Mori, T. Kamegawa and H. Yamashitia, *Chemical Communications*, 2014, **50**, 11645-11648.
91. M. Alvaro, E. Carbonell, B. Ferrer, F. X. Xamena and H. Garcia, *Chemisty-A European Journal*, 2007, **13**, 5106-5112.

92. M. A. Nasalevich, M. Veen, F. Kapteijn and J. Gascon, *CrystEngComm*, 2014, **16**, 4919-4926.
93. Y. Horiuchi, T. Toyao, M. Saito, K. Mochizuki, M. Iwata, H. Higashimura, M. Anpo and M. Matsuoka, *Journal of Physical Chemistry C*, 2012, **116**, 20848-20853.
94. T. Toyao, M. Saito, S. Dohshi, K. Mochizuki, M. Iwata, H. Higashimura, Y. Horiuchi and M. Matsuola, *Chemical Communications*, 2014, **50**, 6779-6781.
95. K. Kalyanasundaram and M. Gratzel, *Helvetica Chimica Acta*, 1980, **63**, 478-485.
96. Y. Liu, A. J. Howarth, J. T. Hupp and O. K. Farha, *Angewandte Chemie International Edition*, 2015, **54**, 9001-9005.
97. J. J. Concepcion, J. W. Jurss, J. L. Templeton and T. J. Meyer, *Journal of the American Chemical Society*, 2008, **130**, 16462-16463.
98. N. D. McDaniel, F. J. Coughlin, L. L. Tinker and S. Bernhard, *Journal of the American Chemical Society*, 2008, **130**, 210-217.
99. J. B. Birks, A. A. Kazzaz and T. A. King, *Proceedings of the Royal Society A: Mathematical, Physical and Engineering Sciences*, 1966, **291**, 556-569.
100. R. Katoh, K. Suzuki, A. Furube, M. Kotani and K. Tokumaru, *Journal of Physical Chemistry C*, 2009, **113**, 2961-2965.
101. M. Dierksen and S. Grimme, *The Journal of Chemical Physics*, 2004, **120**.
102. A. D. McNaught, A. Wilkinson, M. Nic, J. Jirat, B. Kosata and A. Jenkins, *IUPAC. Compendium of Chemical Terminology, 2nd ed. (the "Gold Book").* Blackwell Scientific Publications, 2006.
103. M. Ottonelli, M. Piccardo, D. Duce, S. Thea and G. Dellepiane, *Journal of Physical Chemistry A*, 2012, **116**, 611-630.
104. C. Tai, W. Chuang and B. Wang, *Journal of Luminescence*, 2013, **142**, 8-16.
105. J. Jiang, A. Trewin, D. J. Adams and A. I. Cooper, *Chemical Science*, 2011, **2**, 1777-1781.
106. M. Zhu, Y. Lu, Yukou, J. Li, X. Wang and P. Yang, *International Journal of Hydrogen Energy*, 2011, **36**, 4298-4304.

2. Synthetic and Experimental Techniques.

2.1. Introduction.

The aim of this chapter is to give an overview of the experimental and synthesis techniques used in the synthesis, characterisation and examination of pyrene based MOFs. MOFs are porous crystalline materials and so the primary characterisation technique used is powder X-ray diffraction (PXRD); this measurement shows how crystalline the material is, confirms that the crystal structure matches what is expected and confirms that there are no other crystalline impurity phases present. PXRD however only provides information as to the crystal structure of the MOF not its chemical composition. In order to ensure the synthesised material has the correct composition a combination of CHN combustion analysis and TGA must be used. The CHN combustion analysis identifies the carbon, hydrogen and nitrogen composition of the MOF while the inorganic residue remaining after the TGA has been completed can be used to calculate the metal composition. The TGA is also useful for determining the thermal stability and a suitable activation temperature. However these measurements are difficult to interpret without knowledge of the structure of the MOF, this is determined from the single crystal XRD (SCXRD) pattern. MOFs are porous materials and can adsorb gases onto their internal surface, this can be characterised through the measurement of adsorption isotherms, from which the BET surface area, the pore volume and if repeated at various temperatures the heat of adsorption can all be calculated. Pyrene has interesting optical properties due to its highly aromatic π system, as integration into a rigid MOF framework and coordination to metal cations affects the electronic structure and thus the optical properties these can be examined using UV/Vis and Fluorescence Spectroscopy.

2.2. Synthesis Techniques

2.2.1. Solvothermal Synthesis of MOFs.

Many MOFs are synthesised under solvothermal or hydrothermal, when the solvent used is water, conditions. Solvothermal synthesis utilises sealed reaction vessels capable of operating at high temperatures, in some cases as high as 220 °C and thus high pressures thereby allowing the heating of solvents above their boiling point.[2] MOF synthesis is dependent on a large number of factors, the reaction time, the temperature at which the synthesis is carried out, the solvent system, the concentration of the metal and linker and the ratio of one to the other. Solvothermal reactors allow greater exploration of these conditions not just at higher temperatures but also the higher concentrations as the greater temperature and pressure increases the solubility of the reagents. For reaction temperatures below the boiling point of the solvent system glass vials with Teflon sealed lids can be used which offer the advantage of being cheap, in ready supply and disposable. However, for reaction temperatures greater than the boiling point of the solvent a teflon lined stainless steel Parr autoclave is usually used. These autoclaves are composed of a teflon liner with fitted lid, a stainless steel body into which the teflon liner sits with its lid flush to the top, a corrosion plate to prevent any solvent which may escape from damaging the steel, a bursting disk to allow release of pressure if it becomes too great, a top and bottom plate with a spring between them to allow some expansion when heating but to keep the lid pushed tightly against the liner, all these fit into a steel cap which screws down tightly on top of the reactor. The advantage of using these autoclave reactors is that the range of temperatures and concentrations which can be used for the synthesis is greatly expanded, for high boiling point solvents such as DMF the temperature can be increased to as high as 220 °C before the teflon begins to distort.

However, the teflon liner must be cleaned carefully and thoroughly between uses to prevent contamination and the many component parts of the autoclave must be kept together and not interchanged else leakage could occur.

Solvothermal MOF synthesis operates by dissolving the reagents and then growing crystals out of solution around nucleation sites.[3] The aim of the synthesis reaction design is to find the optimal conditions for this crystal growth whereby the most crystalline crystals are grown, ideally crystals large enough for single crystal X-Ray diffraction but these can often prove difficult to obtain. Crystal growth is determined by a large range of factors meaning many different synthesis conditions will need to be attempted altering a single variable at a time to find the optimum conditions. The temperature of the reaction is important as the MOF is synthesised from solution, the solubility of the reagents being linked to the temperature. The synthesis of a crystalline extended solid framework from reagents in solution is highly entropically unfavourable meaning higher temperatures usually must be used; however, many MOFs are unstable and may decompose or do not form if at too high a temperature, it is essential to get the correct balance. The time of the reaction is also vitally important for crystal growth, if a crystal is left to grow slowly for a long time it will be more highly crystalline than crystals grown quickly; also by heating for longer the process of Ostwald Ripening, where smaller crystallites formed initially are re-dissolved and can grow on larger crystallites producing a more crystalline material. However as with higher temperatures an unstable MOF could begin to decompose if left heated under solvent for too long.[4] The solvent system used, which in many cases contains multiple solvents, is also essential to optimise as different materials exhibit different solubility in different solvents. The ideal solvent system must be found in which the reagents are able to dissolve but it is favourable

for the MOF to precipitate out of solution in a crystalline form. The concentration of the metal cation and the concentration of the linker must also be tailored to encourage crystalline growth of MOF; too low concentrations will result in the reagents remaining in solution with little or no MOF formed while too high concentrations will result in poorly crystalline material and also may result in impure material contaminated with metal oxide or unreacted linker trapped within the pores of the MOF. Also if the ratio of metal to linker used in the synthesis is not optimised impurities of unreacted linker or metal oxide may be formed within the pores of the MOF. The crystallinity may also be enhanced through the addition of a mineralising agent, usually an acid which will shift the deprotonation equilibrium of a carboxylate linker, slowing the reaction and therefore potentially enhancing the crystallinity; however a balance must be struck which will be different for each MOF and each set of synthesis conditions as many MOFs are unstable in acidic conditions. Many MOFs are composed of large clusters and so for some MOFs the crystallinity may be enhanced through the addition of a modulator, a material similar to the linker used but without the connectivity. This may pre-form the SBU of the MOF which may enhance the crystallinity as the linker displaces the modulator. However the addition of too much modulator will shift the equilibrium between preformed SBU and MOF away from the MOF synthesis and so once again a balance must be struck. All of these factors are important and many affect each other so all must be optimised by thoroughly exploring the synthesis conditions changing only a single variable at a time until an optimum set of synthesis conditions are obtained.[5]

Another disadvantage to the synthesis of highly porous materials such as MOFs using Solvothermal techniques is that the pores of the MOF will contain solvent from the reaction mixture which must be removed. The common way of

doing this is to apply dynamic vacuum to the MOF and heat to a temperature at which the solvent is released. However, the surface tension of some solvents acting upon the internal surface of the MOF when removed may cause the pores to collapse, or high boiling point solvents with an affinity to the MOF may require temperatures beyond which the MOF is stable. In these cases the solvent must be exchanged for a more suitable one by soaking the MOF in the more suitable solvent for a period of time until the solvent exchange is complete.[6]

2.2.1.1. Supercritical CO_2 Activation.

For some MOFs it is not possible to exchange the solvent contained within the pores for any other solvent which can be removed without the surface tension causing the pores to collapse upon activation. For these MOFs super critical CO_2 activation must be performed. By heating and pressurising a substance to above the critical point gas and liquid no longer exist as distinct phases but rather combine into a supercritical fluid (see Figure 28). This supercritical fluid expresses some properties of a liquid, such as being able to act as a solvent but exhibits other properties of a gas such as the ability to effuse though solids. The advantage to using supercritical CO_2 activation for MOFs is that without a liquid-gas phase boundary there is no surface tension to act and damage the pores of the MOF when the supercritical CO_2 is removed.[7]

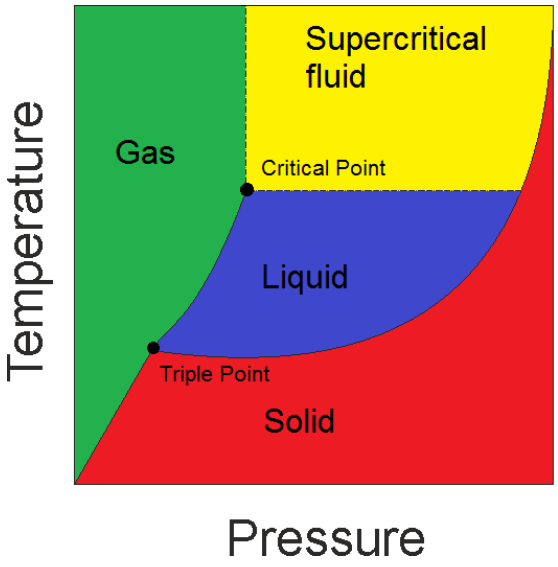

Figure 28: Phase diagram showing the Critical Point where a Supercritical fluid is formed.

In order to perform the supercritical CO_2 activation firstly solvent exchange must take place to exchange the solvents used in the synthesis for a solvent which is soluble in liquid CO_2, ethanol is most commonly used. The MOF is soaked in ethanol, replenishing the Ethanol every 24 h until CHN analysis shows that the solvent exchange has been completed. Keeping the MOF under ehanol to prevent adsorption of moisture from the air, the MOF is transferred to a sealed receptacle permeable to CO_2, this is then placed into a water jacketed pressure reactor with appropriate connectors to introduce liquid CO_2, drain liquids and vent gasses. The pressure vessel is then flushed with liquid CO_2 for 5 min then filled with liquid CO_2 and left for an hour for the ethanol to exchange for CO_2 within the pores of the MOF. This venting and exchange process is repeated up to five times. Using a flow of water with a temperature controlled heater the reactor is then heated to 40 °C, above the critical point of CO_2. After one hour in the supercritical CO_2 the reactor is vented over the course of several hours ensuring no sudden pressure changes cause liquid CO_2 to condense. After the reactor has been fully vented and the pressure returned to atmospheric pressure the MOF is transferred to a suitable container to be kept under dry inert gas as quickly as possible minimising contact with the moisture in the air.[7]

2.3. X-Ray Diffraction.

2.3.1. Principles of X-Ray Diffraction.

A crystalline material is one in which the molecules atoms or ions which compose it are arranged in a repeating 3D structure. The unit cell is defined as the smallest possible volume of the crystal structure containing all the structural and symmetry information to produce the entire crystal structure purely through translation. The unit cell size and shape varies between different materials, this can be described by the lattice parameters, three lengths and three angles; the lengths a, b and c and the angles between them α (between b and c), β (between a and c) and γ (between a and b). The translational symmetry of the unit cell is required for all crystalline materials however other symmetry operations can be applied to certain crystals which produce identical configurations. These different symmetry elements produce seven different crystal systems with different relationships of lattice parameters and are characterised by the presence of essential reflection or rotation symmetry elements. In addition to the crystal systems four different lattice types are possible; they are primitive (P) with a lattice point only on the corners, body centred (I) with a lattice point on each corner and one in the centre, face centred (F) with a lattice point on each corner and one on each face and base centred (A, B or C) with a lattice point on each corner and one on two faces parallel to each other; from this 14 Bravais lattices can be produced. In addition to the 14 Bravais lattices compound symmetry elements such as glide planes and screw axis which combine translation with other symmetry elements are also seen in some crystals. The combination of all crystal systems, Bravais lattices and symmetry elements produces 230 different space groups from which the symmetry of all possible crystal structures can be described.[8]

Table 1: The Seven Different Crystal Systems.

Crystal System	Unit Cell Parameters	Bravais Lattice	Minimum Symmetry Elements.
Cubic	$a = b = c$ $\alpha = \beta = \gamma = 90°$	P, I, F	Four C3 axes
Hexagonal	$a = b \neq c$ $\alpha = \beta = 90°, \gamma = 120°$	P	One C6 axis
Trigonal	$a = b = c$ $\alpha = \beta = \gamma \neq 90°$	P	One C3 axis
Tetragonal	$a = b \neq c$ $\alpha = \beta = \gamma = 90°$	P, I	One C 4 axis
Orthorhombic	$a \neq b \neq c$ $\alpha = \beta = \gamma = 90°$	P, C/A, I, F	Three C2 axes or three mirror planes
Monoclinic	$a \neq b \neq c$ $\alpha = \gamma = 90° \neq \beta$	P, I/C	One C2 axis or one mirror plane.
Triclinic	$a \neq b \neq c$ $\alpha \neq \beta \neq \gamma$	P	None.

The electrons around an atom, molecule or ion produce elastic scattering of X-Rays, this is where the incident X-Ray is scattered outwards by the electrons whilst maintaining the same energy and thus wavelength. In an amorphous solid interference between the scattered X-Rays would cancel out and no pattern would be observed; however in a crystalline solid with a regular array of scattering atoms, ions or molecules when orientated correctly will produce constructive interference between the scattered X-Rays will be seen and a diffraction pattern will form (see Figure 29).[9] The conditions at which constructive interference occurs are determined by Bragg's Law which states that $n\lambda = 2d \sin\theta$ (see Figure 30).[10] However in order to produce a pattern the wavelength used must be similar to the d spacing (the interplanar distance between the scattering atoms, ions or molecules), most crystals this distance is between 1 and 10 Å, X-Rays have a wavelength of between 0.1 and 100 Å and so can be used to produce diffraction patterns.

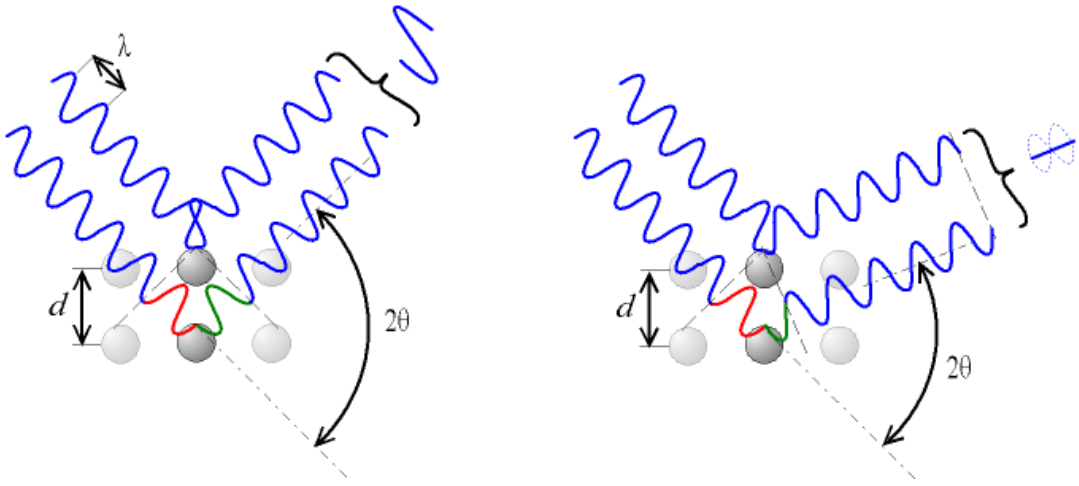

Figure 29: Constructive interference satisfying Bragg's law (left) and destructive interference at a different value of 2θ resulting in no reflection seen (right). Figure from reference[11]

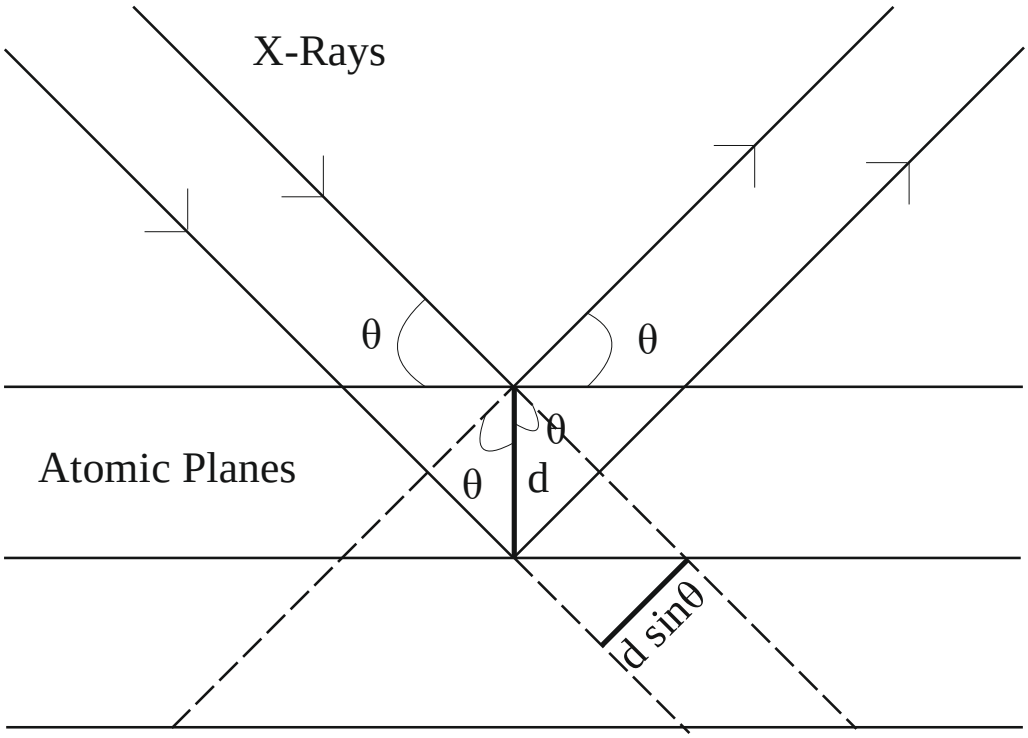

Figure 30: The origin of Bragg's Law where a reflection is seen.

X-Rays are generated by using an electron gun to accelerate electrons usually with a potential of 15 – 45 kV into a metal target, the anode. These high energy electrons then ionise the metal in the anode through multiple collisions removing electrons from the core of the atoms, electrons then decay back into the lower energy positions releasing X-Rays. The X-Rays then pass through a collimator, an optical component comprised of thin sheets of a material opaque to X-Rays which will only allow X-Rays travelling parallel to the gaps between the sheets to pass through, ensuring that the X-Ray beam is only travelling in one direction. It is essential that collimated X-Rays be used as it then passes to a monochromator which will be ineffective if X-rays take different paths through it. Although X-Rays generated in this way will be mostly composed of the $K\alpha_1$ emission there may be components from other emissions especially $K\alpha_2$ which must be removed or multiple diffractions

will be seen for each d spacing. The X-Ray monochromator is composed of a crystal which will diffract the incident X-Rays following Bragg's law, as wavelength is a component of Bragg's Law each wavelength will diffract at a different angle and so the crystal can be rotated to direct the monochromatic X-Rays towards the sample. The monochromatic X-Rays then pass though another collimator and onto the sample which is mounted on a goniometer, a device for the precise measurement of angles, enabling the crystal and detector to be moved, measuring orientations where Bragg's Law is satisfied and diffraction occurs.[12] Some materials may only produce small or poorly diffracting crystals and so much more intense X-Rays would be needed than can be generated by this route, for these samples synchrotron radiation can be used. By deflecting the path of a fast moving charged particle in a particle accelerator very intense radiation is emitted, the wavelength of this can be altered by the degree of deflection. A synchrotron where electrons are accelerated round a storage ring at several GeV can utilise an insertion device composed of several alternating polarity magnets along a straight stretch of the ring to cause the beam of electrons to undulate and emit high intensity radiation, which can be tuned to produce X-Rays.

2.3.2. Single Crystal X-Ray Diffraction.

Single crystal X-Ray diffraction is a very powerful technique in determining the structure of a material. There are several steps which must be taken to produce a crystal structure from a single crystal.

1. A suitable crystal must be identified, ideally between 50-250 μm and without cracks, internal imperfections or twinning (where two or more crystals have grown together). This crystal must then be mounted, usually on a glass fibre or nylon loop, and that then mounted on the goniometer head.

2. An X-Ray diffraction pattern is collected while rotating the crystal through different orientations.
3. Each reflection is indexed whereby it is assigned a Miller index in reciprocal space. From this the unit cell parameters and space group can be calculated.
4. A Fourier transform is then required to convert the reciprocal space into real space, however knowledge the phase is required to do this which is lost during the diffraction this is known as the phase problem. The phase problem can be solved by several different techniques such as Direct Methods, The Patterson Method or other techniques.[13, 14]
5. An electron density map is then produced which can be refined by repeating the process through several iterations to produce a better result.
6. The structure can then be derived from the electron density map and submitted to the Cambridge Crystallographic Data Centre (CCDC), a database of the crystal structure of small molecules.

2.3.3. Powder X-Ray Diffraction.

If large enough crystals can not be produced to measure SCXRD patterns, or in order to check the bulk phase purity of a material a powder XRD (PXRD) pattern can be measured. Whereas a single crystal will diffract X-Rays to produce a point the randomly orientated crystallites in a crystalline powder will produce overlapping reflections which rather than individual points will produce a series of concentric rings. The intensity of these reflections can be measured with varying 2θ angles and a PXRD pattern plotted. The PXRD pattern can be used to calculate the unit cell parameters of a crystalline material or be used to check a sample's phase purity by indexing the peaks measured to known unit cell parameters using a least squares

refinement. It is impossible to directly determine the 3D structure of a material from its PXRD pattern as the 3D data points are overlapping into 1 dimension; however it is possible if a structural modal of the material exists to perform a Rietveld refinement whereby the structure of the model is changed slightly and checked against the PXRD pattern until it fits the data, from this method it is possible to produce 3D structures of materials using PXRD patterns.

2.4. Thermogravimetric Analysis.

Thermogravimetric analysis (TGA) is use to determine the stability of the MOF and can be used to determine the inorganic metal content. TGA heats a sample of the material while simultaneously measuring its weight, this results in a plot of mass loss against temperature. The measurement is normally carried out in an alumina crucible under a flowing atmosphere of air. From this plot there are two distinct mass losses. Initially at lower temperatures if a MOF is unactivated there will be seen a mass loss as the solvent contained within the pores of the MOF is released, next there will appear a plateau up to the maximum temperature the MOF is stable followed by a significant mass loss as the organic linker is burnt off leaving the unchanging mass of the metal present in the MOF now oxidised. Once the mass remains constant at high temperatures indicating that all the metal from the MOF is oxidised the metal content in the MOF can be calculated.

2.5. CHN Combustion Elemental Analysis

CHN Combustion analysis is a very useful method of determining the chemical composition of a small amount of sample, only 2-5 mg is usually needed. The sample is burnt in an excess of oxygen and the gasses given off analysed. By the amount of water vapour, carbon dioxide and NO_x gasses produced the carbon,

hydrogen and nitrogen content of the initial analyte material can be determined. Using other methods like TGA or ICP-OES to determine the metal content the composition of the MOF sample and therefore its purity can be determined by combining these techniques.

2.6. Inductively Coupled Plasma Optical Emission Spectroscopy.

Inductively coupled plasma optical emission spectroscopy (ICP-OES) is a method of microanalysis capable of detecting very small amounts of many elements. Combined with CHN elemental analysis ICP-OES can be used to determine the composition and purity of a material. A disadvantage in using ICP-OES for determining the composition of MOFs is that it is a solution technique and so the solid MOF samples must first be digested usually in strong acid while at all times being aware of the concentration of the solutions produced.

A flow of argon gas is ionised into a plasma using a radio frequency coil to induce intense magnetic fields in the argon. A solution to be analysed is then nebulised into a mist and injected into the plasma. The plasma ionises the analyte, breaking it into its component atoms which are ionised by the plasma, as electrons recombine with the ions a distinct optical emission is produced, characteristic for each element. From the intensity of this emission compared to the emission of a reference standard the concentration of each element in the analyte solution can be determined. As the concentration of material digested is known this can be used to calculate the composition of the MOF.

2.7. Gas Sorption.

Gas sorption is one of the most widely used techniques to probe the characteristics of the surface of a material and is essential in characterising porous

materials such as MOFs. Knowledge of the porous properties of a material is essential for the understanding of its applications and isotherm gas sorption experiments can be used to provide information on the pore volume, surface area, pore size, pore size distribution, the type of interactions between the sorbate and the surface and can be used to calculate the strength of interaction between the sorbate and the surface. There are two distinct types of adsorption; physisorption where the sorbate is weakly and reversibly attracted to the surface of the material through van der Waals interactions and chemisorption which occurs when materials have chemically active sites where the sorbate can chemically bind to the material, sometimes irreversibly or the sorbate may desorb at lower pressure than it was adsorbed, producing a hysteresis loop in the isotherm.[15]

The adsorbate gas is in equilibrium with the adsorbed gas, this equilibrium is shifted with temperature and therefore the measurements are carried out at a constant temperature, usually at the boiling point of the adsorbate gas which in the case of N_2 is 77 K. There are two commonly used adsorption measurement techniques, gravimetric and volumetric. Using gravimetric adsorption isotherm measurements the weight change in the sample is measured as it is exposed to different pressures of adsorbate gas. Volumetric adsorption, the type used in this work, measures changes in adsorbate pressure after dosing the sample contained in a known volume, from this the amount adsorbed can be calculated once the pressure has stopped decreasing after dosing and an equilibrium is reached.[15, 16]

The isotherms measured, providing physisorption is dominant, adopt one of six different characteristic shapes which provide information about the nature of the adsorbate material (see Figure 31). The type I isotherm with its characteristic single low pressure adsorption followed by a plateau is indicative of microporous materials,

materials with pores smaller than 2 nm in diameter. The small pores adsorb a monolayer of adsorbate onto the surface at low pressures but then become saturated unable to adsorb any more. Type II isotherms are indicative of nonporous or macroporous, materials with pores with diameters larger than 50 nm, there is an initial adsorption as a monolayer is formed followed by further unrestricted adsorption as successive multilayer adsorption is built up. Type III isotherms are uncommon and depend upon the adsorbate-adsorbate interactions, this isotherm does not display an initial monolayer adsorption. Type IV isotherms are characteristic of mesoporous materials, materials with pores larger than the 2 nm micropores and so able to adsorb more than a single monolayer but smaller than the 50 nm macropores and so adsorb through capillary condensation which produces the second adsorption step before saturation, type IV isotherms sometimes have a hysteresis loop upon desorption as the capillary condensation occurs at lower pressures than the gas is released. The type V isotherm, like the type III does not display initial monolayer formation and arises due to uncommon adsorbate-adsorbate interactions. Type VI isotherms are indicative of sequential stepwise adsorption of layers of adsorbate onto a nonporous surface. The most common isotherms seen for MOFs are type I for microporous MOFs and type IV for larger mesoporous MOFs.[15]

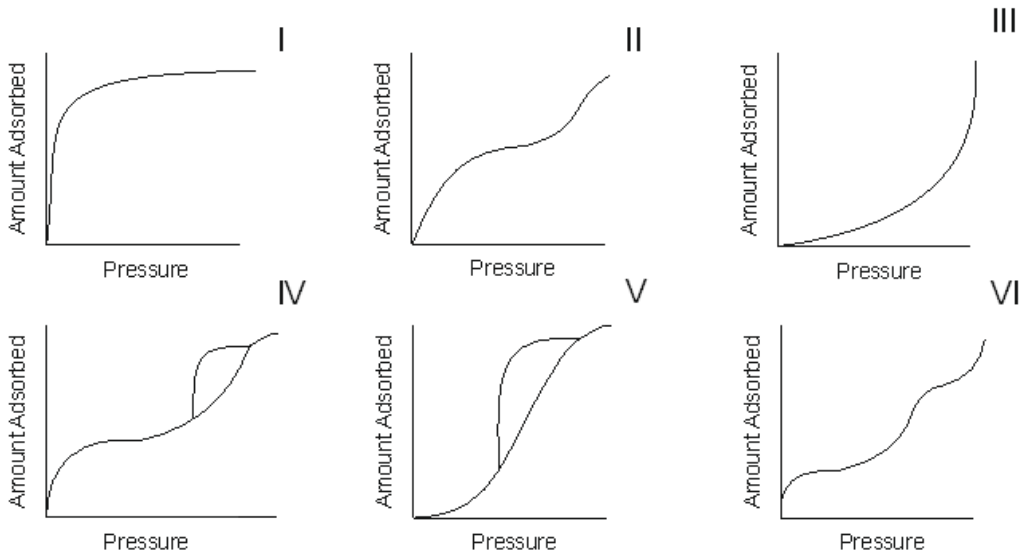

Figure 31: Adsorption Isotherm measurements for different material types.[15]

It is possible to use the data from the isotherm adsorption measurements to quantitatively assess the porosity of a material. Adsorption, especially physisorption, onto the surface of a material is in many ways analogous to the condensation of gas into a liquid therefore by multiplying the volume of gas adsorbed as saturation by the gas-liquid density factor, in the case of N_2 this is 0.0015, the pore volume can be calculated.[15] It is also possible to calculate the surface area using the Brunauer-Emmett-Teller (BET) method.[17] The BET method assumes that the adsorbed layers of guest are in equilibrium with the gas being measured.

$$\frac{p}{v(p^0 - p)} = \frac{1}{v_m c} + \frac{c - 1}{v_m c}\frac{p}{p^0}$$

Equation 1: The Linear BET equation. v is the volume of adsorbent, p/p0 is the relative pressure, v_m is the monolayer capacity and c is a constant.

If $\frac{p}{v(p^0-p)}$ is plotted against $\frac{p}{p^0}$ then a straight line is given, from Equation 1 the gradient of this line will be $\frac{c-1}{v_m c}$ while the intercept will be $\frac{1}{v_m c}$ from these two values a value for the monolayer capacity can be calculated. By multiplying the monolayer capacity by the cross sectional area of the adsorbate and Avagadro's number the surface area of the material is given.[17]

It is also possible to use adsorption isotherms to determine the heat of adsorption (Q_{st}) which is the strength of the interaction between the adsorbate and the adsorbent. In order to calculate Q_{st} several adsorption isotherms must be measured at different temperatures and virial type equations used to determine the coefficients used to calculate Q_{st}.[18] By plotting lnP against the amount adsorbed per gram for three different temperatures the curves can be fitted to Equation 2 to determine values of the virial coefficients a and b. Once these values are known Equation 3 can be used to plot the heat of adsorption against the amount adsorbed, from this the initial heat of adsorption can be determined and compared to other materials.

$$\ln P = \ln N + \frac{1}{T}\sum_{i=0}^{m} a_i N^i + \sum_{i=0}^{n} b_i N^i$$

Equation 2: Viral type equation for the determination of viral coefficients. P is the pressure of adsorption at temperature T, N is the amount adsorbed, a_i & b_i are the viral coefficients and m & n are the number of coefficients needed to describe the isotherm.

$$Q_{st} = -R\sum_{i=0}^{m} a^i N^i$$

Equation 3: Equation to determine Q_{st}. R is the ideal gas constant, N is the amount adsorbed and a_i is the viral coefficient.

2.8. Electron Microscopy.

Due to the Abbe diffraction limit it is impossible to observe any object smaller than ~250 nm using a visible light microscope. In order to observe anything smaller than this a source of illumination with much smaller wavelength must be used. To date no lenses able to focus a beam of light of small enough wavelength to observe very small objects have been developed. However a beam of electrons can have a de Broglie wavelength up to 100,000 smaller than a visible light photon and can be focused using magnetic and electrostatic lenses. Using an electron microscope resolutions smaller than 50 pm can be obtained. However there are disadvantages to electron microscopy, the electron beam can only travel in a vacuum and therefore the sample must be stable when exposed to high vacuums, also the high energy electron beam may damage fragile samples by causing ionisation, in the case of SEM the sample must be evenly coated in a conducting material such as gold or carbon in order to prevent charging from electrons on the material being examined which will deflect electrons and blur the image. There are two main forms of electron microscopy transmission electron microscopy (TEM) whereby a beam of electrons passes through the sample and scanning electron microscopy (SEM) where a beam of electrons scans the surface of the sample and secondary electrons and back scattered electrons are detected.

TEM allows for very high resolution images of materials, capable of detecting even a single column of atoms. TEM focuses a beam of electrons through a very thin sample deposited on a copper grid placed at the focus point of the beam, the absorption of the electrons by the material produce an image. In order to produce a TEM image the sample must be very thin so as to not block the beam entirely, it

also is also difficult to observe any features on the surface of the material and the high energy electron beam may damage the sample.

SEM produces images which show a great deal of detail on the surface of materials. An electron beam is scanned across the surface of the material and electrons produced by ionisation of the material (secondary electrons) or produced by elastic scattering (back scattered electrons) are detected. SEM is highly useful for determining the minute surface characteristics of a material however it is unable to probe deeply into the material. Also samples must be coated in a conducting material to prevent charge build up which will deflect the electron beam and result in blurred images.

2.9. Optical Spectroscopy.

2.9.1. Ultra Violet/Visible Spectroscopy.

Ultra Violet/Visible (UV/Vis) Spectroscopy is a valuable tool for exploring the electronic environment of compounds. The sample is illuminated with monochromatic light and the light transmitted through or reflected off the sample is measured as the wavelength is changed. Light of a suitable wavelength to excite an electronic transition within the material is absorbed and a drop in transmission or reflectance is observed. From the wavelength and intensity this absorption provides information about the electronic structure of the material. In transition metals distinctive absorbances occur due to d-d transitions, the energy gap between them variable with not just the metal but also the oxidation state and coordination environment, this will affect the wavelength absorbed and so the UV/Vis Spectrum can provide information as to the environment the metal is in. Organic compounds especially highly conjugated ones will absorb light due to the $\pi \rightarrow \pi^*$ transition;

generally the more electron rich and conjugated the compound is the lower the wavelength of the absorbed light will be as the HOMO and LUMO in the organic linker move closer together in energy. It is also possible for some metals and ligands to charge transfer between one another either through metal to ligand charge transfer (MLCT) or ligand to metal charge transfer (LMCT). Many of these MLCT and LMCT events occur when a complex absorbs a photon of light and thus will be detectable on a UV/Vis spectrum. Charge transfer is important for many reactions, especially photocatalytic reactions and so UV/Vis will show if this is taking place and give clues as to the nature of it.

For MOFs which are solid materials the UV/Vis Spectra must be measured as diffuse reflectance measurements. The sample is packed into a holder with a quartz window and placed into the spectrometer using an integrating sphere to ensure that 100% of the reflected light is measured regardless of what direction it is reflected in.

2.9.2. Fluorescence Spectroscopy.

Luminescence is the emission of light from a substance and occurs when an electron in an excited state decays back down to a lower energy. There are two main types of luminescence, fluorescence and phosphorescence. Fluorescence arises when the excited electron is in a singlet state, that is paired by opposite spin to a second electron in the ground state, this means that the decay of the excited electron to the ground state is spin allowed and thus occurs rapidly, the excited state lifetime for fluorescence is short and only endures for around 10 ns. Phosphorescence occurs from the excited triplet state where the excited electron has the same spin as the ground state electron, this arises usually due to intersystem crossing from the excited state. The matching spins mean that decay back to the ground state is forbidden and therefore much slower giving a much longer excited state lifetime usually around

milliseconds to seconds, though in some materials such as materials used for “glow in the dark” the excited state lifetime can last many minutes (see Figure 32). In many materials there are many vibrational excited states which are very close in energy to one another to which the excited electron can be excited; however luminescence only occurs from the lowest energy excited state and an excited fluorophore will decay non-radiatively to that level before emitting (see Figure 32). This means that the wavelength of the luminescence will be lower than the wavelength of the excitation as energy is lost during decay to the lowest excited energy level; this is known as the Stokes Shift. Also as luminescence only occurs from the lowest excited energy level the emission wavelength is independent of the excitation wavelength, this is known as Kasha’s rule meaning excitation by any wavelength of light shorter than the minimum energy to excite the fluorophore will result in emission at the same wavelength. Quenching is the process by which the intensity of the emission is decreased, quenching usually occurs due to interactions between the fluorophore and other surrounding molecules retuning the fluorophore to the ground state without the emission of light. The method of quenching can vary depending on the interaction between the fluorophore and the quencher, common mechanisms are charge transfer, intersystem crossing and spin orbit coupleing.[19]

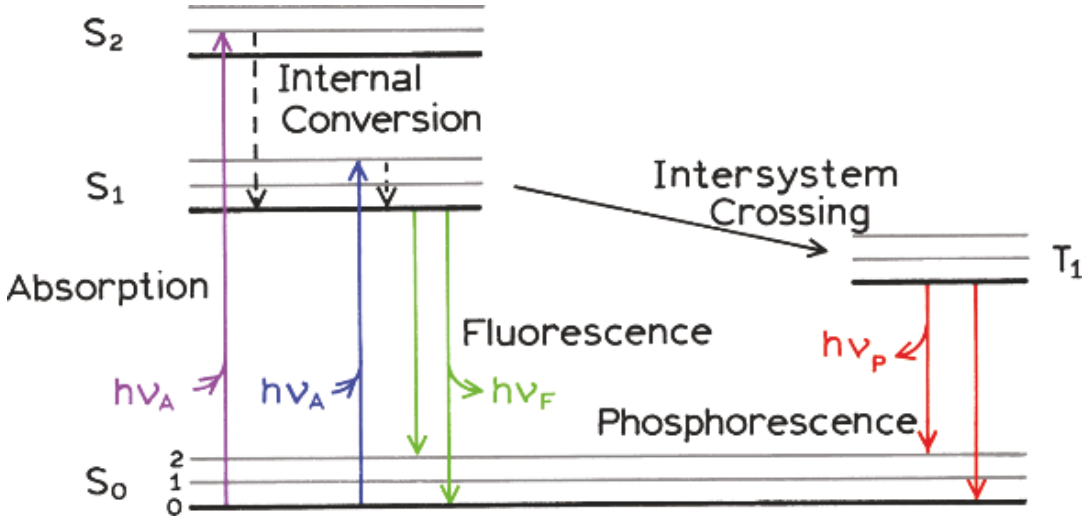

Figure 32: Jablonski diagram showing various forms of luminescence. Displayed are the ground state energy level (S_0) & the vibrational energy levels (0, 1, 2 grey lines). Excitation to the first singlet excited state (S_1) (Blue arrow), excitation to the second excited singlet state (S_2) (purple arrow), non-radiative decay (dashed arrow), fluorescence (green arrows), intersystem crossing into the excited triplet state (black arrow) and phosphorescence (red arrow). Figure adapted from reference [19].

2.10. Gas Chromatography and Thermal Conductivity Detector.

Gas chromatography (GC) is a means of separating different component gasses from a mixture. The sample mixture is injected onto a chromatography column with a flow gas to carry the sample through. The column is packed with a material to which the different gasses have different affinities and so will pass through at different rates. It is essential to choose the correct packing material for the column, one with too strong an affinity for one of the component gasses will trap the gas making the column ineffective and the gas won't be measured, a column with too poor an affinity for two or more of the component gasses however will be unable to separate them. A 5 Å molecular sieve is the most commonly used packing material for a GC column. The column is kept heated at a suitable temperature to prevent any low boiling point gasses from condensing onto the column and to ensure that the gasses pass through the column at a fast enough rate, however if the temperature is

too hot there will be insufficient interaction between the column and the gas and insufficient separation will occur. Temperatures between 60 °C and 160 °C are commonly used for GC columns.

There are many types of detector used for analysis of the gasses separated by GC, mass spectrometry and flame ionisation detection are often used but a thermal conductivity detector (TCD) is used in our case. TCD works by measuring the difference in the thermal conductivity of the gas flowing over a heating filament compared to that of a reference gas. A Wheatstone Bridge circuit is utilised where two resistors are connected parallel to two other resistors and the voltage across the two legs is measured, when the resistance of the two branches is equal no voltage is measured however any change in resistance along one branch produces a measured voltage. In the TCD detector one resistor on each branch is replaced by a heated filament with gas at a set temperature flowing over it, pure reference gas flows over once filament while the column effluent flows over the other (see Figure 33). The filaments are heated to temperatures greater than the gas due to the current running through them, as a gas with a different thermal conductivity to the reference gas flows over the filament off the column the temperature of the filament will change, changing the resistance and therefore the voltage measured. The integrated area under the peak on the chromatogram is proportional to the amount of gas and so by plotting a calibration curve the amount of gas present can be calculated. The larger the difference in thermal conductivity between the reference gas which is also used as the flow gas through the column and the analyte gas the larger the measurement will be, therefore it's important to tailor the flow and reference gas to the measurement required. Of primary interest in this work was hydrogen gas and so therefore argon was chosen as the flow and reference gas, this is because there is a

large difference in the thermal conductivity of hydrogen 230.4 mW $m^{-1}K^{-1}$ at 400 K and argon 22.6 mW $m^{-1}K^{-1}$ at 400 K, the larger the difference in thermal conductivity of analyte gas to flow gas the large the signal measured and thus the sensitivity of the TCD.[20]

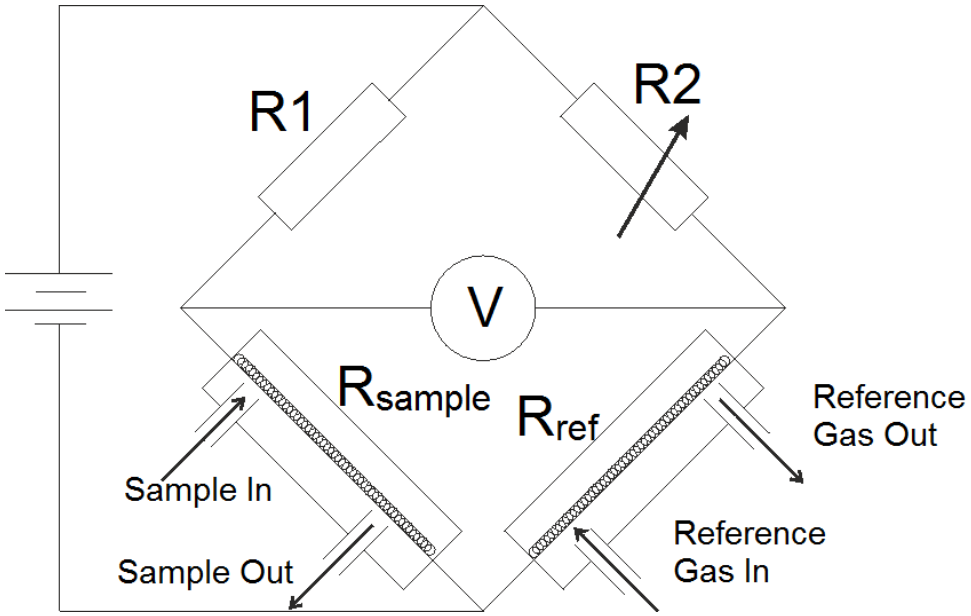

Figure 33: Diagram of a Wheatstone bridge circuit TCD.

2.11. Nuclear Magnetic Resonance Spectroscopy.

Nuclear Magnetic resonance (NMR) is a very useful technique for characterising compounds; it is particularly useful for organic compounds with a large number of different hydrogen environments making the spectra easy to interpret. Many nuclei exhibit spin, a quantised phenomena represented by the nuclear spin quantum number (I). This spin can adopt various directions identified by the magnetic spin quantum number (m_I), m_I adopts values of +I, +(I-1) … -I. The values for m_I are usually degenerate however as the nuclei are charged their spin produces a magnetic field, therefore if an external magnetic field is applied the m_I levels split as the nuclei's magnetic field can be aligned or opposed to the magnetic field. The degree of splitting of the magnetic spin sates is determined by the local

magnetic field felt by the nucleus; this is unique for each nucleus in each different chemical environment as the electrons around the nucleus produce magnetic fields which affect the applied field and alter the degree of splitting. The shielding by the electrons can take two forms, diamagnetic shielding which is opposed to the applied field and thus weakens the magnetic field applied at the nucleus, or paramagnetic shielding which enhances the strength of the magnetic field at the nucleus. Diamagnetic shielding arises from closed shell electrons, non valence electrons or electrons which have spherical or cylindrical geometries, paramagnetic shielding generally arises in small molecules with low lying excited states and so is not often seen however its effects can be dramatic enough to dominate when present. Shielding increases with greater amounts of electron density around the nucleus; therefore generally nuclei bound to more electronegative atoms have lower electron densities so their NMR peaks shifted downfield to higher chemical shift (δ) values as they are less sheilded.[1]

The m_I levels can be considered as a different processional spin as the magnetic moment of the nucleus processes around the applied magnetic field. The frequency of this procession is defined by the Larmor frequency which is defined as $\nu = \frac{\gamma}{2\pi} B$ where B is the external magnetic field at the nucleus and γ is the gyromagnetic ratio, which is $\gamma = \frac{\mu}{I}$ where I is the nuclear spin quantum number and μ is the magnetic moment of the nucleus.[1] Once the magnetic field is applied, along the z axis, the magnetic nuclear spin will align with the magnetic field along the z axis. If a pulse with duration $\frac{\pi}{2\gamma B_1}$ (where B_1 is the strength of the magnetic component of that pulse) of circularly polarised electromagnetic radiation with the magnetic component rotating around the z axis is applied to these nuclei at a

frequency close to the Larmor frequency the nuclear magnetisation tips through 90 °. The nuclear magnetisation will now be rotating at the Larmore frequency in the xy plane and so can be detected by inducing a current in a detector coil. Over time the nuclei return to the lower level z axis aligned with the applied field and a free induction decay (FID) is measured. Using a Fourier transform the FID can then be converted from a plot against time to a plot against frequency producing an interpretable spectrum. ^{1}H NMR spectroscopy is the most widely used form of NMR spectroscopy due to the simple spectra produced and the abundance of ^{1}H present in different chemical environments; ^{1}H NMR spectroscopy is used in this work to characterise the organic linker synthesised. It is also possible for ^{1}H in different magnetic environments to be coupled through the bonds in the molecule; these effects dissipate with distance but are pronounced through three bonds but usually not visible through 4. This coupling can occur in a variety of different methods but for coupling between two ^{1}H nuclei both bonded to a ^{12}C atom, which is without magnetic nuclear spin, the most common method is through coupling of the nuclear spin to the electron spin by Fermi contact. The lowest energy spin of an electron close to a ^{1}H nucleus will be antiparrelell to the nuclear spin, this electron is within a two electron bond and the Pauli Exclusion Principle states that the other electron within the bond must have the opposite spin, the repulsion between these two electrons will likely force them to opposite sides of the bond with this second electron more closely associated with ^{12}C atom. The electrons in the bond between the 2nd ^{1}H atom & the central ^{12}C will be similar to the first with two electrons one

more closely associated to the ^{12}C the other to the ^{1}H, Hund's Rule states that the electron more closely associated to the ^{12}C will adopt parallel spin to the other electron associated with the ^{12}C atom. Thus the same situation applies in this bond where the Pauli Exclusion principle requires the other electron in the bond to have the opposite spin which undergoes a Fermi contact interaction with the second ^{1}H and so provides two different energy levels for the second ^{1}H nuclear spin, antiparelelll or parallel to the electron and thus coupled with the first ^{1}H (see Figure 34). Through this coupling it can be seen that when the two ^{1}H nuclei have the same spin they are at a lower energy than when they have opposite spins providing two different energy levels and thus splitting the peak in the NMR spectrum.[1] The degree of splitting is measured by the coupling constant (J) which is calculated by multiplying the splitting in δ by the spectrometer frequency in MHz. In order for splitting to occur the nuclei must be in different chemical environments, however several equivalent protons in a different environment will have the same coupling constant and so the number of peaks seen due to splitting will be n+1 where n is the number of equivalent nuclei. The intensities of these peaks will follow a Pascal's triangle pattern. This is due to splitting from the second equivalent proton causing peaks to overlap. This is not the case when the protons aren't equivalent as the coupling constants are different producing s second splitting pattern.

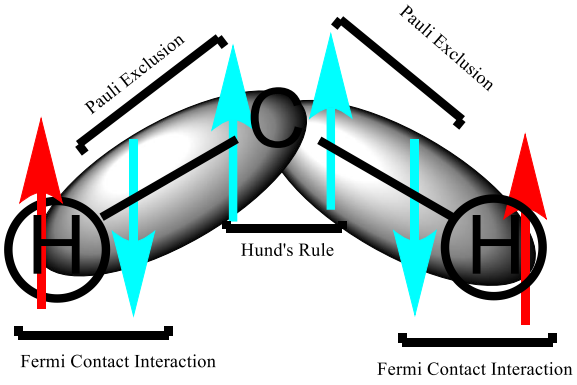

Figure 34: Diagram showing how spin-spin coupling can arise due to electron spin. Nuclear spin is identified with red arrows, Electron spin with blue arrows.[1]

1. P. D. P. Atkins, J, *Atkins' Physical Chemistry*, 8 edn., Oxford University Press, 2006.

2. V. Guillerm, F. Ragon, M. Dan-Hardi, T. Devic, M. Vishnuvarthan, B. Campo, A. Vimont, G. Clet, Q. Yang, G. Maurin, G. Férey, A. Vittadini, S. Gross and C. Serre, *Angewandte Chemie International Edition*, 2012, **51**, 9267-9271.
3. M. E. Davis and R. F. Lobo, *Chemistry of Materials*, 1992, **4**, 756-768.
4. A. D. McNaught and A. Wilkinson, *IUPAC. Compendium of Chemical Terminology, 2nd ed. (the "Gold Book")*, 2007, **79**, 1824.
5. N. Stock and S. Biswas, *Chemical Reviews*, 2011, **112**, 933-969.
6. P. Deria, Y. G. Chung, S. Randall, J. T. Hupp and O. K. Farha, *Chemical Science*, 2015, **6**, 5172-5176.
7. A. P. Nelson, O. K. Farha, K. L. Mulfort and J. T. Hupp, *Journal of the American Chemical Society*, 2009, **131**, 458-460.
8. M. I. Aroyo, U. Muller and H. Wondratschek, *International Tables for Crystallography*, 2004, **A1**, 2-5.
9. M. Birkholz, *Thin Film Analysis by X-Ray Scattering*, Wiley, 2006.
10. W. H. Bragg and W. L. Bragg, *PROCEEDINGS OF THE ROYAL SOCIETY OF LONDON SERIES A-CONTAINING PAPERS OF A MATHEMATICAL AND PHYSICAL CHARACTER*, 1913, **88**, 428-438.
11. C. D. N. Chan, *Loi_de_bragg.png (CC-BY-SA-3.0)*, https://commons.wikimedia.org/wiki/File:Loi_de_bragg.png#file.
12. U. W. Arndt and B. T. Willis, *Single Crystal Diffractometry*, Cambridge University Press, 1966.
13. A. L. Patterson, *Physical Review*, 1934, **46**, 372-376.
14. M. M. Woolfson, *Reports on Progress in Physics*, 1971, **34-417**, 369.
15. K. S. Sing, D. H. Everett, R. A. Haul, L. Moscou, R. A. Pierotti, J. Rouqiérol and T. Siemieniewska, *Pure and Applied Chemistry*, 1985, **57**, 1365-3075.
16. J. Rouquerol, D. Avnir, C. A. Fairbridge, D. H. Everett, J. M. Haynes, N. Pernicone, J. D. Ramsay, K. S. Sing and K. K. Unger, *Pure and Applied Chemistry*, 1994, **66**, 1739-1758.
17. S. Brunauer, P. H. Emmett and E. Teller, *Journal of the American Chemical Society*, 1938, **60**, 309-319.
18. C. Leszek and J. JagiełŁo, *Chemical Engineering Science*, 1989, **44**, 797-801.
19. J. R. Lakowicz, *Principles of Fluorescence Spectroscopy*, 2006.
20. C. F. Poole, K. H. C. Başer, L. M. Blumberg, J. A. Caruso, Q. Chan, E. C. Y. Chan, C. Cruz-Hernandez, P. Dawes, B. Dejaegher, F. Destaillats, F. L. Dorman, S. E. Ebeler, A. R. Fernandez-alba, K. Héberger, Y. V. Heyden, W. G. Jennings, L. Kim, M. S. Klee, M. Mal, P. J. Marriott, A. Martinez-Uroz, M. M. Mexcua, J. G. Millar, J. S. Nadeau, T. Özek, K. K. Pasikanti, K. M. Pierce, M. C. Pietrogrande, E. J. Reiner, V. Schurig, J. V. Seeley, M. J. Sithersingh, J. Smeyers-Verbeke, P. A. Smith, N. H. Snow, S. D. Stearns, R. E. Synovec, A. Tipler, A. Voelkel, T. P. Wampler, C. L. Wilkins and E. Woolfenden, *Gas chromatography*, Elsevier, 2012.

3. AlTBAPy

3.1. Overview.

There are several potential problems for photocatalysts, including not working under visible light irradiation and intermolecular π –π interactions and quenching excited states before reactions can take place.[1, 2] Pyrene has long been known for its optical properties. Including strong adsorption, long excited state lifetime and high quantum yield when excited.[3, 4] By incorporating a visible light absorbing pyrene based linker with a long excited state lifetime into a rigid metal organic framework (MOF) structure it may be possible to circumvent these problems faced by many photocatalysts. The energy levels for pyrene molecular orbitals have been calculated to be suitable for photocatalysis. The excitation energy has been measured to be 4.15 eV which is far larger than the 1.23 eV required to perform a photocatalytic water splitting reaction for hydrogen evolution.[1, 5] Density functional calculations have also been reported for pyrene which show the LUMO to be -2.89 eV relative to the Standard Hydrogen Electrode (SHE), which is below the 0 V standard potential for the reduction of hydrogen, this means that the energy level of the excited electron in Pyrene is suitably reducing to reduce H^+ to H_2.[6] This means that it may be possible to use pyrene based 1,3,6,8-tetrakis(p-benzoic acid)pyrene (TBAPy) incorporated into a MOF as a photocatalyst, in particularly for the splitting of water to produce hydrogen gas.[7, 8] The advantages of using a MOF are many fold, in particular the high surface area; MOFs are known for their highly porous structures which will provide a large internal surface area for catalysis to occur upon, overcoming a major problem with heterogeneous catalysis where the majority of the material is contained within the bulk and thus unable to react. Also the rigid repeating structure of the MOF will hold each of the linkers apart, reducing

quenching of their excited state by intermolecular interactions and allowing more time for the reaction to take place.

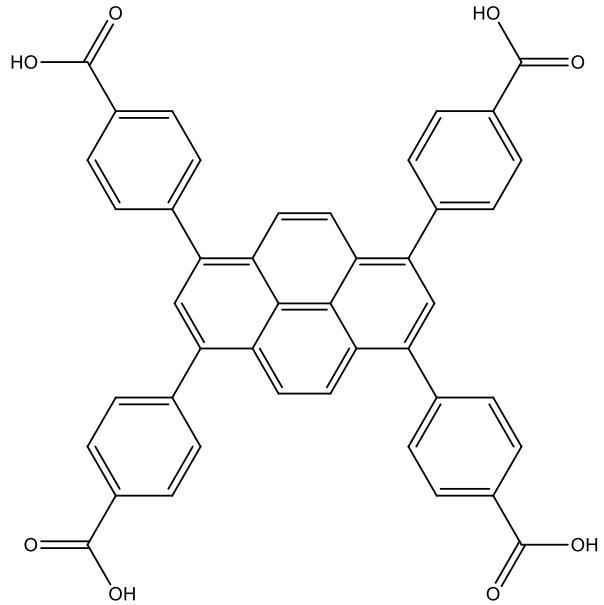

Figure 35: TBAPyH$_4$ linker.

For the MOF to have useful applications it will need to be stable, particularly to water which is a serious problem with many MOFs.[9, 10] Many water stable aluminium MOFs have been reported and shown to have potentially useful applications and so aluminium was considered as a suitable metal for our TBAPy MOF.[11-14] An interesting InTBAPy MOF has been reported by Sytlianou et al.[15] The chemistry of Al and In are very similar and so similar synthesis conditions, properties, characteristics and topology would be expected from an AlTBAPy and an InTBAPy MOF. Like many MOFs composed of metal (III) ions the InTBAPy MOF forms infinite chains of metal octahedra bridged by hydroxide groups in the axial positions. The octahedra are canted over at 60.4° and the carboxylate oxygens from the linker bridge adjacent octahedra bound to the equatorial positions. These infinite chains of metal ions are then linked by the TBAPy linker which orientates itself in parallel layers thereby producing a porous structure (see **Figure 36**)[11, 12, 15, 16]

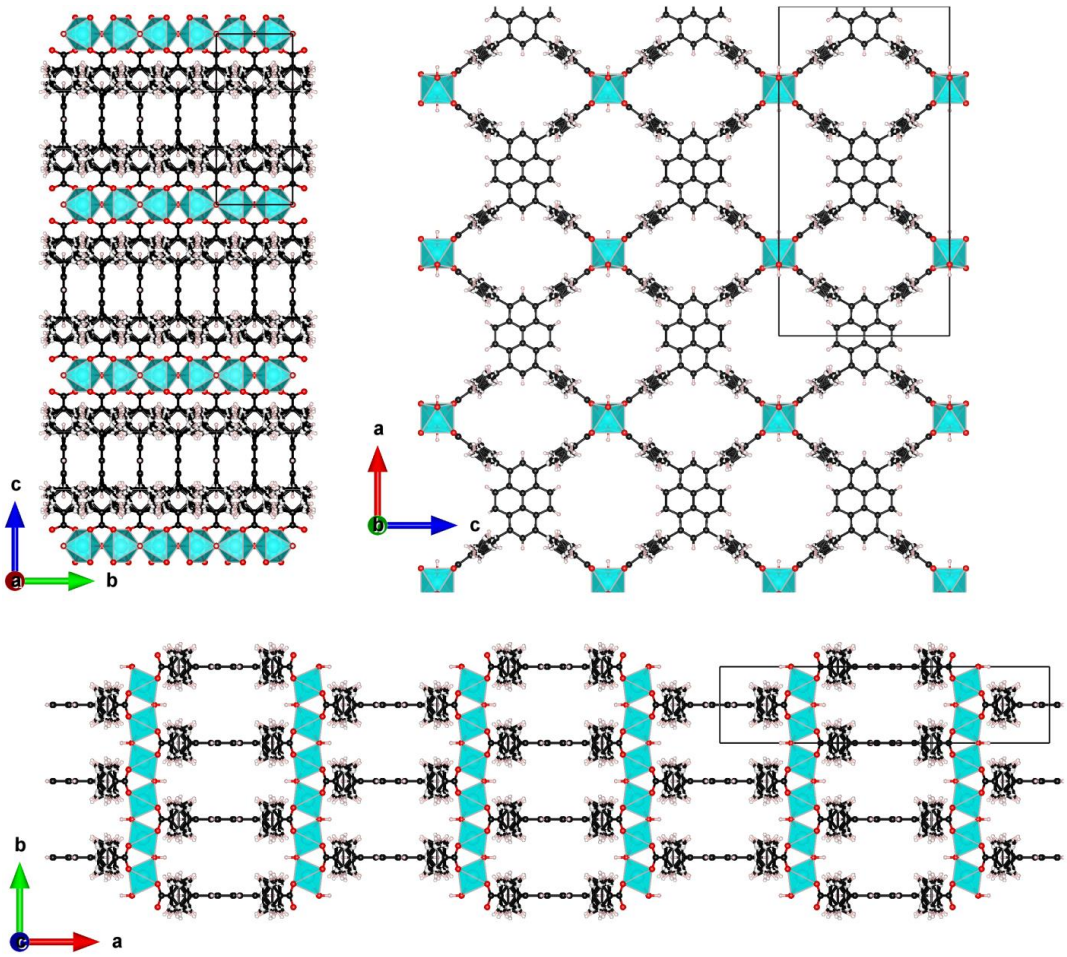

Figure 36: Structure of InTBAPy reported by Stylianou et al.[15] Indium atoms are coloured blue, Oxygen atoms are coloured red, Carbon atoms are coloured black and Hydrogen atoms are coloured white.

A new AlTBAPy MOF was synthesised and characterised by powder X-ray diffraction (PXRD), elemental analysis, thermal gravimetric analysis (TGA), the surface area was calculated and the porosity measured using nitrogen adsorption isotherms, the crystallites were imaged by scanning electron microscopy (SEM) and the optical properties were examined using UV/Vis and fluorescence spectroscopy. Once this material had been characterised it was tested for photocatalytic hydrogen evolution with and without an electron transfer reagent. Although no hydrogen was produced the electron transfer reagent was reduced but remained within the pores of the MOF. The material was analysed by transmission electron microscopy (TEM) and found that the platinum cocatalyst was not entering the pores of the MOF thus

preventing the reaction from proceeding. Platinum nanoparticles were inserted within the pores of the MOF, verified by TEM, nitrogen adsorption isotherms and inductively coupled plasma optical emission spectroscopy (ICP-OES). The photocatalysis reaction was repeated to the same result.

The AlTBAPy MOF was also studied for its carbon dioxide and methane adsorption. The isotherm for each at three different temperatures was measured and the heat of adsorption was calculated. This was compared to that reported for other MOFs and found to be lower than has been reported for CO_2 absorbers; however the initial heat of adsorption for methane is in the area required to be a useful methane storage material.

3.2. Experimental

3.2.1. Synthesis

3.2.1.1. $TBAPyH_4$ Synthesis.

The $TBAPyH_4$ linker was synthesised based on the synthesis reported by Stylianou et al with some improvements to the work up procedure, replacing the recrystallisation which uses a large amount of solvent with a Soxhlet extraction so the solvent can be re-used during the purification.[15] 1,3,6,8-tetrabromopyrene, (4-(methoxycarbonyl)phenyl)boronic acid, palladium tetrakis(triphenylphosphine), potassium carbonate and anhydrous and reagent grade 1,4-dioxane were all purchased from Sigma-Aldrich and used without purification. Tetrahydrofuran (THF), chloroform, sodium hydroxide and 37% hydrochloric acid solution were all purchased from Fisher and used without purification.

3.2.1.1.1. Suzuki Coupling

In dried glassware 1,3,6,8-tetrabromoPyrene (8.80 g 17.0 mmol), (4-(methoxycarbonyl)phenyl)boronic acid (15.4 g 85.5 mmol), palladium tetrakis(triphenylphosphine) (0.308 g 0.267 mmol) and potassium carbonate (18.6 g 134.5 mmol) were dissolved in anhydrous 1,4-dioxane (150 ml) and heated at 85 °C under nitrogen atmosphere for 72 h. After the Suzuki coupling was complete the crude product was filtered from the reaction mixture and washed with water. A Soxhlet extraction was then carried out upon the remaining solid using chloroform. Once the solution in the Soxhlet was running colourless the liquid was removed under vacuum and the resulting 1,3,6,8-tetrakis(4-(methoxycarbonyl)phenyl)pyrene solid was then checked for purity by NMR in deuterated chloroform (see **Figure 37**). The reaction proceeded to produce 11.0 g, 14.9 mmol of 1,3,6,8-tetrakis(4-(methoxycarbonyl)phenyl)pyrene with a yield of 87%.

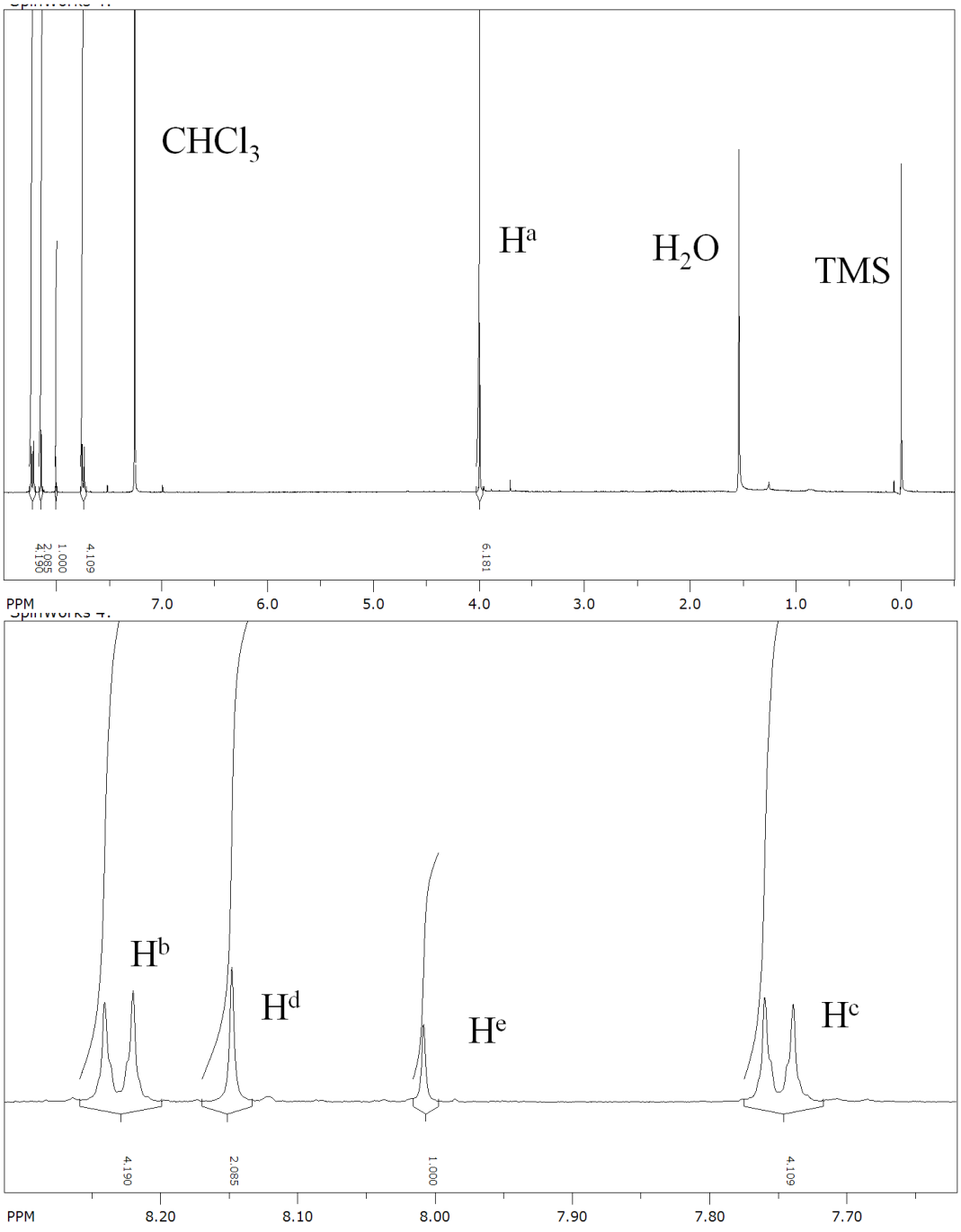

Figure 37: ^{1}H NMR spectrum of 1,3,6,8-tetrakis(4-(methoxycarbonyl)phenyl)pyrene. H^a indicating the methyl group protons, H^b indicating the protons ortho to the ester group, H^c indicating the protons meta to the ester group, H^d indicating the four Pyrene protons on the short axis of the Pyrene while H^e indicates the two protons on the long axis of the Pyrene (see Figure 38).

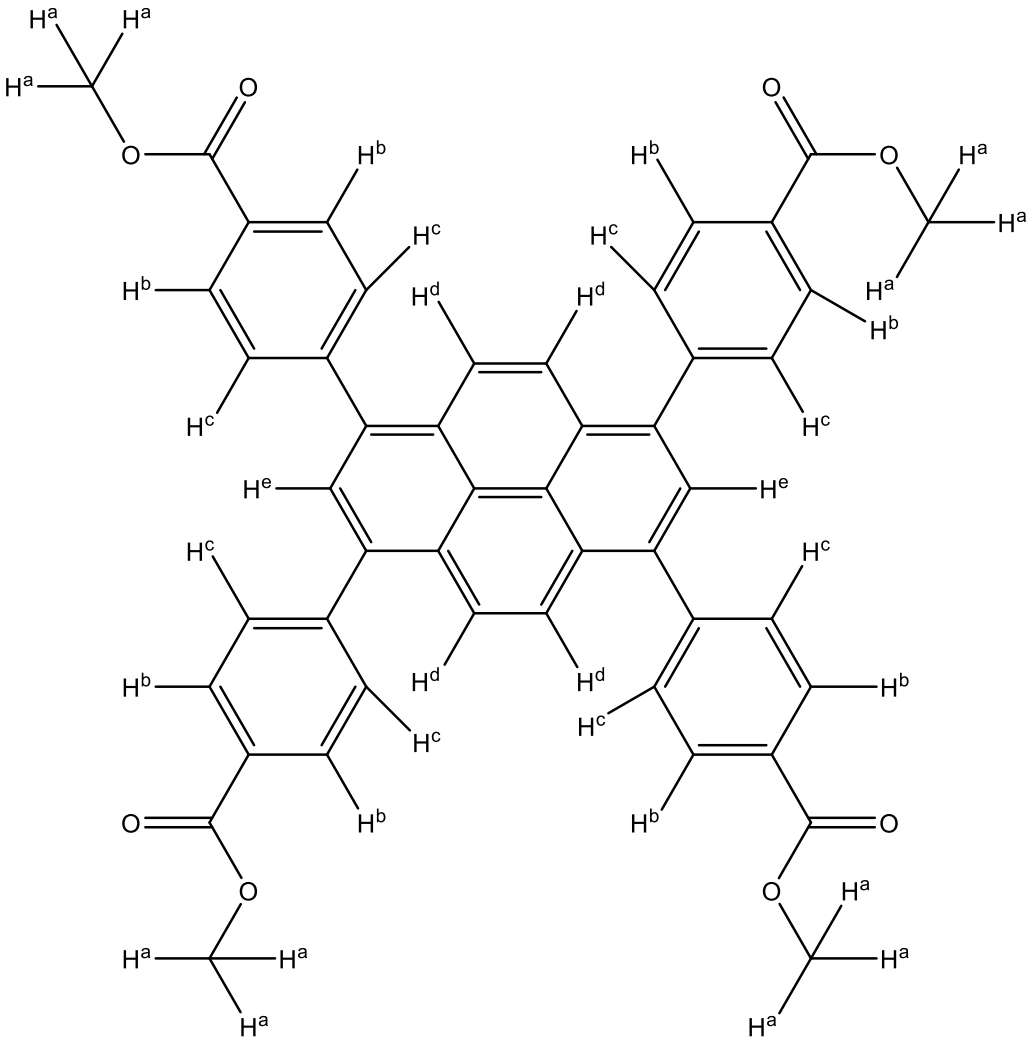

Figure 38: NMR proton assignments of 1,3,6,8-tetrakis(4-(methoxycarbonyl)phenyl)pyrene (see Figure 37).

As can be seen from the ^{1}H-NMR (see **Figure 37**) all the peaks assign to the hydrogen positions on the 1,3,6,8-tetrakis(4-(methoxycarbonyl)phenyl)pyrene or residual solvent.[17] It can also be seen that the peak areas integrate to give the correct values expected for the number of protons in each environment on the 1,3,6,8-tetrakis(4-(methoxycarbonyl)phenyl)pyrene.

3.2.1.1.2. Deesterification.

Next base catalysed deesterification of the 1,3,6,8-tetrakis(4-(methoxycarbonyl)phenyl)pyrene was performed following the procedure reported by Stylianou et al.[15] 1,3,6,8-tetrakis(4-(methoxycarbonyl)phenyl)pyrene (2 g 2.70

mmol) was added to THF (85 ml), 1,4-dioxane (32 ml) and water (32 ml), concentrated sodium hydroxide solution (30 ml) was also added, this was heated at 85 °C overnight. The solvent was then removed under vacuum and the resulting solid dissolved in water. 37% HCl solution was then added to the yellow solution until yellow solid precipitate out at approximately pH2. This solid was then filtered off, washed with water then diethyl either & dried. The purity was checked by ^{1}H-NMR in a solution of deuterated dimethyl sulphoxide (DMSO) (see **Figure 39**). This produced 1.75 g, 2.55 mmol of $TBAPyH_4$ in a 95% yield.

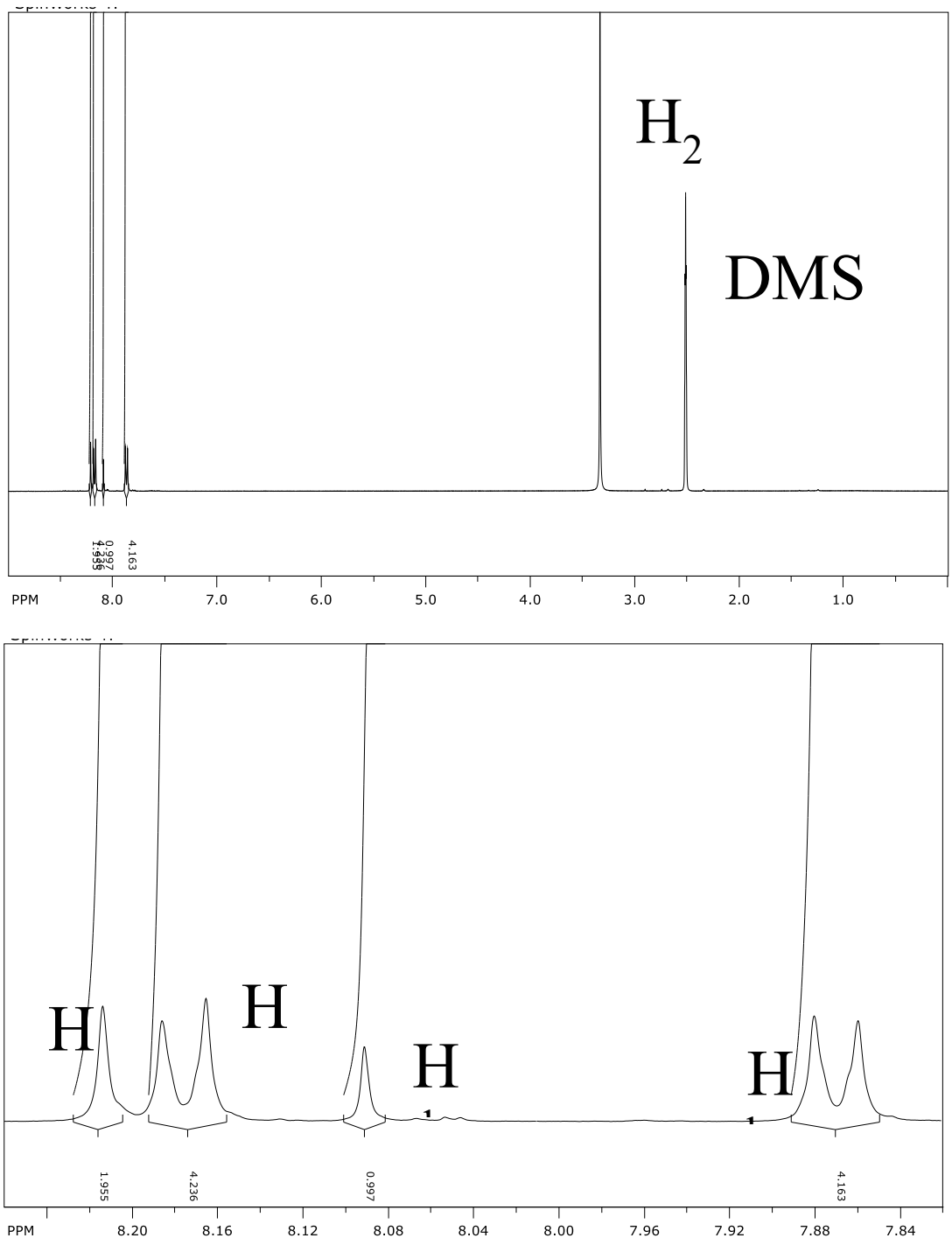

Figure 39: ^{1}H-NMR spectrum of TBAPyH$_4$. H^a indicating the protons ortho to the carboxylic acid group, H^b indicating the protons meta to the ester group, H^c indicating the four Pyrene protons on the short axis of the Pyrene while H^d indicates the two protons on the long axis of the pyrene (see Figure 40).

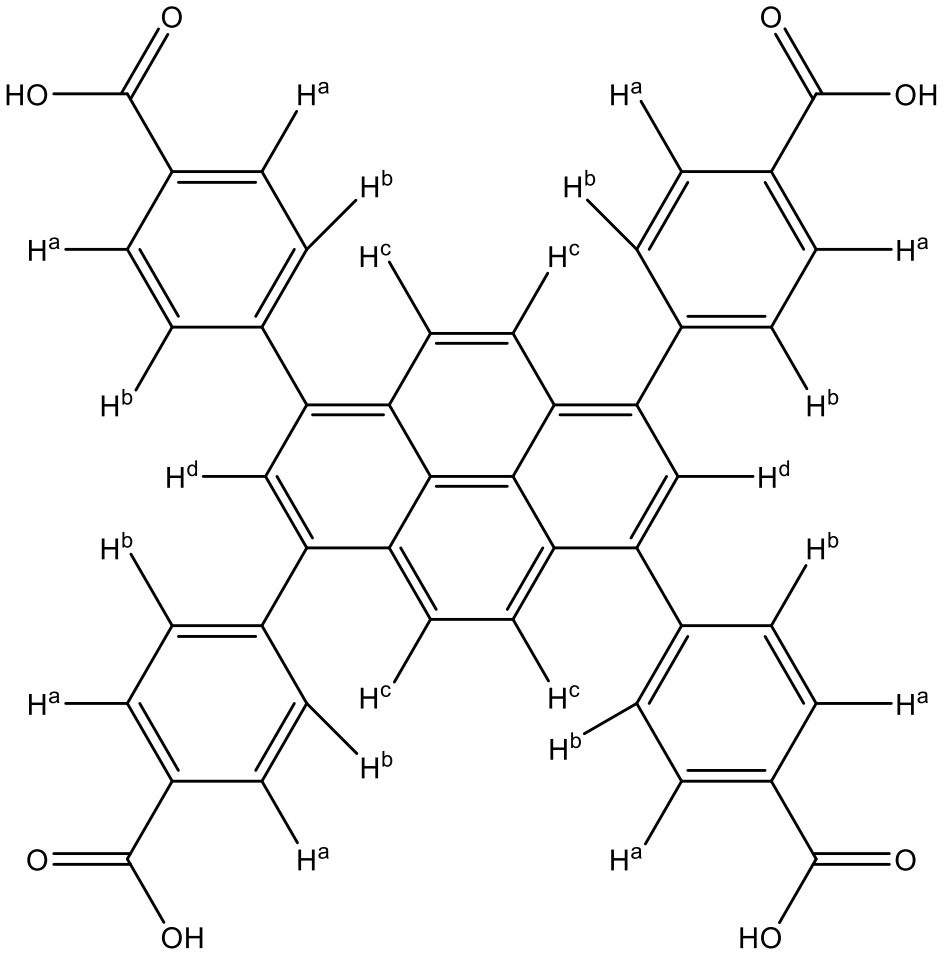

Figure 40: NMR proton assignments for TBAPyH$_4$ (see Figure 39).

All of the peaks present in the NMR spectrum (**Figure 39**) can be assigned to a proton environment on the TBAPy molecule or a solvent.[17] This shows that the synthesis has been a success and TBAPy has been synthesised and is pure, this can now be used for MOF synthesis.

3.2.1.2. AlTBAPy Synthesis.

3.2.1.2.1. Exploration of Synthesis Conditions.

There are many factors which affect the synthesis of MOFs, the reaction time and temperature, solvent system, metal salt and linker concentrations and the ratios of one to the other, the addition of a modulator or a mineralising agent and the amounts thereof must all be optimised to produce phase pure highly crystalline MOF.

Due to the similarity in the chemistry of indium and aluminium the conditions reported by Stylianou et al. for their InTBAPy MOF were used as a starting point, using the concentrations reported and a similar solvent system to explore the thermal conditions for the synthesis.[15] $Al(NO_3)_3.9H_2O$ (11 mg 0.03 mmol) and $TBAPyH_4$ (10 mg 0.015 mmol) were dissolved in (DMF (3 ml) and water (1 ml); all the reactions were attempted with and without addition of 10 µl of 37 % HCl as a mineralising agent, synthesise carried out without the addition of HCl produce an amorphous gel rather than a crystalline powder. These reactions were sealed in 10 ml glass vials with Teflon lined lids. A range of temperatures and times were chosen, 12 h, 24 h and 48 h reactions were run at temperatures of 100 °C, 120 °C and 140 °C. The products were washed with DMF and methanol and allowed to dry in air before being analysed by PXRD using a Bruker D8 Advance with Cu Kα radiation, in transmission geometry in a sealed 0.7 mm borosilicate spun capillary. From the PXRD patterns it could be seen that the most crystalline materials were produced at 120 °C or 12 hour reaction time. Therefore the optimal thermal conditions for synthesis of AlTBAPy MOF were determined to be 120 °C for 12 h; attempts at synthesise for shorter times than 12 h failed to produce sufficient quantities of material. The solvent system was then explored adjusting the ratio of DMF and water in the solvent system. Syntheses were carried out using $Al(NO_3)_3.9H_2O$ (11 mg 0.03 mmol) and $TBAPyH_4$ (10 mg 0.015 mmol) at 120 °C for 12 h, with different solvent systems, DMF (4 ml), DMF (2 ml) with H_2O (2 ml) and DMF (1 ml) with H_2O (3 ml). The resulting products were washed in DMF and methanol and left to dry in air before having their PXRD patterns measured. The most crystalline samples were synthesised in pure DMF, this solvent system also produced the largest amount of material. Next the concentration and ratio of

$Al(NO_3)_3.9H_2O$ and $TBAPyH_4$ were explored, using DMF (4 ml) and a 120 °C 12 h reaction time and temperature, reactions were carried out using 5, 6, 7, 8 and 9 mM concentrations of $Al(NO_3)_3.9H_2O$ each of these amounts of $Al(NO_3)_3.9H_2O$ was reacted with 2.5, 3, 3.5, 4 and 4.5 mM of $TBAPyH_4$. The products from each of these 25 reactions was washed with DMF and methanol then allowed to dry in the air before being analysed by PXRD. The PXRD patterns showed that a slight excess of $TBAPyH_4$ over the stoichiometric 2:1 $Al(NO_3)_3$: $TBAPyH_4$ ratio produced the most crystalline products. It was seen that the most crystalline material was produced using 8 mM $Al(NO_3)_3.9H_2O$ and 4.5 mM $TBAPyH_4$. Therefore these concentrations were used to scale up the reaction to produce enough AlTBAPy to be characterised and studied.

3.2.1.2.2. Optimal AlTBAPy Synthesis.

The synthesis of the AlTBAPy MOF was carried out following a procedure based on the synthesis reported by Stylianou et al for their InTBAPy MOF.[15] All reagents were purchased from Sigma Aldrich except for the HCl solution, DMF and methanol which were purchased from Fischer, all were used without purification. The $TBAPyH_4$ was synthesised in house, see above for synthesis details. $Al(NO_3)_3.9H_2O$ (48.5 mg 0.13 mmol) and $TBAPyH_4$ (51 mg 0.075 mmol) were dissolved in DMF (16 ml) with 37% hydrochloric acid aqueous solution (0.25 ml) added as a mineralising agent. The hydrochloric acid mineralising agent helps to enhance the crystallinity by forcing the deprotonation equilibrium of the $TBAPYH_4$ linker back towards the protonated side, the DMF will decompose to form dimethyl amine which will make the solution basic and will force the equilibrium in the other direction. The HCl mineralising agent in keeping more $TBAPyH_4$ protonated slows down the rate of reaction and thereby increases the crystallinity of the resulting

MOF. The H^+ from the HCl may also re-dissolve some of the smaller crystallites of the AlTBAPy MOF which form and allow the Al^{3+} and TBAPy to grow on larger crystallites instead by the process of Ostwald Ripening enhancing the crystallinity.[18] The reaction mixture was heated at 120 °C for 12 hours in a 40 ml glass vial sealed with a Teflon lined lid before cooling at a rate of 0.2 °C min^{-1} back to room temperature. The MOF was washed with DMF and methanol in order to remove any unreacted $TBAPyH_4$ and $Al(NO_3)_3$ and activated under dynamic vacuum at 175 °C to remove all residual solvent from within the pore space.

3.2.2. Photocatalysis.

3.2.2.1. Platinum nanoparticle suspension synthesis.

A suspension of colloidal platinum was synthesised using the method reported by Darwent et al.[31] All chemicals were purchased from Sigma Aldrich and used without purification. $H_2PtCl_6.6H_2O$ (20.2 mg) was dissolved in water (160 ml) to produce 0.244 mM concentration solution, to this sodium citrate (80.0 mg) was added and the solution was heated at reflux for 4 hours. The orange chloroplatinic acid solution became black with the precipitated colloidal platinum nanoparticles. This suspension was then used for the reactions.

3.2.2.2. Photocatalytic measurements.

The photocatalysis reactions were carried out based on the reported reaction conditions by Fateeva et al for their aluminium porphyrin MOF.[12] Colloidal platinum suspension (10 ml) was diluted with water (28 ml) in a 40 ml vial, Na_2EDTA (195 mg) was added to make a 16 mM solution of Na_2EDTA. This was then buffered to pH 6.0 by adding sodium citrate. To this MOF photocatalyst (5.0 mg) was added and the suspension purged with nitrogen for 30 min. This vial was

then sealed and exposed to the light of a 300 W xenon lamp, with a distilled water IR filter and a <450 nm wavelength Pyrex cut off filter; these two filters ensured that only the reaction mixture was only exposed to visible light. After 24 h a 250 µl sample of the dead space was taken and analysed using a Varian star 3400 CX gas chromatograph with a 5Å molecular sieve column and a TCD detector.

The reaction was also attempted using methyl viologen as an electron transfer reagent following the conditions reported by Fateeva et all for their aluminium porphyrin MOF.[12] The reaction was prepared the same way, by adding the colloidal platinum suspension (10 ml) to water (26 ml) in a 40 ml vial. Na_2EDTA (195 mg, 16 mM) was dissolved in the solution along with methyl viologen (74 mg 8 mM), sodium citrate was then added to buffer the solution to pH6. MOF photocatalyst (5 mg) was then added and the solution was purged with nitrogen for 30 min. The vial was then sealed and then exposed to the light of a 300 W Xenon lamp, with a distilled water IR filter and a <450 nm wavelength Pyrex cut off filter; these to ensure mixture was only exposed to visible light. After 24 h a 250 µl sample of the dead space was taken and analysed using a Varian star 3400 CX gas chromatograph with a 5Å molecular sieve column and a TCD detector.

3.2.2.3. Platinum insertion.

Platinum was photo deposited within the pores of the AlTBAPy MOF. All reagents were purchased from Sigma Aldrich and used without purification. $H_2PtCl_6.6H_2O$ (0.74g) was dissolved in water (50 ml) to produce a 0.0285 M concentration solution, $Na_2EDTA.2H_2O$ (0.093 g) was added as a sacrificial electron donor to produce a 5 mM concentration solution. Sodium citrate was then added to buffer the solution at pH6. AlTBAPy (50 mg) was then added and the suspension purged with nitrogen for 30 min. This was then exposed to UV light from a Hg lamp

overnight. The yellow suspension turned black and the Pt@AlTBAPy was then centrifuged out and washed with water until the liquor was clear and colourless. The green Pt@AlTBAPy was then rinsed with MeOH and allowed to dry in air overnight.

3.3. Characterisation.

3.3.1. PXRD

The powder X-ray diffraction of AlTBAPy MOF was collected using a Bruker D8 Advance with Cu Kα radiation, in transmission geometry in a sealed 0.7 mm borosilicate spun capillary. The powder X-ray pattern produced was then indexed to the unit cell of the reported InTBAPy using a least squares unit cell indexing method to determine if the structure of the AlTBAPy matched that of the InTBAPy as one would expect. Also by ensuring that all the peaks present could be indexed to that unit cell the AlTBAPy could be checked for phase purity.[15] The PXRD of AlTBAPy can be successfully indexed to the unit cell of the reported InTBAPy, this suggests that it has the same structure; this is to be expected with the similarity in the chemistry of Al^{+3} and In^{+3}.

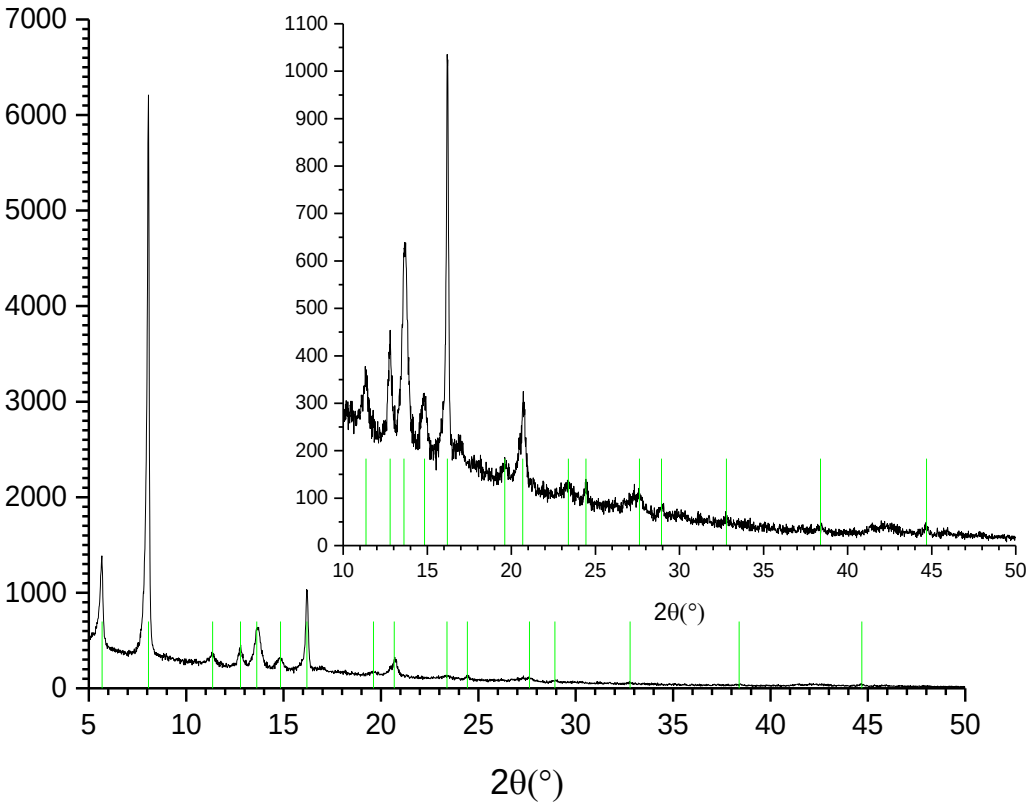

Figure 41: PXRD of AlTBAPy insert, zoomed in on higher angle region of the pattern. Indexed peaks are indicated with a green line.

All the peaks present in the PXRD pattern for the AlTBAPy index to the face centred orthorhombic unit cell with Cmmm space group of the InTBAPy.[15] The unit cell parameters are indexed to a unit cell of dimensions a = 7.14(4) Å, b= 30.67(8) Å, c= 16.0(1) Å with α=β=γ= 90°, this gives a unit cell volume of 3497.53 $Å^3$. The fact that there are no unindexed peaks in the PXRD pattern and that all the peaks present can be indexed to this unit cell suggests that the material is phase pure.

The fact that all the peaks present in the AlTBAPy PXRD pattern index to the same orthorhombic unit cell geometry as the InTBAPy MOF and that the unit cell parameters are so similar suggest very strongly that they have the same topology. This is to be expected from the similarity in chemistry of Al^{+3} and In^{+3} and the way

most 3+ metal ions adopt the same secondary building unit within MOFs.[11, 12, 15, 16] Compared to the unit cell of the reported InTBAPy MOF it can be seen that both materials have very similar unit cell parameters, a= 7.120(4) Å, b= 30.748(18) Å, c= 15.932(9) Å [15] for the InTBAPy compared to a= 7.14(4) Å, b= 30.67(8) Å, c= 16.0(1) Å for the AlTBAPy. This similarity is again to be expected from two MOFs with such similar metal secondary building units, identical linker and the same topology.[15]

This means that the AlTBAPy MOF is composed of infinite chains of aluminium octahedra with the vertices made up of the carboxylate oxygens of the TBAPy linker and a hydroxide in the axial position bridging two aluminium octahedra. The TBAPy linkers lie in planes between the aluminium chains, alternating on either side of the chain as each TBAPy carboxylate bridges two aluminium octahedra. This produces the porous structure of the MOF.

3.3.2. SEM

Scanning electron microscopy (SEM) images were taken of the AlTBAPy MOF. The AlTBAPy MOF was spread on carbon tape on an aluminium stub and coated with gold before being imaged with a Hitachi S-4800 Field Emission SEM. The SEM images of the AlTBAPy MOF (See Figure 42) show that there is only one crystallite morphology present, a thin plate like material which collects together to form clusters. It can also be seen that there is no second crystal phase or amorphous material present. This suggests that the AlTBAPy is phase pure and that there is no alumina produced during the synthesis of the MOF. Each small plate like crystallite can be measured and the diameter of those at the surface of the clusters can be seen to range from 0.3 μm to 0.6 μm.

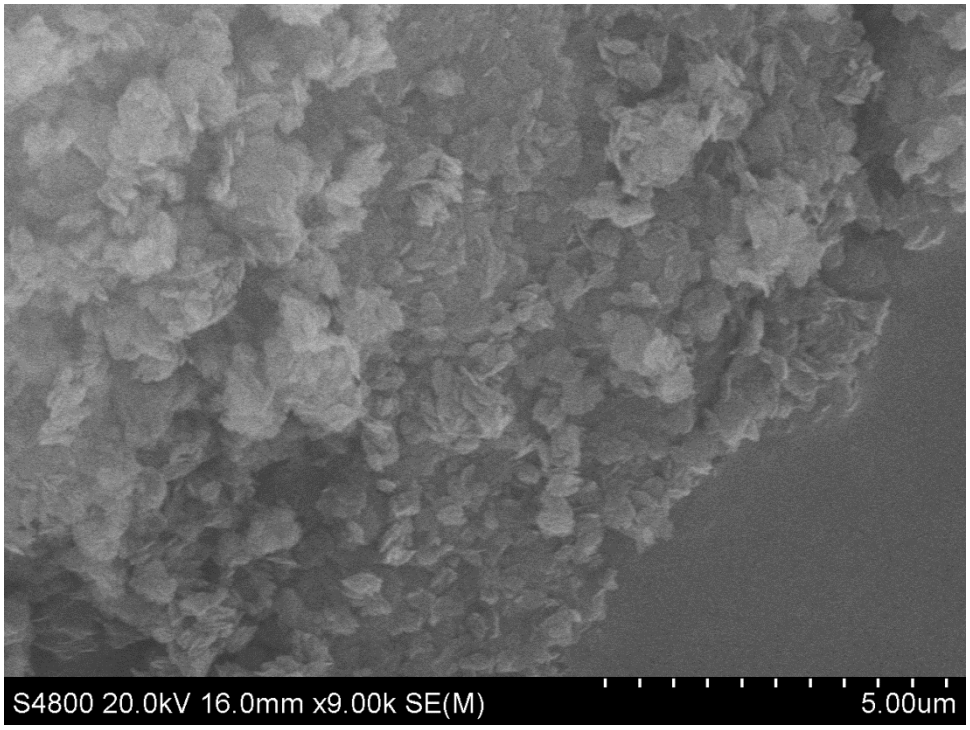

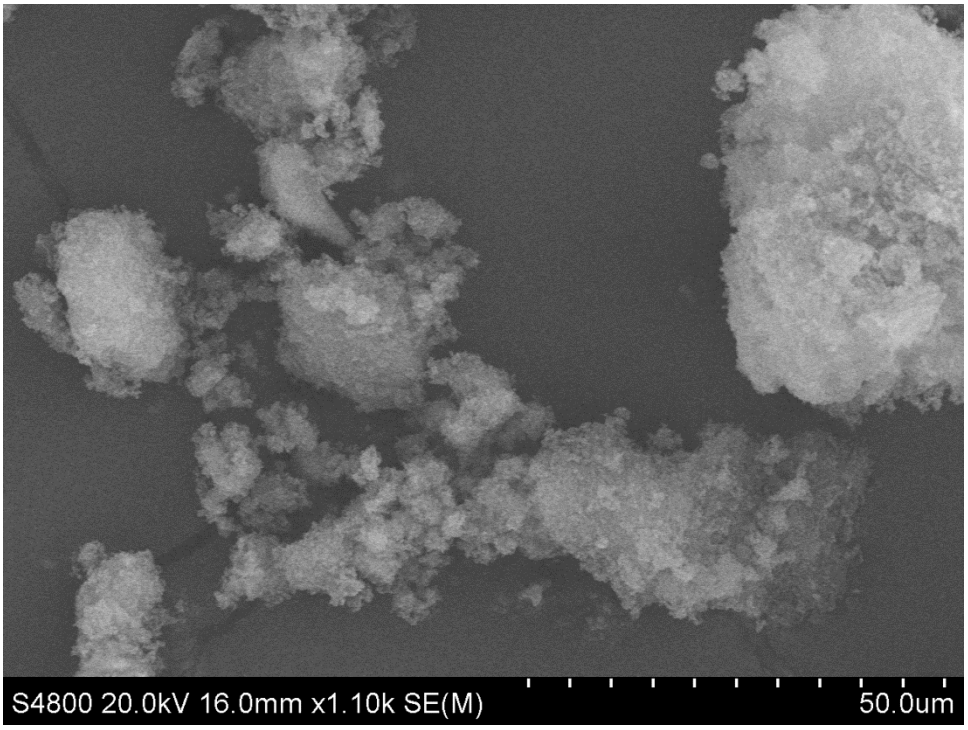

Figure 42: SEM Images of AlTBAPy MOF

3.3.3. TGA

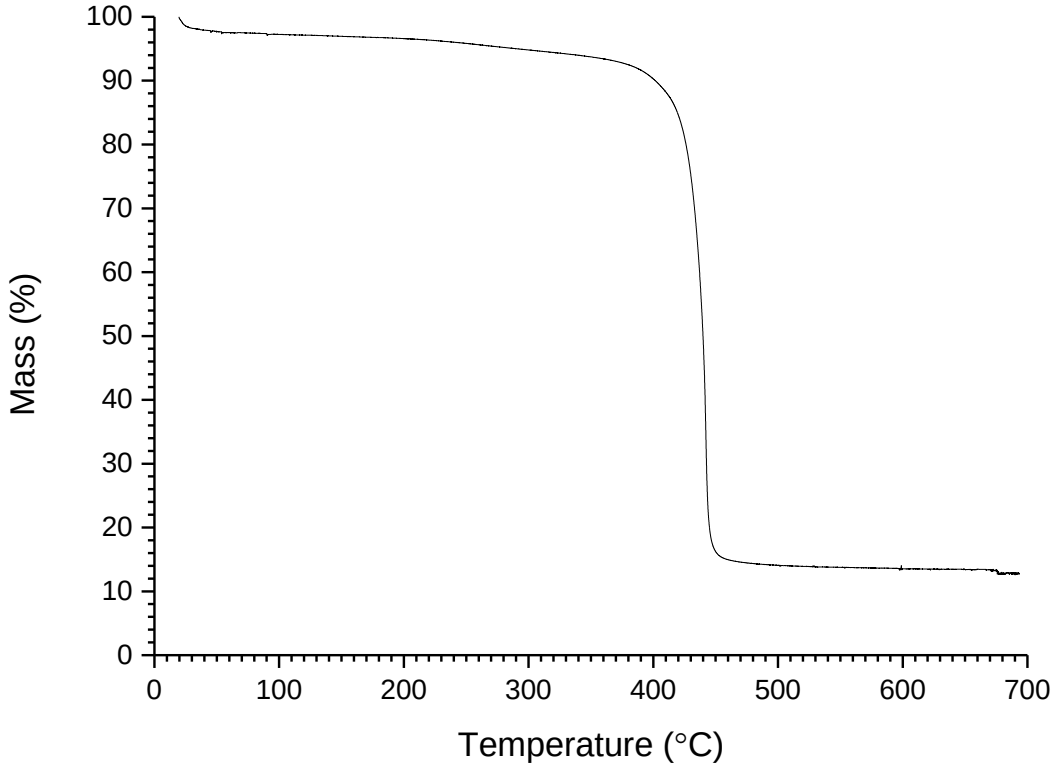

Figure 43: TGA of the activated AlTBAPy MOF.

A thermogravimetric analysis (TGA) was performed on the activated AlTBAPy MOF using a TA Instruments Q600. By heating at a rate of 0.75 °C min^{-1} with a 100 ml min^{-1} flow of air over the sample (see **Figure 43**). The TGA shows that the MOF is thermally stable and only decomposes at 400 °C. It is around this temperature many MOFs decompose at and is associated with the decomposition of the organic linker.[11, 15] The TGA also shows very little initial change before the decomposition of the MOF, this shows that the activation procedure has been successful as little mass loss is seen where solvent would be expelled from the pores of the MOF. Also from the unchanging mass of the inorganic residue at the high temperature end of the analysis, which will be composed of Al_2O_3 the percentage aluminium composition of the AlTBAPy MOF can be calculated. The Al_2O_3

inorganic residue composes 12.69 % of the original mass of starting AlTBAPy MOF, aluminium comprises 52.92% of the mass of Al_2O_3 therefore the starting mass of AlTBAPy is comprised of 6.72 % aluminium, coupled with the CHN elemental analysis this can be used to confirm the composition of the MOF.

3.3.4. Elemental analysis.

A CHN analysis of the AlTBAPy MOF was performed using an Isoprime CHNS Elemental Analyzer. From this it could be seen that the sample contained by mass 62.50 % carbon, 3.02 % hydrogen, and 0% nitrogen. The 0% nitrogen content shows that all the $Al(NO_3)_3$ reagent had been washed out of the MOF and that all the DMF had been removed from the pores of the MOF and therefore the washing and activation procedures were a success. Coupled with the 6.72 % aluminium content determined from the inorganic residue of the TGA this composition can be checked against the expected composition of from the crystal structure. From the crystal structure (see **Figure 36**) it can be seen that the expected composition is $Al_2(OH)_2(C_{16}H_6(C_6H_4CO_2)_4)$, this has a theoretical mass composition of 68.94 % carbon, 3.16 % hydrogen, aluminium 7.04% and oxygen 20.87%. The AlTBAPy MOF is a porous material and so when exposed to the atmosphere will adsorb moisture from the air. If 3.8 molecules of water are added to the theoretical composition of the AlTBAPy MOF it produces a theoretical mass composition of 63.28 % carbon, 3.81 % hydrogen and 6.46 % aluminium. This matches approximately the values measured through CHN & TGA indicating that the AlTBAPy is pure and does have the composition expected from the crystal structure (see **Figure 44**).

$Al_2(OH)_2C_{44}H_{22}O_8 \cdot 3.8H_2O$		
Element	Experimental	Theoretical
C	62.5 %	63.28 %
H	3.02 %	3.81 %
Al	6.72 %	6.46 %

Figure 44: Comparison of the measured mass compositions for AlTBAPy compared to the calculated values for the closet matching composition.

3.3.5. Surface Area Measurements.

From the crystal structure of the AlTBAPy it can be seen there are pores running through the MOF, it is therefore expected that the material will have a large surface area and internal pore volume. The surface area and pore volume of the AlTBAPy MOF has been calculated by measuring a nitrogen adsorption isotherm at 77 K using a Micromeritics 3Flex Surface Characterisation Analyser. The shape of the isotherm with its sharp initial adsorption at low pressure followed by a plateau coupled with its reversibility is characteristic of a Type I isotherm (see **Figure 45**). Type I isotherms are characteristic of microporous materials; where a monolayer of nitrogen condenses on the surface of the pores at low pressure. The plateau arises due to the pore volume becoming filled with the adsorbate, in this case nitrogen, the microporous pores being too small to adsorb further as the material becomes saturated.[19] From the crystal structure the pore size has been measured to be 0.7 nm wide (see **Figure 59**), this fits the IUPAC definition of a microporous material being one with pores with a diameter less than 2 nm and therefore the nitrogen isotherm adsorption results are as expected.[19] It can be seen the sharp increase in adsorbed volume at low pressures as the nitrogen adsorbs within the pores of the AlTBAPy

MOF followed by a flat section before a sudden increase again at higher pressures. The final increase in adsorbed gas at high pressures is due to gas condensing between the plate like crystallites of the AlTBAPy MOF. The SEM images show (see **Figure 42**) that the AlTBAPy MOF forms large clusters of small plates, this high pressure increase is due to condensation of nitrogen between those plates; this suggests that the sample analysed by SEM is characteristic of the bulk of the material.

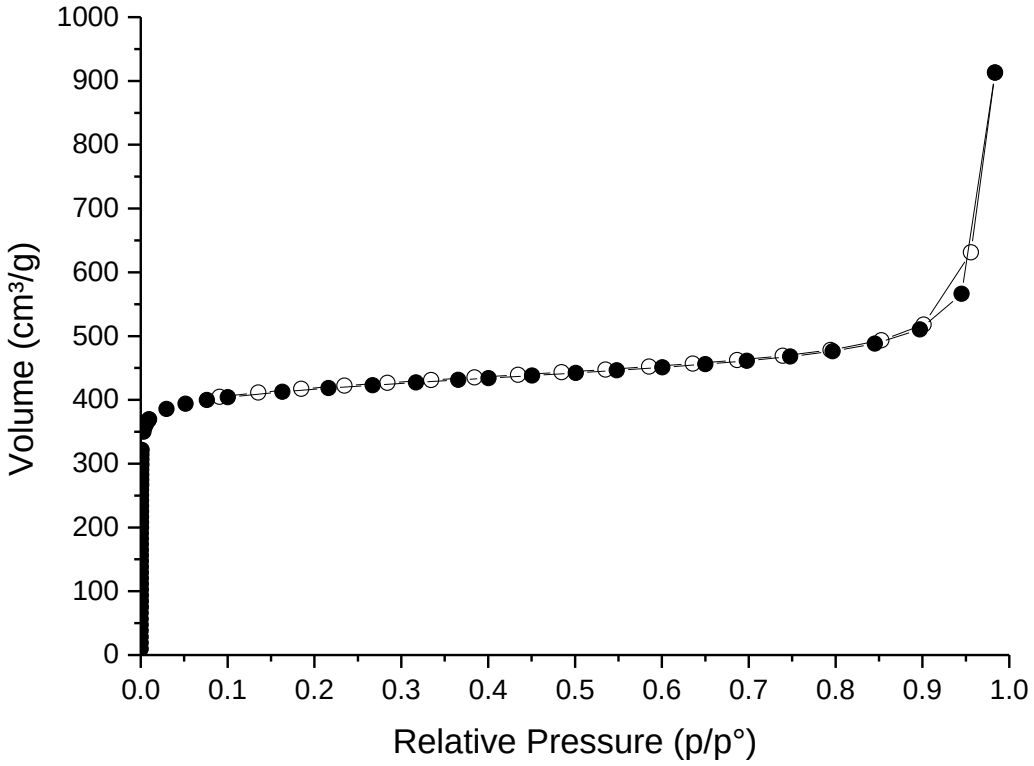

Figure 45: Nitrogen adsorption isotherm at 77K for AlTBAPy, filled circles representing the adsorption isotherm & empty circles representing the desorption isotherm.

The Brunauer-Emmett-Teller (BET) model has been applied to the nitrogen adsorption isotherm (see **Figure 45**) between P/P^0 pressure ranges of 0.003 and 0.03 to give a calculated BET surface area for the AlTBAPy of 1644 m^2g^{-1}.[20] By multiplying the volume of nitrogen adsorbed at P/P^0=27.0 within the MOF by the

nitrogen gas/liquid density factor of 0.0015 the pore volume can be calculated to be 0.646 cm^3g^{-1}.[19] These results when compared to that of the similar InTBAPy MOF reported by Stylianou et al, which has the same structure as the AlTBAPy. A BET surface area of 1189 m^2 g^{-1} and a pore volume of 0.639 cm^3 g^{-1} is reported for the InTBAPy, these values are similar to those measured for the AlTBAPy suggesting again that the AlTBAPy is similar to the reported InTBAPy. It is also possible to calculate the expected pore volume from the crystal structure using OLEX2 crystallographic software, simulating a rolling sphere with probe diameter of 1.8 Å, similar to the diameter of a nitrogen molecule travelling through the pores of the MOF. Using the structure reported for the isostructural InTBAPy MOF this calculates the pore volume to be 0.6482 cm^3g^{-1} which is also close to the value measured for AlTBAPy.[15, 21]

3.3.6. Optical Spectroscopy.

3.3.6.1. UV/Vis

The diffuse reflectance UV/Vis Spectrum of AlTBAPy MOF and the unreacted $TBAPyH_4$ ligand were measured using a Perkin Elmer Lambda 650 S UV/Vis Spectrometer (see **Figure 46**). The spectrum shows a large adsorption at 430 nm for the AlTBAPy MOF and at 480 nm for the free $TBAPyH_4$ linker. These large absorptions in the region of the spectrum from 200 nm to 500 nm are associated with the $\pi \rightarrow \pi^*$ transition.[22] This is to be expected from a molecule like TBAPy with such a highly conjugated pyrene at its core. The absorption wavelength for this $\pi \rightarrow \pi^*$ transition is blue shifted to lower wavelength by 50 nm when the $TBAPyH_4$ is bound to the aluminium oxide hydroxide chains to make the AlTBAPy MOF; this hypsochromic shift is due to the electronegative Al^{3+} withdrawing electron density

from the TBAPy linker and thus widening the gap between the π and π* orbitals.[23] In the AlTBAPy spectrum adsorptions resulting from HOMO-1 → LUMO and HOMO → LUMO+1 from the TBAPy linker can be seen at 245 nm, and 280 nm.[6]

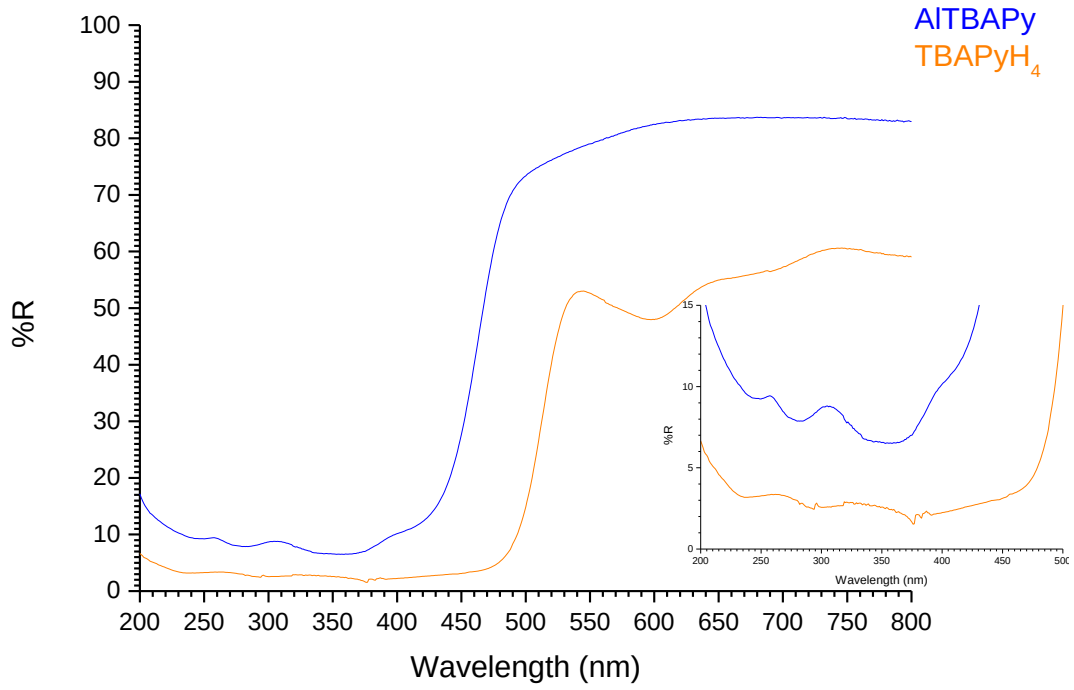

Figure 46: UV/Vis Spectrum of AlTBAPy insert of low wavelength, low reflectance region of the spectra.

From the UV/Vis spectra (see **Figure 46**) it can be seen that there is no strong, sharp adsorption as would be indicative of ligand to metal charge transfer between the TBAPy linker and the $AlO_4(OH)_2$ octahedra. This suggests that each Pyrene based linker is electronically isolated from the others and from the aluminium chains.

3.3.6.2. Fluorescence

The fluorescence spectra of the AlTBAPy MOF & the unreacted $TBAPyH_4$ free linker were measured using a Perkin Elmer LS 55 Fluorescence Spectrometer.

The samples were measured in the solid state using the maximum absorption wavelength, measured by UV/Vis spectroscopy as the excitation wavelength (see **Figure 47**).

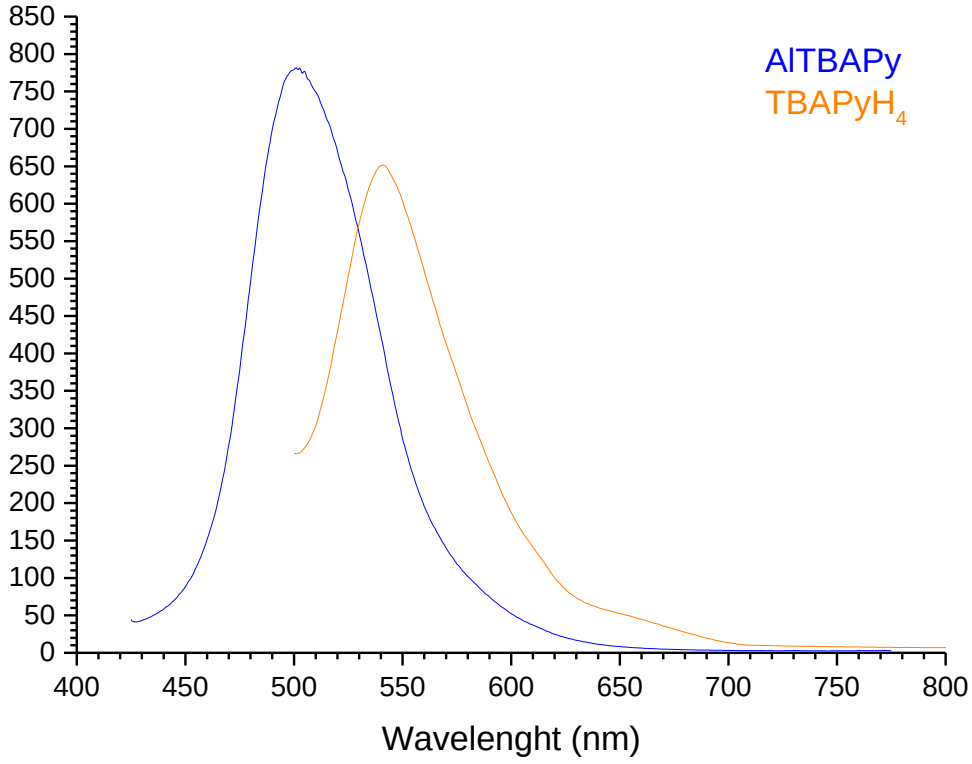

Figure 47: The Solid State Fluorescence Spectra of AlTBAPy MOF (Blue) excited at a wavelength of 400 nm and $TBAPyH_4$ Free Linker (Orange) excited at a wavelength of 470 nm.

The fluorescence spectra show a single emission peak at 500 nm for the AlTBAPy MOF & 550 nm for the free $TBAPyH_4$. This emission peak is due to the $\pi^* \rightarrow \pi$ transition on the pyrene.[24] As with the UV/Vis spectra the florescence peak for AlTBAPy is blue shifted slightly from the fluorescence peak of the free linker. This is due to the electronegative aluminium chain SBUs withdrawing electron density from the TBAPy linker, reducing the energy of the π orbital while increasing the energy of the π^* orbital, the wider gap between the two orbitals thus means more energy will be released upon the decay of the excited state back to the ground state,

thus blue shifting the emission wavelength. It can also be seen that the fluorescence of AlTBAPy is more intense than that of the free $TBAPyH_4$. This is likely due to quenching of the excited state through interactions between $TBAPyH_4$ molecules which are not possible in the AlTBAPy MOF as the ridged framework holds the TBAPy apart.

The lack of ligand to metal charge transfer bands in the optical spectra indicates that the TBAPy linker is electronically isolated from the aluminium oxide hydroxide chains. This suggests that the TBAPy will not be able to act as a sensitiser for the aluminium oxide chains. This is not unexpected, the very large band gap of aluminium oxide coupled with the small excitation energy of the TBAPy due to its extensive conjugation meant that the chance for an overlap between the two was small. However it is possible that the TBAPy can act as a molecular photocatalyst; the structure of the AlTBAPy MOF by holding the TBAPy linkers apart from each other will reduce the likelihood of quenching of the excited state.[15]

3.4. Water stability

One of the major challenges of MOF chemistry is the instability of many MOFs to even small amounts of water; many MOFs decompose even with exposure to the moisture in the air.[9, 10] In order to ensure that the AlTBAPy MOF is water stable and thus able to be used for practical applications the MOF was soaked in water for 24 hours and 72 hours then the PXRD was checked to confirm that the crystallinity and the structure of the MOF had not degraded (see **Figure 48**). The PXRD was measured using a Bruker D8 Advance with Cu Kα radiation, in transmission geometry in a sealed 0.7 mm borosilicate spun capillary

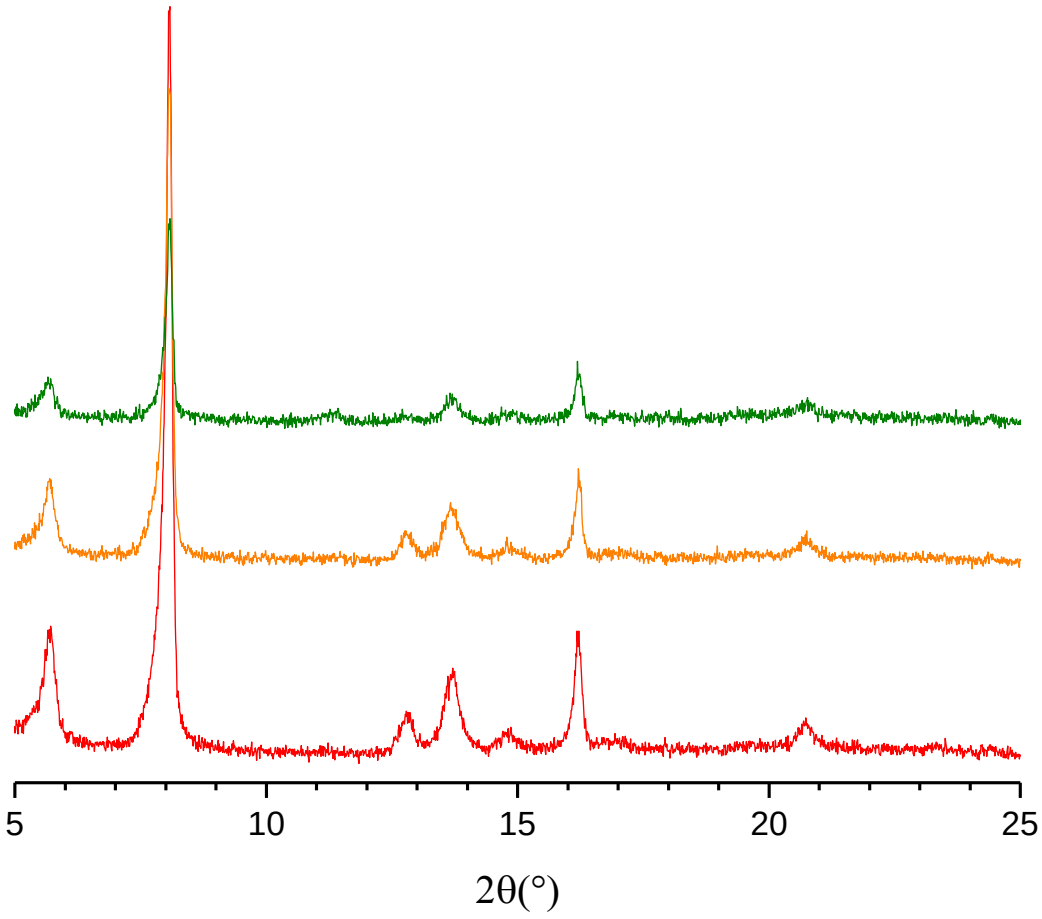

Figure 48: PXRD of AlTBAPy after soaking in water for 0h (Green), 24 h (Orange) & 72 h (Red).

From the PXRD (see **Figure 48**) it is seen that there is no decrease in crystallinity of the MOF as it is soaked in water, all the peaks remain present in the same position and do not broaden, this shows that the crystallinity is not damaged by the water and so the AlTBAPy MOF is stable and therefore may have practical applications. Furthermore the PXRD patterns of the soaked MOF index to the expected unit cell of the unsoaked MOF (see **Figure 49**). This shows that there is no change in the unit cell of the MOF when it is soaked in water. Some MOFs, particularly MOFs composed of aluminium can be flexible and alter the Al coordination environment when exposed to different solvents such as water, the fact

that there is no change in the unit cell parameters for the AlTBAPy MOF when immersed in water shows that this is not the case for this MOF.[11]

Soaking time	0 h	24 h	72 h
a (Å)	7.14(4)	7.14(4)	7.12(4)
b (Å)	30.67(8)	30.6(4)	30.5(4)
c (Å)	16.0(1)	15.8(1)	15.9(1)

Figure 49: Unit Cell parameters for AlTBAPy MOF soaked in water.

3.5. Photocatalysis.

The AlTBAPy MOF was tested as a visible light photocatalyst for a hydrogen evolution water splitting reaction. The AlTBAPy MOF was tested using water, colloidal platinum nanoparticles and Na_2EDTA as a sacrificial electron donor, the platinum is needed to act as a cocatalyst. The reaction was also attempted using methyl viologen as an electron transfer reagent. The AlTBAPy is excited and transfers an electron to the methyl viologen which then in turn transfers the electron to the colloidal platinum nanoparticles and from there onto H^+ to produce the hydrogen.[12] The advantage of using an electron transfer reagent such as methyl viologen is that it can allow much better interaction between the catalysts as it will have a stronger affinity to both the MOF and the colloidal platinum than the platinum does directly to the MOF. The disadvantage is that it involves an extra step in the reaction mechanism making it less efficient and thereby reducing the amount of energy available. However methyl viologen is a well known reagent used in this type of water splitting reaction and has been used successfully many times over

several decades.[8, 12, 27-30] Another potential disadvantage is that the reduced methyl viologen radical which transfers the electron from the photocatalyst to the platinum cocatalyst is highly sensitive to oxygen, this means that all oxygen in solution and in the dead space in the reactor must be thoroughly purged for the reaction to proceed. However many photo catalysts are sensitive to oxygen and so this would need to be done anyway.[29] In all the reactions EDTA will be used as a sacrificial electron donor to replace the electron lost from the AlTBAPy photocatalyst as is common for these reactions.[8, 12]

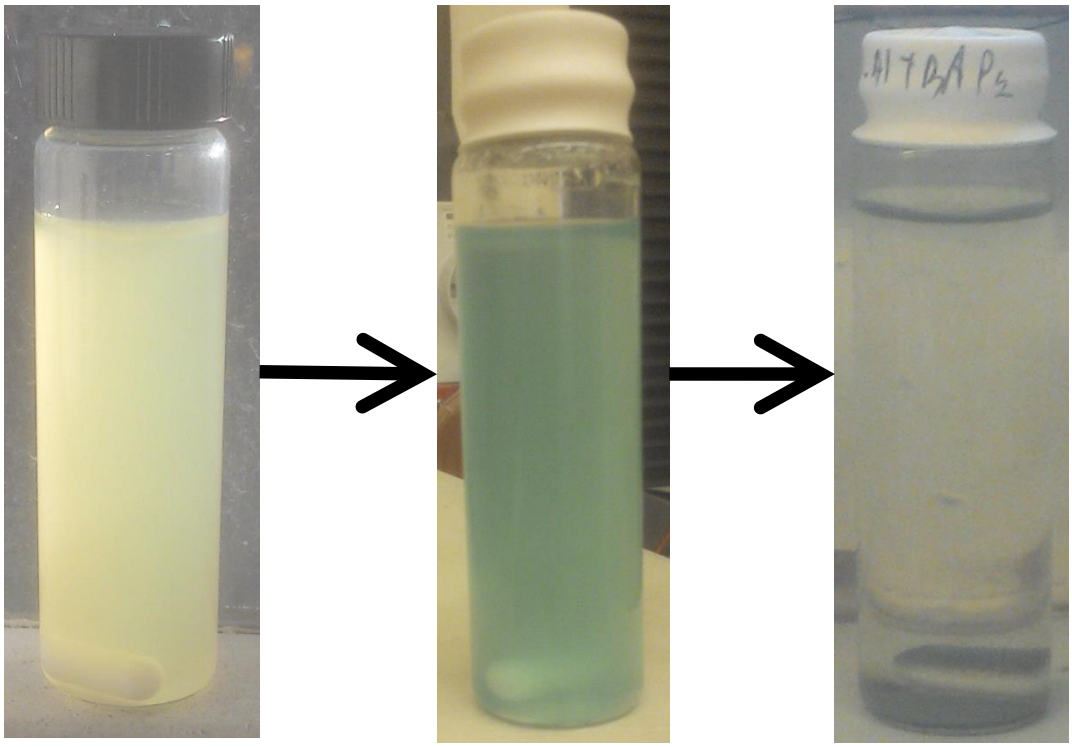

Figure 50: Photographs of AlTBAPy MOF before, after & after photocatalysis reaction using Methyl Viologen as an electron transport reagent. Also photograph showing the reaction mixture after the AlTBAPy MOF had been allowed to settle.

However it could be seen that a reaction had taken place as the reaction mixture had changed from the yellow colour of the AlTBAPy MOF to the distinctive

blue colour of the reduced methyl viologen radical (See **Figure 50**). As the methyl viologen does not adsorb visible light and will not be reduced by irradiation with visible light this shows that a reaction has happened. The AlTBAPy MOF adsorbing the light and reducing the methyl viologen.[32] The transfer of an electron from reduced methyl viologen to colloidal platinum nanoparticles in order to produce hydrogen from water is a well established reaction and so it is unexpected that no hydrogen was produced from this reaction.[8, 12, 27-30] However when the suspension was allowed to settle it became clear that the supernatant remained colourless and the previously yellow MOF had in fact turned blue (see **Figure 50**). This suggests that the methyl viologen in solution remains unreduced while the methyl viologen which entered within the pores of the AlTBAPy MOF was reduced. However the reduced methyl viologen was then unable to exit the pores of the AlTBAPy MOF. Methyl viologen is a charged aromatic bipyridyl compound (see **Figure 51**) and so will interact strongly to the highly aromatic TBAPy linker, through π-π interactions and through cation-π interactions between the 2+ cationic charge on the methyl viologen and the highly electron rich pyrene moiety. These two attractive interactions explain why the methyl viologen can enter the pores of the MOF but then remain trapped on the internal surface within the pores of the MOF. The colloidal platinum nanoparticles should be small enough to enter within the pores of the MOF & react with the reduced methyl viologen trapped within so it is unexpected that the reaction has not taken place. In order to determine if the platinum nanoparticles had entered the pores of the AlTBAPy MOF the sample was examined under transmission electron microscopy (TEM).

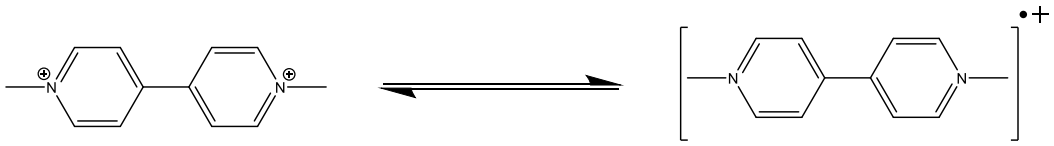

Figure 51: Structure of methyl viologen and the reduced methyl viologen.

3.5.1. TEM

After the unsuccessful attempts at photocatalysis the AlTBAPy MOF was studied under TEM. The samples were deposited using MeOH on a carbon coated copper TEM grid and imaged using a JEOL 2100 TEM at 200 kV. The platinum, with its greater electron density will show up much darker as the highly porous mostly carbon based MOF and it should be clear if it has entered the pores of the MOF.

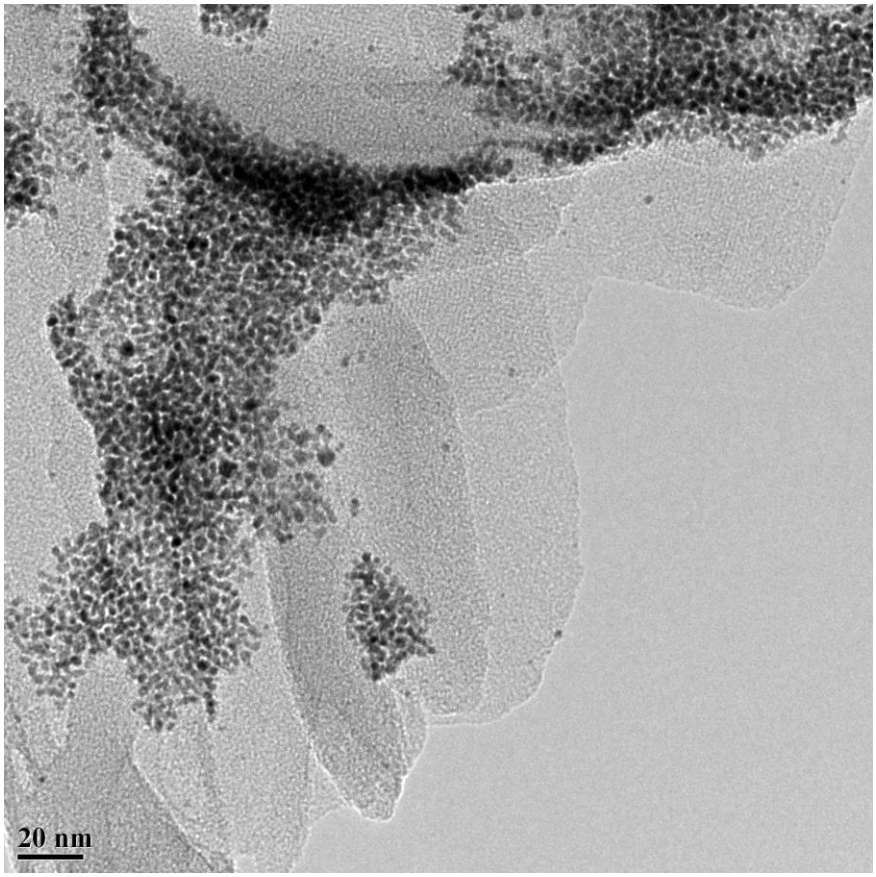

Figure 52: TEM Image of AlTBAPy Post photocatalysis reaction.

It can be seen from the TEM images (See **Figure 52**, **Figure 54** & **Figure 55**) that the platinum nanoparticles are conglomerated on the surface of the MOF. This could be an explanation as to why the reduced methyl viologen was unable to act as an electron transfer reagent that the colloidal platinum nanoparticles agglomerate onto the surface of the AlTBAPy MOF rather than entering the pores and are thus unable to come into contact with and therefore react with the reduced methyl viologen which is trapped within the pores of the MOF.

By applying a brightness threshold to the image a binary image can be produced where only the platinum particles within the MOF are displayed, these can be identified by the software. From this image the number of particles can be counted, their area measured and the Feret diameter calculated (see **Figure 54**).

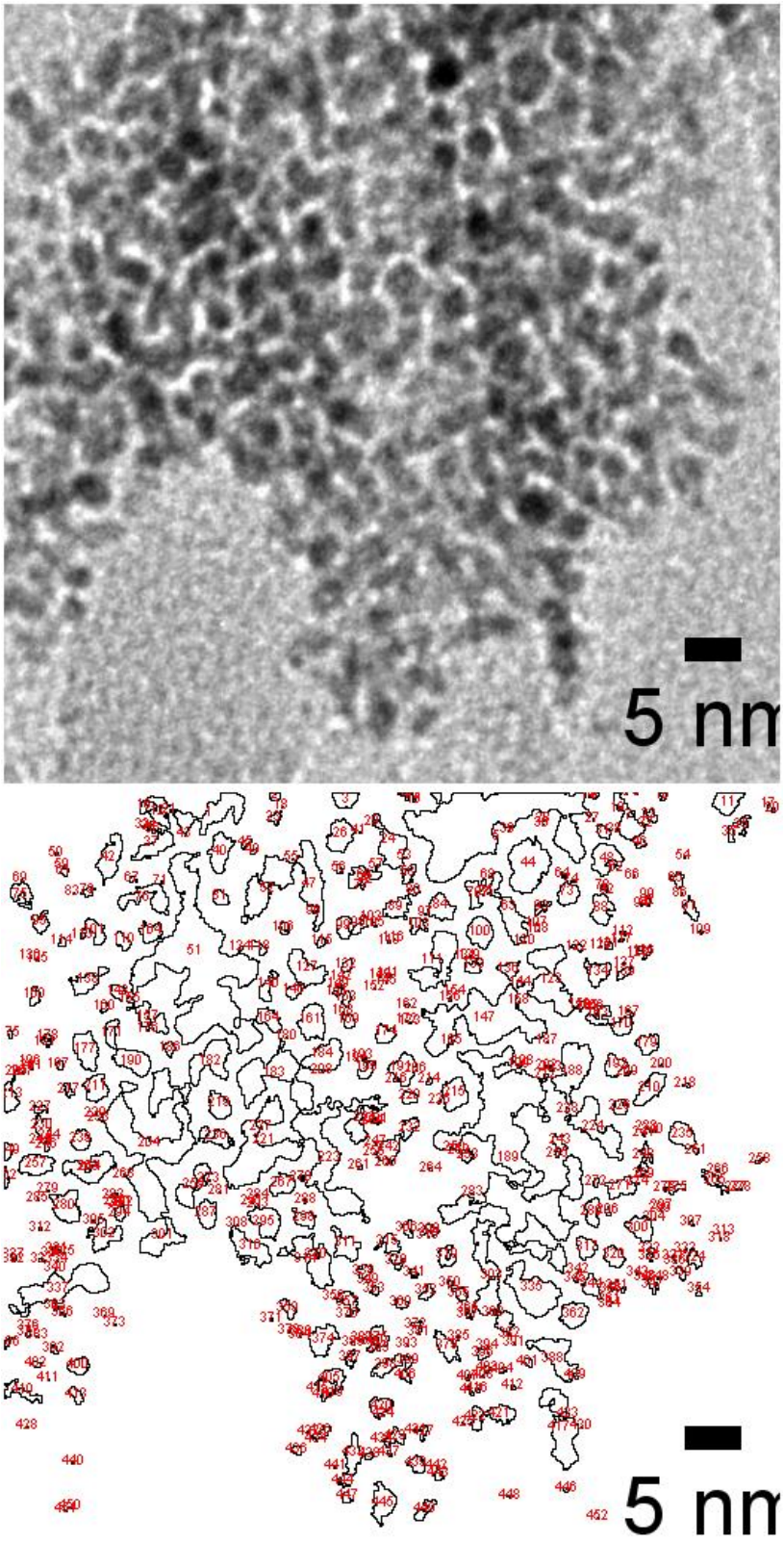

Figure 53: Particle size analysis of Pt on the surface of AlTBAPy post photocatalysis reaction.

452 Particles.	Area/nm^2	Feret/nm	MinFeret/nm
Mean	1.92	1.57	0.93
SD	6.40	2.29	1.28
Min	0.02	0.18	0.13
Max	78.20	21.30	12.73

Figure 54: Results of the particle size analysis of Pt on the surface of AlTBAPy post photocatalysis reaction.

It can be seen from the analysis of the particles that the mean Feret diameter is 15.7 Å, this is larger than the pore size diameter of 5.42 Å measured from the crystal structure (see **Figure 59**). Even the mean minimum Feret diameter is 0.93 nm which is still larger than the pore size; this means that it is impossible that these particles could be within the pores of the MOF. In order for photocatalysis to occur there needs to be an interaction between either the AlTBAPy MOF & the platinum or the AlTBAPy MOF and the methyl viologen, and the methyl viologen and the platinum. As the platinum is agglomerating on the surface of the MOF whilst the methyl viologen is getting trapped within the pores of the MOF there can be no interaction between the two and thus no reaction. Furthermore there can be only a very limited interaction between the MOF & the platinum if the platinum aggregates upon the surface, the majority of the MOF's large internal surface area remains out of contact with the platinum cocatalyst and thus the reaction cannot progress.

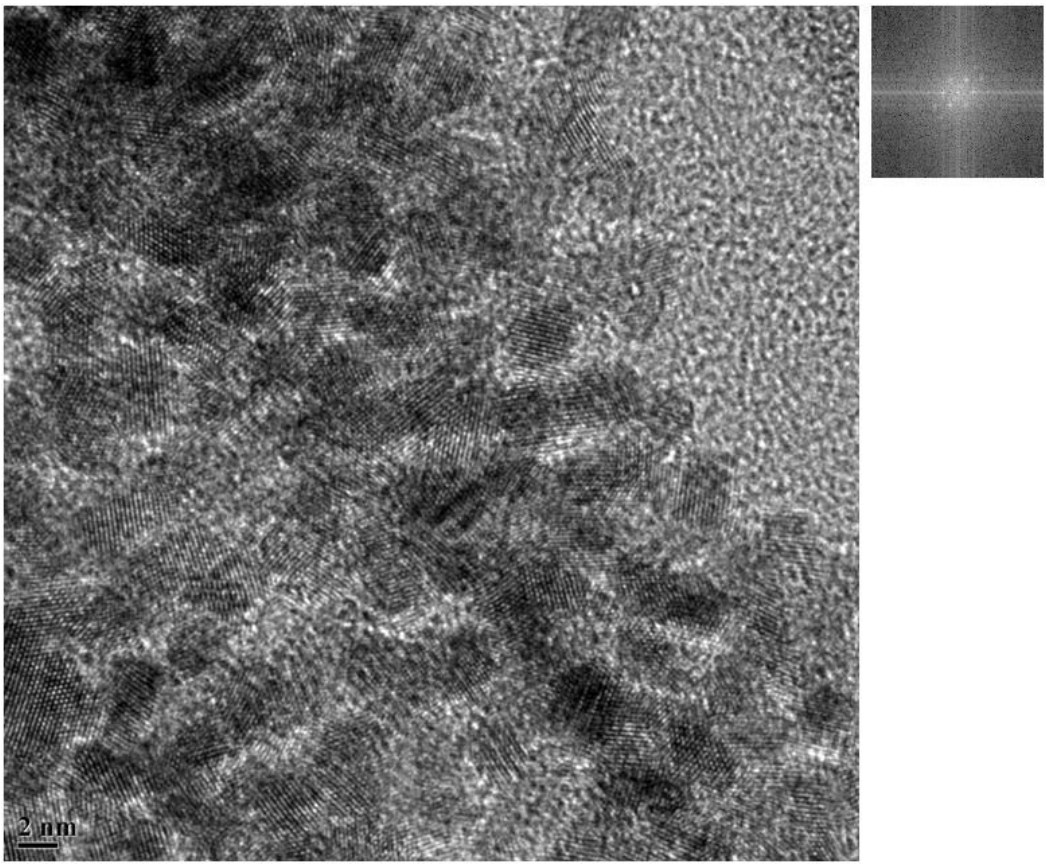

Figure 55: TEM & Electron diffraction of Pt particles on AlTBAPy MOF post reaction.

It can be seen from electron diffraction (see **Figure 55**) of the platinum particles on the AlTBAPy MOF postreaction that the catalytically active 111 plane surface is available for the hydrogen evolution reaction to take place.[33] This confirms it is not the nature of the platinum particles which is preventing the reaction further suggesting that it is rather due to their location.

3.6. Pt@AlTBAPy MOF

In order to try to overcome this lack of interaction between the methyl viologen trapped within the pores of the AlTBAPy MOF and the platinum cocatalyst

stuck on the surface of the MOF it was attempted to deposit the platinum within the pores of the AlTBAPy MOF.

3.6.1. Characterisation.

3.6.1.1. PXRD

The PXRD of Pt@AlTBAPy was measured using a Bruker D8 Advance with Cu Kα radiation, in transmission geometry in a sealed 0.7 mm borosilicate spun capillary and the pattern indexed to the unit cell of the parent AlTBAPy (see **Figure 56**).

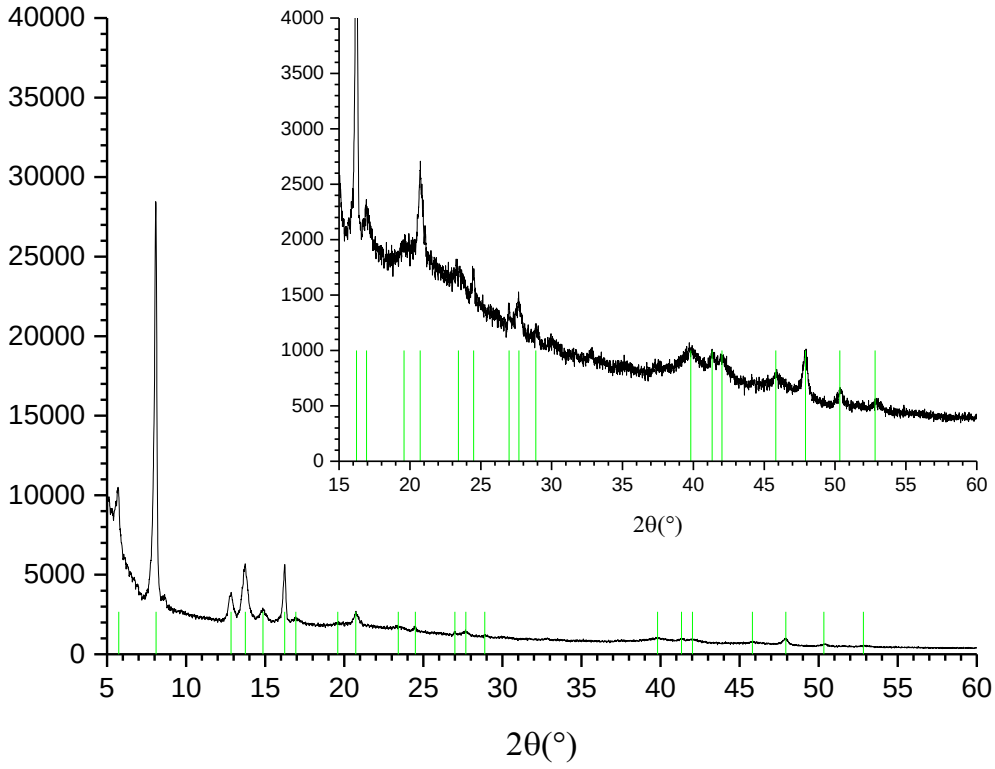

Figure 56: PXRD of Pt@AlTBAPy. Insert of the high angle low intesnsity reigion of the PXRD pattern. Green lines indicate indexed peaks.

All of the peaks indexed to the unit cell parameters of the AlTBAPy and the unit cell parameters are similar to that of the parent AlTBAPy material (see **Figure 57**).

Sample	Pt@AlTBAPy	AlTBAPy
a [Å]	7.10(1)	7.14(4)
b [Å]	30.76(5)	30.67(8)
c [Å]	15.96(3)	16.0(1)
Alpha [°]	90	90
Beta [°]	90	90
Gamma [°]	90	90
Volume [$Å^3$]	3483.76	3497.53

Figure 57: Unit cell refinement results for Pt@AlTBAPy compared to those of the parent AlTBAPy.

It can also be seen that the PXRD pattern of Pt@AlTBAPy when compared the pattern of the Pt@AlTBAPy and AlTBAPy are similar (see **Figure 58**), no new peaks have appeared in the pattern for Pt@AlTBAPy and no peaks have moved position.

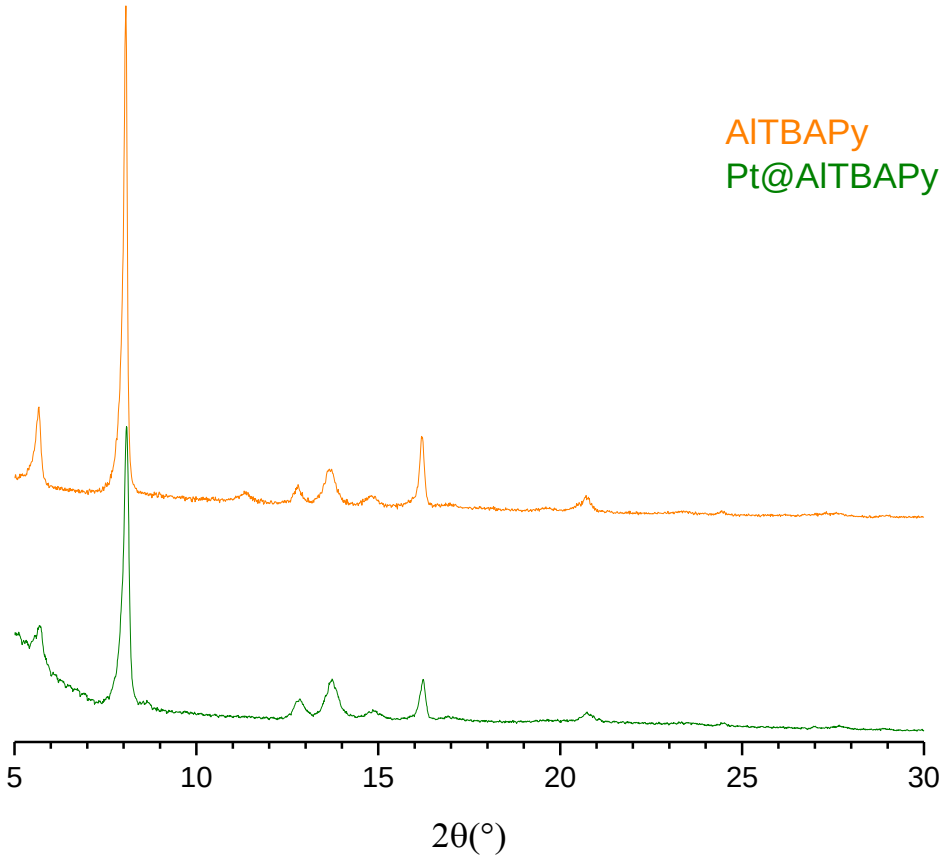

Figure 58: PXRD Comparison of Pt@AlTBAPy (Green) & the parent AlTBAPy (Orange). Insert of the high angle low intensity reigion of the PXRD pattern.

3.6.1.2. TEM

Using the crystal structure of the InTBAPy MOF reported by Stylianou et al, which is isostructural to the AlTBAPy MOF and has a very similar porosity as measured by nitrogen adsorption isotherm, the pore diameter was measured (see **Figure 59**) to be 5.42 Å therefore any platinum particles larger than that cannot be within the pores of the MOF.[15]

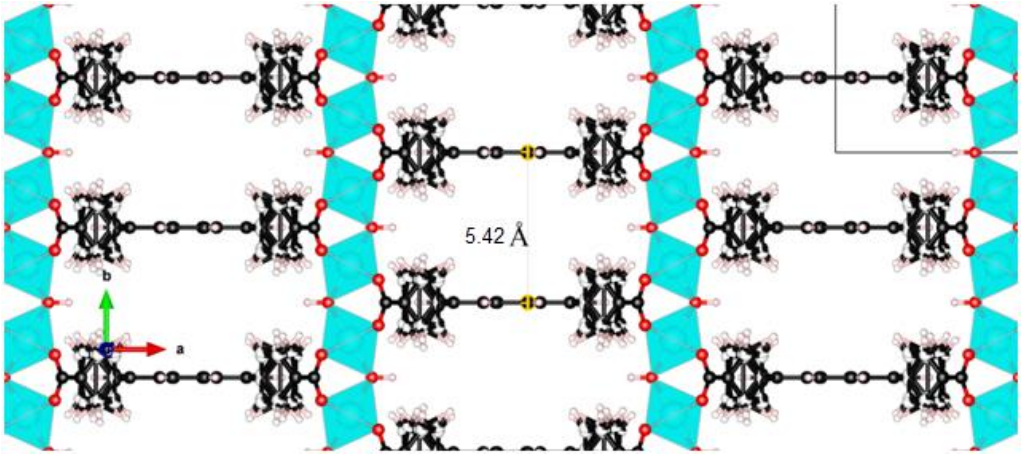

Figure 59: Crystal structure of isostructural InTBAPy[15] showing the pore size.

For TEM the samples were deposited using MeOH on a carbon coated copper TEM grid and imaged using a JEOL 2100 TEM at 200 kV. From these images the size and location of the platinum within the AlTBAPy MOF crystals can be seen (see **Figure 60**).

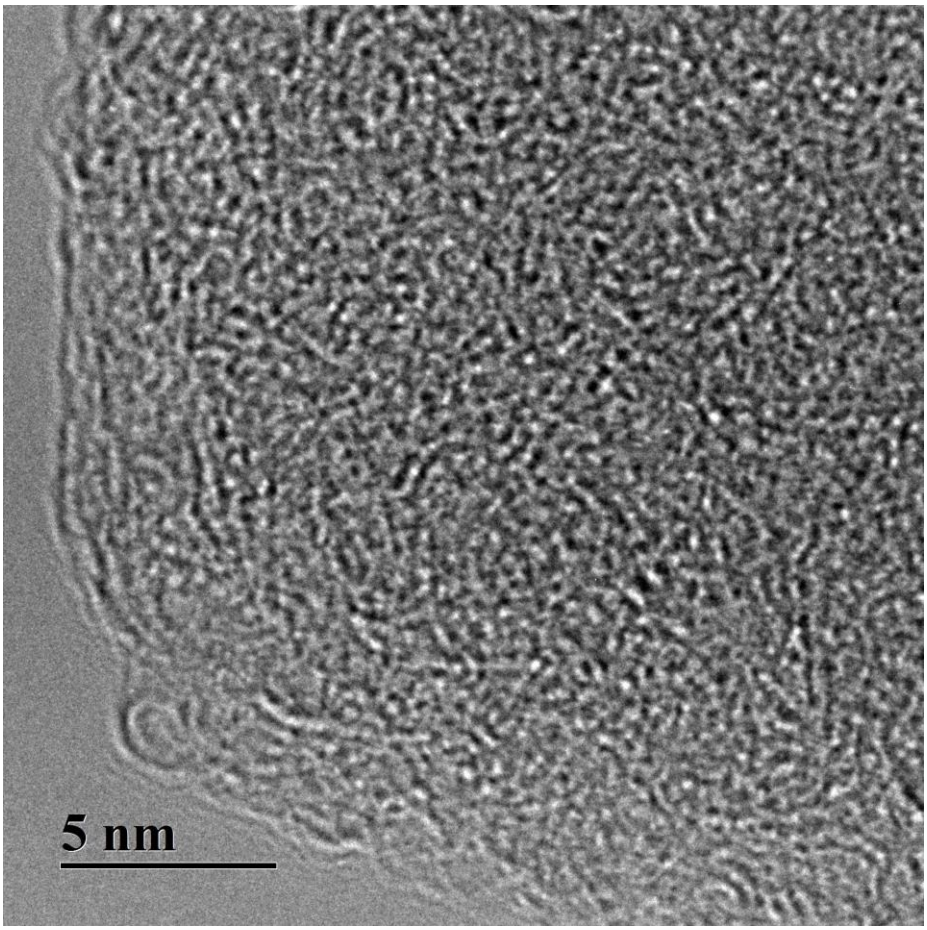

Figure 60: TEM Images of Pt@AlTBAPy.

The difference between these samples and the post reaction AlTBAPy MOF samples is clear to see. The previous samples had clusters of large Pt particles agglomerated upon the surface of the MOF (see **Figure 52**), however from the TEM images of the Pt@AlTBAPy MOF (see **Figure 60**) it can be seen that the darker Pt nanoparticles are now much smaller and more thoroughly dispersed throughout the MOF. The darker platinum particles can be analysed and their area & Feret diameter calculated as before.

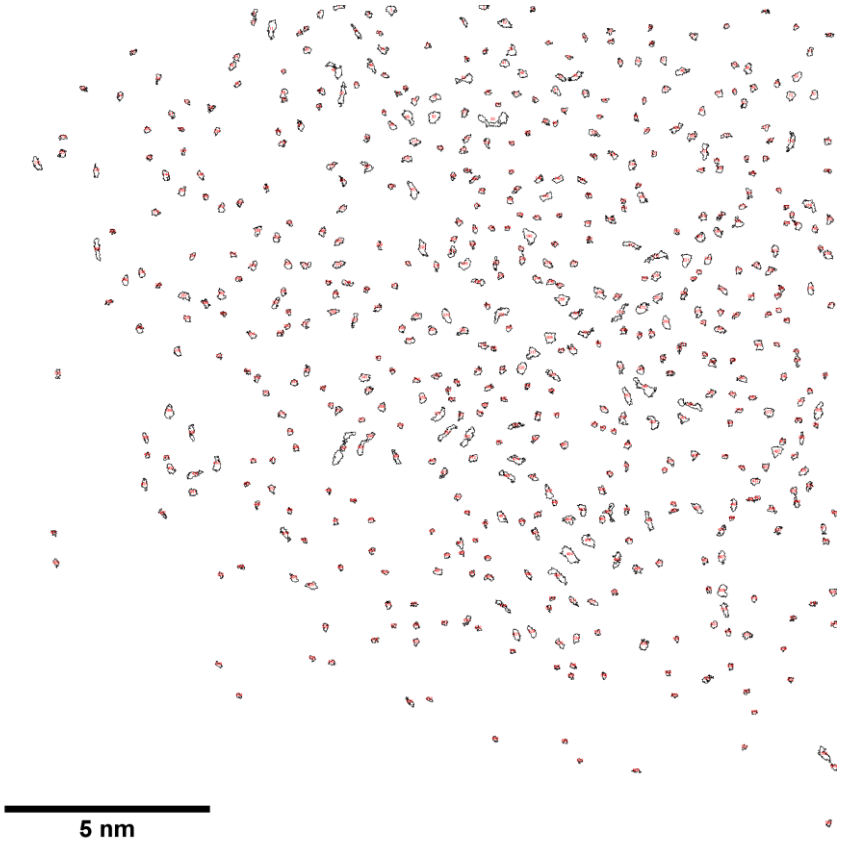

Figure 61: Image of Pt particles analysed within Pt@AlTBAPy .

The 566 particles detected in this image can be analysed (see **Figure 62**) and it can be seen that the mean Feret diameter is 2.54 Å, this is less than the 5.42 Å pore size measured from the crystal structure of the AlTBAPy MOF, showing that it is possible that the Pt particles are inside the MOF. It can also be seen that the range of particle sizes from the largest of 9.7 Å (a particle which is still on the surface of the MOF or perhaps where two particles have overlapped in the image) to just 1.3 Å giving a range of just 8.4 Å compared to the range of 211.2 Å for the particles on the surface of the MOF when added in the reaction supernatant. This suggests that the platinum nanoparticles are being synthesised within the MOF, with the pores restricting their size producing a more uniform particle size as oppose to simple agglomeration of particles upon the surface of the MOF. Furthermore the standard

deviation in Feret diameter is only 0.97 Å, showing that the majority of particles are close to the mean diameter again supporting the hypothesis that the particles are formed and reside within the pores of the MOF.

566	Area/nm2	Feret/nm	MinFeret/nm
Mean	0.019	0.254	0.152
SD	0.013	0.097	0.042
Min	0.007	0.132	0.083
Max	0.095	0.972	0.353

Figure 62: Particle analysis of Pt@AlTBAPy

3.6.1.3. Elemental Analysis

Elemental analysis was also performed on the Pt@AlTBAPy sample, both CHN and ICP-OES. CHN analysis was performed on the dry sample but the MOF must be digested for ICP-OES analysis. The MOF was digested in aqua regia and the aluminium and platinum composition analysed by ICP-OES (see **Figure 63**). The mass compositions of the Pt@AlTBAPy were 60.16 % carbon, 2.93 % hydrogen, 7.31 % aluminium and 4.44 % platinum. This suggests a composition of $Al_2(OH)_2$TBAPy•0.2Pt•3.2H_2O which has a theoretical composition of 61.22 % carbon, 3.55 % hydrogen, 6.25 % aluminium and 4.52 % platinum, it also suggests that there is no residual citrate left within the pores and it has all been washed out as all the carbon content can be accounted for.

$Al_2(OH)_2TBAPy•0.2Pt•3.2H_2O$		
Element	Measured	Theoretical
C	60.61%	61.22%
H	2.93%	3.55%
Al	7.31%	6.25%
Pt	4.44%	4.25%

Figure 63: Elemental Analysis results for Pt@AlTBAPy.

3.6.1.4. Nitrogen adsorption isotherm.

As the platinum has formed within the pores of the MOF a reduction in the surface area and pore volume as measured by nitrogen adsorption isotherm should be seen. The nitrogen adsorption isotherm was measured at 77K using a Micromeritics Tristar II. It could be seen that as predicted there was a reduction in porosity when between the AlTBAPy and the Pt@AlTBAPy (see **Figure 64**).

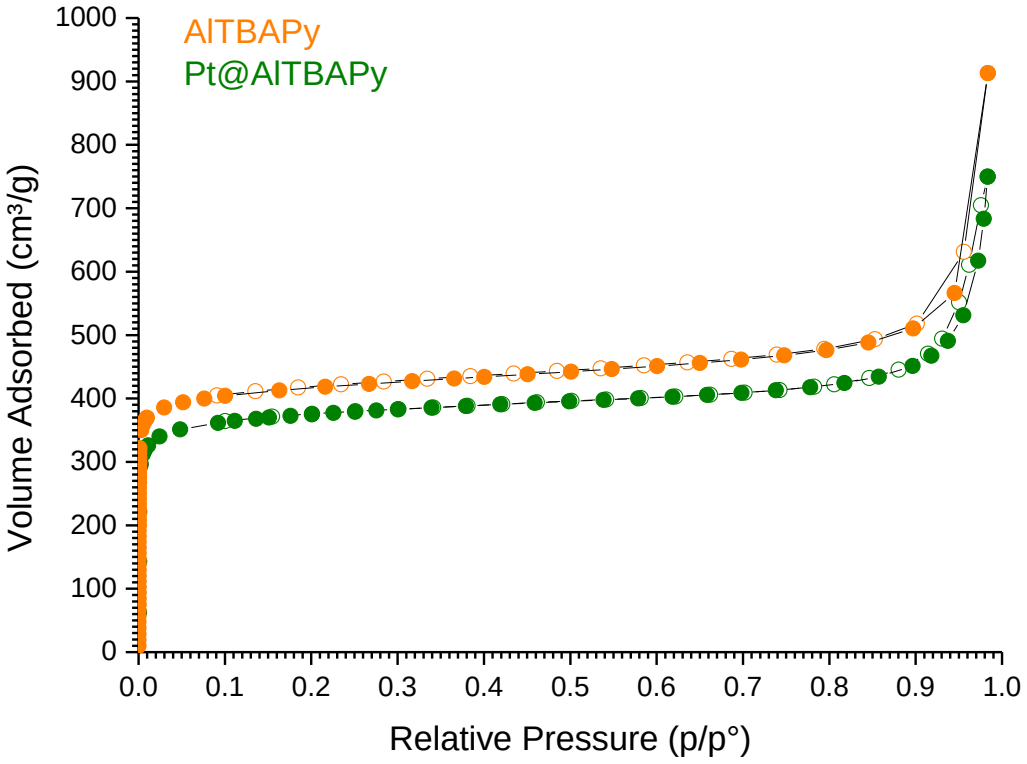

Figure 64: Nitrogen adsorption isotherms of Pt@AlTBAPy (green) and AlTBAPy (orange) at 77K

By comparing the two isotherms measured on both the platinum inserted AlTBAPy MOF and the parent AlTBAPy MOF (see **Figure 64**) it is clear that there is a decrease in the porosity of the AlTBAPy MOF as expected once the platinum is inserted. What's more the BET surface area of the Pt@AlTBAPy can be calculated to be 1464 m^2g^{-1}, a reduction from the 1594 m^2g^{-1} BET surface area of the parent AlTBAPy. Also the pore volume can be seen to be 0.593 cm^3g^{-1} which is significantly lower than the 0.646 cm^3g^{-1} pore volume of the parent AlTBAPy. This decrease in pore volume shows that some of the pore volume is now occupied by the platinum nanoparticles. This clear reduction in the porosity of the material is further evidence that the insertion of Platinum into the pores of the MOF has been successful.

3.6.1.5. Optical Spectroscopy.

After the insertion of the platinum into the pores of the AlTBAPy MOF there was a noticeable colour change from the bright orange/yellow of the AlTBAPy to a much darker green colour of the Pt@AlTBAPy. A diffuse reflectance UV/Vis spectrum was measured of the Pt@AlTBAPy MOF using a Perkin Elmer Lambda 650 S UV/Vis Spectrometer (see **Figure 65**).

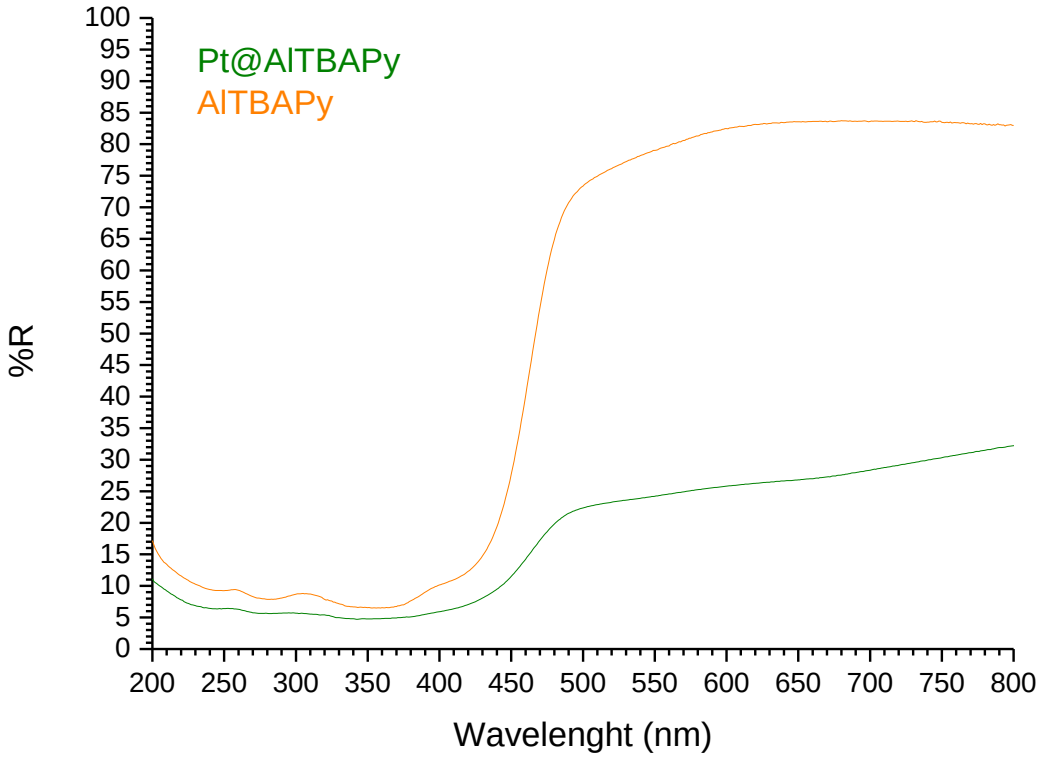

Figure 65: Diffuse reflection UV/Vis spectra of Pt@AlTBAPy (Green) and AlTBAPy (Orange) MOFs.

The UV/Vis spectra when compared to that of the parent AlTBAPy can be seen to be significantly more absorbing of light across the spectrum; this is likely due to the black platinum nanoparticles which will absorb light across the spectrum reducing the reflection. Also it can be seen that the $\pi \rightarrow \pi^*$ adsorption of the AlTBAPy MOF has not been shifted, this suggests that there is no electronic

interaction between the AlTBAPy and the platinum within the pores. Ideally charge transfer from the AlTBAPy MOF to the platinum nanoparticles would take place and thus the photocatalytic hydrogen evolution reaction could proceed without use of an electron transfer reagent as once the electron is on the platinum the water splitting and hydrogen evolution reaction is well established but the UV/Vis spectra suggest that this is not occouring.[12]

3.6.2. Photocatalytic hydrogen evolution.

The photocatalytic reactions performed previously with the AlTBAPy, both with and without methyl viologen as an electron transfer reagent, were repeated as described above using the Pt@AlTBAPy MOF as the photocatalyst and with the same volume of water replacing the colloidal platinum nanoparticle suspension. Again no hydrogen was produced from either of these reactions.

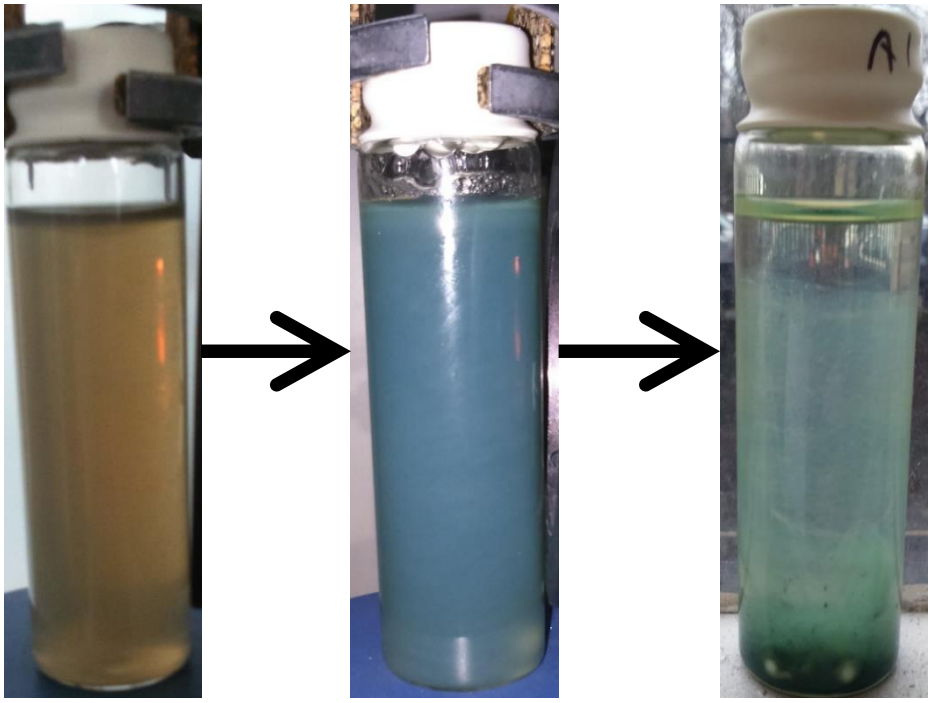

Figure 66: P: Photographs of Pt@ALTBAPy MOF before & after photocatalysis using Methyl Viologen as an electron transport reagent. Also photograph of the sample after the Pt@AlTBAPy MOF had been allowed to settle.

After the reaction it could be seen that despite the lack of hydrogen produced a reaction had taken place as the Pt@AlTBAPy MOF had changed from yellow to blue as a result of the reduced methyl viologen, indicating that the addition of the platinum within the pores of the AlTBAPy MOF had not impeded the photochemical reaction despite the lack of hydrogen produced.[32] After the reaction mixture is allowed to settle again the supernatant reveals itself to be colourless while the sold Pt@AlTBAPy MOF had changed to become the blue colour of the reduced methyl viologen.

The fact that there is still no reaction even when the both the platinum and the reduced methyl viologen within the pores of the MOF suggests the AlTBAPy must be stabilising the reduced methyl viologen. It is already clear that there is a strong interaction between the AlTBAPy MOF as the reduced methyl viologen remains within the pores of the MOF and does not diffuse out. That strong interaction may stabilise the reduced methyl viologen radical to prevent electron transfer to the platinum nanoparticles.[34] It may be also that if the platinum is deposited directly on the internal pore surface of the AlTBAPy MOF while the methyl viologen is closely attracted to the internal surface of the AlTBAPy MOF and neither is able to move within the pores it may be that they are still in different locations within the AlTBAPy MOF and so still unable to interact.

3.7. Heat of adsorption of gasses.

Many MOFs have an affinity to various gases which make them excellent for use in gas storage or separation.[35] By measuring a gas adsorption isotherm using a Micromeritics 3Flex Surface Characterisation Analyser at three different

temperatures it is possible to calculate the heat of adsorption of that gas which is a measure of the affinity that the material has to that gas and an indication of how effective it could be at separation and storage. The heat of adsorption is calculated by fitting virial type thermal expansion equation to the data to determine the virial parameters, from these the heat of adsorption with respect to amount adsorbed can be calculated.[36]

3.7.1. Carbon dioxide

The release of greenhouse gasses, in particularly carbon dioxide, into the atmosphere is a growing problem; a potential solution to this problem would be through carbon capture and storage technology.[37] The current technology uses amine scrubbers which although have a high uptake are difficult to reactivate.[38, 39] Ideally a solid state material would be used to absorb the carbon dioxide from the flue gas. Such a material would need a large pore volume and surface area to withhold the carbon dioxide and a sufficiently large heat of adsorption to remove the carbon dioxide from the flue gas but low enough to allow the material to be regenerated.[38] MOFs have been explored as possible candidates for this purpose and several rather successful candidates have emerged.[38] MOFs appear promising for this application due to their large porosity and surface area coupled with their ease of functionalization to enhance their affinity to different gasses.[35, 38] Carbon dioxide adsorption isotherms for AlTBAPy were measured at three different temperatures; from these results the heat of adsorption could be calculated.

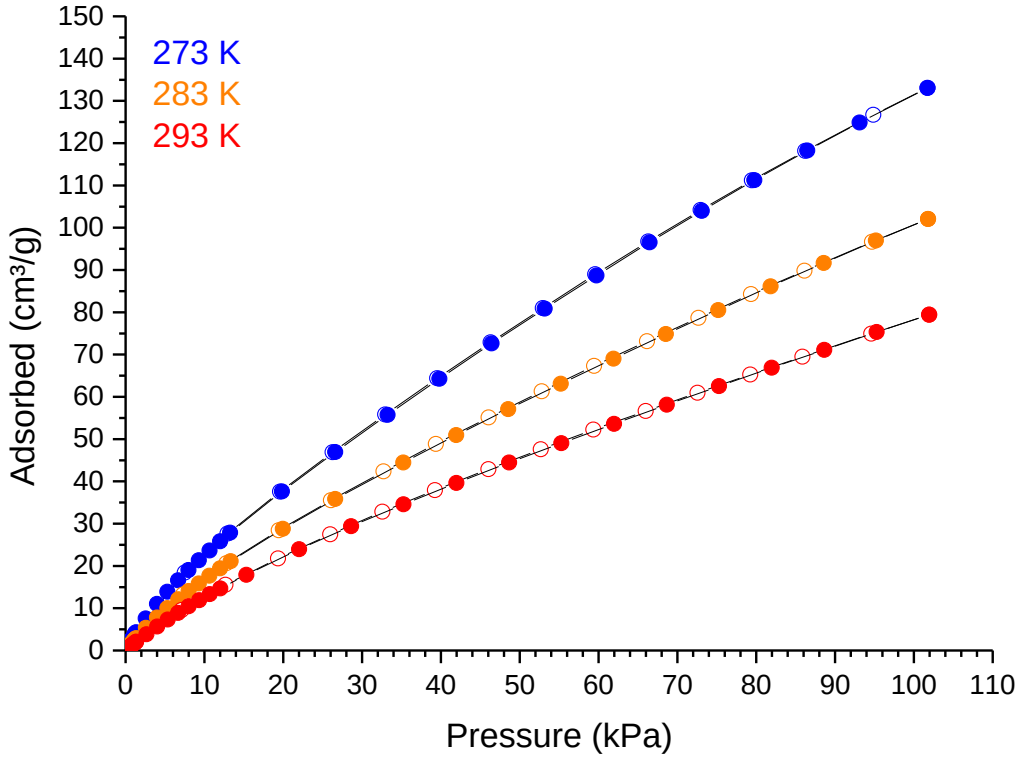

Figure 67: Isotherms for adsorption of Carbon dioxide for AlTBAPy at 273 K (Blue), 283 K (Orange) & 293 k (Red).

The CO_2 adsorption isotherm for AlTBAPy was measured at 273 K, 283 K and 293 K (see **Figure 67**). From this the uptake at 15 kPa at a temperature 293 K can be seen to be 15.3 cm^3g^{-1} or 0.682 mmol g^{-1}. This can be compared to the uptake of other MOFs under similar conditions; these conditions are chosen as it is under these conditions that the absorbent material will be required to operate.[38] Many MOFs have capacities ranging from around 1 to 3 mmol g^{-1} at 0.15 bar and 298 K; however some MOFs under these conditions show capacities of nearly 6 mmol g^{-1}. Many of these MOFs which exhibit exceptionally high adsorption capacities have either free basic groups or open metal sites. The PEI-MIL-101-100 MOF contains polyethyleneimine chains bound to the chromium cluster SBUs, the basicity of which provides an adsorption capacity for CO_2 of 4.02 mmol g^{-1}.[40] While the Mg_2dobdc

MOF exhibits a large adsorption capacity for CO_2 of 4.85 mmol g^{-1} due to its open magnesium metal sites.[41] The SYSU MOF like AlTBAPy is an unfunctionalized but highly aromatic MOF, it has a similar surface area, 1100 m^2 g^{-1}, and pore size, 6.3 Å, to the AlTBAPy MOF which has a BET surface area measured to be 1644 m^2g^{-1} with a pore volume of 7.12 Å. It is therefore unsurprising that SYSU demonstrates a similar capacity for CO_2 with an uptake of 0.81 mmol g^{-1} slightly larger than the 0.682 mmol g^{-1} measured for AlTBAPy.[38] This shows that the AlTBAPy has a capacity for CO_2 adsorption in line with what is expected, however there have been materials reported with much higher capacities and therefore the practical usefulness of AlTBAPy for carbon capture and storage will be limited.

It is possible to calculate the heat of adsorption of CO_2 onto the AlTBAPy MOF with relation to the amount of CO_2 adsorbed; this represents the average binding energy of a molecule of CO_2 at the coverage present at that adsorption level. This is possible by applying virial type equations to the logs of the amount of CO_2 adsorbed and the pressure at which it is adsorbed at three different temperatures to determine the virial coefficients, from which a plot of the heat of adsorption against the amount of CO_2 adsorbed can be plotted (see **Figure 68**).[36]

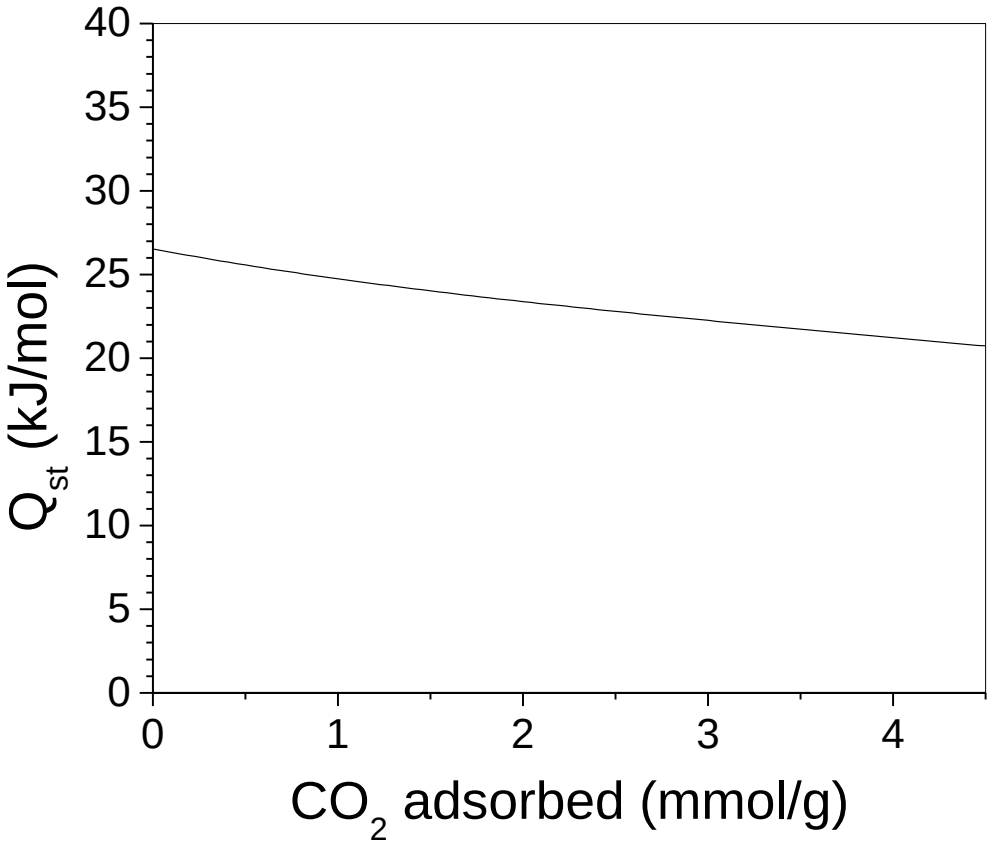

Figure 68: Heat of adsorption of CO in AlTBAPy.

From this plot it can be seen that the initial heat of adsorption of carbon dioxide in AlTBAPy is 26.5 kJ mol^{-1}. This can be compared to other MOFs and porous adsorbents to determine how effective the AlTBAPy MOF is at adsorbing carbon dioxide. Many MOFs exhibit up to and over twice the heat of adsorption of carbon dioxide and even up to 71 kJ mol^{-1} for some rare examples such as mmen-Mg_2dopdc which is functionalised with a large number of basic amine sites.[38, 41] However many of these MOFs which express large heats of adsorption and high adsorption capacities have been post synthetically modified with basic sites or contain free metal sites to enhance the binding of the carbon dioxide.[38] Many MOFs do exhibit heats of adsorption similar to the AlTBAPy ranging from 20 kJ mol^{-1} to 30 kJ mol^{-1}.[38] For instanced MAF-66 reports a heat of adsorption of 26.0 kJ mol^{-1}, very

similar to that of AlTBAPy, this is despite MAF-66 containing basic sites.[42] The heat of adsorption for AlTBAPy is greater than that of CuBTTri which has a reported initial heat of adsorption of 22 kJ mol^{-1} despite CuBTTri having been postsynthetically modified with the addition of amine bases into the pores.[43] However the heat of adsorption for AlTBAPy is less than the heat of adsorption seen for other MOFs composed of the same aluminium hydroxide chains, MIL-53 has been reported to demonstrate an initial heat of adsorption of 50 kJ mol^{-1}.[44] The heat of adsorption for AlTBAPy is comparatively low compared to some specially adapted MOFs, however it is within the range reported by some MOFs and so may still be of use.

These measurements indicate that while AlTBAPy is porous and does have an affinity for the uptake of carbon dioxide its performance is less than that of other previously reported MOFs. It may be possible to add basic groups to the TBAPy linker molecule to enhance the affinity for carbon dioxide and thus increase the uptake and performance of the MOF.

3.7.2. Methane.

A great deal of interest and work is being done into looking for alternative sources of energy; natural gas provides a possible alternative to petrol to be used in vehicles. Natural gas is comprised mostly of methane and therefore with its higher carbon to hydrogen ratio burns much cleaner with lower carbon dioxide and carbon monoxide emissions. Natural gas also contains less nitrogen and sulphur containing impurities and so burns producing lower SO_x & NO_x pollutants.[45] Coupled with this natural gas is more abundant than petrol and newly developed hydraulic fracturing has potential to further increase the supply available; this will make natural gas cheaper than other fossil fuels and will allow its continued use for longer.[46, 47] One of

the primary difficulties with natural gas however is its energy density, far lower than that of other fuels meaning the storage and transport of natural gas in sufficient quantities to be useful proves difficult.[46] A potential solution to this problem would be the liquefaction of the gas, however this is a difficult process and involves several compressions to produce high enough pressures, the infrastructure required to compress methane sufficiently to liquefy the gas is too expensive to become widely available. Also once liquefied the gas must be kept cold to prevent boil off, the insulation required to keep the storage tanks cold make the size of the tanks required prohibitively large.[46, 48] Another potential solution to this would be the adsorption of the methane into a porous material. It has been found that the ideal pore size and shape are long slit like pores with a diameter of 5.42 Å, wide enough to form a monolayer of methane on each side of the pore.[46] It can be seen from the crystal structure of the InTBAPy which is isostructural to AlTBAPy that this MOF is a porous material with elongated slit like pores with a diameter of 5.42 Å (see **Figure 59**), this is very similar to what is reported for the optimum and therefore the AlTBAPy was tested for methane adsorption. An adsorption isotherm for methane in AlTBAPy was measured at 273 K, 283 K and 293 K from 0 kPa to 110 kPa (see **Figure 69**).

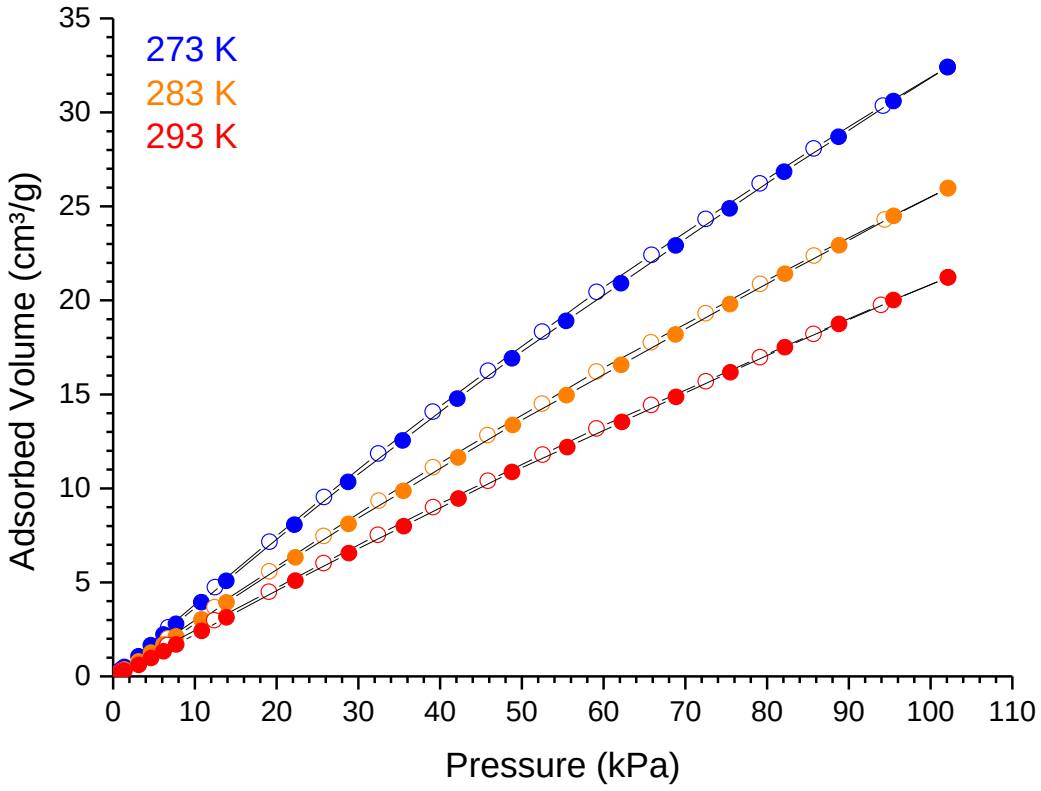

Figure 69: Methane adsorption isotherms for AlTBAPy at 273 K (Blue), 283 k (Orange) and 293 K (Red) Filled circles represent the adsorption isotherms and empty circles represent the desorption isotherms.

It is possible to calculate the heat of adsorption of CH_4 onto the AlTBAPy MOF with relation to the amount of CH_4 already adsorbed; this represents the average binding energy of a molecule of CH_4 at the amount of methane adsorbed. This is possible by fitting virial type equations to a plot of the log of the pressure applied against the amount adsorbed at three different temperatures. The viral coefficients can be calculated and from these a plot of the heat of adsorption against the amount of CH_4 adsorbed can be plotted (see **Figure 70**).

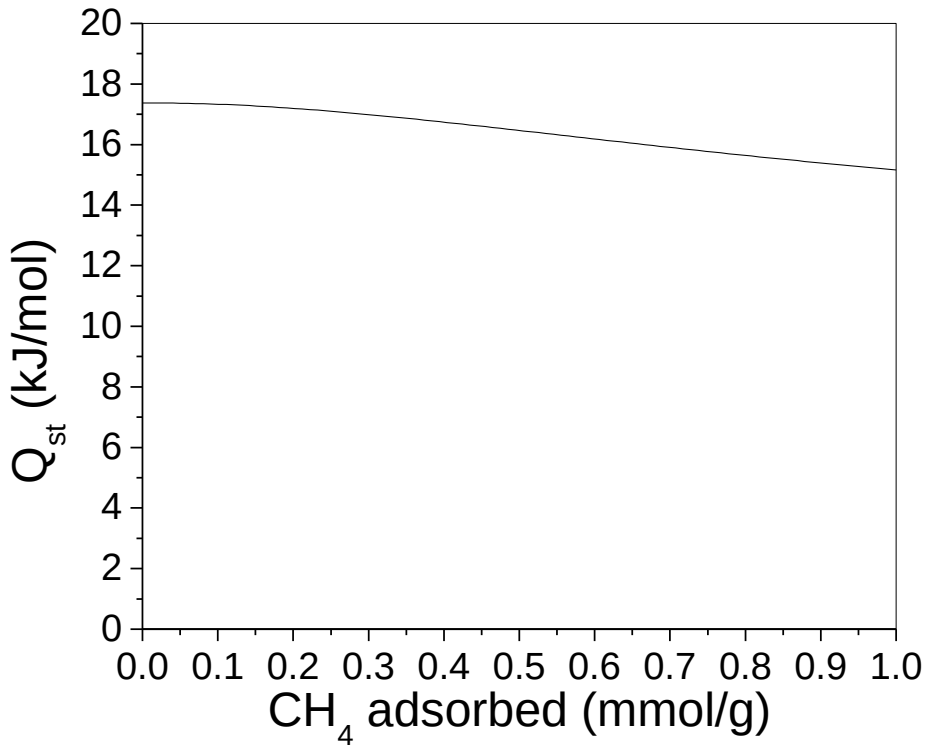

Figure 70: Heat of adsorption for CH_4 in AlTBAPy.

The initial heat of adsorption can be calculated to be 17.4 kJ mol^{-1} (see **Figure 70**). This is slightly less than, but similar to the 18.3 kJ mol^{-1} reported for (Al)MIL-53, a MOF similarly composed of infinite aluminium hydroxide chains.[49] Though the heat of adsorption for MOFs varies significantly in some cases reported as low as 12 kJ mol^{-1} for MOF-5 but up to 21 kJ mol^{-1} for Ni_2dobdc with its exposed hydroxide groups on the dobdc linker.[46] However in order for a material to be useful for storage of natural gas as fuel the heat of adsorption must be large enough that the material has suitable affinity for methane to adsorb it but low enough that the methane can desorb from the surface of the material when required without additional heating. Calculations show that the optimum heat of adsorption for a storage material for methane is 18.8 kJ mol^{-1}, this is very similar to the 17.4 kJ mol^{-1} calculated for the AlTBAPy MOF.[50] The heat of adsorption for the AlTBAPy is very

good for a natural gas adsorber and AlTBAPy may have potential applications for the storage of methane gas.

Conclusion.

A thermally stable and water stable MOF has been synthesised for the first time composed of aluminium and a pyrene based linker. This new MOF has been thoroughly characterised by PXRD to confirm the structure, CHN elemental analysis to confirm the composition, TGA to confirm the thermal stability and the aluminium content, SEM to observe the crystallite morphology and to ensure phase purity, N_2 isotherm adsorption analysis to measure the porosity of the MOF and optical spectroscopy in the form of UV/Vis and Fluorescence spectroscopy to evaluate the interactions between the different parts of the MOF. This MOF adopts a well known structure, common for MOFs composed of 3+ metal ions; which it retains even after exposure to water, retaining its crystallinity as is unusual for MOFs. This MOF, due to its pyrene based linker isolated from other pyrene moieties within the structure, strongly absorbs light in the visible region of the spectrum giving it a bright yellow colour and emits a strong visible light blue fluorescence with little or no quenching. This visible light absorption excites the MOF which can then perform photochemistry by reducing methyl viologen. However there is a strong affinity for the methyl viologen by the MOF and this is therefore unable to proceed with any other useful chemical reactions. Platinum nanoparticles have been photocatalytically deposited within the pores of the MOF and this has been confirmed by TEM, ICP-OES and nitrogen adsorption analysis. The MOF has also been analysed for carbon dioxide and methane adsorption. AlTBAPy does exhibit adsorption of CO_2 though its capacity and heat of adsorption is significantly lower than that reported for other

porous materials. However the heat of adsorption for methane is almost ideal for use as a storage material.

1. R. M. Yerga, M. C. Galvan, F. Valle, V. Mano and J. L. Fierro, *ChemSusChem*, 2009, **2**, 471-485.
2. K. Shirai, M. Matsuoka and K. Fukinishi, *Dyes and Pigments*, 1999, **42**, 95-101.
3. J. B. Birks, A. A. Kazzaz and T. A. King, *Proceedings of the Royal Society A: Mathematical, Physical and Engineering Sciences*, 1966, **291**, 556-569.
4. R. Katoh, K. Suzuki, A. Furube, M. Kotani and K. Tokumaru, *Journal of Physical Chemistry C*, 2009, **113**, 2961-2965.
5. M. Dierksen and S. Grimme, *The Journal of Chemical Physics*, 2004, **120**.
6. M. Ottonelli, M. Piccardo, D. Duce, S. Thea and G. Dellepiane, *Journal of Physical Chemistry A*, 2012, **116**, 611-630.
7. J. Jiang, A. Trewin, D. J. Adams and A. I. Cooper, *Chemical Science*, 2011, **2**, 1777-1781.
8. M. Zhu, Y. Lu, Yukou, J. Li, X. Wang and P. Yang, *International Journal of Hydrogen Energy*, 2011, **36**, 4298-4304.
9. J. A. Greathouse and M. D. Allendorf, *Journal of the American Chemical Society*, 2006, **128**, 10678-10679.
10. D. Ma, Y. Li and Z. Li, *Chemical Communications*, 2011, **47**, 7377-7379.
11. T. Loiseau, C. Serre, C. Huguenard, G. Fink, F. Taulelle, M. Henry, T. Bataille and G. Féré, *Chemistry - A European Journal*, 2004, **10**, 1373-1382.
12. A. Fateeva, P. Chater, C. P. Ireland, A. Tahir, Y. Khimyak, P. Wiper, J. Darwent and M. J. Rosseinsky, *Angewandte Chemie International Edition*, 2012, **51**, 7440-7444.
13. N. A. Khan, J. S. Lee, J. Jeon, C. Jun and S. H. Jhung, *Microporous and Mesoporous Materials*, 2012, **152**, 253-239.
14. T. Loiseau, C. Mellot-Draznieks, H. Muguerra, G. Férey, M. Haouas and F. Taulelle, *Comptes Rendus Chimie*, 2005, **8**, 765-772.
15. K. C. Stylianou, R. Heck, S. Y. Chong, J. Bacsa, J. T. Jones, Y. Z. Khimyak, D. Bradshaw and M. J. Rosseinsky, *Journal of the American Chemical Society*, 2010, **132**, 1-12.
16. R. I. Walton, Alexis, S. Munn, N. Guillou and F. Millange, *Chemistry - A European Journal*, 2011, **17**, 7069-7079.
17. H. E. Gottlieb, V. Kotlyar and A. Nudelman, *Journal of Organic Chemistry*, 1997, **62**, 7512-7515.
18. A. D. McNaught and A. Wilkinson, *IUPAC. Compendium of Chemical Terminology, 2nd ed. (the "Gold Book")*, 2007, **79**, 1824.
19. K. S. Sing, D. H. Everett, R. A. Haul, L. Moscou, R. A. Pierotti, J. Rouqiérol and T. Siemieniewska, *Pure and Applied Chemistry*, 1985, **57**, 1365-3075.
20. S. Brunauer, P. H. Emmett and E. Teller, *Journal of the American Chemical Society*, 1938, **60**, 309-319.
21. O. V. Dolomanov, L. J. Bourhis, R. J. Gildea, J. A. K. Howard and H. Ouschmann, *Journal of Applied Crystalography*, 2009, **42**, 339-341.

22. Y. Zhiu, X. Shen, Chen-Xia, B. Wu and H. Zhang, *European Journal Of Inorganic Chemistry*, 2008, 4280-4289.
23. J. Gascon, M. D. Hernández-Alonso, A. R. Almeida, G. P. van Klink, F. Kapteijn and G. Mul, *ChemSusChem*, 2008, **1**, 981-983.
24. J. Dai, X. Wu, Z. Fu, C. Cui, S. Hu, W. X. Du, L. Wu, H. Zhang and R. Sun, *Inorganic Chemistry*, 2002, **41**, 1391-1396.
25. A. D. McNaught, A. Wilkinson, M. Nic, J. Jirat, B. Kosata and A. Jenkins, *IUPAC. Compendium of Chemical Terminology, 2nd ed. (the "Gold Book").* Blackwell Scientific Publications, 2006.
26. C. Tai, W. Chuang and B. Wang, *Journal of Luminescence*, 2013, **142**, 8-16.
27. A. I. Krasna, *Photochemistry and Photobiology*, 1980, **31**, 75-82.
28. J. R. Darwent, P. Douglas, A. Harriman, G. Porter and M. Richoux, *Coordination Chemistry Reviews*, 1982, **44**, 83-126.
29. C. L. Bird and A. T. Kuhn, *Chemical Society Reviews*, 1981, **10**, 49-82.
30. J. R. Darwent, *Journal of the Chemical Society, Chemical Communications*, 1980, 805-807.
31. J. R. Darwent, *Chemical Communications*, 1982, 798-799.
32. T. Watanabe and K. Honda, *The Journal of Physical Chemistry*, 1982, **86**, 2617-2619.
33. I. A. Pasti, N. M. Gavrilov and S. V. Mentus, *Advances in Physical Chemistry*, 2011, **Article ID 305634**, 8 Pages.
34. A. K. Chandra, *Chemical Physics Letters*, 1970, **5**, 229-231.
35. J. Li, R. J. Kuppler and H. Zhou, *Chemical Society Reviews*, 2009, **38**, 1477-1504.
36. C. Leszek and J. JagiełŁo, *Chemical Engineering Science*, 1989, **44**, 797-801.
37. S. Solomon, G. Plattner, R. Knutti and P. Friedlingstein, *Proceedings of the National Academy of Sciences of the United States of America*, 2008, **106**, 1704-1709.
38. Z. Zhang, Z. Yao, S. Xiang and B. Chen, *Energy & Enviromental Science*, 2014, **7**, 2868-2899.
39. R. S. Haszeldine, *Science*, **325**, 1647-1652.
40. Y. Lin, Q. Yan, C. Kong and L. Chen, *Scientific Reports*, 2013, **3**, 1859.
41. T. M. McDonald, W. R. Lee, J. A. Mason, B. M. Wiers, C. S. Hong and J. Long, *Journal of the American Chemical Society*, 2012, **134**, 7056-7065.
42. R. Lin, D. Chen, Y. Lin, J. Zhang and X. Chen, *Inorganic Chemistry*, 2012, **51**, 9950-9955.
43. A. Demessence, D. M. D'Alessandro, M. L. Foo and J. R. Long, *Journal of the American Chemical Society*, 2009, **131**, 8784-8786.
44. J. Kim, W. Y. Kim and W. Ahn, *Fuel*, 2012, **102**, 574-579.
45. D. Lozano-Castello, J. Alacaniz-Monge, M. A. Casa-Lillo, D. Cazorla-Amoros and A. Linares-Solano, *Fuel*, 2002, **81**, 1777-1803.
46. J. A. Mason, M. Veenstra and J. R. Long, *Chemical Science*, 2014, **5**, 32-51.
47. A. Celzard and V. Fierro, *Energy and Fuels*, 2005, **19**, 573-583.
48. V. C. Menon, S. Komarneni and V. C. Menon, *Journal of Porous Materials*, 1998, **5**, 43-58.
49. P. Rallapalli, K. P. Pransanth, D. Patil, R. S. Somani, R. V. Jasra and H. C. Bajaj, *Journal of Porous Materials*, 2010, **18**, 205-210.

50. S. K. Bhatia and A. L. Myers, *Langmuir*, 2006, **22**, 1688-1700.

4. ZrTBAPy

4.1. Overview.

There are a great many MOFs which utilise the propensity of zirconium to form zirconium oxide and hydroxide clusters; theses clusters provide more binding sites for the linkers, this coupled with the highly oxophilic nature of zirconium this means that it is able to form highly stable carboxylate linker MOFs.[1] Most of these MOFs utilise a $Zr_6O_4(OH)_4$ cluster SBU where 6 zirconium ions form an octahedra bridged across the faces by alternating hydroxide and oxide ions, the carboxylate of the linker then bridges two zirconium ions across the edges of the octahedron (see Figure 72).[2] The most famous of these zirconium cluster MOFs are the UiO series of MOFs, UiO-66, UiO-67 and UiO-68 comprised of this SBU connected by 12 benzene dicarboxylate, biphenyl dicarboxylate and triphenyl dicrboxylate respectively. These MOFs as expected exhibit exceptionally high levels of chemical and thermal stability, despite this some do undergo decomposition when exposed to water.[1, 3] However containing the smaller terephthalate linker, UiO-66 is water stable and has shown potential applications for water splitting photocatalysis. The $Zr_6O_4(OH)_4$ SBU clusters of some

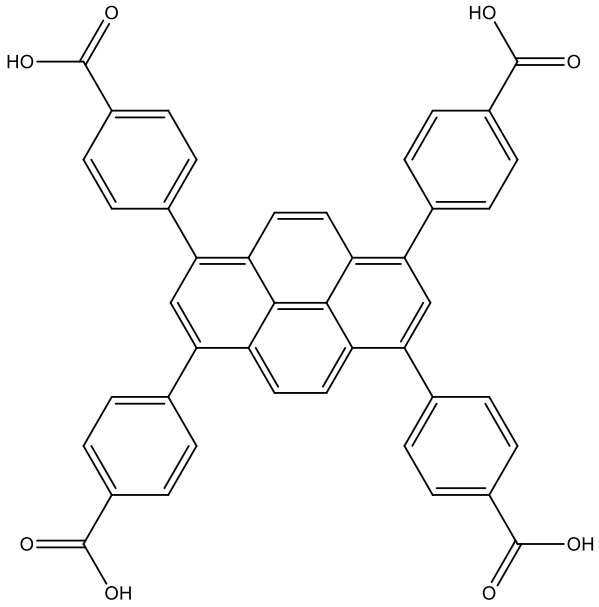

Figure 71:TBAPyH$_4$ Linker.

MOFs have been shown to act like semiconductors where the full oxygen p orbitals merge together to form a valence band and the empty zirconium d orbitals merge to form a conduction band.[4] Semiconductors are highly useful materials, their band gap between valence and conduction bands allows an electron to be excited through the absorption of a photon of light, this excited electron in the conduction band and the vacant hole in the valence band can then proceed to perform chemistry including the splitting of water into hydrogen gas, providing an environmentally friendly fuel produced simply though irradiation by light.[5] However many semiconductors, $Zr_6O_4(OH)_4$ MOFs included, require UV light to be excited, ideally a photocatalyst would be produced which could perform hydrogen evolution water splitting reactions under visible light, as solar UV light is filtered out by the Earth's atmosphere.[4] A way around this is to use a sensitiser; a coloured compound bound to the semiconductor, the sensitiser would be excited under visible light and pass its excited electron onto the semiconductor. It is possible for charge transfer from the linker onto the metal to occur under visible light, this would mean the linker of the MOF acting as a sensitiser for the semiconductor SBU.[4, 6] A brightly coloured linker like 1,3,6,8-tetrakis(p-benzoic acid)pyrene ($TBAPyH_4$) (see Figure 71) could act as an effective sensitizer, pyrene is known for its long excited state lifetime which will provide a greater amount of time for charge transfer from the linker to the SBU to take place before the excited state decays.[7] A Zirconium based MOF using TBAPy pyrene based linkers will be brightly coloured, excited under visible light the linker may then transfer its excited electron to the zirconium oxide hydroxide cluster through ligand to metal charge transfer, it may be possible to utilise this MOF for photocatalytically active for water splitting under visible light.[8]

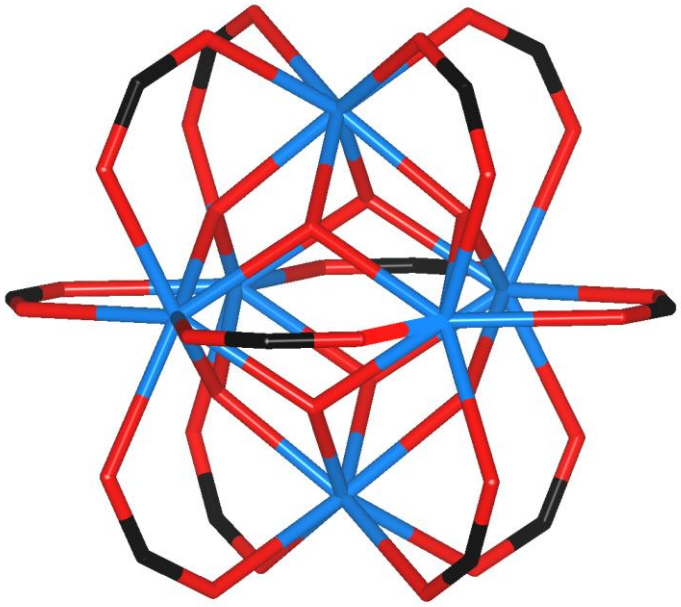

Figure 72: $Zr_6O_4(OH)_4(RCO_2)_{12}$ cluster SBU for UiO type MOFs. Zr is coloured blue, C black and O red. As reported by Valenzano et al.[2]

A ZrTBAPy MOF, NU-1000, was reported recently by Mondloch et al, in this MOF the SBU cluster adopts a slightly different connectivity, the ligands which would normally bridge the equatorial edges of the $Zr_6O_4(OH)_4$ octahedra are instead replaced by hydroxide groups; this allows the TBAPy linkers to form large hexagonal channels through the MOF with the hydroxide groups on the cluster pointing towards the centre of these channels (see Figure 73) resulting in a MOF with a much larger porosity than other zirconium MOFs.[9]

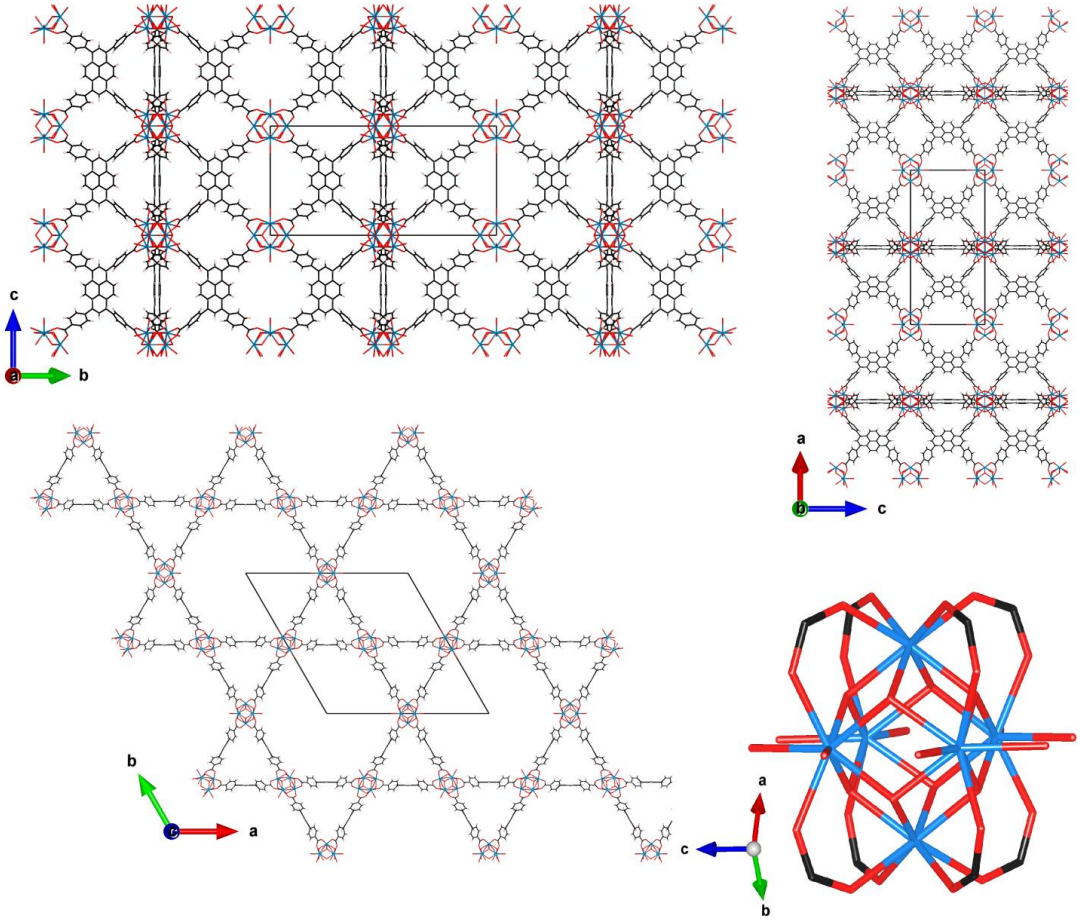

Figure 73: Structure of NU-1000 as reported by Mondlock et al.[9] Zirconium is coloured blue, oxygen red and carbon black.

The NU-1000 MOF was synthesised and characterised by powder X-ray diffraction (PXRD), elemental analysis, thermal gravimetric analysis (TGA), the surface area was calculated and the porosity measured using nitrogen adsorption isotherms, the crystallites were imaged by scanning electron microscopy (SEM) and the optical properties were examined using UV/Vis and fluorescence spectroscopy. Once this material had been characterised it was tested for photocatalytic hydrogen evolution with and without methyl Viologen as an electron transfer reagent. No hydrogen was produced though the electron transfer reagent was reduced but

remained trapped within the pores of the MOF. The MOF was analysed by transmission electron microscopy (TEM) and found that the platinum cocatalyst was not entering the pores of the MOF, preventing the reaction from proceeding. Platinum nanoparticles were successfully inserted within the pores of the MOF, this was verified by TEM, nitrogen adsorption isotherms and inductively coupled plasma optical emission spectroscopy (ICP-OES) and the photocatalytic hydrogen evolution reaction was repeated but produced the same result.

4.2. Experimental

4.2.1. NU-1000 Synthesis.

All reagents, other than the $TBAPyH_4$ which was synthesised in house (see the AlTBAPy chapter for the synthesis method), were purchased from Sigma-Aldrich except for the N,N-Diethylformamide (DEF) which was purchased from Tokyo Chemical Industries and Methanol which was purchased from Fisher, all were used without purification.

Zirconium tetrachloride (202.0 mg 0.866 mmol) was dissolved in DEF. Benzoic acid (5.29 g 50 eq) was added to this solution; the benzoic acid acts as a modulator by preforming the $Zr_6O_4(OH)_4(PhCO_2)_{12}$ SBU cluster, the benzoic acid can then be displaced by the TBAPy linker producing a more crystalline MOF.[10] To this mixture $TBAPyH_4$ (453.7 mg 0.665 mmol) was added, this was sealed in a 25 ml Teflon lined Parr autoclave and heated at a rate of 2.0 °C min^{-1} to 120 °C and held at this temperature for 98 h before being cooled at a rate of 0.2 °C min^{-1} to room temperature. This was then washed in DMF and MeOH and allowed to dry. The use of benzoic acid to preform the zirconium cluster SBU however means that there remains benzoic acid bound to the cluster in the hydroxide position (see Figure 73)

protruding into the pores, reducing the pore volume. In order to remove the benzoic acid the as synthesised NU-1000 (40 mg) is added to DMF (24 ml) and 8M HCl (1 ml) in 40 ml glass vials with a Teflon sealed lid and heated at 100 °C for 24 hours. The NU-1000 is then washed with DMF and MeOH and then activated at 150 °C under vacuum for 24 h to remove the residual DMF from within the pores.[9]

4.2.2. Photocatalysis.

4.2.2.1. Platinum nanoparticle suspension.

Firstly a suspension of colloidal platinum was synthesised using the method reported by Darwent et al.[31] All chemicals were purchased from Sigma Aldrich and used without purification. $H_2PtCl_6.6H_2O$ (20.2 mg) was dissolved in water (160 ml) to produce 0.244 mM concentration solution, to this sodium citrate (80.0 mg) was added and the solution was heated at reflux for 4 hours. The orange chloroplatinic acid solution became black with the precipitated colloidal platinum nanoparticles. This suspension was then used for all the reactions.

4.2.2.2. Photocatalysis.

The photocatalysis reactions without an electron transfer reagent were carried out based on the reported reaction conditions by Fateeva et al for their aluminium porphyrin MOF.[26] Colloidal platinum suspension (10 ml) was diluted with water (28 ml) in a 40 ml vial, Na_2EDTA (195 mg) was added to make a 16 mM solution of Na_2EDTA. This was then buffered to pH 6.0 by adding sodium citrate. To this MOF photocatalyst (5.0 mg) was added and the suspension purged with nitrogen for 30 min. This vial was then sealed and exposed to the light of a 300 W Xenon lamp, with a distilled water IR filter and a <450 nm wavelength Pyrex cut off filter; these two filters ensured that the reaction mixture was only exposed to visible light. After

24 h a 250 µl sample of the dead space was taken and analysed by a Varian Star 3400 CX gas chromatograph with a 5Å molecular sieve column and a TCD detector.

The reaction was attempted using methyl viologen as an electron transfer reagent following the conditions reported by Fateeva et all for their aluminium porphyrin MOF.[26] The reaction was prepared the same way, by adding the colloidal platinum suspension (10 ml) to water (26 ml) in a 40 ml vial. Na_2EDTA (195 mg) was dissolved in the solution along with methyl viologen (74 mg), sodium citrate was then added to buffer the solution to pH6. MOF photocatalyst (5 mg) was then added and the solution was purged with nitrogen for 30 min. The vial was then sealed and then exposed to the light of a 300 W xenon lamp, with a distilled water IR filter and a <450 nm wavelength Pyrex cut off filter; to ensure that the reaction mixture was only exposed to visible light. After 24 h a 250 µl sample of the dead space was taken and analysed by a Varian Star 3400 CX gas chromatograph with a 5Å molecular sieve column and a TCD detector.

4.2.2.3. Platinum insertion.

Platinum was photo deposited within the pores of the NU-1000 MOF. All reagents were purchased from Sigma Aldrich and used without purification apart from the NU-1000 which was synthesised in house, see synthesis section. $H_2PtCl_6.6H_2O$ (3.5g) was dissolved in water (50 ml), $Na_2EDTA.2H_2O$ (5.0 g) was added as a sacrificial electron donor. Sodium citrate was then added to buffer the solution at pH6. NU-1000 (50 mg) was then added and the suspension purged with nitrogen for 30 min. This was then exposed to UV light from a Hg vapour lamp overnight. The yellow suspension turned black and the Pt@NU-1000 was then centrifuged out and washed with water until the liquor was clear and colourless, the green Pt@NU-1000 was then rinsed with MeOH and allowed to dry in air overnight.

4.3. Characterisation.

4.3.1. PXRD

The powder X-ray diffraction (PXRD) of NU-1000 MOF was collected using a Bruker D8 Advance diffractometer with Cu Kα radiation, in transmission geometry in a sealed 0.7 mm borosilicate spun capillary (see Figure 74). The PXRD pattern was indexed to the unit cell of NU-1000 reported by Mondloch et al using a least squares unit cell refinement technique and found to match.[11] This shows that the MOF synthesised has the same topology as NU-1000 suggesting the synthesis has been a success. Not only does the unit cell match that reported but also all the peaks measured can be indexed to the reported unit cell, the fact that there are no peaks present which can not being indexed shows that there are no other crystalline phases present suggesting that the material is phase pure.

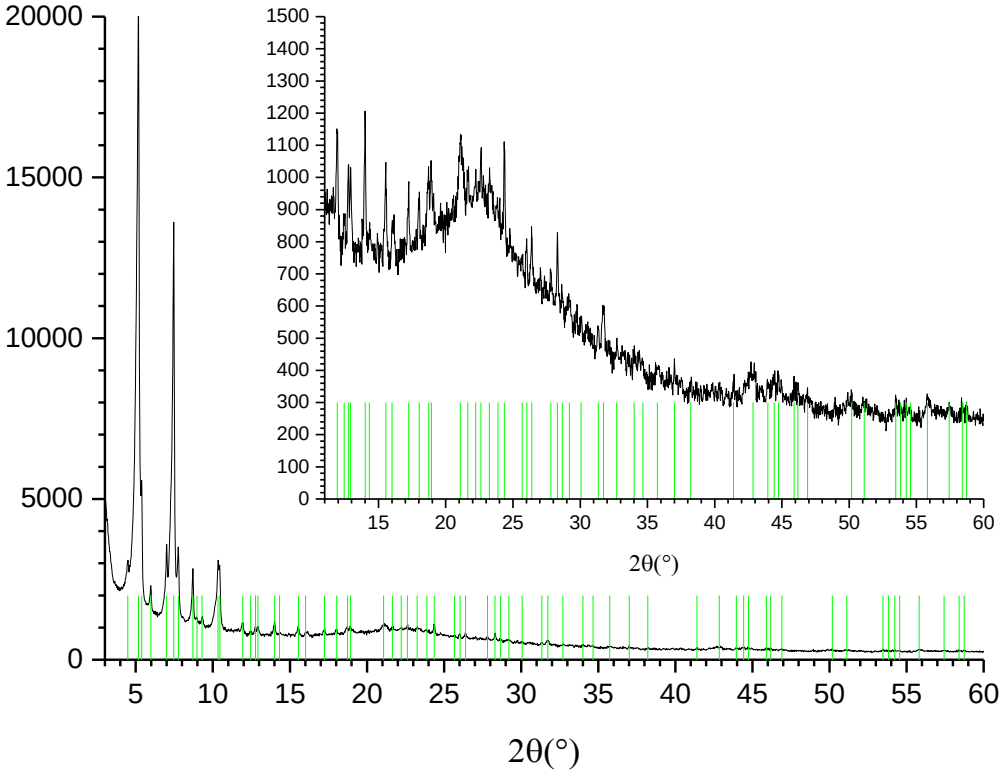

Figure 74: PXRD Pattern of NU-1000 MOF, insert of the high angle, low intensity region of the pattern. Indexed peaks are indicated with green lines.

All the peaks present in the PXRD pattern can be indexed to the hexagonal P6/mmm unit cell. The unit cell parameters calculated from this pattern are a=39.86(5) Å, b=39.386(5) Å, c=16.496(2) Å while α=β= 90°, γ=120° giving a unit cell volume of 22160.53 $Å^3$. These unit cell parameters are very similar to those reported by Mondloch et al for NU-1000 which where a= 39.3875(7) Å, b= 39.3875(7) Å, c= 16.4829(3) Å, α=β= 90°, γ=120° with a unit cell volume of 22145.3 $Å^3$; this similarity again suggests that the materials have the same topology and structure suggesting that the same material has been synthesised.

4.3.2. SEM

Scanning electron microscopy (SEM) images were taken of the NU-1000 MOF in order to examine the crystallites present. The NU-1000 MOF was spread on carbon tape on an aluminium stub and coated with gold before being imaged with a Hitachi S-4800 Field Emission SEM. The SEM images (see Figure 75) show that there is only one crystallite morphology present supporting the PXRD pattern to suggest that the material is phase pure. There is also no amorphous material visible which again suggests that the material is pure and the synthesis has been a success. The NU-1000 produces long thin needle like crystals which can be seen to vary in length from 8.7 µm to 1.7 µm however have a fairly consistent width from 0.66 µm to 0.90 µm; these crystallites can be seen the cluster together.

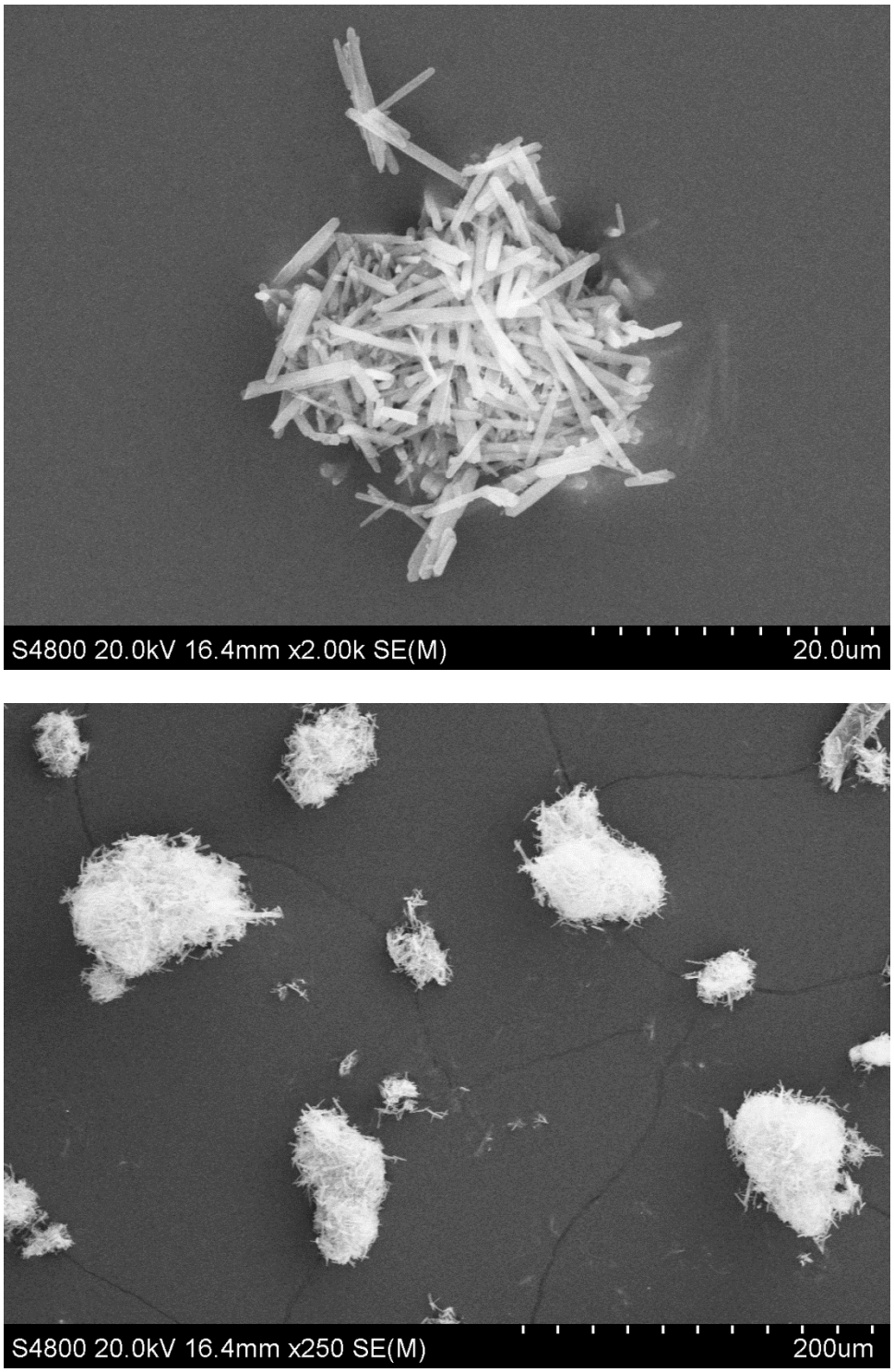

Figure 75: SEM Images of NU-1000 Crystallites.

4.3.3. TGA

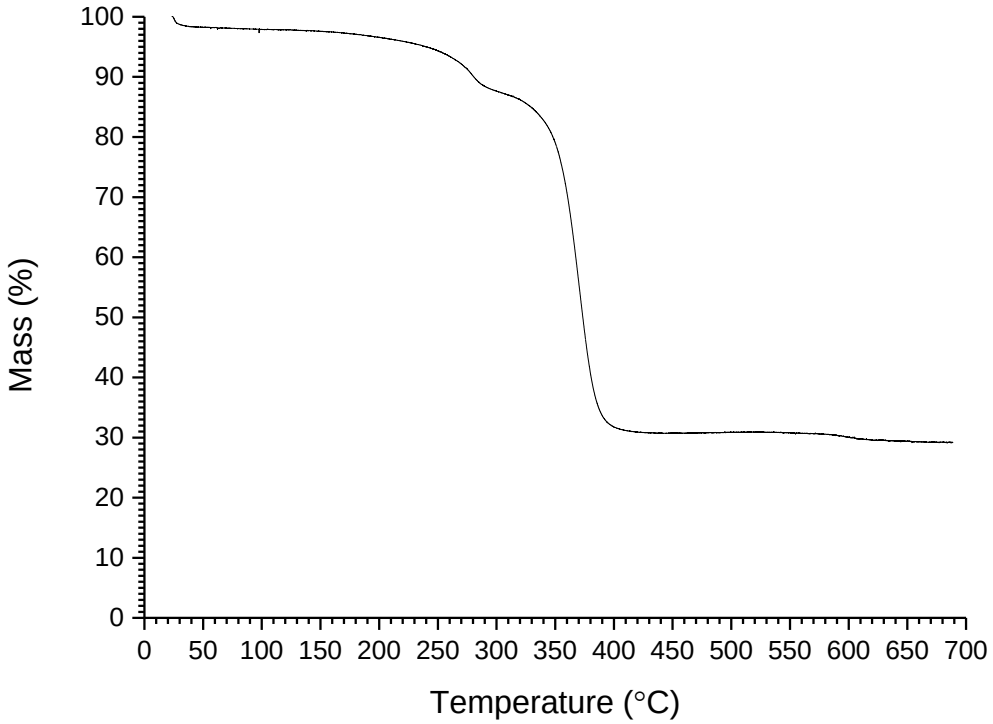

Figure 76: TGA of activated NU-1000.

A Thermogravimetric analysis (TGA) was performed on the activated NU-1000 using a TA Instruments Q600. By heating at a rate of 0.75 °C min^{-1} with a 100 ml min^{-1} flow of air over the sample (see Figure 76). From the TGA it can be seen that the NU-1000 is thermally stable decomposing at 330 °C, a temperature associated with the decomposition of the organic linker.[12] Also from the unchanging mass of the inorganic residue remaining at the end of the analysis the zirconium content can be calculated; the inorganic residue will be composed of ZrO_2 which has a Zr composition of 74.03 % by mass, as the inorganic residue comprises 29.2% of the starting mass of the NU-1000 this means that the NU-1000 contains 21.6 % zirconium by mass. This can be combined with the results of CHN elemental analysis to determine the chemical composition of the MOF (see Figure 77). Before

the decomposition of the MOF at 330 °C there can be seen a small mass loss at 250 °C, it has been reported that UiO-66, a MOF composed of a similar $Zr_6O_4(OH)_4$ SBU cluster undergoes reversible loss of 2 H_2O to form a cluster of Zr_6O_6 at these temperatures, this mass loss shows that the SBU of NU-1000 undergoes a similar loss of H_2O.[3]

4.3.4. Elemental analysis.

A CHN analysis of the activated NU-1000 was carried out using an Isoprime CHNS Elemental Analyzer. This showed that the NU-1000 contained by mass 49.22 % carbon, 2.63 % hydrogen and 0% nitrogen. The 0% nitrogen content showed that all the DMF had been successfully removed during the activation. These values can be combined with the 21.6 % zirconium content as determined by the inorganic residue from the TGA. The measured composition can then be compared to the theoretical values obtained from the crystal structure composition of $Zr_6(OH)_{16}TBAPy_2$, which gives mass compositions of 25.61% zirconium, 47.22% carbon and 3.21% hydrogen. These values are similar to the measured values however it is reported that NU-1000 can contain structural defects where a pore may be blocked by an additional $Zr_6O_4(OH)_4(TBAPyH_2)_6$ which could also affect the composition.[9] By adding $0.15(Zr_6O_4(OH)_4TBAPy_6)$ to the theoretical composition this gives a theoretical composition of 50.25 % carbon, 3.74 % hydrogen and 22.70 % zirconium; this theoretical composition more closely matches the composition measured for NU-1000 (see Figure 77). These results though are close enough to what is expected to suggest that the sample of NU-1000 synthesised is pure and has the expected composition from the crystal structure.

$Zr_6(OH)_{16}TBAPy_2(Zr_6O_4(OH)_4TBAPy_6)_{0.15}$		
Element	Experimental	Theoretical
C	49.22 %	50.25 %
H	2.63 %	3.74 %
Zr	21.6 %	22.70 %

Figure 77: Table of elemental analysis results compared to the theoretical resulsts from the suggested composition.

4.3.5. Surface Area Measurements.

From the crystal structure of the NU-1000 we can see that there are very large pores running through it, this suggest that the MOF will be highly porous and will have a large internal surface area with large pore volume. In order to determine if this is the case a nitrogen adsorption isotherm was measured at 77K using a Micromeritics Tristar II. From the nitrogen adsorption isotherm (see Figure 78) it can be seen that the NU-1000 is indeed highly porous and a type IV isotherm is measured. Type IV isotherms are indicative of mesoporous materials where the Nitrogen is adsorbed in a signal layer upon the surface of the material, as indicated by the initial low pressure adsorption, followed by a slight plateau as the surface reaches saturation, this is then followed by a further adsorption as the adsorbate then condenses within the channels.[13] IUPAC defines a mesoporous material as one with pores of a diameter larger than 2 nm but smaller than 50 nm, from the crystal structure of NU-1000 reported by Mondloch et al the pore size diameter is measured to be 3.0 nm, this fits with the IUPAC definition for a mesoporous material and so the type IV isotherm measured is therefore what would be expected.[9, 13]

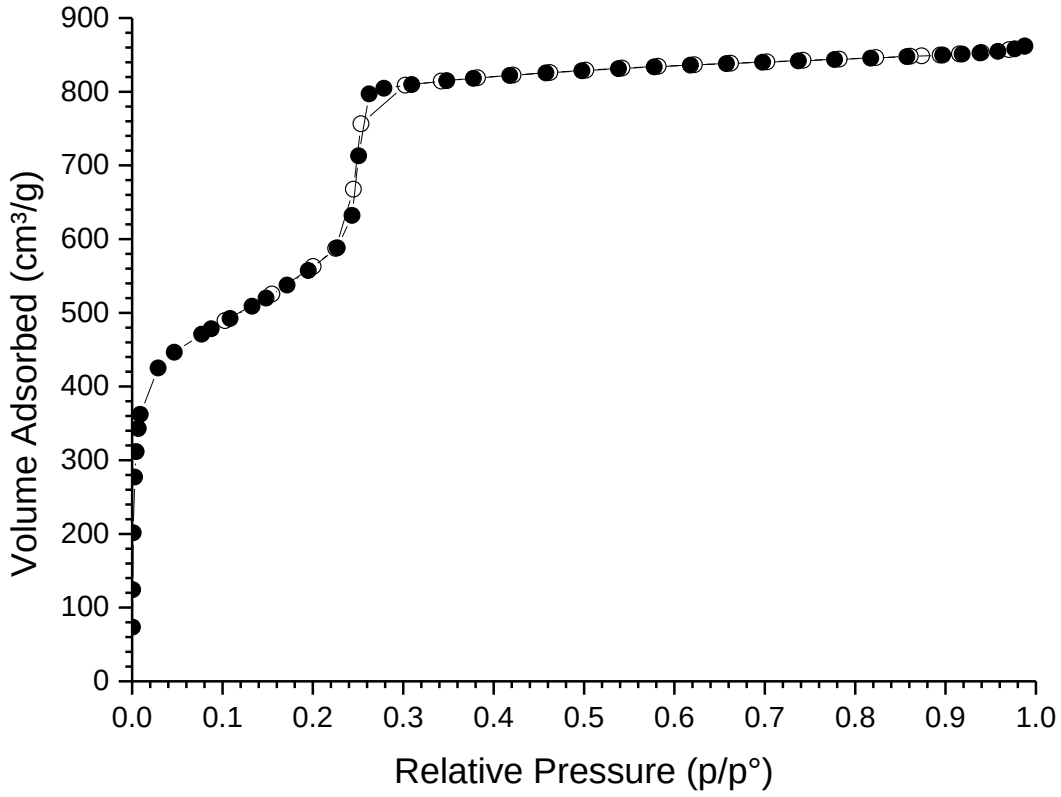

Figure 78: N_2 Adsorption Isotherm at 77K for NU-1000. Adsorption isotherm indicated by filled circles, desorption isotherm indicated by empty circles.

From the nitrogen adsorption isotherm the pore volume can be calculated by multiplying the volume of nitrogen adsorbed at $P/P^0 = 0.9$ by the nitrogen gas/liquid density factor of 0.0015, from this the pore volume is calculated to be 1.277 $cm^3\ g^{-1}$; this is similar to the 1.4 $cm^3 g^{-1}$ reported by Mondloch et all for NU-1000.[9] However using OLEX2 crystallographic software the pore volume can be calculated from the crystal structure by simulating a rolling sphere with probe diameter of 1.8 Å, similar to that of a nitrogen molecule travelling through the pores of the MOF. The calculation shows that the NU-1000 MOF should have a pore volume of 1.626 $cm^3 g^{-1}$, slightly larger than the pore volume measured.[14] Many zirconium MOFs contain defects in the structure where linkers and SBUs may be missing or added, NU-1000 is no exception and it has been reported that some of the channels running though the

structure can be blocked by a $Zr_6O_4(OH)_4TBAPy_6$ with the TBAPy also bound to the zirconium cluster SBUs of the framework instead of one of the hydroxide groups usually present; as has been shown from the elemental analysis it is likely that the NU-1000 contains these blocked pores which will reduce the pore volume from what would be expected from the calculations from the crystal structure.[9]

The Brunauer-Emmett-Teller (BET) model has been applied to the nitrogen adsorption isotherm between P/P^0 pressure ranges of 0.004 and 0.23 to give a calculated BET surface area for NU-1000 of 1988 m^2g^{-1}.[15] This is again slightly lower than the BET surface area reported by Mondloch et al of 2320 m^2g^{-1} but a slight discrepancy is expected from the blocked pores.[9]

Both the pore volume measured and the surface area calculated although slightly smaller than those reported for this MOF and the expected values from the crystal structure are sufficiently close to suggest the synthesis has been successful and a porous material has been produced. The surface area measured is significantly larger than that reported for MOFs with a similar composition, zirconium based MOF UiO-66 only reports a surface area of 1187 m^2g^{-1}, while pyrene based InTBAPy reports a surface area of 1189 m^2g^{-1}.[3, 12]

4.3.6. Optical Spectroscopy.

4.3.6.1. UV/Vis

The diffuse reflectance UV/Vis Spectrum of NU-1000 and the unreacted free $TBAPyH_4$ ligand were measured using a Perkin Elmer Lambda 650 S UV/Vis Spectrometer (see Figure 79). The spectra show a large absorption at 400 nm for the NU-1000 and at 480 nm for the free $TBAPyH_4$ linker. This absorption is due to the $\pi \rightarrow \pi^*$ transition of the pyrene moiety of the TBAPy molecule; a strong adsorption

between a wavelength of 200 nm and 500 nm is to be expected from a molecule as conjugated as TBAPy.[16] The adsorption for NU-1000 is blue shifted by 80 nm, this hypsochromic shift is due to the electronegative $Zr_6(OH)_8$ SBU clusters withdrawing electron density from the TBAPy linker, reducing the energy of the π orbital while increasing the energy of the π* orbital and thus increasing the amount of energy required to excite the molecule.[17]

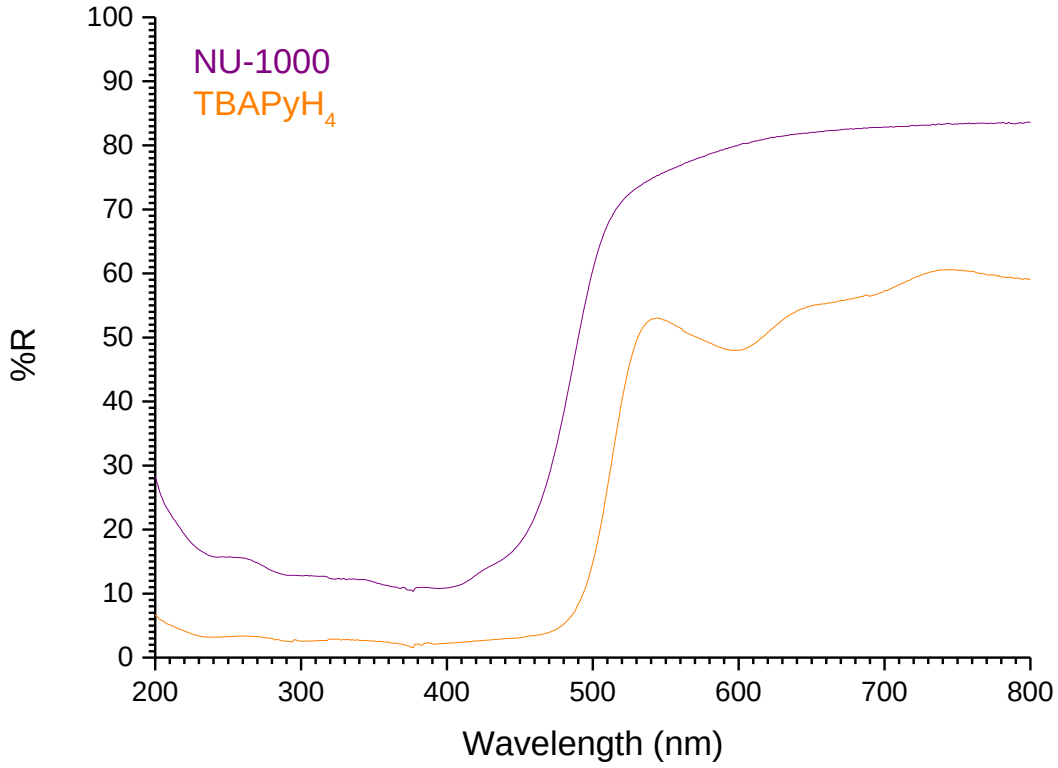

Figure 79: Diffuse Reflectance UV/Vis spectra of NU-1000 (purple) and free $TBAPyH_4$ linker (orange).

From the UV/Vis spectra (see Figure 79) no strong, sharp adsorptions can be seen which would indicated ligand to metal charge transfer between the TBAPy linker and the $Zr_6(OH)_8$ SBU clusters which would be expected at around 293 nm; this suggests that the pyrene is not acting as a sensitizer for the $Zr_6(OH)_8$ SBU

clusters within the MOF, rather that each pyrene based linker is electronically isolated.[2]

4.3.6.2. Fluorescence

The fluorescence spectra of the NU-1000 & the unreacted $TBAPyH_4$ free linker were measured using a Perkin Elmer LS 55 Fluorescence Spectrometer. The samples were measured in the solid state using the maximum absorption wavelength, measured by UV/Vis spectroscopy as the excitation wavelength (see Figure 80).

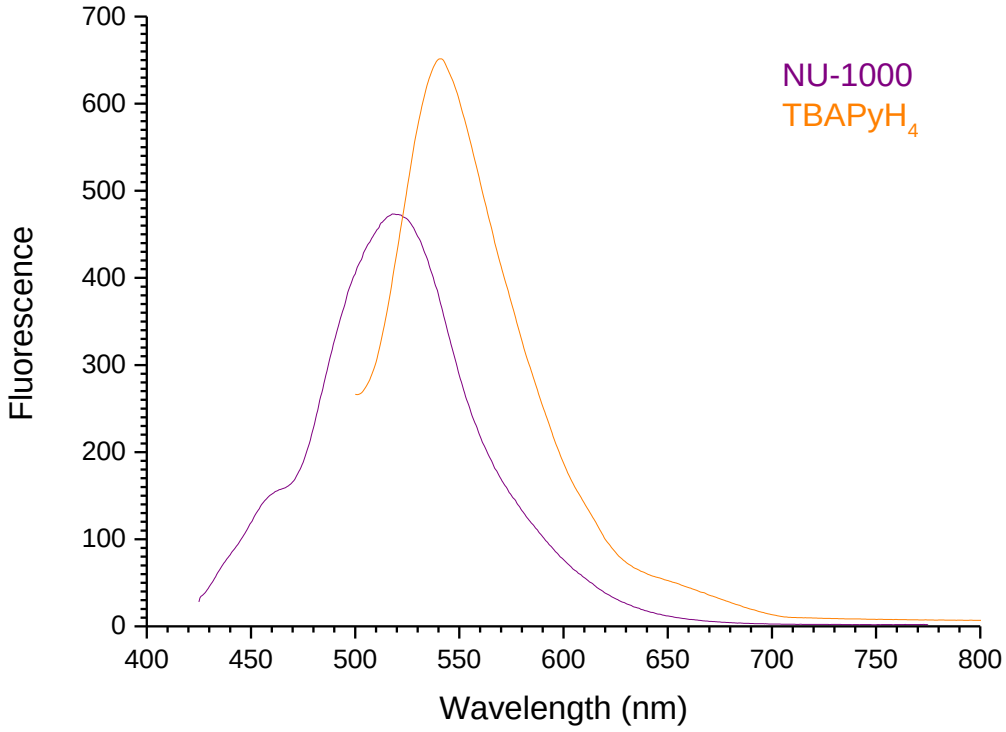

Figure 80: Solid state Fluorescence of NU-1000 (purple) excited at 400 nm wavelength and free $TNAPyH_4$ linker (orange) excited at 470 nm wavelength.

The fluorescence spectra show an emission peak at 520 nm with a shoulder at 460 nm for the NU-1000 and an emission peak at 550 nm for the free $TBAPyH_4$. Again the NU-1000 florescence peak is blue shifted slightly from the fluorescence peak of the free linker, this is due to the electronegative $Zr_6(OH)_8$ SBU clusters

withdrawing electron density from the TBAPy linker, reducing the energy of the π orbital while increasing the energy of the π* orbital, the wider gap between the two orbitals thus means more energy will be released upon the decay of the excited state back to the ground state thus blue shifting the emission wavelength. The fluorescence of the N-1000 MOF is lower intensity than for the free $TBAPyH_4$ linker, this suggests that some quenching is taken place, this may be due to transfer of energy to the Zr SBU from the excited TBAPy.

4.4. Water stability

One of the major challenges of MOF chemistry is the instability of many MOFs to even small amounts of water, including some MOFs composed of zirconium.[1, 18, 19] In order to ensure that NU-1000 is stable to water samples were soaked in water for 8 h, 24 h and 72 h before the NU-1000 was centrifuged out of suspension and the crystallinity checked using PXRD (see Figure 81). The PXRD was measured using a Bruker D8 Advance with Cu Kα radiation, in transmission geometry in a sealed 0.7 mm borosilicate spun capillary.

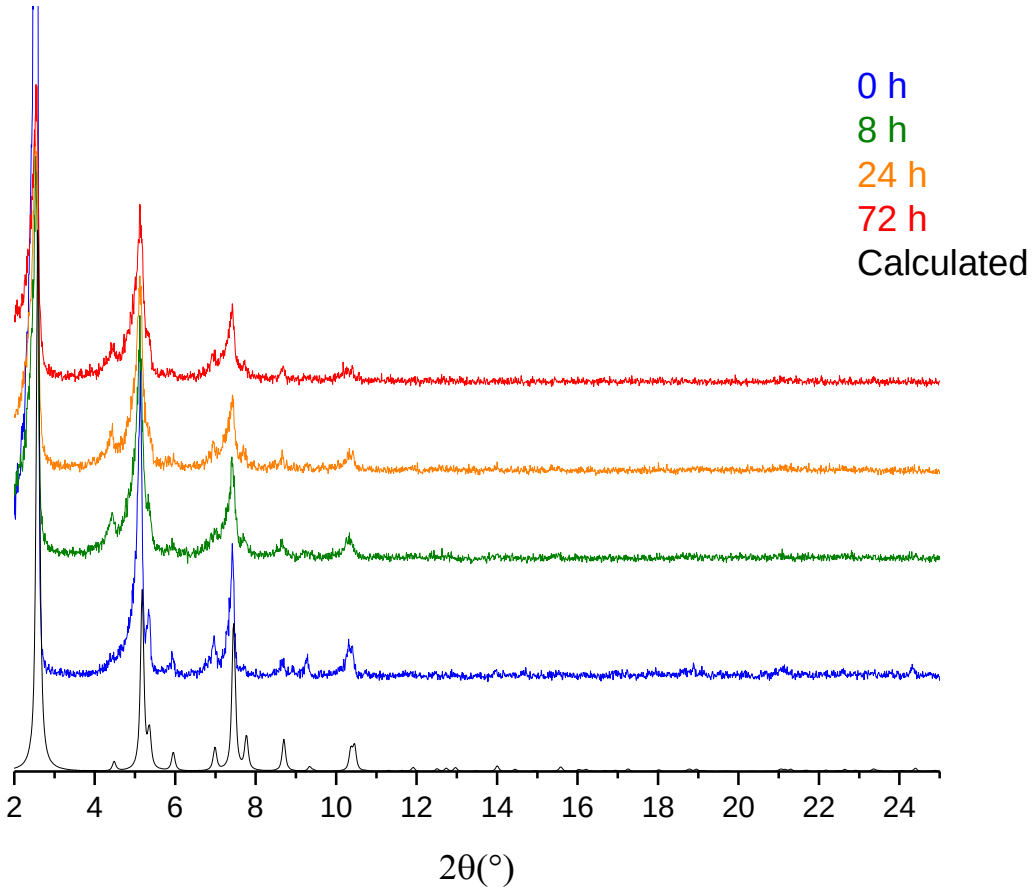

Figure 81: PXRD patterns of NU-1000 soaked in water for 0 hours (blue), 8 hours (green), 24 hours (orange) and 72 hours (red), also the PXRD pattern calculated from the crystal structure (black).

From the PXRD (see Figure 81) it can be seen that there is an initial slight reduction in the crystallinity as the peak intensity is reduced, however the MOF still remains highly crystalline and there is no further reduction in the crystallinity, as seen by the lack of peak broadening and the relative peak intensities not reducing further after this point thus demonstrating that NU-1000 is water stable. Furthermore the PXRD patterns can all still be indexed to the unit cell of NU-1000 using a least squares method unit cell refinement, with no unindexed peaks in the pattern. An additional peak appears in the PXRD patterns after the material is soaked in water at a 2θ angle of 4.5 °, this peak can be indexed to the unit cell of NU-1000 and can be

seen in the PXRD pattern calculated from the crystal structure showing that it is not arising from any phase change in the material. However the unit cell parameters for a and b reduce slightly while the c axis remains unaffected (see Figure 82), the pores of NU-1000 run along the c axis of the crystal (see Figure 73) and so this slight contraction of the unit cell along a and b indicate that the water is entering the pores and closing them slightly reducing the size of the unit cell in the a and b direction. However the change is only slight and the PXRD pattern can still be indexed using the original unit cell with no new peaks appearing, this shows that the material remains phase pure and there is little change in the topology of the MOF merely a slight change in the coordination environment of the zirconium oxide hydroxide cluster SBU.

Soaking Time	0 h	8 h	24 h	72 h
a /Å	39.86(5)	39.49(1)	39.40(7)	39.63(4)
b /Å	39.386(5)	39.49(1)	39.40(7)	39.63(4)
c /Å	16.496(2)	16.48(3)	16.62(8)	16.37(2)

Figure 82: Unit Cell Parameters for NU-1000 before soaking and after soaking in water for various times.

4.5. Photocatalysis.

The photocatalytic production of hydrogen from water under visible light is a much desired process to produce a renewable carbon free fuel and it is possible that a pyrene based MOF could perform this reaction, therefore it was attempted using NU-1000. [24, 25]

NU-1000 was tested as a visible light photocatalyst for a hydrogen evolution water splitting reaction. The NU-1000 was tested using water, colloidal platinum nanoparticles and Na_2EDTA as a sacrificial electron donor. Platinum nanoparticles

are needed for photocatalytic hydrogen evolution reactions to act as a cocatalyst. The platinum is required to remove an electron from the photocatalysis in order to prevent the excited electron from decaying to the ground state and also to bind to the protons which will be reduced to produce the hydrogen gas. Without platinum no hydrogen evolution reaction could take place. The reaction was also attempted using methyl viologen as an electron transfer reagent. The NU-1000 will be excited and transfer an electron to the methyl viologen which then in turn transfers the electron to the colloidal platinum nanoparticles and from there onto H^+ to produce the hydrogen.[26] Electron transfer reagents like methyl viologen provide the advantage that they can allow much better interaction between the catalysts as they will have a stronger interaction to both the MOF and the colloidal platinum than the platinum does directly to the MOF. The disadvantage is that an extra step in the reaction mechanism is involved, making it less efficient and thereby reducing the amount of energy available. However methyl viologen is a well known reagent used in this type of water splitting reaction and has been used successfully many times over several decades.[25-30] Another potential disadvantage is that the reduced methyl viologen radical which transfers the electron from the photocatalyst to the platinum cocatalyst is highly sensitive to oxygen, therefore all oxygen in solution and in the dead space in the reactor needs to be thoroughly purged for the reaction to proceed. However many photo catalysts are sensitive to oxygen and so this would need to be done anyway.[29] A sacrificial electron donor will be needed to replace the electron lost from the NU-1000 photocatalyst, in all the reactions Na_2EDTA is used for this purpose as is common for these reactions.[25, 26] No hydrogen was produced from either of these reactions.

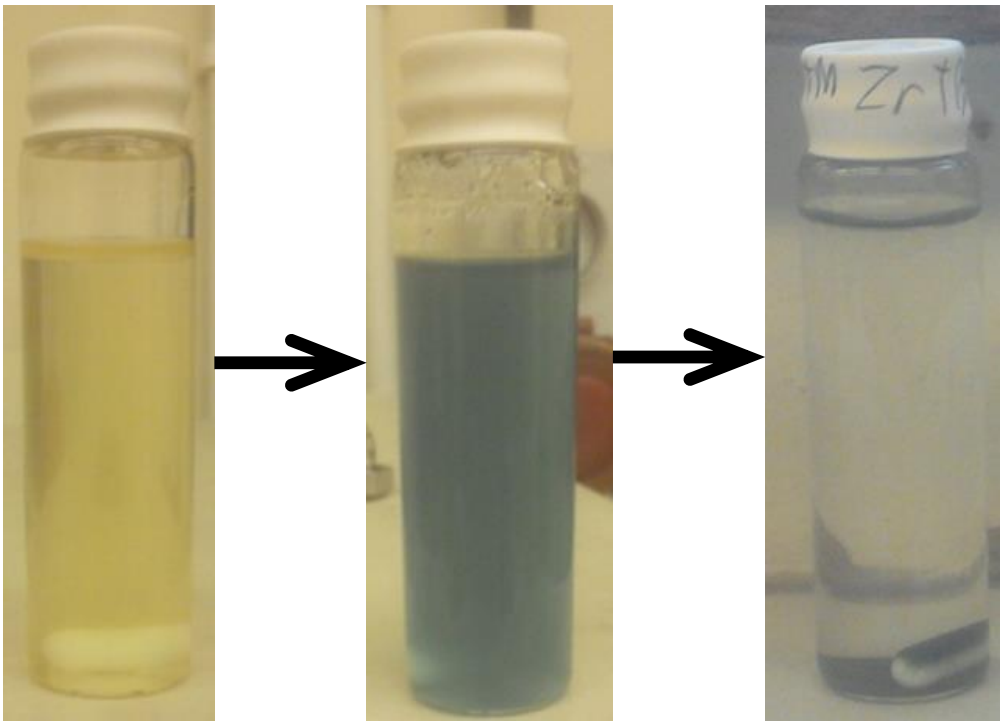

Figure 83: Photographs of NU-1000 MOF before, after & after photocatalysis reaction using Methyl Viologen as an electron transport reagent. Also photograph showing the reaction mixture after the NU-1000 MOF had been allowed to settle.

However it could be seen that a reaction had taken place as the reaction mixture had changed from the yellow colour of the NU-1000 to the distinctive blue colour of the reduced methyl viologen radical (See Figure 83). The fact the methyl viologen has been reduced when the reaction mixture was exposed to visible light irradiation, methyl viologen can only be directly reduced under UV light, shows that the NU-1000 has absorbed the light and then gone on to reduce the methyl viologen.[32] The transfer of an electron from reduced methyl viologen to colloidal platinum nanoparticles in order to produce hydrogen from water is a well-established reaction and so it is unexpected that no hydrogen was produced from this reaction.[25-30] However when the suspension was allowed to settle it became clear that the supernatant remained colourless and the previously yellow MOF had in fact turned

blue rather than the solution itself (see Figure 83). This suggests that the methyl viologen in solution remains unreduced while the methyl viologen which entered within the pores of the NU-1000 MOF was reduced as would be expected. However the reduced methyl viologen was then unable to exit the pores of the NU-1000 MOF; the charged aromatic bipyridyl methyl viologen (see Figure 84) will interact strongly to the highly aromatic TBAPy linker, through π-π interactions and through cation-π interactions between the 2+ cationic charge on the methyl viologen and the highly electron rich pyrene moiety. These two attractive interactions explain why the methyl viologen can enter the pores of the MOF but then remain trapped within the pores stuck on the internal surface of the MOF. The colloidal platinum nanoparticles should be small enough to enter within the pores of the MOF & react with the reduced methyl viologen trapped within so it is unexpected that no hydrogen has been produced. In order to determine if the platinum nanoparticles had entered the pores of the NU-1000 the sample was examined under transmission electron microscopy (TEM).

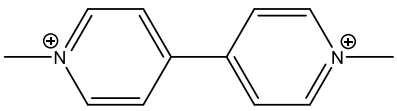

Figure 84: Structure of methyl viologen

4.5.1. TEM

After the unsuccessful attempts at photocatalysis the NU-1000 MOF was studied under TEM post reaction. The samples were deposited using MeOH on a carbon coated copper TEM grid and imaged using a JEOL 2100 TEM at 200 kV. The platinum, with its greater electron density will show up much darker than the mostly carbon based highly porous NU-1000.

From the TEM images (see Figure 85) it can be seen that the platinum is conglomerated on the surface of the MOF and that no platinum can be seen within the pores of the MOF. This could be an explanation as to why the reduced Methyl Viologen trapped within the pores of the MOF is unable to transfer its electron to the platinum, with the platinum on the surface and the methyl viologen within the pores there will be no interaction between them possible and thus no reaction can proceed.

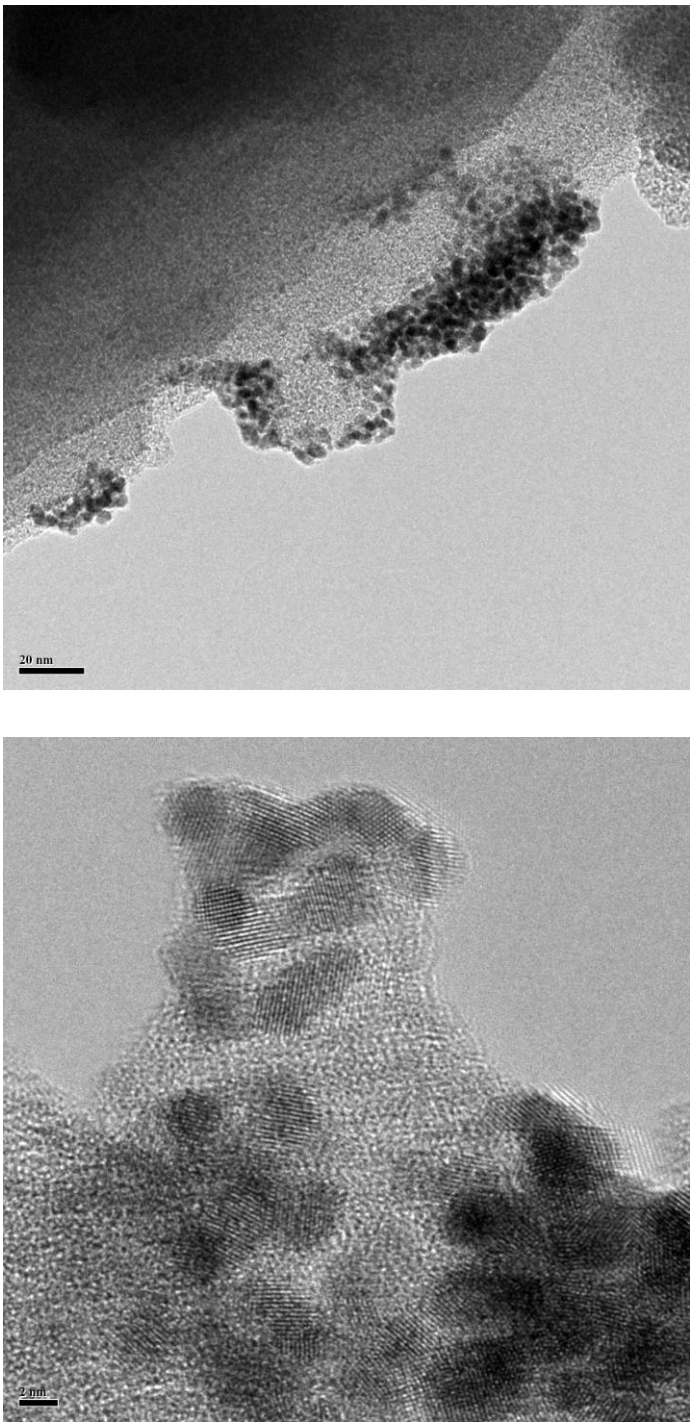

Figure 85: TEM Image of NU-1000 after photocatalytic reaction.

4.6. Pt@NU-1000 MOF

In order to attempt to overcome this lack of interaction between the methyl viologen within the pores and the platinum nanoparticles on the surface of the MOF

platinum nanoparticles were deposited within the pores of the NU-1000 MOF before the catalysis reaction.

4.6.1. Characterisation.

4.6.1.1. PXRD

The PXRD of Pt@NU-1000 was measured using a Bruker D8 Advance with Cu Kα radiation, in transmission geometry in a sealed 0.7 mm borosilicate spun capillary and the pattern indexed to the unit cell of the parent NU-1000 (see Figure 86).

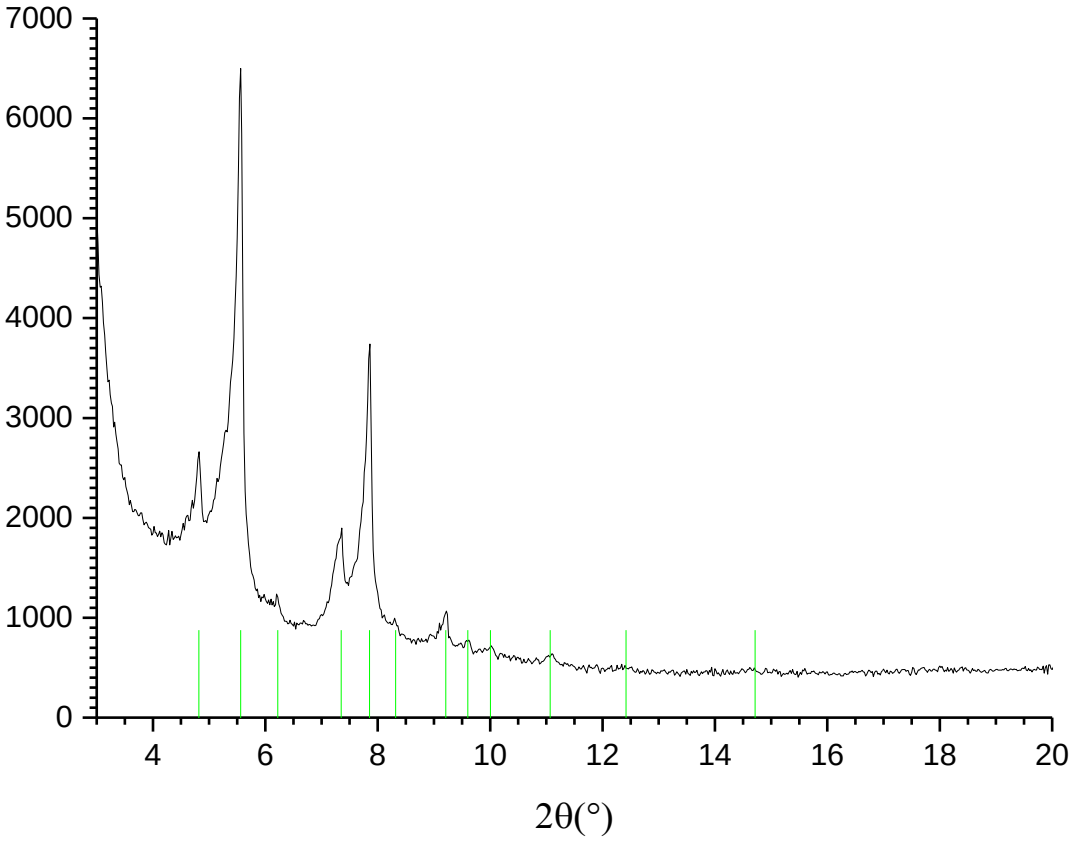

Figure 86: PXRD pattern of Pt@NU-1000. Indexed peaks are indicated with green lines.

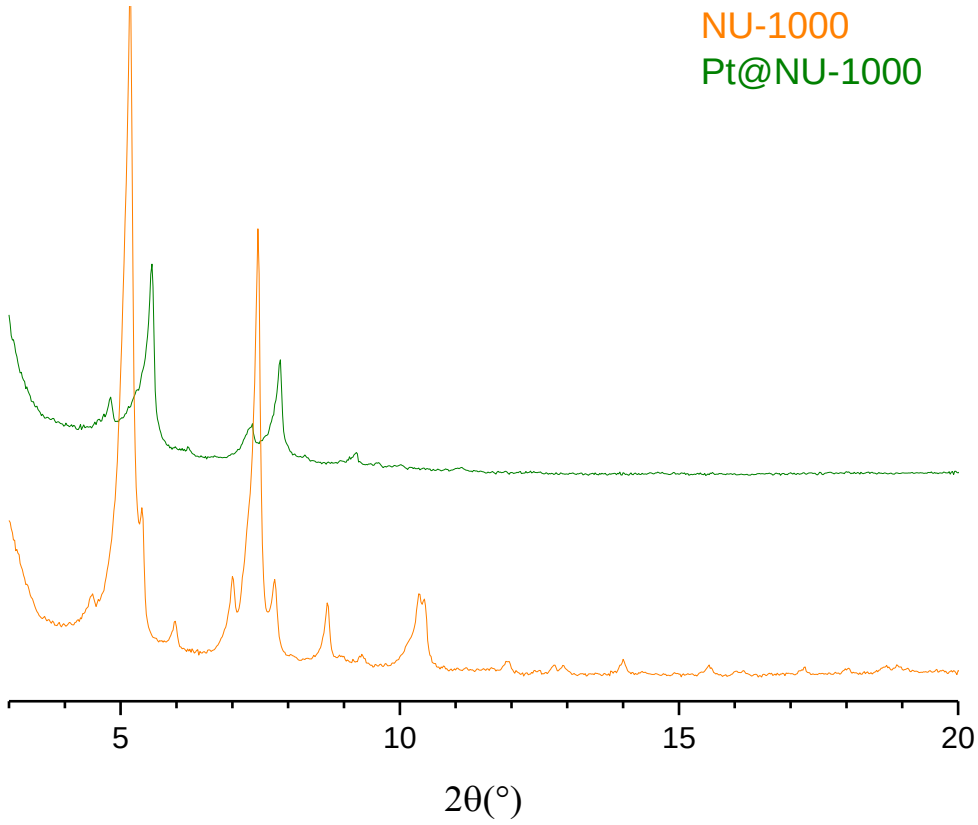

Figure 87: Comparison of PXRD patterns for NU-1000 (orange) and Pt@NU-1000 (green).

From the PXRD patterns (Figure 87) it can be seen that there are differences between the pattern for the Pt@NU-1000 and the parent NU-1000, the peaks have shifted position to a higher 2θ angle. The pattern can still be indexed to the unit cell of the parent material unit cell (see Figure 86) with no unindexed peaks present within the pattern despite the changes in peak position. However the unit cell parameters calculated for Pt@NU-1000 are slightly different to those calculated for the parent material. Pt@NU-1000 has a unit cell of a=39.8(2) Å, b=39.8(2) Å, c=16.3(3) Å giving a slightly larger unit cell volume of 22422.35 $Å^3$ compared to the unit cell parameters for the parent NU-1000 material which are a=39.86(5) Å, b=39.386(5) Å, c=16.496(2) Å giving a unit cell volume of 22160.53 $Å^3$. As has

been seen previously the NU-1000 MOF is slightly flexible and so it is not unexpected that the unit cell parameters will change slightly upon the addition of platinum nanoparticles to the pores of the MOF. The PXRD shows that the NU-1000 is stable when it undergoes the insertion of the platinum nanoparticles within the pores, other than a slight change in the unit cell parameters the NU-1000 retains its structure and topology after the insertion of platinum.

4.6.1.2. TEM

From the crystal structure reported by Mondloch et al the pore size can be measured, this can be seen to be 31.52 Å (see Figure 88) ; therefore any platinum nanoparticles seen by TEM larger than this size cannot possibly be within the MOF.[9]

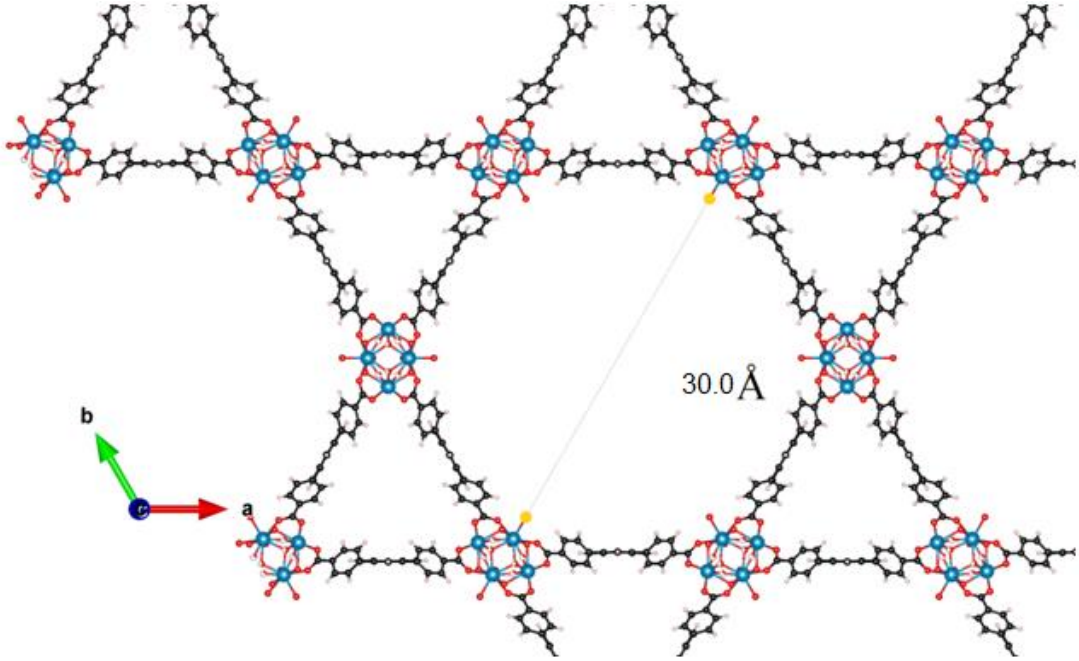

Figure 88: Pore size measured from the crystal structure reported by Mondloch et al.[9]

For TEM the samples were deposited using MeOH on a carbon coated copper TEM grid and imaged using a JEOL 2100 TEM at 200 kV (see Figure 89). From these images the darker platinum nanoparticles can be seen to be much smaller than

previously and are much more dispersed throughout the MOF crystallites; the platinum nanoparticles are no longer simply conglomerated on the surface of the material. This suggests that the platinum insertion has been successful.

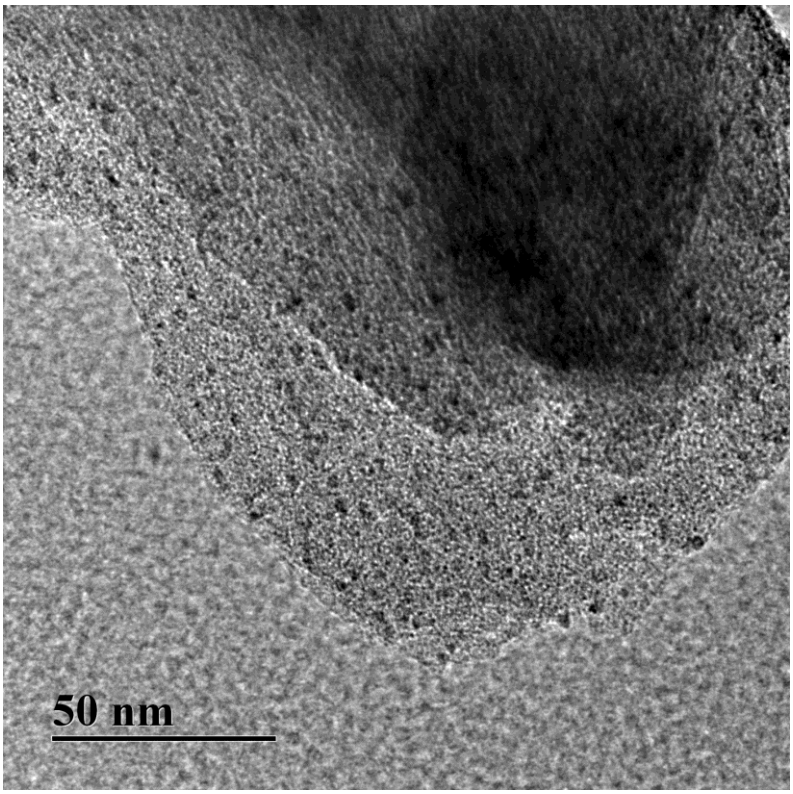

Figure 89: TEM Image of Pt@NU-1000

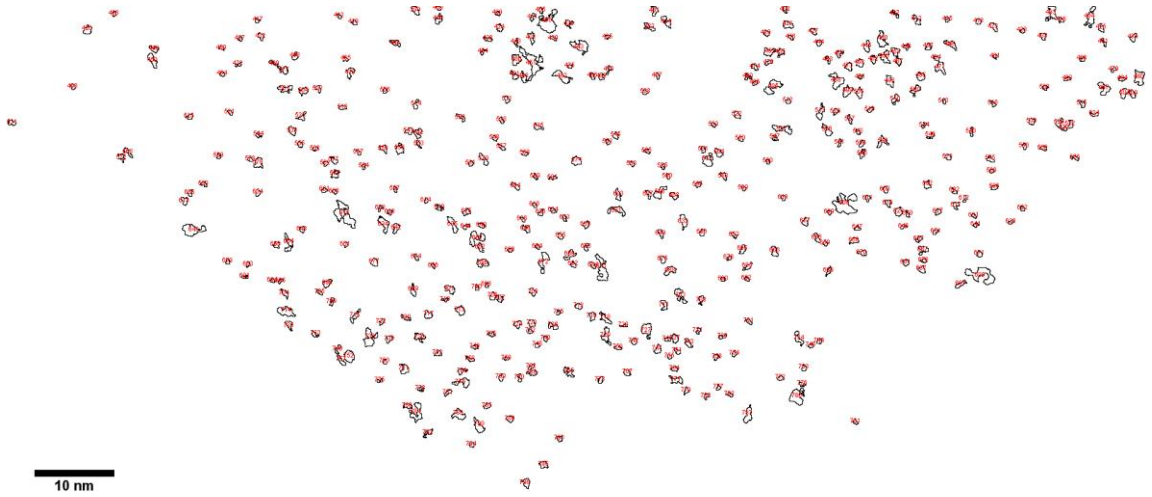

	Area/ nm^2	Ferret Diameter /nm	Min Ferret Diameter / nm
Mean	0.53969	1.22493	0.73795
SD	0.49909	0.55338	0.31277
Min	0.20637	0.65381	0.34340
Max	4.16418	4.50692	2.61727

Figure 90: Particle analysis for Pt@NU-1000.

It is possible to measure the size of the particles to confirm that they are small enough to fit within the pores of the MOF. To do this a threshold was applied to the image so only the darker platinum was seen. From this the Ferret diameter of the particles could be automatically measured for each particle (see Figure 90). From this it can be seen that the mean Ferret diameter is 12.24 Å, much less than the pore size diameter of 30.0Å measured from the crystal structure, this suggests that the platinum nanoparticles are inside the pores of the MOF. The standard deviation in the Ferret diameter is only 5.53 Å, the fact this is so small suggests that the

particles are being synthesised within the pores of the MOF meaning the pores are regulating the particle size keeping all the particles a similar size. The maximum Ferret diameter is 45.1 Å which is larger than the pore size, this particle cannot therefore be within the pores of the NU-1000 indicating that there are still some platinum nanoparticles on the surface of the MOF, though most appear to be inside the pores.

In order to confirm that these particles are within the pores of the MOF the Pt@NU-1000 was encased and set in resin, this was then sliced through the crystallites using a microtome in order to obtain a cross section of some of the crystallites, removing the surface and any platinum nanoparticles that may be conglomerated on the surface (see Figure 91). These slices where then deposited on a carbon coated copper TEM grid and images were taken with a JEOL 2100 TEM at 200KV.

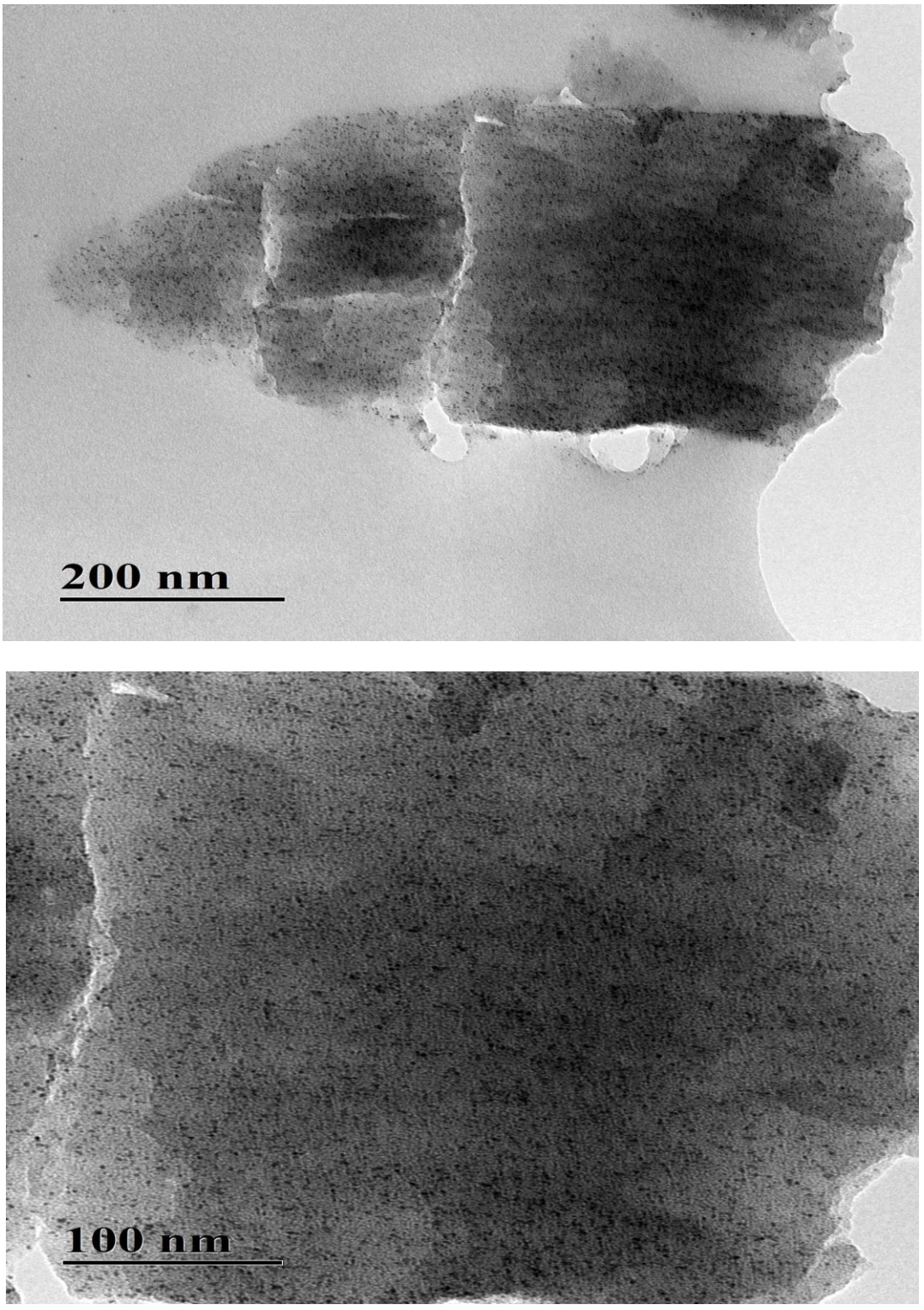

Figure 91: TEM Images of Pt@NU-1000 after Microtome Treatment.

From these images (see Figure 91) it can be seen that the platinum nanoparticles are within the bulk and therefore the pores of the MOF. This technique shows that the platinum is not simply on the surface of the crystallites.

It is also possible to do the same analysis on these samples as previously to determine the Ferret diameter of the particles to confirm that they are small enough to be within the pores of the NU-1000 MOF (see Figure 92).

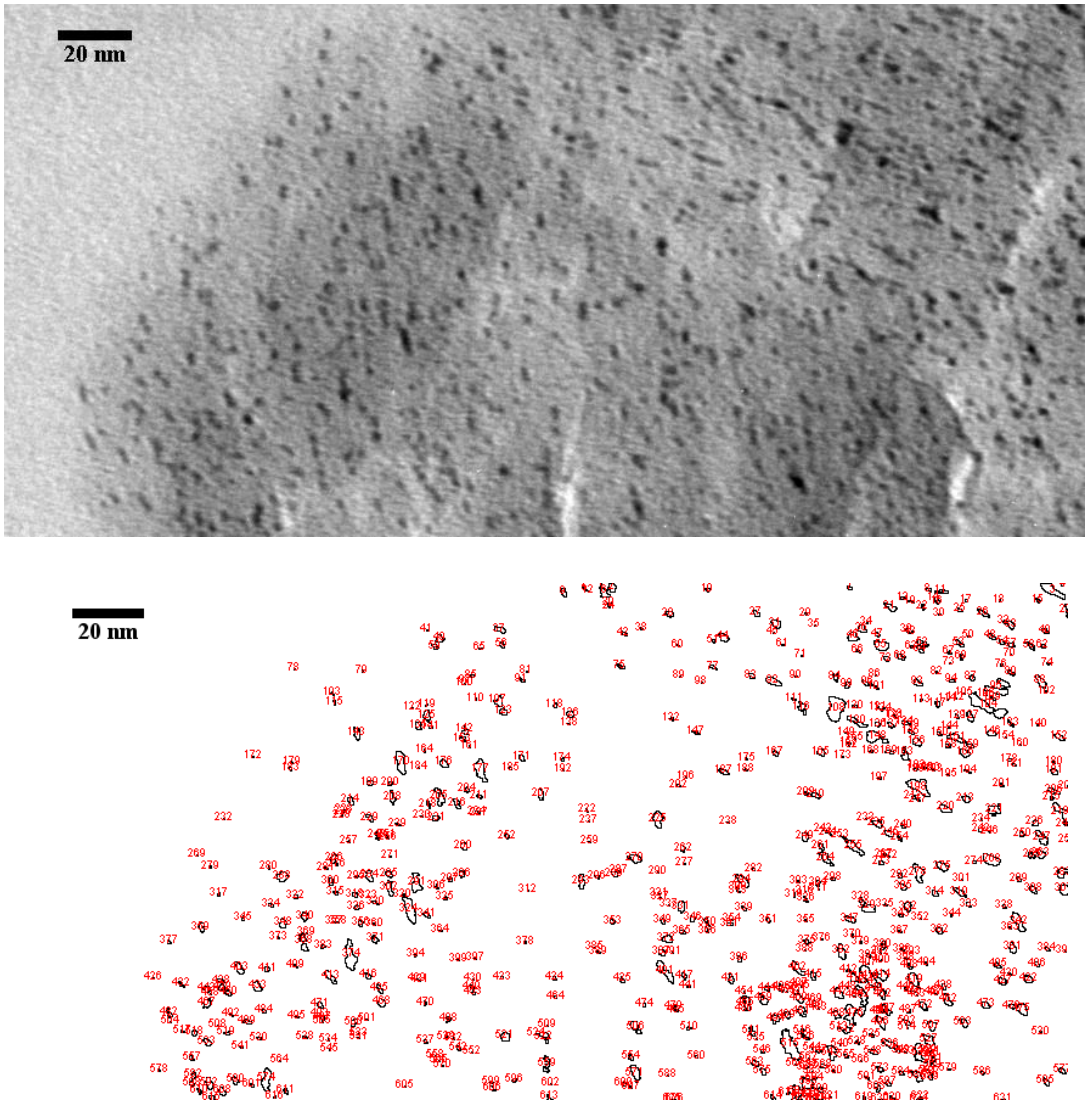

	Area/ nm^2	Ferret Diameter / nm	Min Ferret Diameter / nm
Mean	1.86665	1.97786	1.10057
SD	2.82302	1.58866	0.77998
Min	0.11196	0.47321	0.33461
Max	23.06444	11.82549	5.40550

Figure 92: Particle Suize analysis from Microtome treatment of Pt@NU-1000.

From these results it can be seen that the mean Ferret diameter is 19.78 Å which is smaller than pore size. However the maximum Ferret diameter is 118.3 Å, this is much larger than the pore size or any other particle measured, this may however be due to the microtome treatment, damaging the MOF and causing two or more platinum particles to merge together.

The TEM results strongly suggest that the platinum insertion into NU-1000 has been successful, the majority of the particles are well below the maximum size to fit within the pores of NU-1000 and by slicing the crystallites into segments using a microtome it is possible to see the platinum nanoparticles within the bulk of the material.

4.6.1.3. Elemental Analysis.

Elemental analysis in the form of both CHN, using an Isoprime CHNS Elemental Analyzer and ICP-OES and was carried out on the Pt@NU-1000 in order to determine its composition and the amount of platinum inserted into the pores. For ICP-OES analysis Pt@NU-1000 (2.0 mg) was digested in H_2SO_4 (5 ml) then diluted with HNO_3 (20 ml). These results showed that Pt@NU-1000 by mass contains 26.7 % zirconium, 5.2 % platinum, 49.28 % carbon and 3.08 % hydrogen. The best theoretical composition to match this composition is $Zr_6(OH)_{16}TBAPy_2.0.34Pt$ which

has a theoretical mass composition of 47.12 % carbon, 2.7 % hydrogen, 2.96 % platinum and 24.4 % zirconium.

$Zr_6(OH)_{16}TBAPy_2.0.34Pt$		
Element	Measured Mass	Theoretical Mass
C	49.28 %	47.1 %
H	3.08 %	2.7 %
Zr	26.7 %	24.4 %
Pt	5.2 %	3.0 %

Figure 93: Elemental analysis results for Pt@NU-1000 and a comparison to the theoretical results expected baased on the composition.

4.6.1.4. Nitrogen adsorption isotherm.

As the platinum has formed within the pores of the MOF a reduction in the surface area and pore volume as measured by nitrogen adsorption isotherm should be seen. The nitrogen adsorption isotherm was measured at 77K using a Micromeritics Tristar II. It could be seen that as predicted there was a reduction in porosity between the Pt@NU-1000 and the parent NU-1000 (see Figure 94). Furthermore it can also be seen in the adsorption isotherm for the Pt@NU-1000 a hysteresis loop is present; this is strongly indicative that there are particles within the pores of this material. As the pressure increases enough to enter within the pores of the Pt@NU-1000 the nitrogen is able to adsorb on to the surface of the platinum nanoparticles at higher pressures which is then only released at lower pressures thus forming the hysteresis loop. Also the parent NU-1000 clearly showed a type IV isotherm with two stages of adsorption characteristic of a mesoporous material; the Pt@NU-1000

however does not have the second adsorption at P/P^0=0.20 to 0.23, this strongly indicates that the mesopores have been blocked by the Platinum nanoparticles.

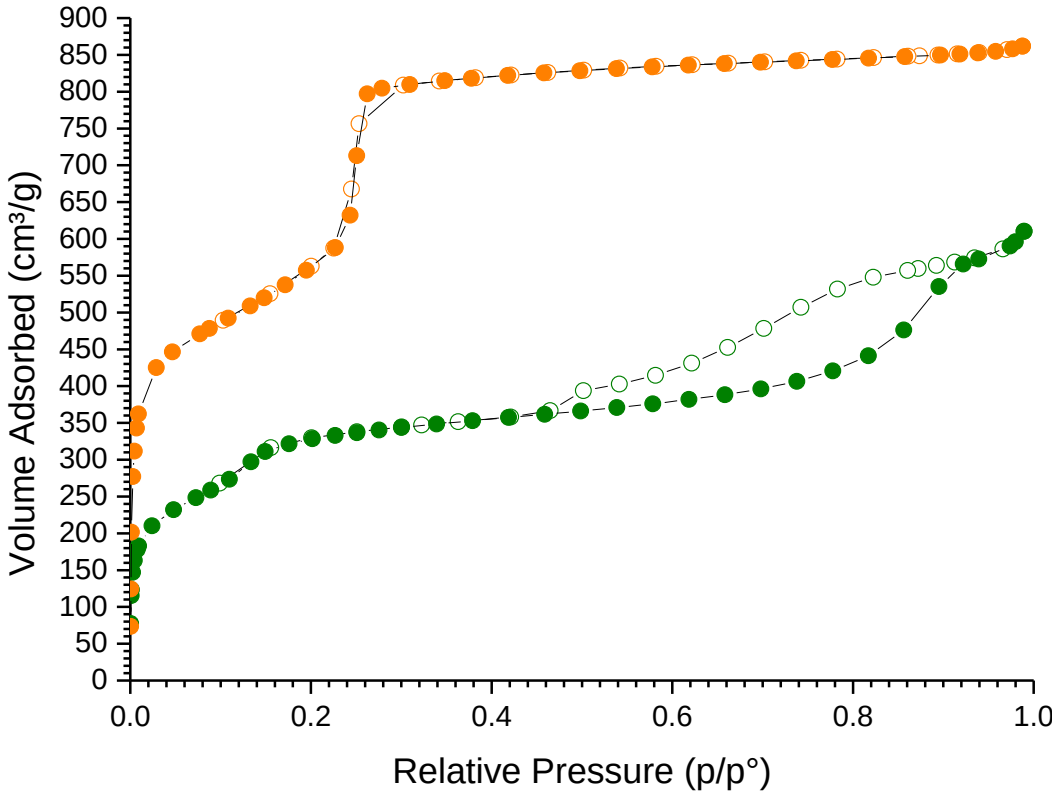

Figure 94: N_2 Adsorption Isotherm measured at 77 K for NU-1000 (orange) & Pt@NU-1000 (Green) Filled circles representing the adsorption measurements and while empty circles represent the measurements.

From the nitrogen adsorption isotherm measured for Pt@NU-1000 the pore volume and surface area can be calculated and compared to that of the parent NU-1000 material. The pore volume for Pt@NU-1000 can be calculated to be 0.792 cm^3g^{-1} at P/P^0 =0.94, significantly less than the 1.277 cm^3g^{-1} calculated for the parent NU-1000. The BET surface area, calculated between P/P^0=0.02 and 0.12 is reduced to 1107 m^2g^{-1} from 1988 m^2g^{-1} of the parent NU-1000. This reduction in the porosity of NU-1000 upon insertion of platinum nanoparticles shows that the platinum is within the pores of the MOF and thus that the insertion has been successful.

4.6.1.5. Optical Spectroscopy.

After the insertion of the platinum into the pores of NU-1000 there was a noticeable colour change from the bright orange/yellow of the NU-1000 to a much darker green colour of the Pt@NU-1000. A diffuse reflectance UV/Vis spectrum was measured of the Pt@NU-1000 using a Perkin Elmer Lambda 650 S UV/Vis Spectrometer (see Figure 95).

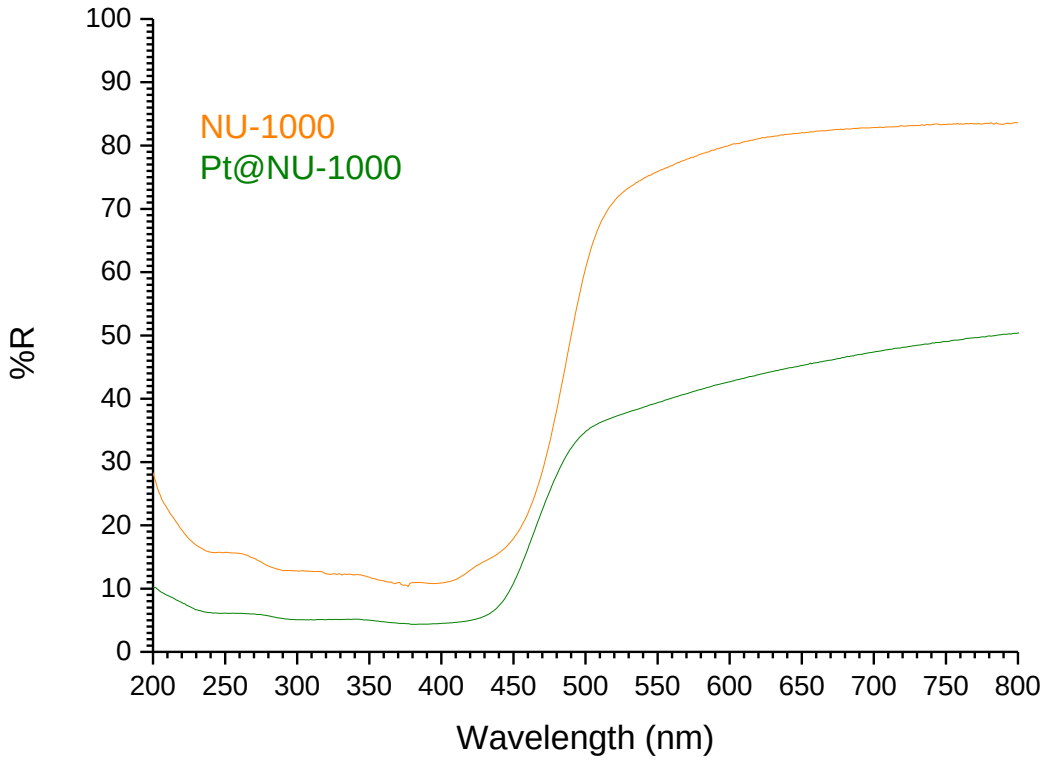

Figure 95: Diffuse Reflectance UV/Vis Spectra of NU-1000 (orange) and Pt@NU-1000 (green).

The UV/Vis spectra when compared to that of the parent NU-1000 can be seen to be significantly more absorbing of light across the spectrum; this is likely due to the black platinum nanoparticles which will absorb light across the spectrum reducing the reflection. Despite this however it can be seen that the $\pi \rightarrow \pi^*$ adsorption of the NU-1000 has not been shifted and remains at 450 nm for both

materials. This suggests that there is no interaction between the chromophore pyrene in the TBAPy linker and the platinum nanoparticles within the pores.[16] Also no additional peaks can be seen from a ligand to metal charge transfer, indicating that there is no charge transfer between the NU-1000 MOF and the platinum nanoparticles within the pores. Ideally charge transfer from the NU-1000 MOF to the platinum nanoparticles would take place and thus the photocatalytic hydrogen evolution reaction could proceed without use of an electron transfer reagent as once the electron is on the platinum the water splitting and hydrogen evolution reaction is well established.[26]

4.6.2. Photocatalytic hydrogen evolution.

The photocatalytic reactions performed previously with the NU-1000, both with and without methyl viologen as an electron transfer reagent, were repeated as before using the Pt@NU-1000 MOF as the photocatalyst and with the same volume of water replacing the colloidal platinum nanoparticle suspension. Neither reaction produced any hydrogen.

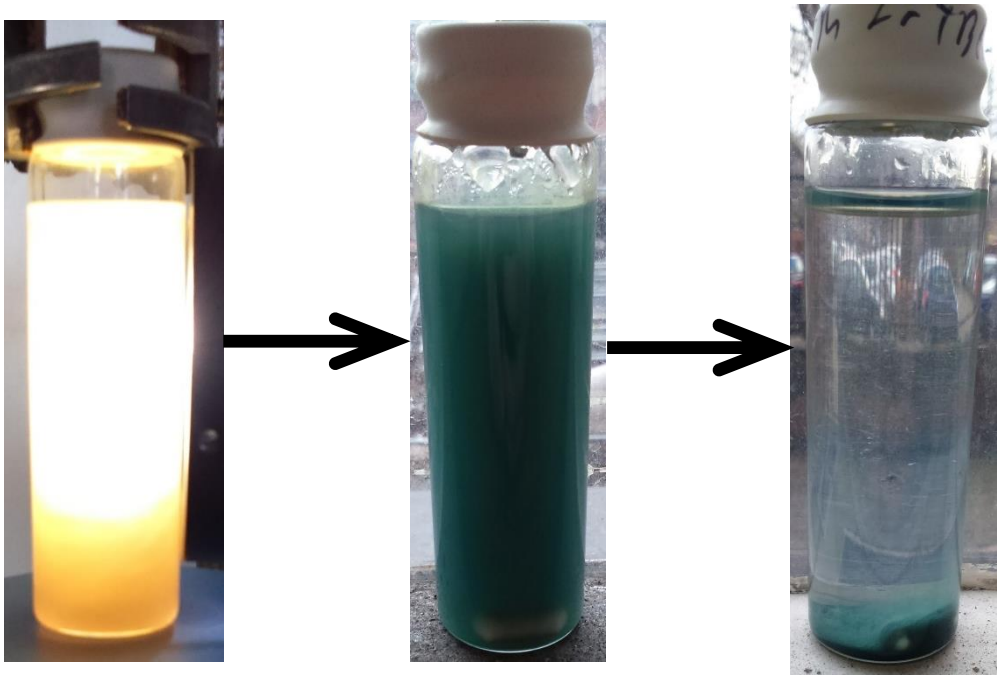

Figure 96: Photographs of Pt@NU-1000 before & after photocatalysis using Methyl Viologen as an electron transport reagent. Also photograph of the sample after the Pt@NU-1000 had been allowed to settle.

After the reaction it could be see that despite the lack of hydrogen produced a reaction had taken place as the Pt@NU-1000 MOF had changed from green/yellow to blue as a result of the reduced methyl viologen (see Figure 96), indicating that the addition of the platinum within the pores of the NU-1000 MOF has not impeded that photocatalytic reaction despite the lack of hydrogen produced.[32] After the reaction mixture is allowed to settle again the supernatant reveals itself to be colourless while the solid NU-1000 MOF itself had changed to become the blue colour of the reduced methyl viologen.

The fact that there is still no reaction even when both the platinum and the reduced methyl viologen are within the pores of the MOF suggests the NU-1000 may be stabilising the reduced methyl viologen meaning it is unable to transfer its electron onto the platinum nanoparticles. It is already clear that there is a strong

interaction between the NU-1000 MOF as the reduced methyl viologen remains within the pores of the MOF and does not diffuse out, that strong interaction may stabilise the reduced methyl viologen radical to prevent electron transfer to the platinum nanoparticles.[33] It may be also that if the platinum is deposited directly on the internal pore surface of NU-1000 and unable to move throughout the pores while the methyl viologen is also closely attracted to the internal surface of NU-1000 and neither is able to move within the pores it may be that they are still in different locations within NU-1000 and so still unable to interact.

4.7. Conclusion.

NU-1000 has been successfully synthesised and characterised. For the first time the photocatalytic properties of NU-1000 have been explored and it has been found to exhibit some photocatalytic activity, able to reduce methyl viologen but unable to proceed any further with the reaction due to the affinity of NU-1000 for methyl viologen. The deposition of platinum nanoparticles has been achieved within the pores of NU-1000 for the first time and this material has been successfully characterised; however the prescience of platinum within the pores does not enhance the photocatalytic activity.

1. M. Kim and S. M. Cohen, *Crystal Engeneering Comunications*, 2012, **14**, 4096-4104.
2. L. Valenzano, B. Civalleri, S. Chavan, S. Bordiga, M. H. Nilsen, S. Jakobsen, K. P. Lillerud and C. Lamberti, *Chemistry of Materials*, 2011, **23**, 1700-1718.
3. J. H. Cavka, S. Jakobsen, U. Olsbye, N. Guillou, C. Lamberti, S. Bordiga and K. P. Lillerud, *Journal of the American Chemical Society*, 2008, **130**, 13850-13851.
4. C. G. Silva, I. Luz, F. X. Llabrés, A. Corma and H. García, *Chemistry - A European Journal*, 2010, **16**, 11133-11138.
5. R. M. Yerga, M. C. Galvan, F. Valle, V. Mano and J. L. Fierro, *ChemSusChem*, 2009, **2**, 471-485.
6. C. H. Hendon, D. Tiana, M. Fontecave, C. Sanchez, L. D'arras, C. Sassoye, L. Rozes, C. Mellot-Draznieks and A. Walsh, *Journal of the American Chemical Society*, 2013, 1-4.
7. J. B. Birks, A. A. Kazzaz and T. A. King, *Proceedings of the Royal Society A: Mathematical, Physical and Engineering Sciences*, 1966, **291**, 556-569.

8. Y. Horiuchi, T. Toyao, M. Saito, K. Mochizuki, M. Iwata, H. Higashimura, M. Anpo and M. Matsuoka, *Journal of Physical Chemistry C*, 2012, **116**, 20848-20853.
9. J. E. Mondloch, W. Bury, D. Fairen-Jimenez, S. Kwon, E. J. DeMarco, M. H. Weston, A. A. Sarjeant, S. T. Nguyen, P. C. Stair, R. Q. Snurr, O. K. Farha and J. T. Hupp, *Journal of the American Chemical Society*, 2013, **135**, 10294-10297.
10. A. Schaate, P. Roy, A. Godt, J. Lippke, F. Waltz, M. Wiebcke and P. Behrens, *Chemistry - A European Journal*, 2011, **17**, 6643-6651.
11. P. Deria, J. E. Mondloch, E. Tylianakis, P. Ghosh, W. Bury, R. Q. Snurr, J. T. Hupp and O. K. Farha, *Journal of the American Chemical Societry*, 2013, 1-4.
12. K. C. Stylianou, R. Heck, S. Y. Chong, J. Bacsa, J. T. Jones, Y. Z. Khimyak, D. Bradshaw and M. J. Rosseinsky, *Journal of the American Chemical Society*, 2010, **132**, 1-12.
13. K. S. Sing, D. H. Everett, R. A. Haul, L. Moscou, R. A. Pierotti, J. Rouqiérol and T. Siemieniewska, *Pure and Applied Chemistry*, 1985, **57**, 1365-3075.
14. O. V. Dolomanov, L. J. Bourhis, R. J. Gildea, J. A. K. Howard and H. Ouschmann, *Journal of Applied Crystalography*, 2009, **42**, 339-341.
15. S. Brunauer, P. H. Emmett and E. Teller, *Journal of the American Chemical Society*, 1938, **60**, 309-319.
16. Y. Zhiu, X. Shen, Chen-Xia, B. Wu and H. Zhang, *European Journal Of Inorganic Chemistry*, 2008, 4280-4289.
17. J. Gascon, M. D. Hernández-Alonso, A. R. Almeida, G. P. van Klink, F. Kapteijn and G. Mul, *ChemSusChem*, 2008, **1**, 981-983.
18. J. A. Greathouse and M. D. Allendorf, *Journal of the American Chemical Society*, 2006, **128**, 10678-10679.
19. D. Ma, Y. Li and Z. Li, *Chemical Communications*, 2011, **47**, 7377-7379.
20. R. Katoh, K. Suzuki, A. Furube, M. Kotani and K. Tokumaru, *Journal of Physical Chemistry C*, 2009, **113**, 2961-2965.
21. M. Dierksen and S. Grimme, *The Journal of Chemical Physics*, 2004, **120**.
22. M. Ottonelli, M. Piccardo, D. Duce, S. Thea and G. Dellepiane, *Journal of Physical Chemistry A*, 2012, **116**, 611-630.
23. A. D. McNaught, A. Wilkinson, M. Nic, J. Jirat, B. Kosata and A. Jenkins, *IUPAC. Compendium of Chemical Terminology, 2nd ed. (the "Gold Book").* Blackwell Scientific Publications, 2006.
24. J. Jiang, A. Trewin, D. J. Adams and A. I. Cooper, *Chemical Science*, 2011, **2**, 1777-1781.
25. M. Zhu, Y. Lu, Y. Du, J. Li, X. Wang and P. Yang, *International Journal of Hydrogen Energy*, 2011, **36**, 4298-4304.
26. A. Fateeva, P. Chater, C. P. Ireland, A. Tahir, Y. Khimyak, P. Wiper, J. Darwent and M. J. Rosseinsky, *Angewandte Chemie International Edition*, 2012, **51**, 7440-7444.
27. A. I. Krasna, *Photochemistry and Photobiology*, 1980, **31**, 75-82.
28. J. R. Darwent, P. Douglas, A. Harriman, G. Porter and M. Richoux, *Coordination Chemistry Reviews*, 1982, **44**, 83-126.
29. C. L. Bird and A. T. Kuhn, *Chemical Society Reviews*, 1981, **10**, 49-82.
30. J. R. Darwent, *Journal of the Chemical Society, Chemical Communications*, 1980, 805-807.
31. J. R. Darwent, *Chemical Communications*, 1982, 798-799.
32. T. Watanabe and K. Honda, *The Journal of Physical Chemistry*, 1982, **86**, 2617-2619.
33. A. K. Chandra, *Chemical Physics Letters*, 1970, **5**, 229-231.

5. EuTBAPy

5.1. Overview.

Unlike transition metals which have set coordination geometries where ligands coordinate along the d orbitals lanthanides with their non-valence f orbitals are free to adopt a wider range of geometries. Lanthanides also usually adopt much greater coordination number than transition metals which could enhance the stability of a MOF.[1] This geometrical freedom means that lanthanides have been used to produce a wide range of MOF topologies which would be impossible using transition metals.[1-6] Lanthanide complexes are also highly studied due to their unique fluorescent properties, the f-f transitions provide very sharp fluorescent peaks; however the f-f transition is Laporte forbidden and so a light absorbing antenna capable of exciting the lanthanide is required.[7] Pyrene has long been known for its optical properties, strong absorption of light, long excited state lifetime up to 113 ns and high fluorescence quantum yield of 0.68, these properties may make a pyrene based MOF linker such as 1,3,6,8-tetrakis(p-benzoic acid)pyrene ($TBAPyH_4$) (see Figure 97) a suitable antenna for sensitising europium flourescence.[8-10]

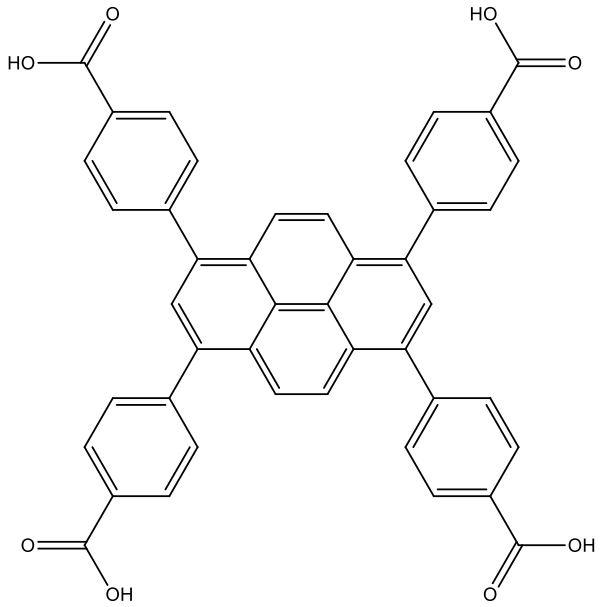

Figure 97: $TBAPyH_4$ Linker Molecule.

A new EuTBAPy MOF was synthesised and characterised by single crystal X-ray diffraction (SCXRD), powder X-ray diffraction (PXRD), CHN elemental

analysis and thermal gravimetric analysis (TGA), the crystallite morphology was examined using scanning electron microscopy (SEM), the porosity was examined using gas adsorption isotherms and the optical properties were measured using UV/Vis spectroscopy and fluorescence spectroscopy. The synthesis reaction space was thoroughly examined utilising high throughput techniques and instrumentation to test a wide range of solvent conditions and reagent concentrations and ratios.

5.2. MOF Synthesis.

$Eu(NO_3)_3.5H_2O$ and 1,4-dioxane were purchased from Sigma Aldrich and used without purification, dimethylformamide (DMF), methanol, ethanol and tetrahydrofuran (THF) were purchased from Fischer and used without purification, $TBAPyH_4$ was synthesised in house, see AlTBAPy chapter for details.

5.2.1. High Throughput Synthesis.

Many different lanthanide MOFs have been reported but due to the nature of the lanthanides, where ligands pack around the cation rather than having set geometries, a great many synthesis conditions have been reported where the conditions have a big impact on the topology of the MOF. Thus it was essential to explore as wide a range of synthesis conditions as possible to ensure the MOF was being produced in greatest yield, phase pure and as crystalline as possible. Also to ensure that any other phases of EuTBAPy MOF possible would be discovered. To perform so many different syntheses would take a great deal of time measuring out the reagents and solvents individually and so high throughput robots were utilised to fully explore the reaction space. A Chemspeed Accelerator SLT synthesis platform was used to dispense fine ground powders of $TBAPyH_4$ and $Eu(NO_3)_3.5H_2O$, this equipment was capable of dispensing the powder at a variable rate weighing the

amount dispensed as it did so. The solvents were dispensed using a Perkin Elmer Auto-pipette. These pieces of equipment can be used to automatically dispense reagents and mix solvent systems into the reaction vials quickly and reproducibly; the amounts of reagent and solvent system can be varied easily saving a great deal of time which would be necessary to prepare each synthesis individually.

Common solvents used for lanthanide MOF synthesis include DMF, 1,4-dioxane, water, methanol and ethanol.[11, 12] Many lanthanide MOF syntheses report a mix of solvents, in particularly a mix of water and another solvent; so each solvent was used on its own (4 ml) and with 1 ml replaced with water (solvent (3 ml) and water (1 ml)).[4, 6, 13] Also some of the reported complex solvent systems, 1,4-dioxane (2 ml), water (1 ml), DMF (0.5 ml) and methanol (0.5 ml); DMF (2 ml), ethanol (1.25 ml) and water (0.75 ml); DMF (3 ml), water (0.5 ml) and ethanol (0.5 ml); and DMF(2 ml), 1,4-dioxane (1 ml) and THF (1ml), were also used as solvent systems in the high throughput exploration (see Figure 98).[5, 14]

Solvent/ml	A	B	C	D	E	F	I	J	K	G	H	M	N
DMF	4					3			0.5	2	3	2	
Dioxane			4				3		2			1	
MeOH		4						3	0.5				
H_2O				4		1	1	1	1	0.75	0.5		2
EtOH					4					1.25	0.5		2
THF												1	

Figure 98: Table displaying the Solvent Systems used in the exploratory high throughput syntheses.

Just as important as the solvent system are the concentration of the reagents used and the ratio of metal cation to linker used in the synthesis. Once again lanthanide chemistry results in a great variation of reagent concentrations reported

for MOF synthesis, commonly ranging from 5 mM up to 50 mM. [4-6, 11-14] Preliminary experiments were carried out at 120 °C for 72 h in DMF (4 ml) and a mixture of DMF (3 ml) & H_2O (1ml) using a 1:1 ratio of $TBAyH_4$ to $Eu(NO_3)_3.5H_2O$ at concentrations of 5mM, 10mM, 25mM, 40 mM & 50 mM. These preliminary reactions showed that at concentrations of $TBAPyH_4$ greater than 40 mM large amounts of $TBAPyH_4$ remain undissolved and thus unreacted during the course of the reaction; DMF is a solvent in which $TBAPyH_4$ is comparatively highly soluble therefore this problem would be worse in other solvent systems. At concentrations of $Eu(NO_3)_3.5H_2O$ lower than 10 mM, very little solid is precipitated from the reaction mixture, these upper and lower concentrations were used as the basis for this experiment design. Four different concentrations of $Eu(NO_3)_3.5H_2O$ between these two limits were chosen to cover a wide range of the reaction space, 10 mM, 20 mM, 30 mM and 40 mM. Obtaining the correct ratio of metal to linker is also essential in MOF synthesis design for optimising the crystallinity and also for reducing impurities, if too much metal cation is used then metal oxide can be formed within the pores of the MOF, if too much linker is used the yield will be poor and organic linker, and the time taken to synthesise it, will be wasted. There are a range of ratios reported in the synthesis of lanthanide MOFs however the amount of lanthanide used is often greater than or equal to the amount of linker used; based on this ratios of $Eu(NO_3)_3.5H_2O$:$TBAPyH_4$ of 1:1, 3:2 and 2:1 were chosen, also 4:3 which would provide the charge balanced ratio between the Eu^{+3} and the $TBAPy^{-4}$. [4-6, 11, 13, 14] Starting with the four $Eu(NO_3)_3.5H_2O$ concentrations identified and using these ratios to determine the concentrations of $TBAPyH_4$ to be used provides sixteen different reagent concentrations to use in the synthesis (see Figure 99). By

combining each of the 14 solvent systems (see Figure 98) with each concentration of reagents 224 different synthesis conditions to be explored were produced.

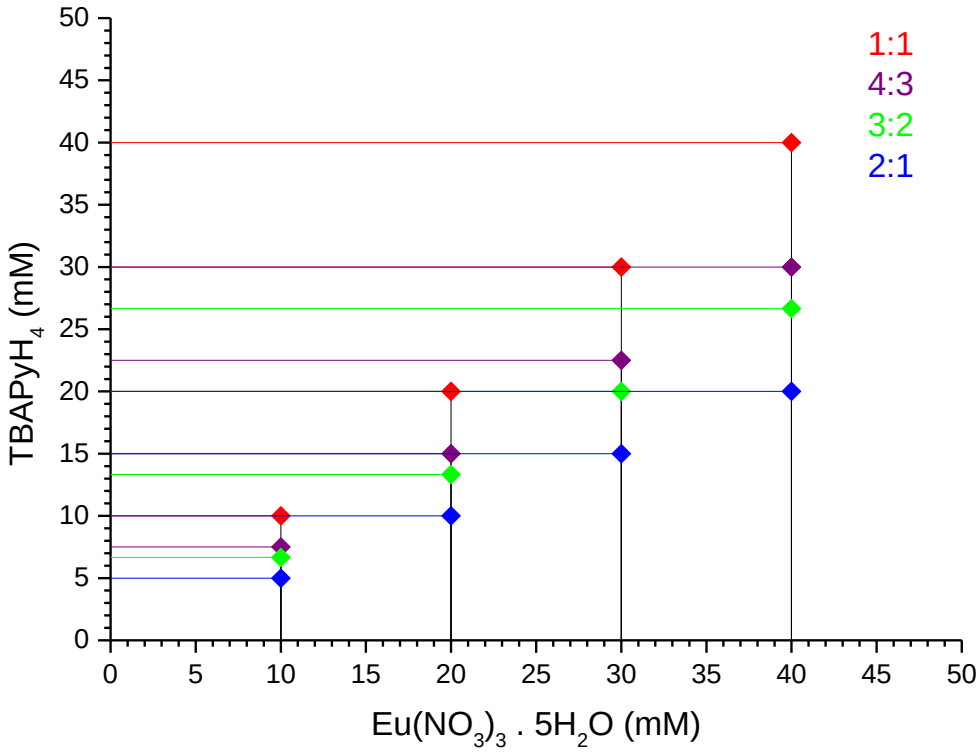

Figure 99: Graph showing the different concentrations of reagents used in the exploratory high throughput syntheses.

Each of these reactions were heated to 120 °C at 2.0 °C min^{-1} and held at this temperature for 72 h before being cooled back to room temperature at a rate of 0.2 °C min^{-1}. Once the reaction was complete any solid present was filtered from the reaction mixture, washed with DMF and then methanol before being left to dry. The products were characterised by PXRD using a PANalytical diffractometer using CuKα as a source in transmission-film geometry on a Mylar foil high throughput plate. Many of the synthesise produced amorphous or very poorly crystalline material and were discounted. The synthesise which produced more crystalline material has their PXRD patterns compared to each other to determine if there were

any similarities or differences such as the number, intensity and sharpness of peaks and peak positions or if any new peaks appeared in the patterns, between synthesise performed in the same solvent, at the same concentration or the same ratio and to look for any differences as concentrations or ratios were adjusted. Also each sample was examined under optical microscopy to try to find large enough single crystals to be used for SCXRD. Once single crystals were found and the structure calculated from their SCXRD pattern a least squares unit cell refinement was performed on the crystalline PXRD patterns to determine if the material synthesised was the same material as the crystals.

From the PXRD patterns it was found that solvent conditions had the largest effect, changes in concentration and ratio had some effect on the crystallinity but not the peak positions and relative intensities; suggesting that it is the solvent system which is most important in determining the material synthesised while the concentrations and ratios optimise the crystallinity. The synthesis which used 1,4-dioxane (4 ml), with ratios of 4:3 and 1:1 produced large enough single crystals to measure a SCXRD pattern. However the PXRD of the bulk phase of these samples showed peaks which could not be indexed to the unit cell of the structure calculated from the SCXRD pattern (see Figure 100), this shows that the product is not phase pure and that another material is present. The unindexed peaks increased in number and relative intensity to the other peaks as the concentration of reagents increased suggesting this other phase precipitates more readily at higher concentrations. The best synthesis conditions at producing highly crystalline powders was identified to be those which used the 1,4-dioxane (2 ml), water (1 ml), DMF (0.5 ml) and methanol (0.5 ml) solvent system. These reaction conditions produced the most crystalline PXRD patterns with the sharpest and most peaks which were phase pure as

determined by a least squares unit cell refinement using the unit cell calculated from the single crystal structure (see Figure 103). The PXRD patterns for this solvent system were all much better than for other solvent systems and again a ratio of 1:1 produced the most crystalline patterns with the greatest number of peaks. Although higher concentrations of reagents lead to a greater amount of product at the highest concentrations used peaks were present within the PXRD pattern which could not be indexed to the unit cell calculated from the SCXRD pattern, showing that these synthesis conditions did not lead to a phase pure product. However at lower concentrations of 10 mM highly crystalline phase pure material was synthesised. Attempts to increase the amount of impurity present within the sample by increasing the concentration of reagents still further in order to identify it could not proceed sufficiently due to the limited solubility of $TBAPyH_4$.

5.2.2. Single Crystal Synthesis.

$Eu(NO_3)_3.5H_2O$ (17 mg) and $TBAPyH_4$ (27 mg) were dissolved in 1,4-dioxane (4 ml) in a glass vial and sealed with a Teflon lined lid. This was heated at a rate of 2.0 °C min^{-1} to a temperature of 120 °C and held at that temperature for 72 h before being cooled back to room temperature at 0.2 °C min^{-1}. The reaction mixture contained crystals which were large enough to be used for single crystal X-ray diffraction (SCXRD), these crystals diffracted and a diffraction pattern was measured from which a structure could be calculated (see Figure 102).

This reaction was also produced a yellow powder; this was then filtered from the reaction mixture and washed with DMF and Methanol and the PXRD pattern measured and SEM images taken (see Figure 100 & Figure 101).

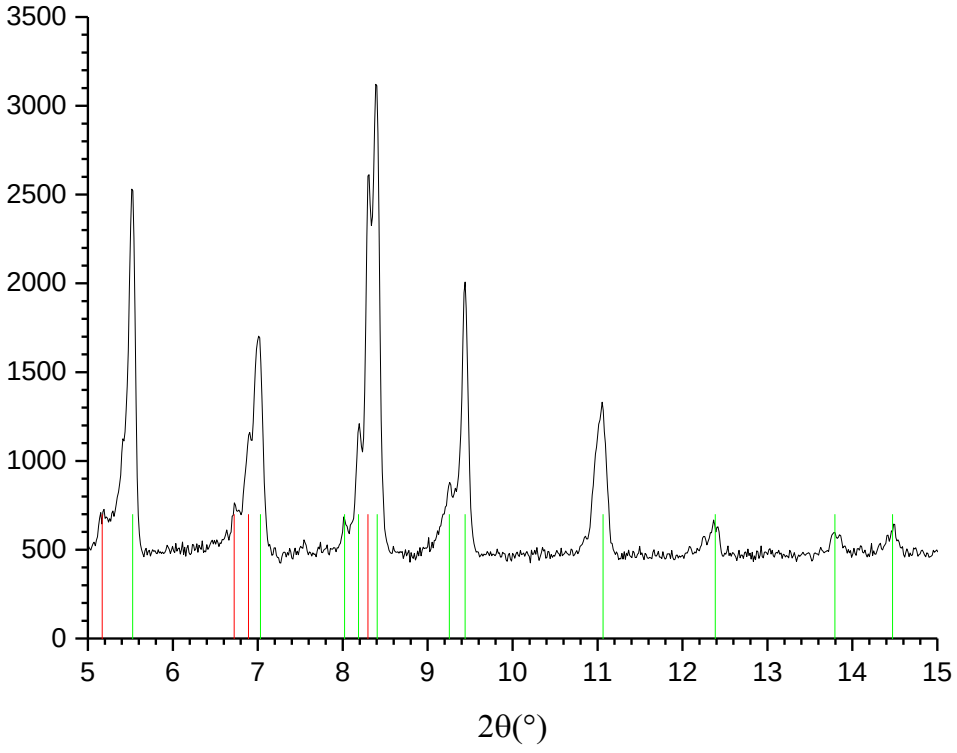

Figure 100: PXRD pattern of the bulk powder material from the EuTBAPy synthesis producing single crystals. Peaks which index to the unit cell of the single crystal structure are indicated with a green line while peaks which do not index to that unit cell are indicated with a red line.

The PXRD pattern (see Figure 100) showed the bulk material from the sample which contained single crystals to be crystalline, however when a least squares unit cell refinement was performed using the unit cell parameters from the single crystal structure there were peaks present in the pattern that did not index to the unit cell of the large crystals within the sample. This shows that this synthesis does not produce phase pure material, rather a mixture of two different crystalline phases. When examined using SEM (see Figure 101) the two different phases can be seen. There can be seen to be long thin needle like crystallites and larger blockier ones which look to be composed of stacked layers. These are two clearly different phases and so clearly show that this synthesis does not produce phase pure material.

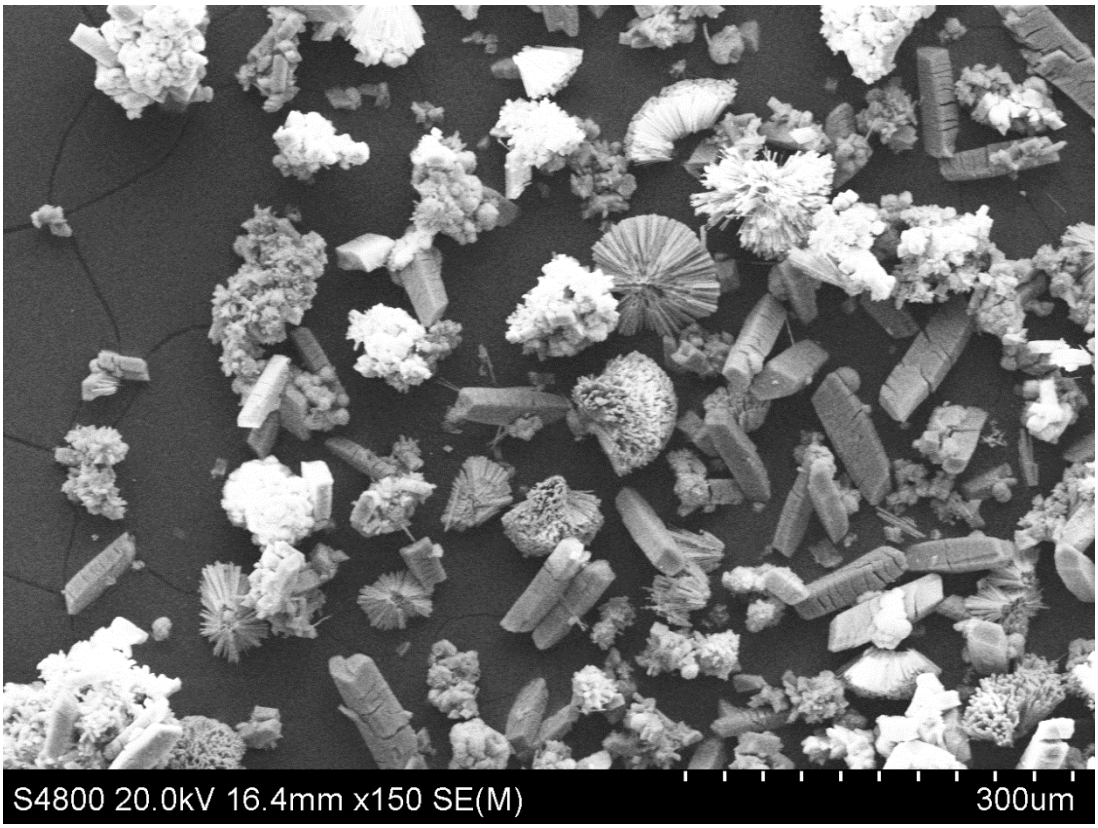

Figure 101: SEM Image of the product from the synthesis which produces diffracting single crystals.

5.2.3. Phase Pure Powder Synthesis.

Another synthesis, identified through the high throughput exploration, was carried out. $Eu(NO_3)_3.5H_2O$ (68.5 mg 10 mM) and $TBAPyH_4$ (109 mg 10 mM) were dissolved in 1,4-dioxane (8ml), water (4 ml), DMF (2 ml) and MeOH (2 ml) in a 40 ml glass vial with a Teflon lined lid. This was then heated at a rate of 2.0 °C min^{-1} to 120 °C and held at this temperature for 72 h before being cooled at a rate of 0.2 °C min^{-1} to room temperature. The resultant yellow solid was filtered and washed with DMF and MeOH.

Attempts to activate this material by conventional means, heating the material under dynamic vacuum and solvent exchange for methanol then applying high vacuum at room temperature both proved unsuccessful as the MOF would lose crystallinity when exposed to vacuum even at room temperature, this is not

uncommon for some MOFs.[15] The solvent within the pores has an attraction to the pore wall of the MOF through surface tension and by removing it can cause the MOF structure to collapse; this can be circumvented by using supercritical CO_2 drying.[16] The EuTBAPy was soaked in ethanol for 24 hours in order to displace all the solvent within the pores. The MOF was then transferred into a cellulose cup keeping it under ethanol at all times. This was then transferred into the supercritical CO_2 drying apparatus. Liquid carbon dioxide was used to flush all of the ethanol out of the pressure vessel. The EuTBAPy is allowed to soak in the liquid CO_2 for several hours flushing with CO_2 every hour to ensure all the ethanol is removed from the pores of the MOF. The pressure vessel is then heated to 38 °C which raises the temperature and pressure above the critical point for CO_2. The super critical CO_2 is then vented slowly overnight ensuring that no liquid CO_2 is formed. This activates the EuTBAPy without affecting the crystallinity as the super critical CO_2 has no surface tension to collapse the pores.

5.3. Characterisation.

5.3.1.SCXRD

From the synthesis in pure 1,4-dioxane large enough crystals were synthesised to attempt single crystal X-ray diffraction (SCXRD). These crystals were found to be diffracting on the Diamond Synchrotron I19 beamline. The high intensity synchrotron light was needed in order to produce a measurable diffraction pattern from the small, mostly carbon and therefore weakly diffracting MOF crystals. From this pattern the structure of the EuTBAPy MOF could be calculated (see Figure 102). From the crystal structure it can be seen that EuTBAPy contains two different

sized pores along the a axis, one 10.6 Å by 5.0 Å and a narrower pore 8.37 Å by 14.1 Å high of which 75% are filled with 1,4-dioxane from the reaction mixture.

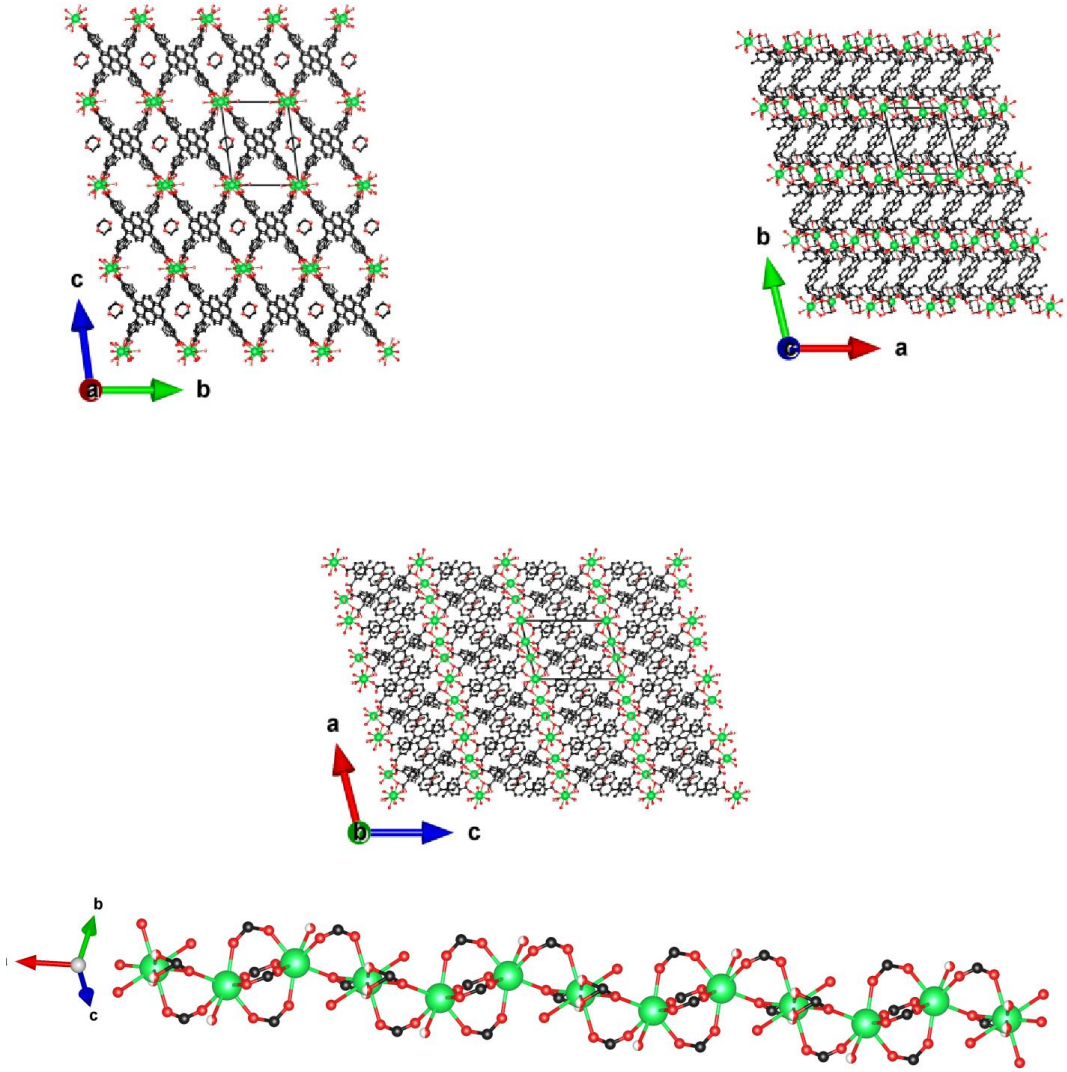

Figure 102: Structure of EuTBAPy from the single crystal X-ray diffraction. Also the Europium chain SBU. Eu is coloured green, O red and C black, partial occupancy is indicated by partially coloured atoms.

The europium secondary building unit (SBU) of the EuTBAPy MOF is composed of infinite chains of europium linked by the TBAPy carboxylates, these chains are made up of three repeating europium ions. Of these three europium ions the central ion is coordinated to two hydroxide ions at 180 ° from each other

perpendicular to the europium chain pointing into the pores of the MOF. This europium ion is also linked to another europium ion on either side by two carboxylates from two TBAPy linkers. The two peripheral europium ions in the three membered repeating chain adopt coordination environments the mirror image of each other; along with the two carboxylate groups shared with the central Europium ion there is also half an hydroxide coordinated to each europium while four TBAPy carboxylate groups link the peripheral europium ion to the first peripheral europium ion in the next three member repeating moiety.

From this single crystal structure shows that the EuTBAPy MOF has a composition of $Eu_3(OH)_3TBAPy_2$ this composition is not charged balanced and has a -2 charge suggesting that there is non-crystalline ions within the MOF to balance the charge. The EuTBAPy MOF adopts a triclinic P-1 space group with unit cell parameters of a= 11.7391(13) Å, b= 13.0474(16) Å, c= 16.460(2) Å, α= 94.775(5) °, β= 102.948(4) °, γ= 101.805(5) °, with a unit cell volume of 2382.93 $Å^3$. Using this unit cell it is possible to identify the presence of this material and the phase purity of the bulk composition of subsequent synthesise using PXRD.

5.3.2. PXRD

The powder X-ray diffraction of EuTBAPy MOF was collected using a Bruker D8 Advance with Cu Kα radiation, in transmission geometry in a sealed 0.7 mm borosilicate spun capillary. The PXRD pattern was indexed using a least squares unit cell refinement to the triclinic P-1 unit cell calculated from the single crystal structure of the EuTBAPy. All the peaks could be indexed using this method showing that the material matched the structure of the single crystal, also ensuring that all the peaks do index to this unit cell showing that the material is phase pure and that there are no other crystalline phases present.

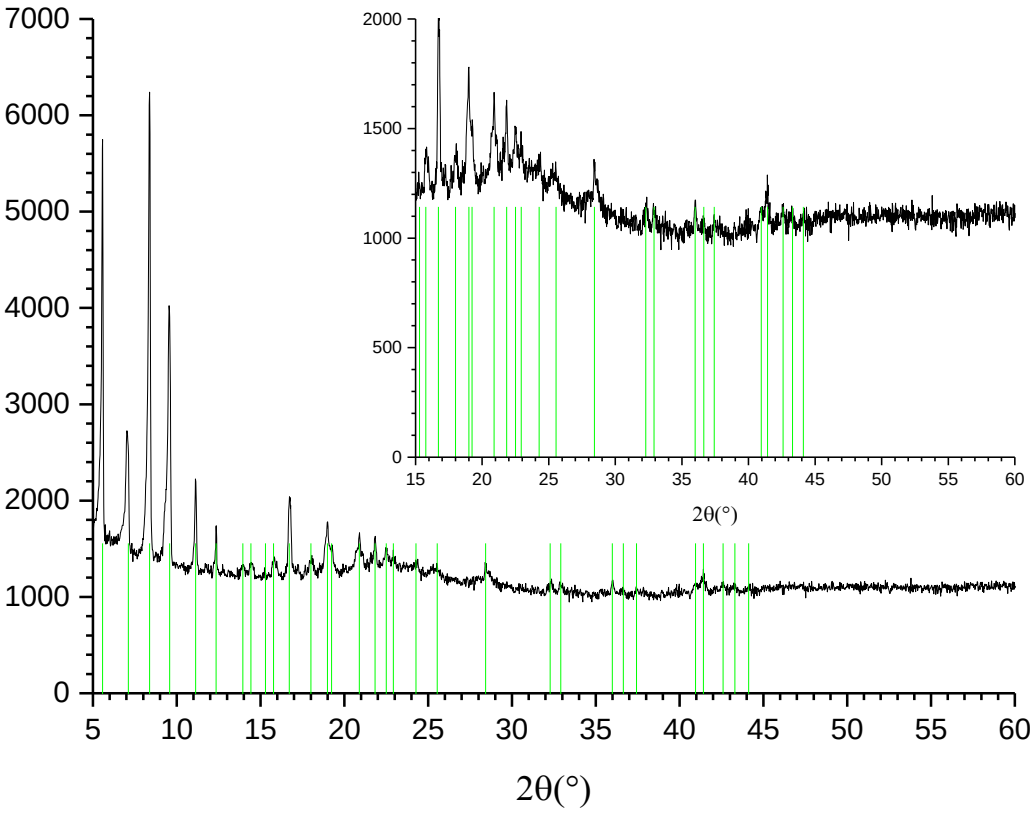

Figure 103: PXRD Pattern of EuTBAPy. Insert of the high angle low intensity region of the pattern. Indexed peaks are identified by green lines.

All the peaks of the PXRD pattern index to the Triclinic P-1 unit cell from single crystal structure (see Figure 103) and give unit cell parameters of a= 11.79(8) Å, b= 13.0(1) Å, c= 16.5(1) Å α= 94.9(1) °, β= 102.85(1) °, γ= 101.76(1) °, with a unit cell volume of 2386.11 $Å^3$. These values are similar to the unit cell parameters calculated from the SCXRD pattern a = 11.7391(13) Å, b= 13.0474(16) Å, c= 16.460(2) Å, α= 94.775(5) °, β= 102.948(4) °, γ= 101.805(5) °, giving a unit cell volume of 2382.9(5) $Å^3$. The fact all the peaks index to this unit cell and the parameters calculated are so similar to those calculated from the SCXRD structure show that the EuTBAPy synthesised adopts the same structure as the single crystal thus suggesting that it is the same material as the single crystal.

5.3.3. SEM

The EuTBAPy was also imaged using SEM to examine the crystallites and to ensure that the material is phase pure and does not contain any amorphous material. The EuTBAPy MOF was spread on carbon tape on an aluminium stub and coated with gold before being imaged with a Hitachi S-4800 Field Emission SEM. From the SEM images (see Figure 104) it can be seen that only one crystallite morphology is present a long rectangular crystallite of varying size. It can be seen that this is the only crystallite present and also that there is no amorphous material present; this again suggests that the EuTBAPy is phase pure.

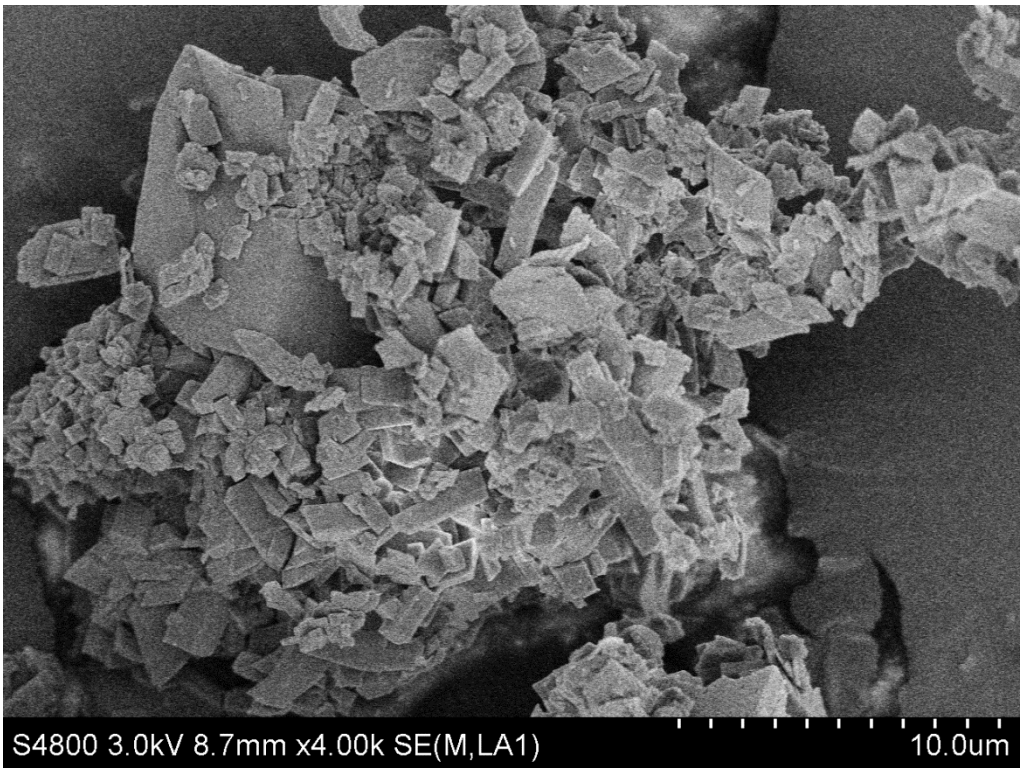

Figure 104: SEM Images of EuTBAPy MOF.

5.3.4. TGA

A TGA analysis was carried out on the EuTBAPy activated by super critical CO_2 drying using a TA Instruments Q600 heating with a heating rate of 0.75 °C min^{-1} with a 100 ml min^{-1} flow of air over the sample (see Figure 105). The TGA shows that the EuTBAPy is thermally stable and only decomposes at a temperature of around 350 °C, this is consistent with MOFs and is associated with the decomposition of the TBAPy linker.[17] Also from the unchanging inorganic residue remaining at high temperatures the europium content of the EuTBAPy MOF can be calculated by multiplying the residual 25.96 % composed of Eu_2O_3 by the europium mass composition for Eu_2O_3 which is 86.36%. This shows that EuTBAPy has an europium composition of 22.41 %. This can be combined with the carbon and hydrogen composition determined by CHN-Elemental analysis and compared to the composition expected from the crystal structure.

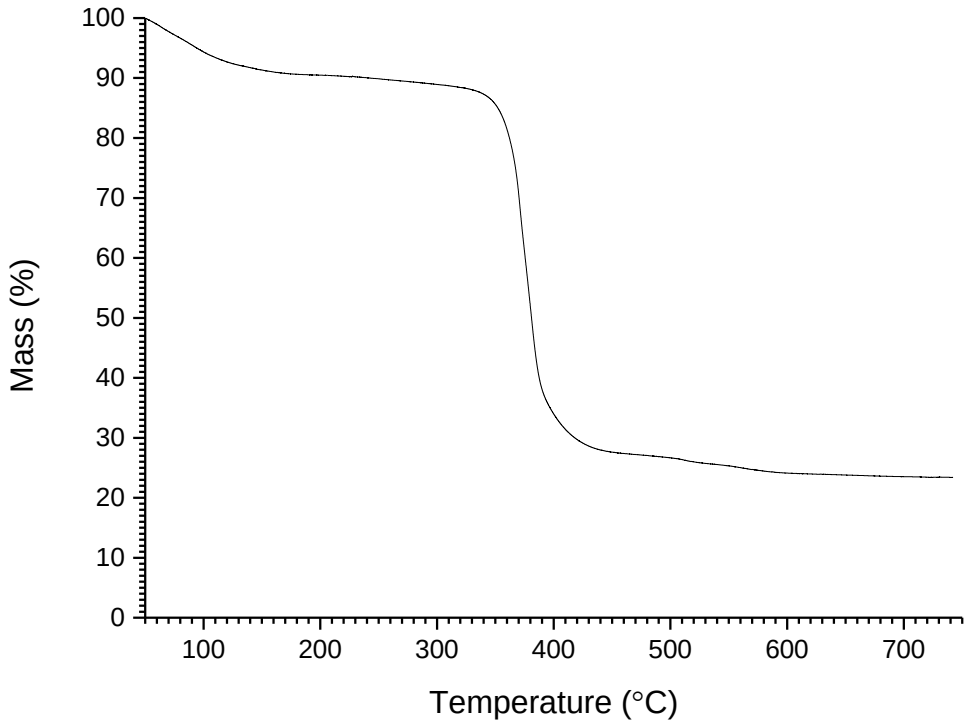

Figure 105:TGA of EuTBAPy.

Also from the TGA it can be seen that there is a large mass loss between 50 °C and 150 °C of 8.88 %. This corresponds to the loss of solvent from within the pores of the MOF. As this MOF has been activated this is due to moisture adsorbed from the air, an 8.88% mass loss corresponds to 10.08 molecules of H_2O per $Eu_3(OH)_3TBAPy_2$. This is a large amount of water adsorbed by the MOF from the atmosphere. The amount of water adsorbed can be checked by elemental analysis.

5.3.5. Elemental analysis.

A CHN elemental analysis was carried out on the EuTBAPy using an Isoprime CHNS Elemental Analyzer, from this it could be seen that the sample contained by mass 55.87 % carbon, 3.14 % hydrogen and 0 % nitrogen; the 0 % nitrogen composition shows that all the $Eu(NO_3)_3$ was removed during the washing and all the DMF was removed during the activation procedure. These results can be combined with the 22.41 % europium content obtained from the TGA to show the composition of the EuTBAPy MOF. From the single crystal structure it is known that the expected composition of the MOF is $Eu_3(OH)_3TBAPy_2$, this has a composition of 56.70 % carbon, 2.54 % hydrogen and 24.45 % europium. The expected carbon and europium composition is higher than the measured values while the expected hydrogen composition is lower than the values measured. As EuTBAPy is a porous MOF it will adsorb moisture from the air as can clearly be seen on the TGA, by adding 12.3 molecules of H_2O to the theoretical composition a theoretical mass composition of 50.67 % carbon, 3.46 % hydrogen and 21.86 % europium is calculated; this is much closer to the measured composition (see Figure 106). The 12.3 molecules of water per $Eu_3(OH)_3TBAPy_2$ is similar to the 10.8 molecules measured by the TGA, this is a large amount of water to be adsorbed quickly from

the air. However as determined from the crystal structure the EuTBAPy MOF contains unsaturated europium sites, europium has a strong affinity to hard electron donors such as the oxygen in water and will coordinate to it readily, this could explain why so much water is adsorbed so quickly from the atmosphere.

$Eu_3(OH)_3(C_{16}H_6(C_6H_4CO_2)_4)_2.\ 12.3H_2O$		
Element	Measured composition	Theoretical Composition
C	50.13 %	50.67 %
H	3.11 %	3.46 %
Eu	22.41 %	21.86 %

Figure 106: Table comparing the measured and expected mass compositions for the EuTBAPy MOF.

5.3.6. Surface Area Measurements.

We can see from the crystal structure of EuTBAPy that the MOF contains several different microporous channels running through the material (see Figure 102). The surface properties of EuTBAPy MOF were therefore studied using a Micromeritics 3Flex Surface Characterisation Analyser utilising N_2 as an adsorbate at 77K. The adsorption isotherm was measured (see Figure 107) and shows sharp initial adsorption at low pressure followed by a plateau, this is characteristic of a Type I isotherm. Type I isotherms are characteristic of microporous materials; where a monolayer of nitrogen condenses on the surface of the pores at low pressure before the pore volume becomes filled with the adsorbate the microporous pores being too small to adsorb further and become saturated.[18] From the crystal structure the pore size diameter can be seen to be under the 2nm defined by IUPAC as the maximum size for a microporous material and therefore the type I isotherm seen is as would be expected.[18]

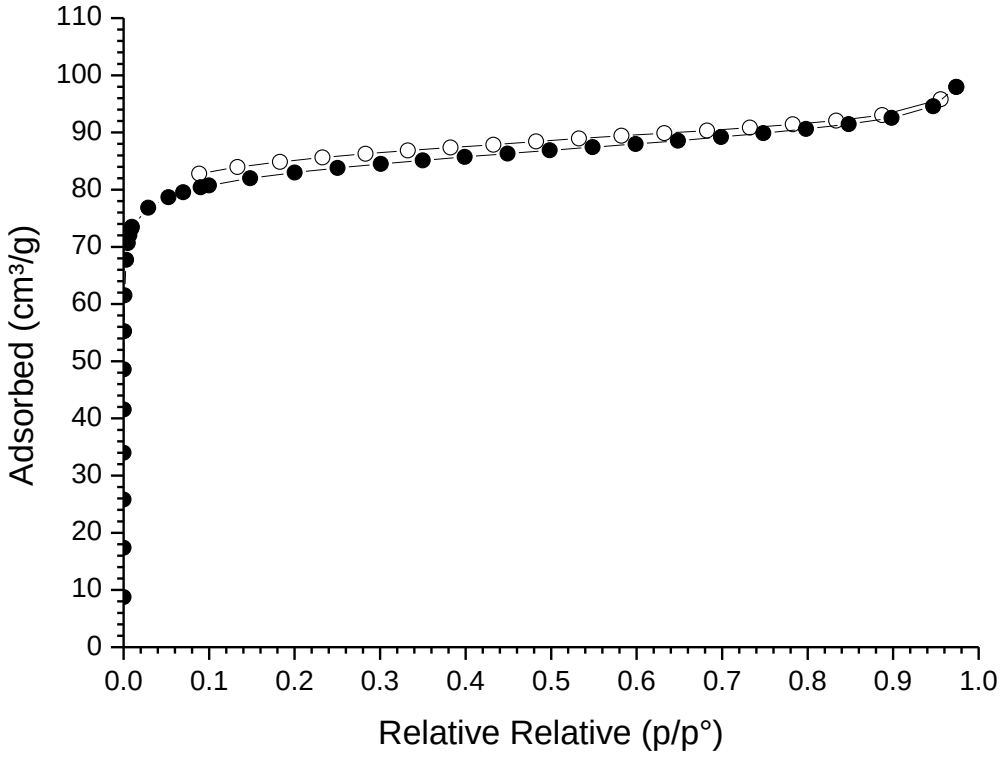

Figure 107: Nitrogen adsorption isotherm at 77K for EuTBAPy, filled circles representing the adsorption isotherm & empty circles representing the desorption isotherm.

The adsorption volume however is much smaller than would be expected; at P/P^0= 0.90 the volume of nitrogen adsorbed can be seen to be 93.3 cm^3g^{-1}, by multiplying this by the nitrogen gas/liquid conversion factor of 0.0015 this shows that the pore volume of EuTBApy is 0.140 cm^3g^{-1}. [18] Using OLEX2 crystallographic software the pore volume can be calculated from the crystal structure by simulating a rolling sphere with probe diameter of 1.8 Å, similar to that of a nitrogen molecule travelling through the pores of the MOF. The calculation shows that the EuTBAPy MOF should have a pore volume of 0.253 cm^3g^{-1}this is much larger than the measured pore volume of 0.140 cm^3g^{-1}.[19] The Brunauer-Emmett-Teller (BET) model has been applied to the nitrogen adsorption isotherm between P/P^0 pressure ranges of 0.005 and 0.03 to give a calculated BET surface area for EuTBAPy of

329.1 m^2g^{-1}.[20] This surface area is very low for what should be a highly porous material.

The PXRD of the EuTBAPy after the adsorption isotherm was measured and it could be seen that there was a significant reduction in the crystallinity (see Figure 108). It is known from the elemental analysis that EuTBAPy has a high affinity for water and will readily adsorb moisture from the air, it is also known from attempts to activate the material that exposure to vacuum results in a reduction in crystallinity. It is apparent that even though the sample was transferred from the supercritical CO_2 pressure vessel, into the BET tube and placed under vacuum as quickly as possible enough moisture was adsorbed from the air into the pores of the EuTBAPy to cause the pores to collapse when exposed to vacuum. How quickly moisture is adsorbed and how much of an effect it has on the crystallinity when removed again suggests that the moisture from the air is coordinating to the unsaturated europium ions in the MOF which will have a large affinity for hard electron donors such as the oxygen in water and when removed will damage the lanthanide chain SBU which holds the MOF together.[15]

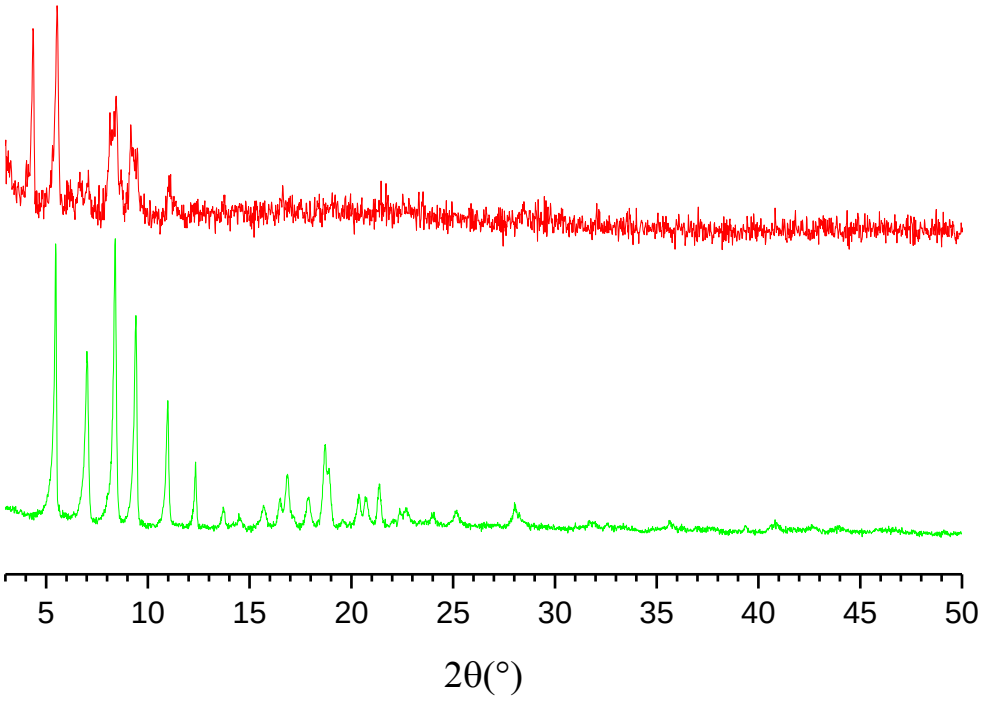

Figure 108: PXRD of EuTBAPy after supercritical CO_2 activation but before the adsorption isotherm was measured (green) and PXRD of EuTBAPy after adsorption isotherm measurement (red).

5.3.7. Optical Spectroscopy.

5.3.7.1. UV/Vis

The diffuse reflectance UV/Vis Spectrum of EuTBAPy MOF and the unreacted $TBAPyH_4$ ligand were measured using a Perkin Elmer Lambda 650 S UV/Vis Spectrometer (see Figure 109). The spectrum shows a large adsorption at 450 nm for the EuTBAPy MOF and at 480 nm for the free $TBAPyH_4$ linker. These large absorptions in the region of the spectrum from 200 nm to 500 nm are associated with the $\pi \rightarrow \pi^*$ transition.[21] This is to be expected from a molecule like TBAPy with such a highly conjugated pyrene at its core. The absorption wavelength for this $\pi \rightarrow \pi^*$ transition is blue shifted to lower wavelength by 50 nm when the $TBAPyH_4$ is bound to the europium in the MOF to make the EuTBAPy MOF, this

hypsochromic shift is due to the electronegative Eu^{3+} withdrawing electron density from the TBAPy linker and thus widening the gap between the π and π* orbitals.[22]

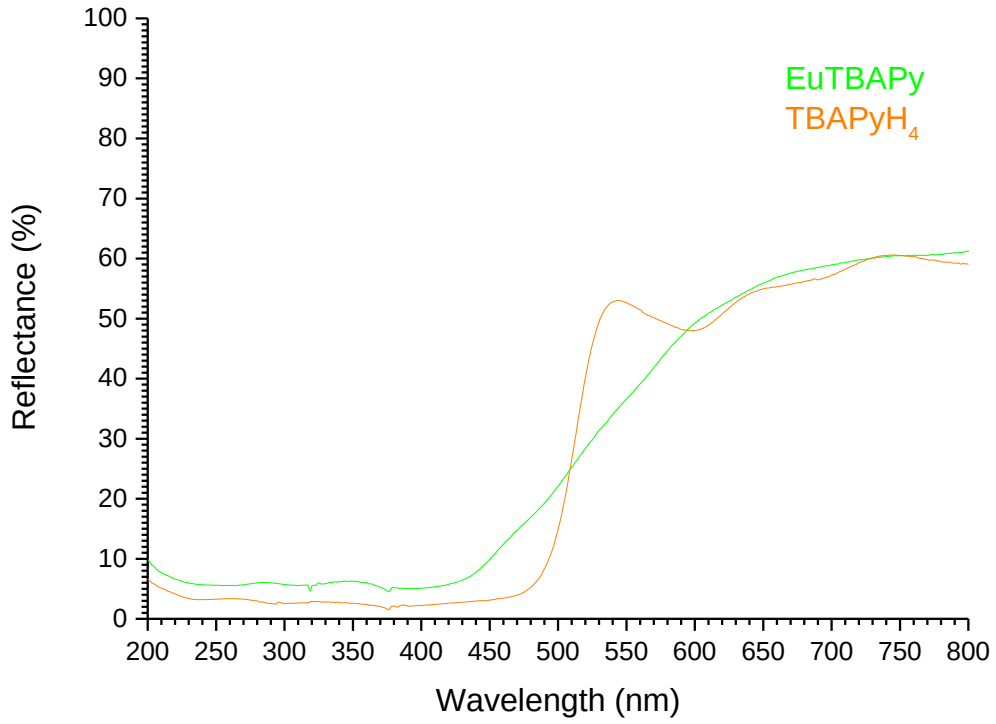

Figure 109: Diffuse reflectance UV/Vis Spectra for EuTBAPy MOF (green) and $TBAPyH_4$ linker (orange).

5.3.7.1. Fluorescence

The fluorescence spectra of the EuTBAPy MOF & the unreacted $TBAPyH_4$ free linker were measured using a Perkin Elmer LS 55 Fluorescence Spectrometer. The samples were measured in the solid state using the maximum absorption wavelength, measured by UV/Vis spectroscopy as the excitation wavelength (see Figure 110).

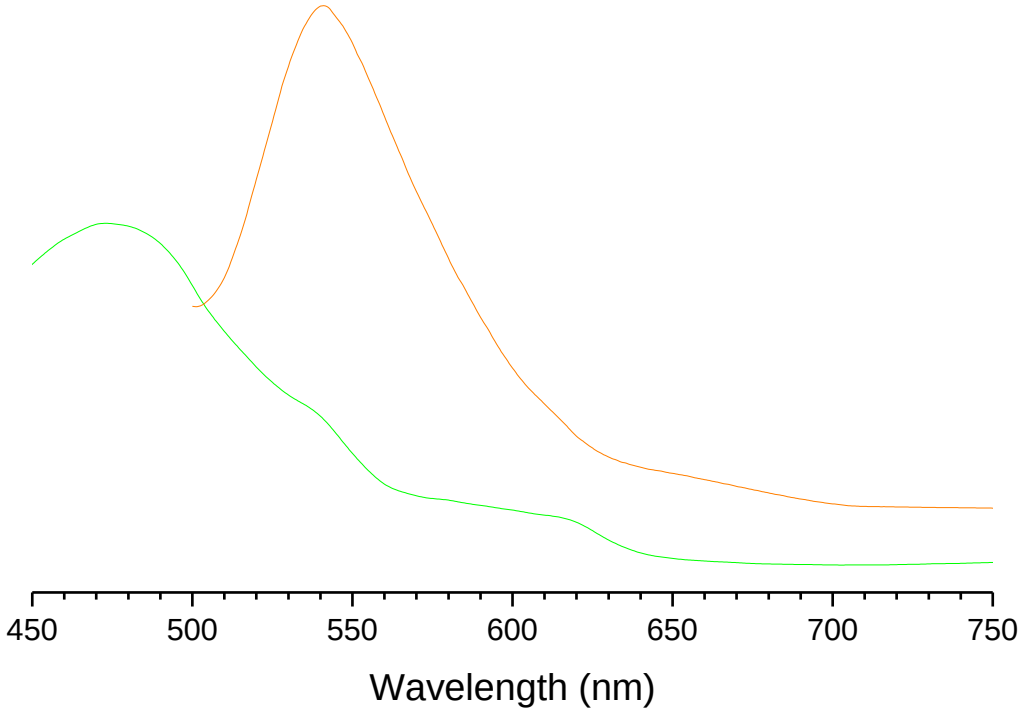

Figure 110: Florescence Spectra of EuTBAPy MOF (green), excited at 400 nm wavelength and TBAPyH$_4$ linker (orange) excited at 470 nm wavelength.

The fluorescence spectrum for EuTBAPy shows a large peak at 470 nm arising from the π* → π transition on the TBAPy linker, like the absorption in the UV/Vis spectrum the fluorescence wavelength has been shifted to a lower wavelength than in the free TBAPyH$_4$ linker due to the electronegative Eu withdrawing electron density from the TBAPy linker, increasing the energy difference between the π and π* orbitals.

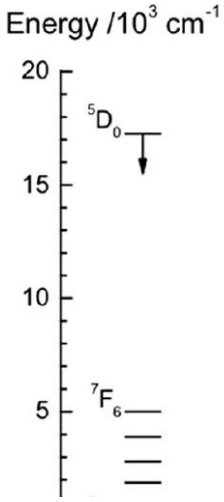

Figure 111: Simplified energy level diagram for Eu^{+3} f orbitals. Figure adapted from reference [14].

The pyrene fluorescence intensity is also significantly reduced suggesting that the energy is being transferred possibly onto the europium ions. There are some small peaks present at 540 nm and 620 nm, these arise from $^5D_0$

$\rightarrow {}^7F_0$ and ${}^5D_0 \rightarrow {}^7F_2$ transitions on the europium (see Figure 111).[2] This europium fluorescence suggests that the TBAPy is acting as an antenna for the europium. However the fluorescence spectrum is still dominated by the pyrene fluorescence suggests that energy transfer is not very efficient. Although the weakness of the europium fluorescence may be due to quenching of the europium excited state by the hydroxide which is known to be coordinated to the europium from the crystal structure or the large amount of water readily adsorbed into the pores measured by CHN analysis. The fact that these small lanthanide fluorescence peaks are not visible in unactivated samples or activated samples which have been left exposed to the moisture in the atmosphere also suggests that their low intensity is due to quenching.[10]

5.4. Conclusion

A new EuTBAPy MOF has been synthesised and characterised, the first lanthanide TBAPy MOF. Through a thorough exploration of reaction conditions utilising high throughput synthesis techniques two reaction conditions have been identified, one able to produce large amounts of phase pure EuTBAPy MOF the other able to produce crystals of suitable size for SCXRD analysis. From the SCXRD analysis it has been possible to calculate the structure of the EuTBAPy MOF and to see that it is composed of chains of $Eu(OH)_2$ connected through the carbonyl groups of 3 TBAPy linkers to $Eu(OH)_{0.5}$, these three member SBUs are linked through 4 TBAPy carbonyls with each TBAPy linker linking 4 of these chains producing a porous structure. With knowledge of the crystal structure it has then been possible to characterise the phase pure powder material by PXRD, elemental analysis, TGA, UV/Vis and Fluoresce spectroscopy.

1. Y. Chen and S. Ma, *Reviews in Inorganic Chemistry*, 2012, **32**, 81-100.
2. S. Dang, E. Ma, Z. Sun and H. Zhang, *Journal of Materials Chemistry*, 2012, **22**, 16920-16926.
3. C. G. Efthymiou, E. J. Kyprianidou, C. Milios, M. J. Manos and A. J. Tasiopoulos, *Journal of Materials Chemistry A*, 2013, **1**, 5061-5069.
4. X. Zhao, Teng, M. Xue, G. Zhu, Q. Fang and S. Qui, *Journal of Molecular Structure*, 2009, **931**, 25-30.
5. Y. Cui, H. Xu, Y. Yue, Z. Guo, J. Yu, Z. Chen, J. Gao, Y. Yang, G. Qian and B. Chen, *Journal of the American Chemical Society*, 2012, **134**, 3979-3982.
6. H. Li, Z. Niu, T. Han, Z. Zhang, W. Shi and P. Cheng, *Science China: Chemistry*, 2011, **54**, 1423-1429.
7. E. G. Moore, A. P. Samuel and K. N. Raymond, *Accounts of Chemical Research*, 2009, **42**, 542-552.
8. J. B. Birks, A. A. Kazzaz and T. A. King, *Proceedings of the Royal Society A: Mathematical, Physical and Engineering Sciences*, 1966, **291**, 556-569.
9. R. Katoh, K. Suzuki, A. Furube, M. Kotani and K. Tokumaru, *Journal of Physical Chemistry C*, 2009, **113**, 2961-2965.
10. J. S. Sohna and F. Fages, *Thtrahedron Letters*, 1997, **38**, 1381-1384.
11. K. A. White, D. A. Chengelis, K. A. Gogick, J. Stehman, N. L. Rosi and S. Petoud, *Journal of the American Chemical Society*, 2009, **131**, 18069-18071.
12. T. Liu, W. Zhang, W. Sun and R. Cao, *Inorganic Chemistry*, 2011, **50**, 5242-5248.
13. J. Luo, H. Xu, Y. Liu, Y. Zhao, L. L. Daemen, C. Brown, T. Timofeeva, S. Ma and H. Zhou, *Journal of the American Chemical Society*, 2008, **130**, 9626-9627.
14. R. Decadt, K. Hecke, D. Depla, K. Leus, D. Winberger, I. Driessche, P. Voort and R. Deun, *Inorganic Chemistry*, 2012, **51**, 11623-11634.
15. P. Deria, Y. G. Chung, S. Randall, J. T. Hupp and O. K. Farha, *Chemical Science*, 2015, **6**, 5172-5176.
16. A. P. Nelson, O. K. Farha, K. L. Mulfort and J. T. Hupp, *Journal of the American Chemical Society*, 2009, **131**, 458-460.
17. K. C. Stylianou, R. Heck, S. Y. Chong, J. Bacsa, J. T. Jones, Y. Z. Khimyak, D. Bradshaw and M. J. Rosseinsky, *Journal of the American Chemical Society*, 2010, **132**, 1-12.
18. K. S. Sing, D. H. Everett, R. A. Haul, L. Moscou, R. A. Pierotti, J. Rouqiérol and T. Siemieniewska, *Pure and Applied Chemistry*, 1985, **57**, 1365-3075.
19. O. V. Dolomanov, L. J. Bourhis, R. J. Gildea, J. A. K. Howard and H. Ouschmann, *Journal of Applied Crystalography*, 2009, **42**, 339-341.
20. S. Brunauer, P. H. Emmett and E. Teller, *Journal of the American Chemical Society*, 1938, **60**, 309-319.
21. Y. Zhiu, X. Shen, Chen-Xia, B. Wu and H. Zhang, *European Journal Of Inorganic Chemistry*, 2008, 4280-4289.
22. J. Gascon, M. D. Hernández-Alonso, A. R. Almeida, G. P. van Klink, F. Kapteijn and G. Mul, *ChemSusChem*, 2008, **1**, 981-983.

6. Conclusion.

The aim of this work was to synthesise pyrene based metal organic frameworks, to characterise them and to test their applications for photocatalysis. A new aluminium pyrene based MOF (AlTBAPy) was synthesised based on the reported indium pyrene MOF. The AlTBAPy MOF was thoroughly characterised and shown to be phase pure when synthesised, highly porous, strongly absorbing of visible light and fluorescent. The water splitting photocatalytic properties of AlTBAPy and the reported zirconium TBAPy MOF NU-1000 were explored for the first time. It was discovered that although no hydrogen is produced. However it was found that these MOFs are optically active, capable of reducing methyl viologen, a common electron transfer reagent which should be able to proceeded with the hydrogen evolution reaction. It was clear after allowing the suspension to settle that the methyl viologen although reduced was trapped within the pores of the MOF. TEM images confirmed that the essential platinum cocatalyst was conglomerating on the surface and not entering the pores thus no reaction could proceed. Platinum nanoparticles were deposited within these MOFs for the first time and this procedure was confirmed to be successful through TEM, nitrogen adsorption isotherms and elemental analysis. The photocatalysis experiment was repeated to the same result. This suggests that despite both the reduced methyl viologen and the platinum nanoparticles being within the pores of the MOFs there was still no interaction between them; or the methyl viologen had been stabilised through strong $\pi - \pi$ and cation $- \pi$ interactions with the MOFs. The AlTBAPy also was measured for carbon capture and storage and methane adsorption. The heat of adsorption for methane was close to the required value. Despite AlTBAPy having similar sized and shaped pore channels to what has been theoretically calculated as optimum and a comparable heat

of adsorption and capacity for other MOFs of its type there are superior MOFs reported for CO_2 adsorption.

Also a new europium TBAPy MOF was synthesised utilising high throughput techniques to thoroughly explore the reaction space. Single crystals were produced and the structure calculated from the single crystal XRD pattern. A phase pure powder was also synthesised by a different set of conditions and characterised. However the EuTBAPy MOF had a large affinity to water and was unstable when this was removed meaning a complex activation procedure involving solvent exchange and super critical drying was required and that an adsorption isotherm of the MOF was difficult to measure.

These pyrene based MOFs do show promise for the future, the fact that they are capable of reducing methyl viologen when exposed to visible light shows that they are photochemically active, it may be possible to use a different electron transfer reagent or adjust the interaction between the methyl viologen and the surface of the MOF to enable them to produce hydrogen gas. The addition of metal nanoparticles to the pores of MOFs also opens up opportunities for catalysis and gas adsorption the fact that AlTBAPy and ZrTBAPy can undergo platinum insertion and retain their crystallinity and structure could lead to other applications. The AlTBAPy MOF showed some promise for gas storage applications, a useful heat of adsorption for methane and acceptable absorption properties for CO_2. Using the TBAPy linker in a MOF with open metal sites or incorporating an amine functional group to the pyrene could enhance the adsorption properties of the MOF. The EuTBAPy MOF though difficult to activate does show some interesting fluorescent properties where the pyrene can act as an antenna for the europium. However the europium

fluorescence is quickly quenched by moisture in the air, this suggests that it could have sensing applications in anhydrous environments.